

Seton Hall University

eRepository @ Seton Hall

Seton Hall University Dissertations and Theses
(ETDs)


Seton Hall University Dissertations and Theses

Fall 12-19-2018

Stabilized, Hybrid Solid-State Photocatalysts for Water Purification: Preparation, Properties and Performance under Visible Light Irradiation

Karpagavalli Ramji
kramji7@gmail.com

Follow this and additional works at: <https://scholarship.shu.edu/dissertations>

 Part of the [Analytical Chemistry Commons](#), [Environmental Chemistry Commons](#), [Inorganic Chemistry Commons](#), [Materials Chemistry Commons](#), [Organic Chemistry Commons](#), [Other Chemistry Commons](#), and the [Polymer Chemistry Commons](#)

Recommended Citation

Ramji, Karpagavalli, "Stabilized, Hybrid Solid-State Photocatalysts for Water Purification: Preparation, Properties and Performance under Visible Light Irradiation" (2018). *Seton Hall University Dissertations and Theses (ETDs)*. 2603.

<https://scholarship.shu.edu/dissertations/2603>

**Stabilized, Hybrid Solid-State Photocatalysts for Water
Purification: Preparation, Properties and Performance
under Visible Light Irradiation**

DISSERTATION

*Submitted to the faculty of the Department of Chemistry and Biochemistry
in the School of Arts and Sciences as partial fulfillment of the requirements for the degree of
Doctor of Philosophy.*

*Seton Hall University
400 South Orange Avenue
South Orange, New Jersey 07079*

Karpagavalli Ramji

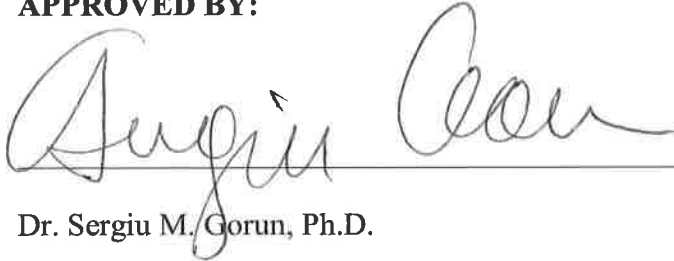
December 2018

Copyright © 2018 by Karpagavalli Ramji

ALL RIGHTS RESERVED

We certify that we have read this dissertation and that in our opinion it is adequate in scientific scope and quality as a dissertation for the degree of Doctor of Philosophy.

APPROVED BY:



12/4/2018

Dr. Sergiu M. Gorun, Ph.D.

Date

Research Mentor, Member of Dissertation Committee

Seton Hall University



12/5/18

Dr. Stephen P. Kelty, Ph.D.

Date

Reader, Member of Dissertation Committee

Seton Hall University



12.05.2018

Dr. Alexander Fadeev, Ph.D.

Date

Member of Dissertation Committee

Seton Hall University



12/5/18

Dr. Stephen P. Kelty, Ph.D.

Date

The Chair, Department of Chemistry and Biochemistry

Seton Hall University

ABSTRACT

Stabilized heterogeneous photocatalysts that use only solar light and air have been prepared and successfully employed to decontaminate water by removing organic pollutants. Organic dye pollutants present, for example in textile effluents are one of the major sources of water pollution owing to their limited biodegradability, toxicity and potential carcinogenic risks. Before certifying water for public consumption, reuse in industries or for discharge in surface water the organic pollutants must be degraded, an effort that is energy intensive and currently requires complex methodologies.

We report solid-state photocatalysts that use only visible light and air to treat wastewater. Perfluoroalkyl perfluoro-substituted zinc phthalocyanine $F_{64}PcZn$, an efficient and stable photocatalyst, deposited on micrometer to nanometer size SiO_2 and TiO_2 particles as well as on polytetrafluoroethylene, polyethersulfone and polypropylene membranes has been shown to be active for the photodegradation of the model organic pollutants methyl orange, rhodamine B and methyl red.

Our investigation suggests $F_{64}PcZn$ is adsorbed on TiO_2 through the interaction of central zinc atom and fluorine atoms of peripheral $-CF_3$ group. Total organic carbon and total dissolved nitrogen in water decreased after photoreactions catalyzed by $F_{64}PcZn/SiO_2$ and $F_{64}PcZn/TiO_2$. The fragmentation of organic dye pollutants is confirmed by 1H -NMR, HPLC and LC-MS studies. Moreover, HPLC and LC-MS analyses suggest the adsorption of rhodamine B is different on bare TiO_2 as compared to $F_{64}PcZn/TiO_2$, possibly because of the difference in their surface charges. Zeta potential measurements show that the surface of $F_{64}PcZn/TiO_2$ contains negative charges, thus readily interacting with positive groups of dye pollutants. The examination of the effect of

variable F₆₄PcZn loading amounts on SiO₂ and TiO₂ by fluorescence and UV-Vis-NIR spectral measurements indicate an optimum amount of F₆₄PcZn needs to be deposited on SiO₂ and TiO₂ particles. Too much of F₆₄PcZn deposition leads to either aggregation or decrease in the fluorescence of the hybrid photocatalyst. F₆₄PcZn/TiO₂ is stable even under UV light irradiation in contrast to hybrids produced with commercial phthalocyanines, namely H₁₆PcZn/TiO₂ and F₁₆PcZn/TiO₂. The F₆₄PcZn/TiO₂ catalytic efficiency is higher than that of H₁₆PcZn/TiO₂ and F₁₆PcZn/TiO₂. F₆₄PcZn/TiO₂ can be used for several cycles without any loss in the catalyst efficiency. Hence, a stable as well as an efficient hybrid photo catalyst is synthesized to purify water using renewable resources.

The current study also reveals that there is no orbital coupling between F₆₄PcZn and the matrices SiO₂ and TiO₂. In contrast, when F₆₄PcZn is deposited on NiO, a narrow-gap semiconductor an orbital coupling does occur, resulting in the quenching of the photoproduction of singlet oxygen by F₆₄PcZn/NiO under white light illumination. An electron transfer from the conduction band of excited NiO into the singly-occupied HOMO of excited F₆₄PcZn, followed by the opposite transfer from the singly-occupied LUMO of excited F₆₄PcZn to NiO is assumed to rapidly return the excited phthalocyanine to its singlet-ground state and thus block the inter-system crossing process necessary to produce singlet oxygen.

ACKNOWLEDGEMENTS

It is a pleasure to thank my research mentor Prof. Sergiu M. Gorun and Prof. Stephen P. Kelty, the Chair of the Department, for giving me the opportunity to join as a graduate student in the Department of Chemistry at Seton Hall University in 2012. I would like to express my sincere gratitude to Prof. Gorun for his continuous support, patience and motivation during the PhD research work and thesis writing. Special thanks to Prof. Kelty and Prof. Alexander Y. Fadeev for their comments and guidance on scientific research and reading my thesis. Besides my thesis readers, I want to thank rest of the thesis committee, Prof. Wyatt R. Murphy and Prof. James E. Hanson for their insightful comments and encouragement.

Special thanks go to Hemantbhai H. Patel and Erik N. Carrion for providing purified phthalocyanine compounds, without their timely support this work is impossible. Thanks Hemant for your advices and continuous encouragement. My hearty thanks to Marius Pelmus, Olivia C. Xiao and Christopher A. Colomier for their wonderful last-minute favors. I have greatly benefitted from other group members especially Abdul Azeez and Mufeda Zhort during several occasions. I want to thank Marius and Mufeda for their help with $^1\text{H-NMR}$ experiments. Special thanks to Abdul Azeez for his kind help with HPLC, LC/MS and couple of other experiments in my absence. I do want to express my appreciation to my fellow lab mates past and present for their sustainable assistance, cooperation and wonderful suggestions.

I want to acknowledge the Department of Chemistry, Seton Hall University for providing teaching assistantship throughout the PhD program. I also want to thank the Department of Defense for extending financial support and providing XRD data for the photocatalysts.

I want to extend my gratitude to Dr. Roman Brukh in the Chemistry instrumentation facility at Rutgers, Newark and Dr. Ryan Thorpe at Rutgers, Piscataway for aiding with SEM, FTIR and XPS analyses.

I am grateful to the secretary in the Chemistry Department, Ms. Maureen Grutt for assisting me in many ways. My sincere thanks go to Mr. Gabriel F. Benavides, Electric Propulsion Engineer at NASA Glenn Research Center, Cleveland, Ohio for offering me the summer internship from Jun to Aug 2018 that lead to an opportunity to work on a diverse exciting project.

Finally, I thank my lovable parents Mr. Ramji Kanagasabapathi and Mrs. Rajalakshmi Ramji who always offer unconditional support and affection. Most importantly, I want to thank my spouse Mr. Sundaresan Subramaniam for his all-time moral support. There are no words to thank my daughter Punya S. Sundaresan for her cooperation in staying with her grandparents, easing her Mom with thesis writing, wrapping up PhD work and job hunting.

CONTENTS

Abstract.....	iv
Acknowledgments.....	vi
Contents	viii
List of Tables	xv
List of Figures	xvi
1 Introduction: Solid-State Photocatalysts for Wastewater Treatment.....	1
1.1 Organic Pollutants in Wastewater.....	1
1.2 Advanced Oxidation Processes for Wastewater Treatment.....	2
1.3 Photocatalytic Wastewater Treatment using Titanium Dioxide	3
1.4 Stabilized Perfluoroalkyl Perfluoro Phthalocyanine as Photosensitizer for Wastewater Treatment	4
1.5 Hybrid F ₆₄ PcZn Deposited Solid-State Photocatalysts for Wastewater Purification.....	6
1.6 Model Organic Dyes: Methyl Orange, Rhodamine B and Methyl Red.....	8
References.....	10
2 Perfluoroalkyl Perfluoro Phthalocyanine Supported on SiO ₂ for Water Decontamination.....	13
2.1 Introduction.....	13
2.2 Materials and Methods.....	16
2.2.1 Materials	16
2.2.2 Preparation of hybrid catalysts.....	17
2.2.3 Photochemical Reactions	18

2.2.4	Fluorescence Emission Intensity Measurements	19
2.2.5	Particle Size and Zeta Potential Measurements	20
2.2.6	Determination of Total Organic Carbon (TOC) and Total Dissolved Nitrogen (TDN)	20
2.2.7	UV-Vis-NIR Reflectance Spectral Measurements of Hybrid Catalysts	20
2.2.8	X-ray Diffraction Analysis of F ₆₄ PcZn/SiO ₂	20
2.2.9	X-ray Photoelectron Spectroscopy Analysis of F ₆₄ PcZn/SiO ₂	21
2.3	Results and Discussion	21
2.3.1	Efficiency of F ₆₄ PcCu/SiO ₂ to Degrade MO under Visible Light Irradiation.....	21
2.3.2	Comparison of Photocatalytic Efficiency of F ₆₄ PcCu/SiO ₂ and F ₆₄ PcZn/SiO ₂	22
2.3.3	Evaluation of Photostability of F ₆₄ PcCu and F ₆₄ PcZn Deposited on SiO ₂ ..	25
2.3.4	F ₆₄ PcCu/SiO ₂ Versus F ₆₄ PcZn/SiO ₂	26
2.3.5	Variation in Catalyst Ratio of F ₆₄ PcZn/SiO ₂ Composite Particles	26
2.3.6	Influence of Particle Size, Type, Surface Area, and Pore Structure on the Efficiency of Hybrid Photocatalysts	28
2.3.7	Particle Size Distribution of F ₆₄ PcZn/SiO ₂ Catalysts	29
2.3.8	Kinetics Study on Degradation of MO Catalyzed by F ₆₄ PcZn Deposited on 63-200 μm, 4-12 μm, 10-20 nm and 40 nm SiO ₂	31
2.3.9	Fluorescence intensity of F ₆₄ PcZn/10-20 nm SiO ₂ and F ₆₄ PcZn/OX50 catalysts.....	34

2.3.10	Influence of Oxygen on the Photocatalytic Activity of F ₆₄ PcZn/SiO ₂	35
2.3.11	Rhodamine B (RhB) Photodegradation Catalyzed by F ₆₄ PcZn/SiO ₂ 10-20 nm and F ₆₄ PcZn/SiO ₂ OX50.....	38
2.3.12	Mechanism Involved in the Photodegradation Process of Organic Pollutants.....	41
2.3.13	Determination of TOC and TDN for Photodegraded RhB Catalyzed by F ₆₄ PcZn/SiO ₂	42
2.3.14	Change in Zeta Potential for F ₆₄ PcZn/ SiO ₂ Catalysts.....	44
2.3.15	Influence of F ₆₄ PcZn Molar Concentration on Photo Efficiency and Fluorescence Intensity	45
2.3.16	UV-Vis-NIR Spectral Analysis of Catalysts with Various Amounts of F ₆₄ PcZn Deposited on SiO ₂	48
2.3.17	Hybrid catalyst characterization by XRD analysis	49
2.3.18	Mode of F ₆₄ PcZn Adsorption on SiO ₂	50
2.3.19	Recycling Ability of F ₆₄ PcZn/SiO ₂ Hybrid Catalysts	54
2.4.	Conclusions.....	55
	References.....	56
3	Enhanced Visible Light Photocatalysis using Perfluoroalkyl Perfluoro Phthalocyanine Zinc/TiO ₂ Hybrid Photocatalyst for Water Purification	59
3.1	Introduction.....	59
3.2	Experimental Section	63
3.2.1	Materials	63
3.2.2	Synthesis of F ₆₄ PcZn/P25 and F ₆₄ PcZn/P90 Hybrid Catalysts.....	63

3.2.3	Photochemical Reactions	64
3.2.4	Fluorescence Emission Spectral Measurements for H ₁₆ PcZn, F ₁₆ PcZn and F ₆₄ PcZn Deposited on TiO ₂	66
3.2.5	Photoreaction under UV only, UV +Visible and red-light Irradiations.....	66
3.2.6	Photostability of F ₆₄ PcZn in Comparison to H ₁₆ PcZn and F ₁₆ PcZn Deposited on P25 under UV Light Irradiation.....	67
3.2.7	Particle Size and Zeta Potential Measurements	67
3.2.8	UV-Vis-NIR Reflectance Spectral Measurements	68
3.2.9	X-ray Photoelectron Spectroscopy Measurements	68
3.2.10	X-ray Diffraction Analysis	68
3.2.11	¹ H NMR Analysis	68
3.2.12	High-Pressure Liquid Chromatography and Liquid Chromatography/Mass Spectrometry Analysis of Photodegradation Intermediate Products	69
3.3	Results and Discussion	69
3.3.1	Photodegradation of MO Catalyzed by F ₆₄ PcZn/P25 under Visible Light Irradiation.....	69
3.3.2	RhB Photodegradation Catalyzed by P25 and F ₆₄ PcZn/P25 under Visible Light Irradiation	72
3.3.3	Particle Size Analysis	74
3.3.4	F ₆₄ PcZn/P90 as Photocatalyst for Photodegradation of MO and RhB	76
3.3.5	Kinetic Studies	79
3.3.6	Fluorescence emission spectra for F ₆₄ PcZn deposited on P25 and P90 TiO ₂	83

3.3.7	Commercial Phthalocyanines Versus F ₆₄ PcZn	84
3.3.8	Photostability of F ₆₄ PcZn in Comparison to H ₁₆ PcZn and F ₁₆ PcZn Deposited on P25 under UV Light Irradiation.....	87
3.3.9	Zeta Potential Measurement	89
3.3.10	Influence of UV-Light, Visible-Light, UV + Visible Light and Red-Light Illumination on Catalysis	91
3.3.11	Effect of Visible Light Intensity	95
3.3.12	Radical Intermediates in the Photoinduced Reactions.....	96
3.3.13	Total Organic Carbon (TOC) and Total Dissolved Nitrogen (TDN) Analysis.....	98
3.3.14	pH Determination.....	100
3.3.15	Effect of F ₆₄ PcZn amount deposited on P25.....	100
3.3.16	Change in Fluorescence Intensity with F ₆₄ PcZn Deposition Amount on P25	101
3.3.17	Light Absorption Efficiency of F ₆₄ PcZn/P25 with Varying Amounts of F ₆₄ PcZn: Evaluation using UV-Vis-NIR Spectral Measurements.....	103
3.3.18	Adsorption of Pcs on P25: X-Ray Photoelectron Spectroscopy (XPS) Analyses.....	105
3.3.19	Characterization of F ₆₄ PcZn/P25 Before and After Photocatalytic Reactions using X-Ray Diffraction (XRD) Analysis.....	113
3.3.20	NMR Analysis of RhB Photodegradation Products.....	115
3.3.21	HPLC and LC/MS Analysis of Photodegradation Products of RhB	

Catalyzed by P25 and F ₆₄ PcZn/P25	118
3.3.22 Photostability of F ₆₄ PcZn Deposited on TiO ₂	131
3.4. Conclusions.....	133
References.....	135
Supplementary Material.....	141
4 NiO as a Supporting Matrix for Perfluoroalkyl Perfluoro Phthalocyanine.....	142
4.1 Introduction.....	142
4.2 Materials and Methods.....	142
4.3 Results and Discussion	143
4.4. Conclusions.....	147
References.....	148
5 Zinc Perfluoroalkyl Perfluoro Phthalocyanine Impregnated Polymer Membranes for Water Purification.....	149
5.1 Introduction.....	149
5.2 Materials and Methods.....	153
5.2.1 Materials	153
5.2.2 Development of Hybrid F ₆₄ PcZn Incorporated Polymer Membranes	153
5.2.3 Surface Modification of Polypropylene Membrane: Functionalized Polypropylene Membrane.....	154
5.2.4 Incorporation of F ₆₄ PcZn into Functionalized Polypropylene Membrane	155
5.2.5 Photodegradation Measurements	156
5.2.6 Dynamic Flow Measurements	158

5.2.7	Structural integrity of F ₆₄ PcZn/PP Membrane after MR Photodegradation	159
5.2.8	Microstructural Characterization using Optical and Scanning Electron Microscopy	159
5.2.9	Hydrophobicity of F ₆₄ PcZn Incorporated PTFE Membrane	160
5.3	Results and Discussion	160
5.3.1	Microstructure of F ₆₄ PcZn Loaded PTFE, PES Membranes	161
5.3.2	Contact Angle Measurements for F ₆₄ PcZn Coated PTFE	163
5.3.3	F ₆₄ PcZn/PTFE and F ₆₄ PcZn/PES Membranes: Photodegradation of MO	164
5.3.4	F ₆₄ PcZn/PP Membrane Photocatalytic Degradation of Methyl Red under Static Condition	166
5.3.5	Photodegradation of MR using F ₆₄ PcZn/FPP Membrane for Three Repeated Cycles under Dynamic Condition	167
5.3.6	Evaluation of the Integrity of FPP Membranes after Photoreaction under Dynamic Conditions	168
5.3.7	Comparison of the Microstructure of F ₆₄ PcZn/FPP Membrane before and after MR Photodegradation Reaction	170
5.3.8	Effect of F ₆₄ PcZn Loading Density on Catalytic Efficiency of F ₆₄ PcZn/FPP Membrane	171
5.3.9	Red and White LEDs as Light Sources	173
5.4.	Conclusions	175
	References	176

LIST OF TABLES

Table	Page
2.3.14 Zeta potential for F ₆₄ PcZn hybrid photocatalysts	44
3.3.3 Mean particle size of P25, P90, Pc/P25 and F ₆₄ PcZn/P90 measured in de-ionized water .	76
3.3.5 Reaction rate (<i>k</i>) and regression coefficient (<i>R</i> ²) values for the photodegradation reactions	81
3.3.9 Zeta potential in de-ionized water for TiO ₂ and phthalocyanine/TiO ₂ catalysts.....	89
3.3.14 pH of the Test Solutions Before and After Photoreaction	100
3.3.15 Reaction Rate (<i>k</i>) and Half-life (<i>t</i> _{1/2}) for F ₆₄ PcZn/P25 with Different Deposition Amounts of F ₆₄ PcZn	101
3.3.18 Core Level Binding Energies of Elements.....	107
3.3.19 Particle Sizes Determined from XRD Patterns of P25 and F ₆₄ PcZn/P25	113
3.3.21 Products of <i>N</i> -deethylation of RhB (1). <i>N</i> , <i>N</i> -diethyl- <i>N</i> -ethyl-rhodamine (2), <i>N</i> , <i>N</i> - diethyl-rhodamine (3), <i>N</i> -ethyl-rhodamine (4) and Rhodamine (5)	123
3.3.21 Molecular Structure of the Photodegradation Products Formed due to the Removal of Carboxylic Acid Functional Group.....	127
3.3.21 Confirmation of Predominant <i>N</i> -deethylation of RhB catalyzed by F ₆₄ PcZn/P25	130
4.3 Reaction rates (<i>k</i>) for MO photodegradation catalyzed by F ₆₄ PcZn/NiO, H ₁₆ PcZn/NiO, F ₁₆ PcZn/NiO and F ₆₄ PcCu/NiO.....	146

LIST OF FIGURES

Figure	Page
Chapter 1	1
1 AOPs: Dark and light driven processes	2
2 Principle of AOPs	3
3 Mechanism of UV induced photocatalysis in the degradation of organic pollutants using TiO ₂	4
4 The chemical structure of F ₆₄ PcZn	6
5 Schematic representation of F ₆₄ PcZn deposited on SiO ₂ , TiO ₂ and NiO particles, and PTFE, PES and FPP membranes. The possible F ₆₄ PcZn/support interactions are also shown.	8
6 The structure of (a) MO, (b) RhB and (c) MR.....	9
Chapter 2	13
1 Chemical structure of zinc perfluoroalkyl perfluorophthalocyanine (F ₆₄ PcZn)	16
2 Preparation of F ₆₄ PcZn/SiO ₂ hybrid catalyst	17
3 UV-Vis spectra of F ₆₄ PcZn in acetone extracted from F ₆₄ PcZn/SiO ₂	18
4 Spectral distribution of tungsten halogen lamp used as a visible light source.....	19
5 Photodegradation of MO catalyzed by F ₆₄ PcCu/SiO ₂ under visible light irradiation	22
6 The influence of F ₆₄ PcZn/SiO ₂ catalyst on the photodegradation of MO	23
7 Comparison of photocatalytic efficiency of F ₆₄ PcCu/SiO ₂ with F ₆₄ PcZn/SiO ₂	24

8	UV-Vis spectra of (a) F ₆₄ PcCu and (b) F ₆₄ PcZn extracted using acetone from F ₆₄ PcCu/SiO ₂ and F ₆₄ PcZn/SiO ₂ before and after photodegradation process of MO	25
9	MO photodegradation in the presence of 0.005 mM F ₆₄ PcZn/SiO ₂	27
10	Photocatalytic efficiency of F ₆₄ PcZn/SiO ₂ at lower concentration of 0.005 mM. Kinetic plots for the degradation of MO.....	28
11	Particle size distribution for (a, b) 10-20 nm SiO ₂ and F ₆₄ PcZn/SiO ₂ , (c, d) OX50 SiO ₂ and F ₆₄ PcZn/SiO ₂ (before photoreaction), (e) OX50 F ₆₄ PcZn/SiO ₂ after photoreaction.....	30
12	Comparison of MO photodegradation catalyzed by F ₆₄ PcZn, F ₆₄ PcZn/63-200 μm SiO ₂ , F ₆₄ PcZn/4-12 μm SiO ₂ , F ₆₄ PcZn/10-20 nm SiO ₂ and F ₆₄ PcZn/OX50 (40 nm SiO ₂) under illumination of 390,000 lx visible light.....	33
13	Fluorescence emission spectra for SiO ₂ 10-20 nm, SiO ₂ OX50, F ₆₄ PcZn/ SiO ₂ 10-20 nm and F ₆₄ PcZn/OX50 catalysts.....	35
14	Effect of oxygen: MO photodegradation catalyzed by F ₆₄ PcZn/SiO ₂ in argon and air atmospheres.....	37
15	Decolourization of MO with irradiation time. Aliquotes taken every 2 hours, from left to right, 0, 2, 4, 6, 8 and 10 hours	37
16	Photodegradation of RhB catalyzed by F ₆₄ PcZn/OX50	38
17	RhB photodegradation catalyzed by F ₆₄ PcZn/10-20 nm SiO ₂ and F ₆₄ PcZn/OX50 irradiated with visible light	40
18	Radical mechanisms involved in the photodegradation of MO catalyzed by F ₆₄ PcZn/SiO ₂ ..	41

19	Percentages of (a) TOC and (b) TDN after photodegradation of RhB for 10 h. F ₆₄ PcZn/OX50 is more efficient than F ₆₄ PcZn/SiO ₂ 10-20 nm	43
20	Effect of increasing F ₆₄ PcZn molar concentration deposited on SiO ₂ . Change in reaction rate of MO photodegradation.....	46
21	Fluorescence intensity for 0.005, 0.01 and 0.03 mM F ₆₄ PcZn/SiO ₂ catalysts.....	47
22	Adsorption of various amount of F ₆₄ PcZn on SiO ₂ . Highest amount of F ₆₄ PcZn forms multi-layer coating on SiO ₂	47
23	UV-Vis-NIR spectra of F ₆₄ PcZn deposited on SiO ₂ in varying concentrations in comparison with F ₆₄ PcZn in ethanol.....	49
24	XRD analysis of SiO ₂ (10-20 nm) and F ₆₄ PcZn/ SiO ₂ (10-20 nm) (i) before and (ii) after MO photodegradation reaction	50
25	High resolution XPS spectra of C _{1s} , O _{1s} , Zn _{2p} , F _{1s} and N _{1s} for F ₆₄ PcZn	51
26	(a) Survey spectra and (b) High resolution XPS spectra of O _{1s} and Zn _{2p} for SiO ₂ and F ₆₄ PcZn/SiO ₂	53
27	Mode of adsorption of F ₆₄ PcZn on SiO ₂ : Electrostatic interaction of Zn ²⁺ and Si-O ⁻ from F ₆₄ PcZn and SiO ₂ , respectively.....	54
28	Repeated cycles for MO photodegradation in the presence of F ₆₄ PcZn/OX50.....	55
Chapter 3		60
1	(a) Direct band gap as in rutile and (b) indirect band gap like in anatase. Energy, ϵ , is plotted against k -space or momentum (wave number) space	60

2	Chemical structure of (a) F ₆₄ PcZn, (b) methyl orange and (c) rhodamine B	65
3	Spectral distribution for the tungsten halogen lamp used as a visible light source	66
4	UV-Visible Spectra for the photodegradation of MO catalyzed by (a) P25 and (b) F ₆₄ PcZn/P25	71
5	UV-Vis spectra for photodegradation of RhB (a) P25 no hypsochromic/blue shift; (b) F ₆₄ PcZn/P25 hypsochromic/blue shift	73
6	UV-Vis spectra of F ₆₄ PcZn extracted from F ₆₄ PcZn/P25 before and after photochemical reaction.....	74
7	UV-Visible spectra of MO photodegradation with time. (a) P90 and (b) F ₆₄ PcZn/P90.....	77
8	UV-Visible spectra display RhB photodegradation under visible light illumination catalyzed by (a) P90 and (b) F ₆₄ PcZn/P90. A blue shift in peak absorbance occurred for the reaction catalyzed by F ₆₄ PcZn/P90.....	78
9	Kinetics plots for MO photodegradation catalyzed by P25, P90, F ₆₄ PcZn/P25 and F ₆₄ PcZn/P90.....	79
10	Kinetics plots for RhB photodegradation catalyzed by P25, P90, F ₆₄ PcZn/P25 and F ₆₄ PcZn/P90.....	80
11	Fluorescence emission spectra of hybrid catalysts F ₆₄ PcZn/P25 and F ₆₄ PcZn/P90 deposited on substrates P25 and P90	84
12	Comparison of MO photodegradation rates between P25, H ₁₆ PcZn/P25, F ₁₆ PcZn/P25 and F ₆₄ PcZn/P25.....	85

13	Fluorescence emission comparison for F ₆₄ PcZn/P25 with H ₁₆ PcZn/P25 and F ₁₆ PcZn/P25 ..	85
14	UV-Vis spectra of H ₁₆ PcZn and F ₁₆ PcZn extracted from H ₁₆ PcZn/P25 and F ₁₆ PcZn/P25 before and after 10 h of MO photodegradation reaction.....	86
15	Photostability of (a) H ₁₆ PcZn, (b) F ₁₆ PcZn and (c) F ₆₄ PcZn deposited on P25 under UV (254 nm) light irradiation	88
16	Mode of adsorption of RhB on the surface of TiO ₂ and F ₆₄ PcZn/TiO ₂	90
17	Kinetic plots for the photodegradation of RhB catalyzed by P25 and F ₆₄ PcZn/P25 upon illumination with only visible light, and with the combination of UV + Visible light.....	92
18	UV-Visible spectra of F ₆₄ PcZn extracted from F ₆₄ PcZn/P25 after RhB photodegradation using UV + Visible light	94
19	Photodegradation of RhB using F ₆₄ PcZn/P25. Effect of red, visible and UV lights illumination	94
20	RhB reaction rate under the influence of <i>tert</i> -butanol that is added to confirm the role of •OH radical.....	97
21	The mineralization of RhB catalyzed by P25, P90, F ₆₄ PcZn/P25 and F ₆₄ PcZn/P90. (a) % of total dissolved carbon (TOC) and (b) % of total dissolved nitrogen (TDN)	99
22	Change in fluorescence intensity with increasing amount of F ₆₄ PcZn deposited on P25	102
23	(a) UV-Vis-NIR spectra for P25 and F ₆₄ PcZn/P25 with different amounts of F ₆₄ PcZn deposited on 25. (b) Plot of Q-band absorption intensities with increasing amounts of F ₆₄ PcZn deposited on P25.....	104

24	High resolution XPS spectra of C 1s, O 1s, Zn 2p, F 1s and N 1s for F ₆₄ PcZn	105
25	XP survey spectra for P25 and F ₆₄ PcZn/P25	106
26	Deconvoluted O 1s spectra for P25 TiO ₂ and F ₆₄ PcZn/P25	108
27	Deconvoluted O 1s spectra for F ₁₆ PcZn/P25 and H ₁₆ PcZn/P25	108
28	High resolution XPS spectra: N 1s spectra for F ₆₄ PcZn and F ₆₄ PcZn/P25.....	110
29	High resolution XPS spectra: F 1s spectra for P25 TiO ₂ and F ₆₄ PcZn/P25.....	110
30	Proposed mode of interaction: F ₆₄ PcZn deposited on P25	112
31	XRD patterns for P25 and F ₆₄ PcZn/P25 before and after 3 runs of MO photodegradation reactions. One run lasts for 10 h	114
32	Proton assignments in the molecular structure of RhB.....	115
33	¹ H-NMR spectra for RhB in D ₂ O. (a) before photoreaction, (b) photodegradation catalyzed by P25 and (c) photodegradation reaction catalyzed by F ₆₄ PcZn/P25	116
34	Comparison of HPLC chromatograms obtained for the degradation products of RhB catalyzed by (a) P25 and (b) F ₆₄ PcZn/P25.....	119
35	Relative peak area determined from the above displayed HPLC chromatograms; (a) P25 and (b) F ₆₄ PcZn/P25	120
36	MS results obtained for the degradation products formed after (a-f) 0, 2, 4, 6, 8 and 10 hours of RhB photodegradation for P25	121
37	MS for the degradation products formed after (a-f) 0, 2, 4, 6, 8 and 10 hours of RhB photodegradation catalyzed by F ₆₄ PcZn/P25.....	122

38	Mode of RhB adsorption on TiO ₂ and cleavage of nearby bonds by h [⊕] / OH [•] radicals	128
39	<i>N</i> -deethylation of RhB dominates for F ₆₄ PcZn/P25 photocatalyst	128
40	Five recycles of (a) F ₆₄ PcZn/P25 and (b) F ₆₄ PcZn/P90 for MO photodegradation reactions	132
41	UV-Vis spectra of F ₆₄ PcZn extracted from F ₆₄ PcZn/P25 before and after 5 consecutive cycles of photoreactions.....	133
Chapter 4		144
1	Kinetic plots for MO photodegradation catalyzed by NiO, F ₆₄ PcZn/NiO, H ₁₆ PcZn/NiO, F ₁₆ PcZn/NiO and F ₆₄ PcCu/NiO under visible light irradiation	145
2	Fluorescence emission intensity for NiO, F ₆₄ PcZn/NiO, H ₁₆ PcZn/NiO, F ₁₆ PcZn/NiO and F ₆₄ PcCu/NiO catalysts	146
3	UV-Vis spectra of F ₆₄ PcZn extracted from F ₆₄ PcZn/NiO before and after photocatalytic reaction. F ₆₄ PcZn structure is unaffected by the catalytic reaction	147
Chapter 5		151
1	Optical images of (a) F ₆₄ PcZn/PES, F ₆₄ PcZn/PTFE, (b) F ₆₄ PcZn/PP (middle layer) and (c) the outer uncoated layers used to sandwich F ₆₄ PcZn/PP membrane	154
2	Polypropylene membranes functionalized with sulfonic acid groups. (a) FPP outer protecting layers and (b) FPP inner membrane layer.....	155
3	The molecular structures of (a) MO and (b) MR.....	157
4	The colors of MR versus pH.....	158

5	Chemical structure of (a) PTFE, (b) PES and (c) PP	161
6	Optical micrographs of PES, PTFE, F ₆₄ PcZn/PES, and F ₆₄ PcZn/PTFE filter membranes. F ₆₄ PcZn impregnated membranes fluorescent under light.....	162
7	SEM micrographs of bare PES, PTFE and F ₆₄ PcZn deposited membranes such as F ₆₄ PcZn/PES and F ₆₄ PcZn/PTFE.....	163
8	Comparison of visible light MO photodegradation rate for F ₆₄ PcZn/PES and F ₆₄ PcZn/PTFE membranes under 130,000 lx intensity of visible light irradiation.....	166
9	MR visible light photodegradation by F ₆₄ PcZn coated PP membrane	167
10	Three cycles of MR photodegradation using F ₆₄ PcZn/FPP membrane	168
11	Comparison of IR spectra of F ₆₄ PcZn/FPP before and after 3 cycles of MR photodegradation reaction.....	169
12	Optical micrographs showing the structural robustness of F ₆₄ PcZn/PP membrane before and after MR photodegradation. Magnification: 4X.....	170
13	Effect of F ₆₄ PcZn loading density in F ₆₄ PcZn/FPP membrane on the photodegradation rate of MR, followed by monitoring the variation of the: a) dye concentration, b) reaction rate. c) reaction half-life, t _{1/2}	172
14	Comparison of different light sources such as tungsten halogen light, LED white light and LED red light for MR photodegradation process using 0.8 μmol/cm ² F ₆₄ PcZn loaded F ₆₄ PcZn/FPP membrane.....	174

Chapter 1. Introduction: Solid-State Photocatalysts for Wastewater Treatment

1.1. Organic Pollutants in Wastewater

Synthetic organic dyes are employed to produce consumer products in textile, leather, plastic, printing and other industries. Since the azo dyes are produced via a simple diazotization reaction in large amounts, they are widely used as a colorant.¹ Azo dyes are characterized by the presence of azo groups substituted with aromatic amines. Sulfonic acid group has also been substituted to obtain sulfonated azo dyes that find many applications in different industries. The azo dyes and their metabolites are mutagenic to both human and aquatic life.³ Another class of dyes, xanthene dyes, have been used in industries like food, pharmaceuticals, cosmetics, textile and paper due to their high coloring properties. These dyes exhibit poor biodegradability and some of them are toxic.^{4,5} The industrial waste effluents may contain more than 50 % of the unused organic dyes that needed to be treated before discharging into common watercourses.⁶ Wastewater treatment involves various stages of treatment known as primary, secondary and tertiary. Primary treatment mainly involves filtration, sedimentation and flocculation to remove insoluble solid wastes. The secondary treatment includes biological treatment known as the activated sludge process. The waste organic matters are biologically broken down followed by a sedimentation process. The tertiary treatment is the final process before discharging water into waterways. In this process heavy metal ions, nitrates and phosphates are removed by precipitation and ion exchange methods.⁷ Many advanced oxidation processes (AOPs) are utilized in the tertiary treatment to remove biologically toxic substances like aromatics, pesticides, petroleum products and volatile organic compounds.^{8,9}

1.2. Advanced Oxidation Processes for Wastewater Treatment

Advanced oxidation processes (AOPs) are a set of chemical oxidation procedures to remove organic and inorganic contaminants from wastewater. They are broadly categorized into two different types, dark/non-light and light driven AOPs (Figure 1).¹⁰ The AOPs utilize strong oxidizing agents like ozone (O₃) and hydrogen peroxide (H₂O₂), catalysts and light irradiation separately or in combination that produce reactive oxygen species (ROS) such as hydroxyl radicals (•OH) and superoxide radicals (O₂•⁻), UV light to induce ROS production (Figure 2).¹¹ ROS can attack the organic matters to produce other active radicals (equation 1), which are further split into smaller molecular fragments via chain radical reactions.

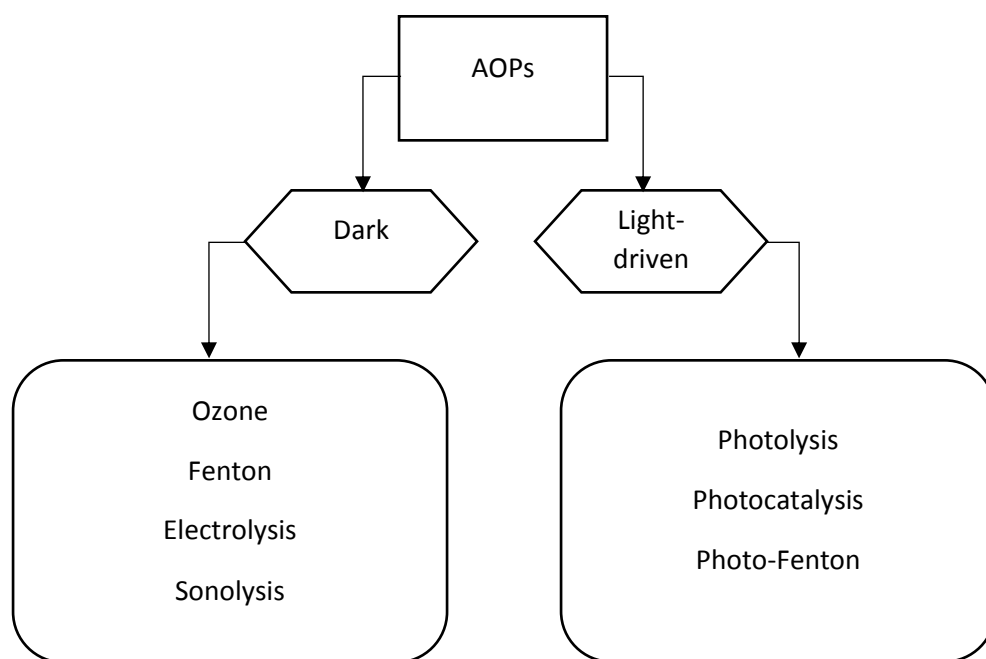
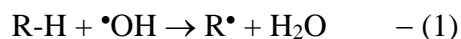


Figure 1. AOPs: Dark and light driven processes.

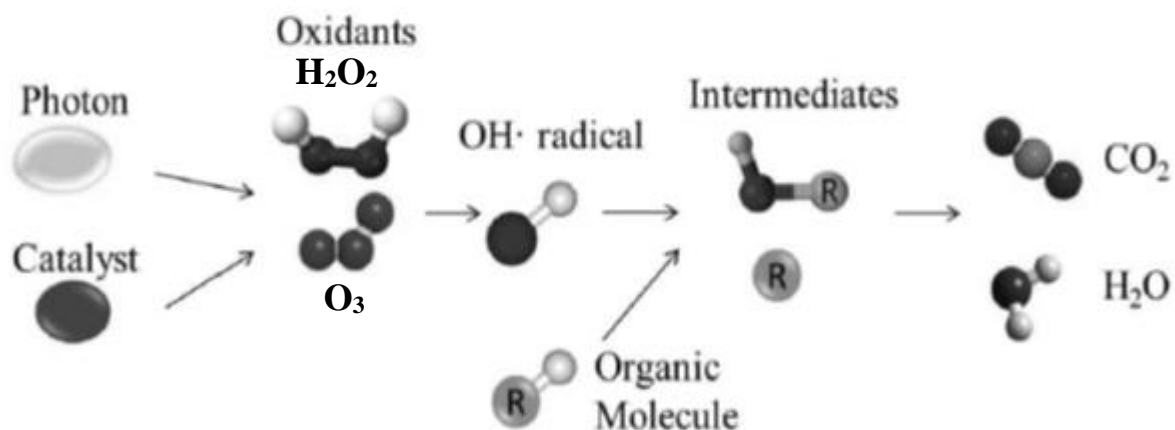


Figure 2. Principle of AOPs.¹¹

Among these tertiary water treatment methods, the light driven photocatalysis become the most prominent technology.¹¹

1.3. Photocatalytic Wastewater Treatment using Titanium Dioxide

Semiconductor-mediated photocatalysis is a well-known process employed in the treatment of wastewater. Titanium dioxide, TiO_2 combined with UV light illumination is a widely applied AOP technology for environmental remediation.¹² Figure 3 depicts the mechanism of the photodegradation process of organic pollutants using TiO_2 . Photodegradation using TiO_2 is of interest because of the catalyst stability and its non-toxicity.¹³ Disadvantages include the wide energy band gap that leads to high energy utilization costs. Specifically, TiO_2 has a wide band gap of 3.2 eV which can absorb only UV light.¹⁴ There exists a requirement for photocatalysts that can utilize the naturally available Sun light. Phthalocyanines are extensively investigated as

homogenous and heterogenous photocatalysts because they can absorb visible light.^{15,16} They are also thermally stable compounds.¹⁷

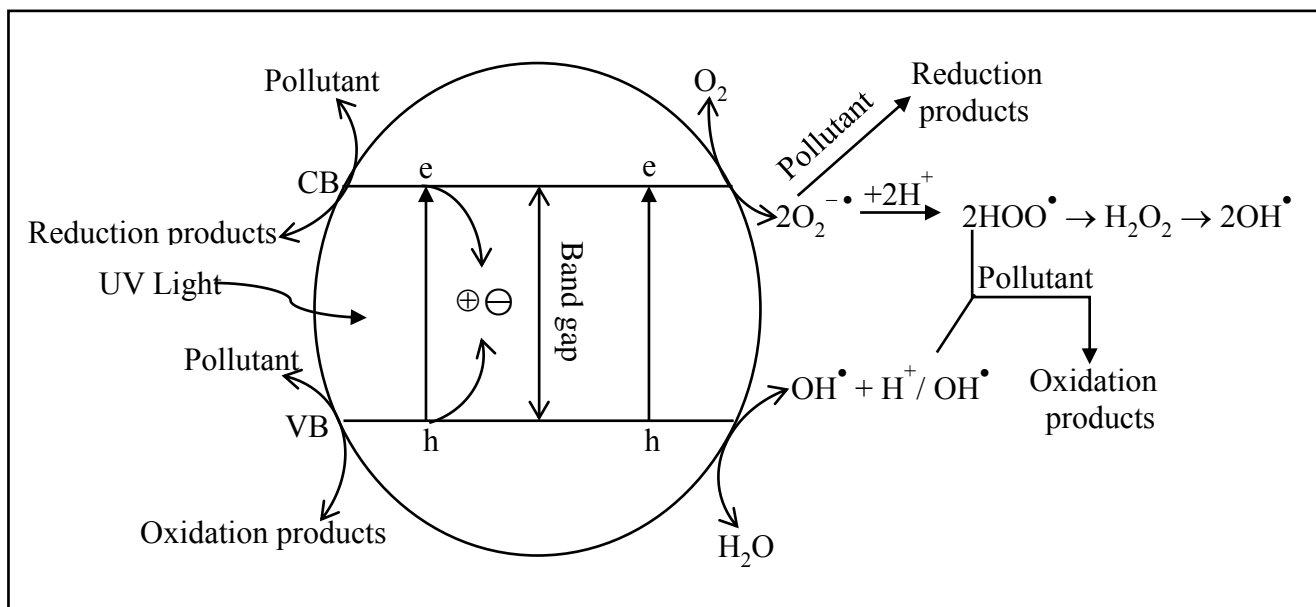


Figure 3. Mechanism of UV induced photocatalysis in the degradation

of organic pollutants using TiO₂. Symbols: CB - conduction band; VB - valance band; O₂^{-•} - superoxide radical; OH[•] - hydroxyl radical; HOO[•] - hydroperoxide radical; H₂O₂ - hydrogen peroxide.

1.4. Stabilized Perfluoroalkyl Perfluoro Phthalocyanine as Photosensitizer for Wastewater Treatment

Phthalocyanines (Pcs) do not exist in Nature but they have an analogue structure to porphyrins, and chlorophyll involved in functions like photo absorption and photo induced electron transfer and charge separation for photosynthesis, in addition to heme based transport of oxygen in blood. An important difference in the characteristics spectral features of phthalocyanines and

porphyrins is the well-resolved intense Q band near 670 nm of the Pcs, compared to the intense B band near 410 nm for porphyrins.¹⁸ In general, Pcs have two characteristic, strong and broad electronic bands; the Soret band due to $\pi \rightarrow \pi^*$ transitions in the near UV and the Q band, due to $n \rightarrow \pi^*$ transitions on the red portion of the spectrum.¹⁹ Because of the strong absorption of light in the visible region, Pcs found applications in a variety of industrial, technological and medical fields including catalyst, solar cell, gas sensor, electrochromic display, photodynamic therapy of cancer. Owing to their planar aromatic structure Pcs have a great tendency to form aggregates. This characteristic of Pcs due to stacking π - π interaction is a major drawback because it shortens the life time of excited states. Many strategies have been employed to prevent Pcs aggregation.

Bench *et al* synthesized nonplanar, biconcave, zinc perfluoroalkyl perfluoro phthalocyanine, $F_{64}PcZn$ which does not aggregate in solution due to the peripheral bulky perfluoroalkyl groups. $F_{64}PcZn$ is photostable, does not self-degrade in the radical photoreaction environment because of the encapsulation of metal center in a refractory C-F based organic environment.²⁰ The chemical structure of $F_{64}PcZn$, which is used as a solid-state catalyst in the present investigation is shown in Figure 4. Several papers are reported on the crystal structure, photophysical and chemical properties of $F_{64}PcZn$.^{21,22} It has also been reported that $F_{64}PcZn$ is photochemically active upon illumination with radiation in the visible region, besides being structurally robust due to the presence of perfluoroalkyl groups located at the peripheral positions.²³

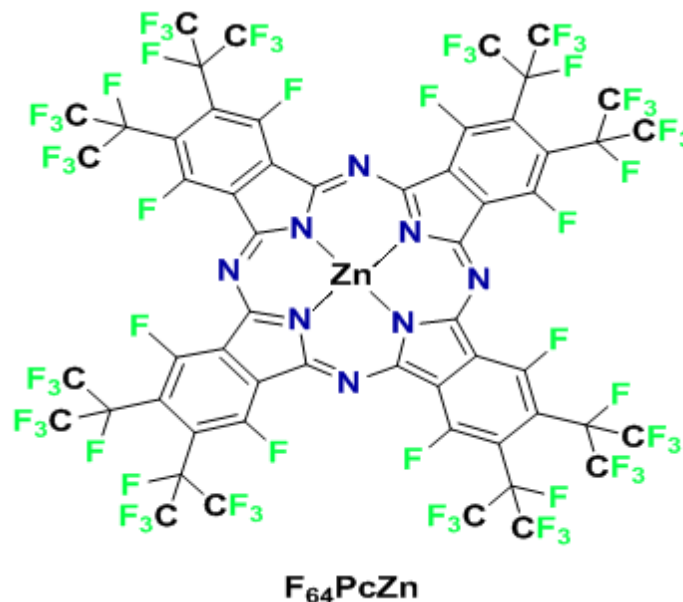


Figure 4. The chemical structure of F₆₄PcZn.²⁰

1.5. Hybrid F₆₄PcZn/Support, Solid-State Photocatalysts for Wastewater Purification

Phthalocyanines have been deposited on solid-state substrates like clay, SiO₂ and TiO₂ to be used as photocatalysts for wastewater treatment.²⁴⁻²⁶ Toledo *et al* synthesized cobalt phthalocyanine adsorbed on porous SiO₂ matrix and investigated the electrochemical oxidation of oxalic acid.²⁷ They concluded that there is a potential to use CoPc/SiO₂ as an electrochemical sensor for oxalic acid. Ranjit *et al* reported that the photocatalytic efficiency of Fe^{III}Pc/TiO₂ is significantly enhanced as compared to nonmodified TiO₂. The authors found that the photodegradation of organic pollutants such as *p*-aminobenzoic acid, *p*-nitrobenzoic acid, *p*-chlorophenoxyacetic acid, salicylic acid and aniline was significantly enhanced when using Fe^{III}Pc/TiO₂ as a photocatalyst. They suggested the cooperative functions of the two components

in the generation of $\bullet\text{OH}$ radicals might be responsible for the enhanced photoactivity of $\text{Fe}^{\text{III}}\text{Pc}/\text{TiO}_2$.²⁸ Even though these reports are discussing an improved photoactivity due to the application of hybrid catalysts, most importantly the catalyst stability is not reported. There are investigations showing repeated catalytic cycles, for example 3 cycles with similar efficiency, but the Pc stability is not described.^{29,30}

In the present investigation, we deposited F_{64}PcZn on solid substrates. The influence of paramagnetic and diamagnetic metal centers on the ability to degrade organic pollutant is analyzed by using both $\text{F}_{64}\text{PcCu}/\text{SiO}_2$ and $\text{F}_{64}\text{PcZn}/\text{SiO}_2$ as catalysts. F_{64}PcZn is deposited on inert SiO_2 particles and photoactive, wide band-gap TiO_2 particles to obtain hybrid materials. F_{64}PcZn is also deposited on narrow band-gap NiO to evaluate any possible orbital interactions. The photo efficiency and photostability of these hybrid catalysts under visible light irradiation are examined. In addition to solid-state particles F_{64}PcZn is incorporated onto polymer filter membranes with the scope of combining the filtration technique with an organic pollutant degradation process under visible light. The hybrid filter membranes $\text{F}_{64}\text{PcZn}/\text{polytetrafluoroethylene}$ (PTFE) and $\text{F}_{64}\text{PcZn}/\text{poly}$ (ether sulfones) (PES) are prepared and their efficiency in degrading methyl red (MR) under illumination with visible light have been examined. F_{64}PcZn is assumed to be adsorbed on the above-mentioned matrices via weak van der Waals forces. In contrast, F_{64}PcZn is immobilized on sulfonic acid functionalized polypropylene membrane (PP) to obtain FPP membrane. The photocatalytic efficiency of this membrane is studied under white, red and tungsten halogen vapor lamp, the light source we used for the other photoreactions. The effect of illuminating with lights of different wavelengths is discussed.

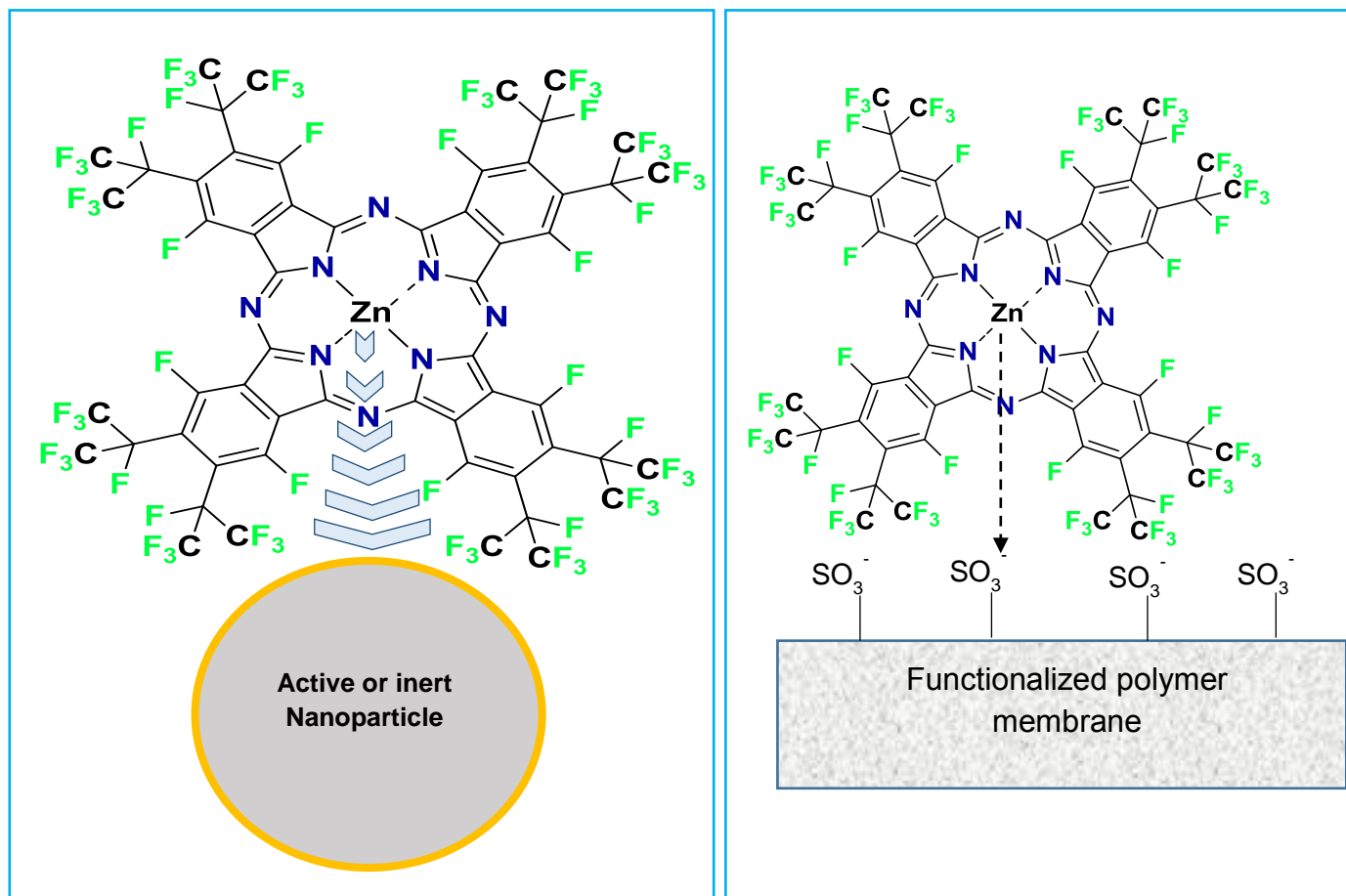


Figure 5. Schematic representation of $F_{64}PcZn$ deposited on SiO_2 , TiO_2 and NiO particles, and PTFE, PES and FPP membranes. The possible $F_{64}PcZn$ /support interactions are also shown.

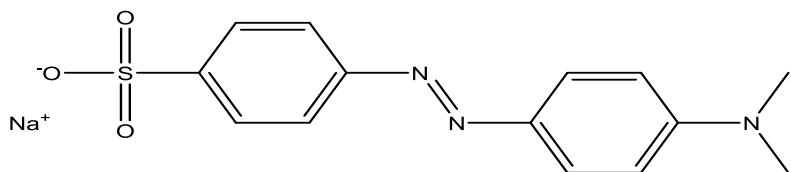
1.6. Model Organic Dyes: Methyl Orange, Rhodamine B and Methyl Red

In our investigation, we used methyl orange (MO), rhodamine B (RhB) as representatives of pollutant dyes to analyze the efficiency of the hybrid catalysts, $F_{64}PcZn/SiO_2$, $F_{64}PcZn/TiO_2$ and $F_{64}PcZn/NiO$ in performing photodegradation reactions under visible light irradiation. Methyl red (MR) was employed as a model dye pollutant for photo reactions involving the hybrid filter membranes $F_{64}PcZn$ /polytetrafluoroethylene (PTFE), $F_{64}PcZn$ /polyethersulfones (PES) and

F₆₄PcZn/functionalized polypropylene (FPP).

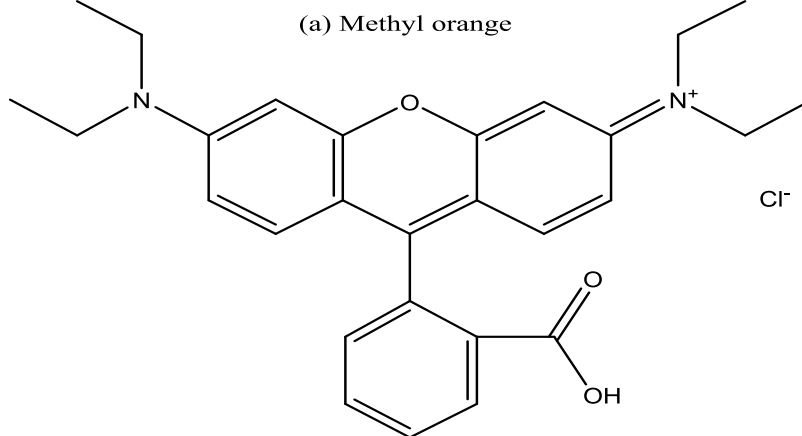
The chemical structures of MO, RhB and MR

are given in Figure 6.



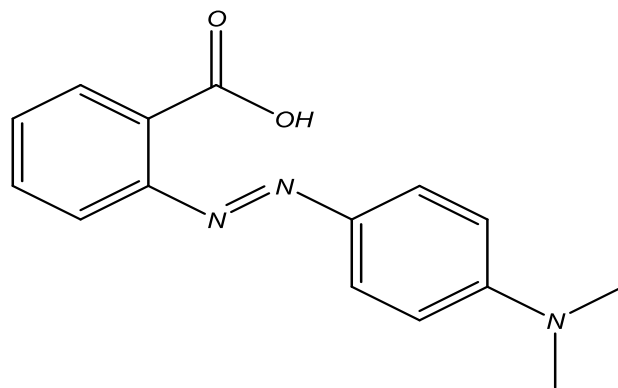
(*E*)-4-((4-(dimethylamino)phenyl)diazenyl)benzenesulfonate

(a) Methyl orange



N-(9-(2-carboxyphenyl)-6-(diethylamino)-3*H*-xanthen-3-ylidene)-*N*-ethylethanaminium

(b) Rhodamine B



2-(*N,N*-dimethyl-4-aminophenyl) azobenzenecarboxylic acid

(c) Methyl red

Figure 6. The structure of (a) MO, (b) RhB and (c) MR.

MO and MR are azo dyes while RhB is a xanthene dye. The molecular fragments formed due to the photodegradation process are identified. The type of F₆₄PcZn adsorption on the solid supports is discussed. A possible mechanism of radical reaction pathways with the addition of bare TiO₂ and F₆₄PcZn/TiO₂ is proposed.

REFERENCES

- (1) Chung, K. T.; Cerneglia, C. E. *Mutat. Res.* **1992**, *277*, 201-220.
- (2) Chequer, F. M. D.; Lizier, T. M.; Felicio, R.; Zanoni, M. V. B.; Deboni, H. M.; Lopes, N. P.; Marcos, R.; Oliveira, D. P. *Toxic. In Vitro*, **2011**, *25*, 2054-2063.
- (3) Nam, S.; Renganathan, V. *Chemosphere*, **2000**, *40*, 351-357.
- (4) Wang, H.; Lu, L.; Zhu, S.; Li, Y.; Cai, W. *Curr. Microbiol.* **2006**, *52*, 1-5.
- (5) Tsuda, S.; Murakami, M.; Matsusaka, N.; Kano, K.; Taniguchi K.; Sasaki, Y. F. *Toxicol. Sci.* **2001**, *61*, 92-99.
- (6) Hoffmann, M. R.; Martin, S.T.; Choi, W.; Bahnemann, D.F. *Chem. Rev.* **1995**, *95*, 69-96.
- (7) Muralikrishna, I. V.; Manickam, V. *Environmental Management: Science and Engineering for Industry, Waste water treatment technology*, Butterworth-Heinemann, 2017, pp. 249-293.
- (8) Glaze, W.; Kang, J. W.; Chapin, D. H. *Ozone: Sci. & Eng.* **1987**, *9*, 335-352.
- (9) Audenaert, W. T. M.; Vermeersch, Y.; Van Hulle, S. W. H.; Dejans, P.; Dumouilin, A.; Nopens, I. *Chem. Eng. J.* **2011**, *171*, 113-126.
- (10) (a) Suresh, C. A. (Ed.), *Advanced oxidation processes for wastewater treatment: Emerging green chemical technology*, Academic Press, 2018. (b) Yao, H. Application of advanced oxidation

processes for treatment of air from livestock buildings and industrial facilities, Department of Engineering, Aarhus University, Denmark, *Technical Report BCE-TR-8*, **2013**, pp 36.

(11) Oller, I.; Malato, S.; Sánchez-Pérez, J.A. *Sci. Tot. Environ.* **2011**, *409*, 4141-4166.

(12) Madden, T. H.; Datye, A. K.; Fulton, M.; Prairie, M. R.; Majumdar, S. A.; Stange, B. M. *Environ. Sci. Technol.* **1997**, *31*, 3475-3481.

(13) Lang, X.; Ma, W.; Chen, C.; Ji, H.; Zhao, J. *Acc. Chem. Res.* **2014**, *47*, 355-363.

(14) Sun, S.; Gao, P.; Yang, Y.; Yang, P.; Chen, Y.; Wang, Y. *ACS. Appl. Mater. Interfaces*, **2016**, *8*, 18126-18131.

(15) Sorokin, A. B. *Chem. Rev.* **2013**, *113*, 8152-8191.

(16) Sevim, A. M.; Ilgun, C.; Gul, A. *Dyes & Pigments*, **2011**, *89*, 162-168.

(17) Lawton, E. A. *J. Phys. Chem.* **1958**, *62*, 384-384.

(18) Mansour, H.B.; Corroler, D.; Barillier, D.; Ghedira, K.; Chekir, L.; Mosrati, R. *Food Chem. Toxicol.* **2007**, *45*, 1670–1677.

(19) The Porphyrine Handbook, *16, Phthalocyanines: Spectroscopic and Electrochemical Characterization*, Kadish., K. M.; Smith, K. M.; Guillard, R. (Eds), Academic Press, 2003.

(20) Bench, B. A.; Beveridge, A.; Sharman, W. M.; Diebold, G. J.; Lier, J. E.; Gorun, S. M. *Angew. Chem. Int. Ed.* **2002**, *41*, 747-750.

(21) Bench, B. A.; Brennessel, W. W.; Lee, H. J.; Gorun, S. M. *Angew. Chem. Int. Ed.* **2002**, *41*, 750.

(22) Liao, M. S.; Watts, J. D.; Gorun, S. M.; Scheiner, S.; Huang, M-J. *J. Theor. Comp. Chem.* **2008**, *7*, 541.

- (23) Drozda, D.; Szczubialka, K.; Lapok, L.; Skiba, M.; Patel, H.; Gorun, S. M.; Nowakowska, S. *M. Applied Catalysis B: Environmental* **2012**, *125*, 35.
- (24) Xiong, Z.; Xu, Y.; Zhu, L.; Zhao, J. *Langmuir*, **2005**, *21*, 10602-10607.
- (25) Chen, X.; Zou, J.; Liu, L.; Zhang, Y.; Huang, J. *Appl. Spectrosc.* **2010**, *64*, 552-557.
- (26) Souza, J. S.; Pinheiro, M. V. B.; Krambrock, K.; Alves, W. A. *J. Phys. Chem. C*, **2016**, *120*, 11561-11571.
- (27) Toledo, M.; Lucho, A.M.S.; Gushikem, Y. *J. Mater. Sci.* **2004**, *39*, 6851-6854.
- (28) Ranjit, K.; Willner, I.; Bossmann, S. H. *J. Phys. Chem.* **1998**, *102*, 9397-9403.
- (29) Zhang, M.; Shao, C.; Guo, Z.; Zhang, Z.; Mu, J.; Cao, T.; Li, Y. *ACS Appl. Mater. Inter.* **2011**, *3*, 369-377.
- (30) Sacco, O.; Stoller, M.; Vaiano, V.; Ciambelli, P.; Chianese, A.; Sannino, D. *Int. J. Photoenergy*. **2012**, 1-8.

Chapter 2. Perfluoroalkyl Perfluoro Phthalocyanine Supported on SiO₂ for Water Decontamination

2.1. INTRODUCTION

F₆₄PcCu and F₆₄PcZn are highly hydrophobic due to the C-F scaffold which makes them insoluble in aqueous media and thus form aggregates. The C-F bond is highly dipolar, relatively nonpolarizable and not involved in any hydrogen bonding with water. Since there are no hydrophilic sites on the fluorinated surface, electrostatic interactions with water is absent. Hence, the interaction between perfluoroalkyl perfluorinated F₆₄PcM and water is mainly depending on the van der Waals forces. In room temperature, water tends to maintain hydrogen bonding network structure at the fluorocarbon interface which lacks hydrophilic sites. Therefore, the fluorinated surface has poor van der Waals interaction with water.¹ Thus, F₆₄PcM forms aggregates in water that lead to a much lower photoactivity when added to water by itself which is discussed in the following results section. F₆₄PcM readily dissolves in organic solvents to form homogenous solution, so provides higher photocatalytic activity.² Similar aggregation effects in water versus organic solvents and the resulting decrease in photoactivity has been reported in the literature. Tsubone *et al* reported the aggregation behavior of phthalocyanine hydroxide aluminum (OHPcAl) in water.³ They evaluated the aggregation behavior by following the fluorescence emission intensity of OHPcAl in water/ethanol mixture. The fluorescence emission intensity almost fell to zero because of aggregation by increasing water content to more than 70%.

To achieve a better molecular distribution in aqueous media, Pcs are deposited on solid supports like SiO₂ particles and zeolites.⁴⁻⁹ Many investigators focused on the synthesis of Pc

immobilized SiO₂ composites to use as a photocatalyst, but they added oxidizing agents to support the reaction kinetics. For example, Becerra *et al*⁴ evaluated Cl₁₆PcFe immobilized on -NH₂ functionalized SiO₂ with the addition of *t*-butyl hydroperoxide (TBHP) as an oxidant to catalyze the oxidation of α -pinene. The authors found PcCl₁₆Fe-NH₂-SiO₂/TBHP is an efficient catalyst for the allylic oxidation of α -pinene under mild reaction conditions. They reported that the radicals involved in reaction kinetics are generated not only from heterogenous Cl₁₆PcFe-NH₂-SiO₂ but also homogenously produced by TBHP. Raja and Ratnasamy⁵ used Pcs encapsulated in zeolites in combination with oxidizing agents O₂/*tert*-butyl hydroperoxide to convert methane to a mixture of methanol and formaldehyde. They used FeCl₁₆Pc-Na-X, CuCl₁₆Pc-Na-X, CoCl₁₆Pc-Na-X, Cu(NO₂)₄Pc-Na-X and CuCl₁₆Pc-Na-Y in which all or most of the ring hydrogens of Pcs have been substituted by electron withdrawing groups such as halogens or nitro groups. Again, the reaction rate is controlled by the oxidant O₂/*tert*-butyl hydroperoxide in addition to Pc. DeOliveira *et al* reported a mesoporous catalyst Si-F₁₆PcCu obtained by covalent anchoring method.⁶ A recalcitrant organic pollutant, 2,4-dichlorophenoxyacetic acid was photooxidized using Si-CuF₁₆Pc with the addition of an oxidant hydrogen peroxide, H₂O₂. As oppose to all the above-mentioned methods, such aggressive oxidizing agents are not added in the present study. The reaction mixture consists of only F₆₄PcM deposited on SiO₂ as a catalyst.

Fluorinated phthalocyanine is deposited on SiO₂ particles with a range of sizes from micro to nanometer, a simple way to change the available surface area for Pc adsorption that directly affects the molecular distribution. Iliev *et al*⁷ reported CuPc(COOH)₄, CoPc(COOH)₄ and ZnPc(COOH)₄ exhibited better photocatalysis when immobilized on zeolites. Perfluoroalkyl perfluoro phthalocyanine (F₆₄PcZn) was incorporated into smectite interlayers of a naturally occurring phyllosilicate bentonite clay (Ben) which serves as a support for the photoactive dye.¹⁰

Under visible light irradiation $F_{64}PcZn \in Ben$ is able to photodegrade Acid Orange 7 ($C_{16}H_{11}N_2NaO_4S$), in aqueous media.

Another important factor to consider is the chemical stability of phthalocyanine after photoreactions. Liu *et al* reported the photo instability of 29*H*,31*H*-phthalocyanine ($C_{32}H_{18}N_8$), metal free, and oxovanadium phthalocyanine ($C_{32}H_{16}OV$) deposited on TiO_2 under UV illumination.¹¹ They concluded the Pcs degraded because of the photo activity of TiO_2 under UV irradiation. Bench *et al*¹² reported the introduction of bulky perfluoroalkyl groups ($-CF_3$) at the periphery of perfluorophthalocyanines yields photostability for $F_{64}PcZn$ molecules under harsh reaction conditions. Hence, we expect a better photostability for $F_{64}PcZn$ deposited on SiO_2 because of the $-CF_3$ groups at the peripheral positions.

We investigated the photoactivity of $F_{64}PcCu$ and $F_{64}PcZn$ deposited on commercially available SiO_2 particles. Cu and Zn metal centers are chosen to compare the influence of diamagnetic and paramagnetic metal centers on the photoactivity of Pc while deposited on SiO_2 . The molecular structure of $F_{64}PcZn$ is shown in Figure 1. Commercially available planar Pcs aggregate due to π - π stacking interaction that cancels their photoactivity.¹² The specialty of $F_{64}PcCu$ and $F_{64}PcZn$ is the bulky peripheral $-CF_3$ substituents which prevent the π - π stacking of these molecules.

In the present investigation, the effect of particle size of SiO_2 on photocatalytic efficiency is examined. The kinetics involved in the photodegradation of organic dyes such as methyl orange (MO) and Rhodamine B (RhB) in the presence of $F_{64}PcZn/SiO_2$ hybrid material is explained. The photostability of $F_{64}PcZn/SiO_2$ catalyst after photoreactions is tested. The change in particle size and zeta potential after the deposition of $F_{64}PcZn$ on SiO_2 is evaluated. The mode of adsorption of Pc on SiO_2 is analyzed using X-ray diffraction, UV-Vis-NIR spectroscopy and X-ray photoelectron

spectroscopy. Finally, a possible mechanism involved in the photodegradation of organic pollutants will be discussed.

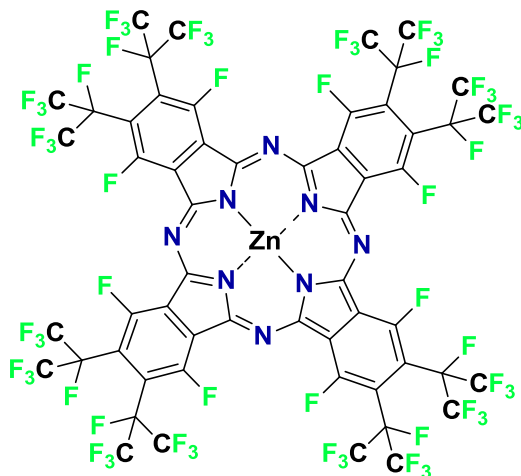


Figure 1. Chemical structure of zinc perfluoroalkyl perfluorophthalocyanine ($F_{64}PcZn$).

2.2. MATERIALS AND METHODS

2.2.1. Materials

SiO_2 particles of 63-200 μm size was purchased from Scientific Absorbents Incorporated, USA. The perfluoroalkyl perfluorinated phthalocyanines with Cu and Zn central metal atoms were synthesized by the members of our research group using an already reported method¹² and provided for this investigation. The synthesis involves reaction of perfluorophthalonitrile and perfluoropropene to produce perfluoro-4,5-di-(isopropyl)phthalonitrile. This compound was then reacted with zinc acetate or copper acetate to form $F_{64}PcZn$ and $F_{64}PcCu$.

2.2.2. Preparation of Hybrid Catalysts

1 mg of either F₆₄PcCu or F₆₄PcZn was dissolved in ethanol. 100 mg of SiO₂ was added to this solution. The solvent was removed by roto vaporization to obtain hybrid solid state catalysts, F₆₄PcCu/SiO₂ and F₆₄PcZn/SiO₂ (Figure 2). Then the composite photocatalysts were dried in the oven at 110 °C for 12 h before using for MO and RhB photodegradation studies.

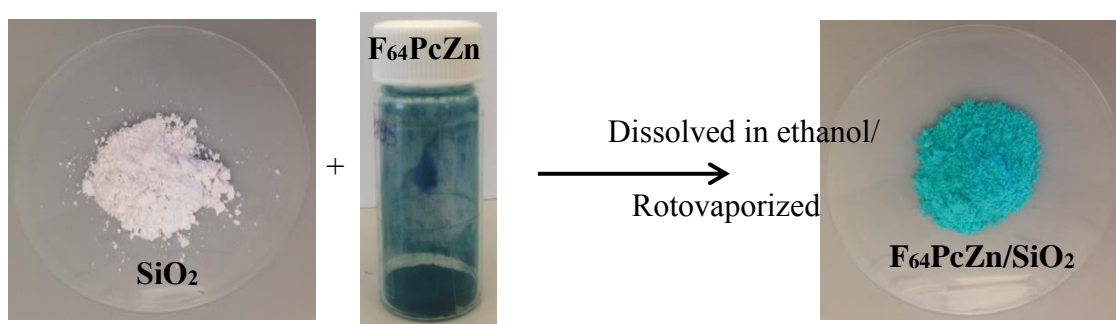


Figure 2. Preparation of F₆₄PcZn/SiO₂ hybrid catalyst.¹³

F₆₄PcM was extracted from the hybrid catalyst F₆₄PcM/SiO₂ using acetone to determine the amount deposited. The following example illustrates the method for determining the amount of F₆₄PcM, for example F₆₄PcZn, deposited on SiO₂ using UV-Vis spectrophotometer (ThermoFisher Scientific, USA).

Figure 3 shows the UV-Vis spectra for 10.5 mg of F₆₄PcZn/SiO₂ in 5 mL acetone. After extracting the Pc into acetone, the absorbance (A) was measured using UV-Vis spectroscopy. This was repeated three times. From the A value concentration (c) was calculated using the Beer-Lambert law as follows. Molar absorptivity (ϵ) of F₆₄PcZn in acetone at 686 nm is $1.73 \times 10^5 \text{ M}^{-1} \cdot \text{cm}^{-1}$.¹²

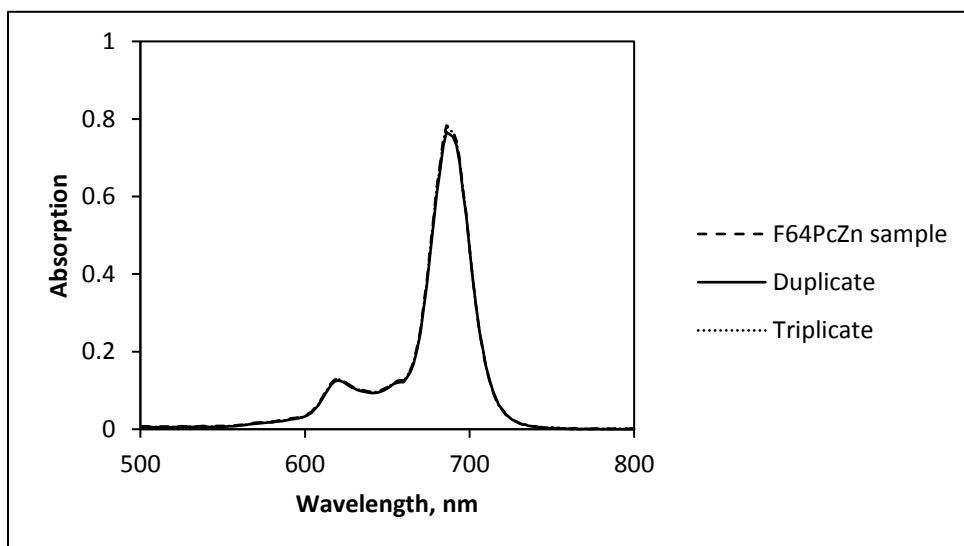


Figure 3. UV-Vis spectra of F₆₄PcZn in acetone extracted from F₆₄PcZn/SiO₂.

According to Beer-Lambert law,

$$\log I_0/I = \epsilon l c \text{ i.e., } A = \epsilon l c$$

$$l = 1 \text{ cm; } \epsilon = 1.73 \times 10^5 \text{ M}^{-1} \cdot \text{cm}^{-1} \text{ (in acetone at 686 nm)}^{12}$$

$$c = 0.005 \text{ mM/L}$$

In this example, $0.005 \text{ mM/L} \times 2066 \text{ g/mol} = 10.33 \text{ mg/L}$

Density of SiO₂ = 2.17g/ml; 1000 g of SiO₂ = 0.461 L. We added 30 mg F₆₄PcZn/1000 mg of SiO₂, in which 23 mg of F₆₄PcZn is deposited on 1000 mg of SiO₂.

2.2.3. Photochemical Reactions

To perform MO and RhB degradation measurements, 0.01 mM of catalyst was added to 50 mL of 0.1 mM MO/RhB solution. The system was kept under constant stirring at 1000 rpm speed and constant temperature of 25 °C, using a recirculating water bath. A tungsten halogen lamp was

used as a visible light source. The visible light intensity was 390,000 lx, i.e. 57 mW/cm² with the wavelengths ranging from 450 to 750 nm (approx. 3 Suns). The spectral distribution of tungsten halogen vapor lamp, as provided by the manufacturer, is given in Figure 4. The degradation of MO during photoreaction was followed by UV-Vis spectral measurements.

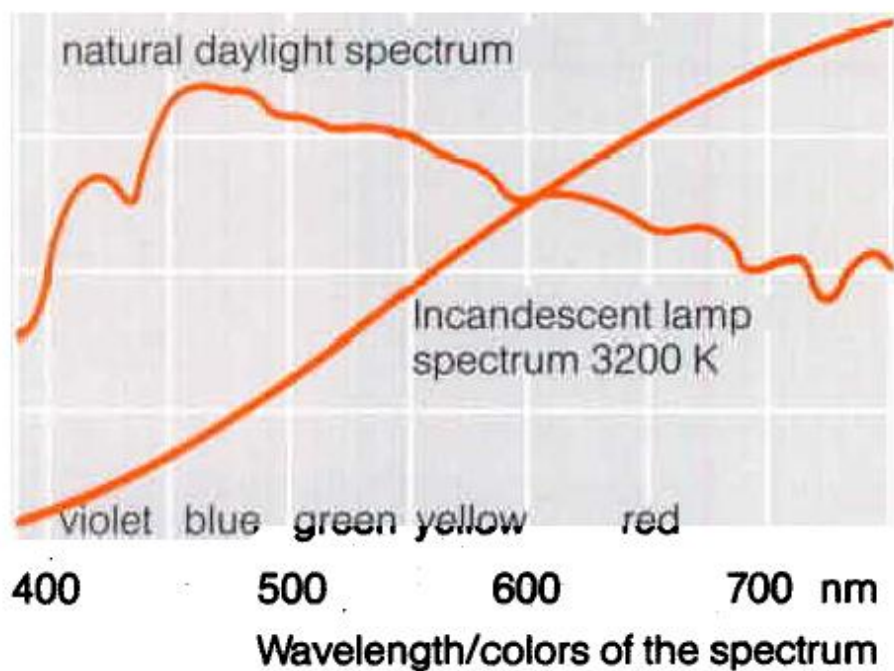


Figure 4. Spectral distribution of tungsten halogen lamp used as a visible light source (Copyright

© OSRAM SYLVANA Inc. 2001-2017).

2.2.4. Fluorescence Emission Intensity Measurements

The fluorescence emission spectra were recorded from 660 to 800 nm using a Spex model Fluoromax-3 spectrofluorometer by exciting F₆₄PcZn deposited on SiO₂ at the wavelength of 650

nm. Fluorescence intensities were recorded for 0.005, 0.01 and 0.03 mM of F₆₄PcZn deposited on SiO₂ (10-20 nm and OX50).

2.2.5. Particle Size and Zeta Potential Measurements

The particle size and zeta potential for the hybrid catalysts F₆₄PcZn/SiO₂ (10-20 nm) and F₆₄PcZn/OX50 were measured in de-ionized water using Zetasizer Nano ZS, Malvern Panalytical, USA.

2.2.6. Determination of Total Organic Carbon (TOC) and Total Dissolved Nitrogen (TDN)

The percentage of total organic carbon (TOC) and total dissolved nitrogen (TDN) were determined before and after 10 h of photodegradation of RhB catalyzed by F₆₄PcZn/SiO₂ (10-20 nm) and F₆₄PcZn/OX50 using Shimadzu TOC-VCPH Total Organic Carbon Analyzer.

2.2.7. UV-Vis-NIR Reflectance Spectral Measurements of Hybrid Catalysts

UV-Vis-NIR reflectance spectra for F₆₄PcZn/SiO₂ (10-20 nm) containing different amounts of F₆₄PcZn were recorded using a Perkin-Elmer Lambda 950 UV-Vis-NIR spectrophotometer capable of making measurements in the range of 190 to 3300 nm.

2.2.8. X-ray Diffraction Analysis of F₆₄PcZn/SiO₂

X-ray powder diffraction patterns were recorded for the F₆₄PcZn/SiO₂ (10-20 nm) catalyst using Siemens D-500 diffractometer with CuK α radiation source and scintillation counter detector. The XRD patterns were analyzed with the help of JADE XRD analysis software.

2.2.9. X-ray Photoelectron Spectroscopy Analysis of F₆₄PcZn/SiO₂

F₆₄PcZn and F₆₄PcZn/SiO₂ (OX50) were characterized using X-ray photoelectron spectroscopy (Thermo Scientific spectrometer). All spectra were taken using Al K α micro-focused monochromatized source (1486.6 eV) with a resolution of 0.6 eV. The spot size was 400 μ m and the operating pressure was 5×10^{-9} Pa.

2.3. RESULTS AND DISCUSSION

2.3.1. Efficiency of F₆₄PcCu/SiO₂ to Degrade MO under Visible Light Irradiation

The decrease in absorbance for MO with the addition of F₆₄PcCu/SiO₂ (63-200 μ m) composite particles is shown in Figure 5. In this initial study, 0.01 mM F₆₄PcCu deposited on SiO₂ is added to 0.002 mM MO solution. In general, the catalyst addition to the system should be minimum compared to the concentration of the active constituent in the reaction mixture, for example MO in this case. But, we can notice that the catalyst is added 5 times higher in concentration than MO.

The peak maximum for MO is centered at \approx 464 nm. The absorbance at 464 nm corresponds to the chromophore azo group -N=N- of MO.¹³

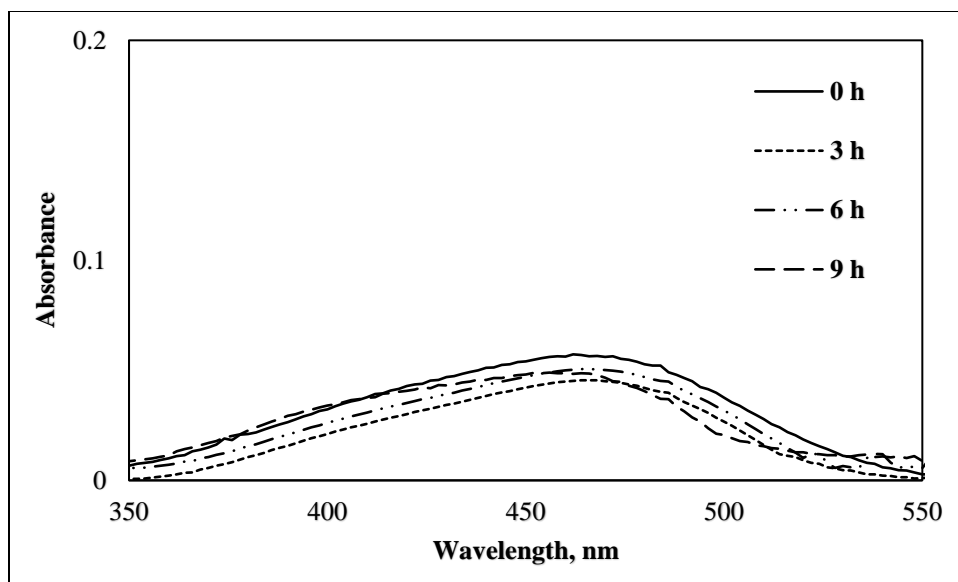


Figure 5. Photodegradation of MO catalyzed by $F_{64}PcCu/SiO_2$ under visible light irradiation.

There is a 17% reduction in the peak absorbance maxima from 0 to 9 h, again we must keep in mind the 5 times higher concentration of the catalyst added in the system. This result indicates, although the photoactivity of $F_{64}PcCu$ deposited on SiO_2 is not zero, in practice the application of this catalyst is questionable. $Cu(II)$ is paramagnetic with d^9 electronic configuration, the excited state of $F_{64}PcCu$ can be easily quenched by the unpaired electron in the d orbital of Cu . Hence, we decided to pursue $F_{64}PcZn$ with Zn as a metal center deposited on SiO_2 because $Zn(II)$ is diamagnetic with d^{10} electronic configuration.

2.3.2. Comparison of Photocatalytic Efficiency of $F_{64}PcCu/SiO_2$ and $F_{64}PcZn/SiO_2$

Figure 6 depicts the UV-Vis spectra for MO degradation catalyzed by $F_{64}PcZn/SiO_2$. The molar ratio between MO and Pc was 10:1. A slight decrease in absorbance is observed after 3 h

photodegradation reaction. A further decrease in the 464 nm peak reveals the destruction of MO azo group. The peak at 270 nm is related to the π - π transitions of the aromatic rings in the MO molecule.^{14,15} The intensity of 270 nm peak also diminished while a new peak started appearing at the lower wavelength of 236 nm.

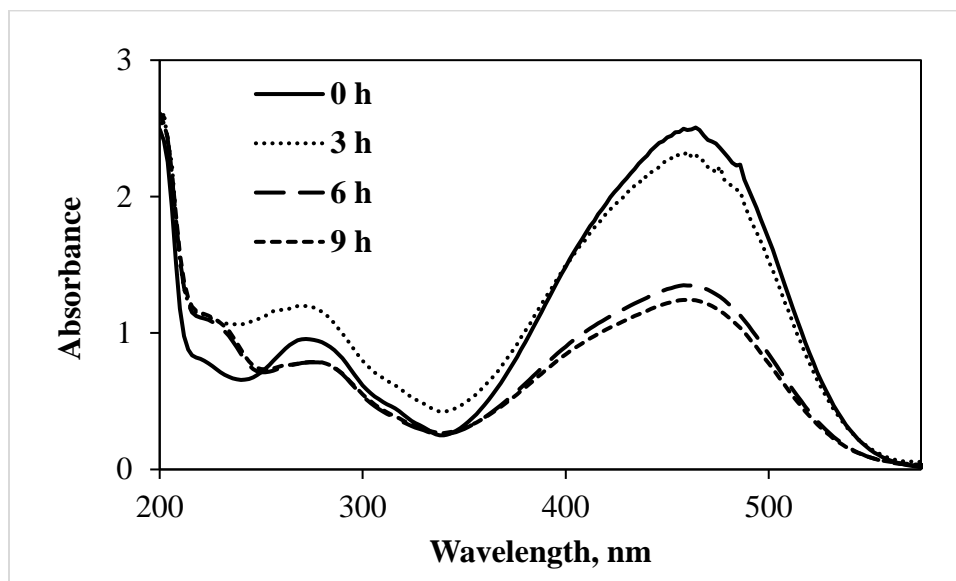


Figure 6. The influence of $F_{64}PcZn/SiO_2$ catalyst on the photodegradation of MO.

This new peak can be attributed to sulfanilic acid.¹⁵ The formation of sulfanilic acid as one of the MO degradation products can be confirmed by comparing the UV-Vis spectra for degradation products and pure sulfanilic acid from Literature.^{16,17} This observation proved the destruction of MO azo bond to form smaller molecular fragments due to the oxidative catalysis of $F_{64}PcZn/SiO_2$.

Figure 7 depicts the higher photocatalytic efficiency of $F_{64}PcZn/SiO_2$ than $F_{64}PcCu/SiO_2$. Only 1% of MO is degraded photocatalytically by $F_{64}PcCu/SiO_2$ after 9 h of visible light irradiation. While $F_{64}PcZn/SiO_2$ at the same concentration photodegraded 52% of MO. Following these observations, we want to examine the photostability of $F_{64}PcCu$ and $F_{64}PcZn$ deposited on SiO_2 after MO photodegradation reaction. The results are given below in Figure 8.

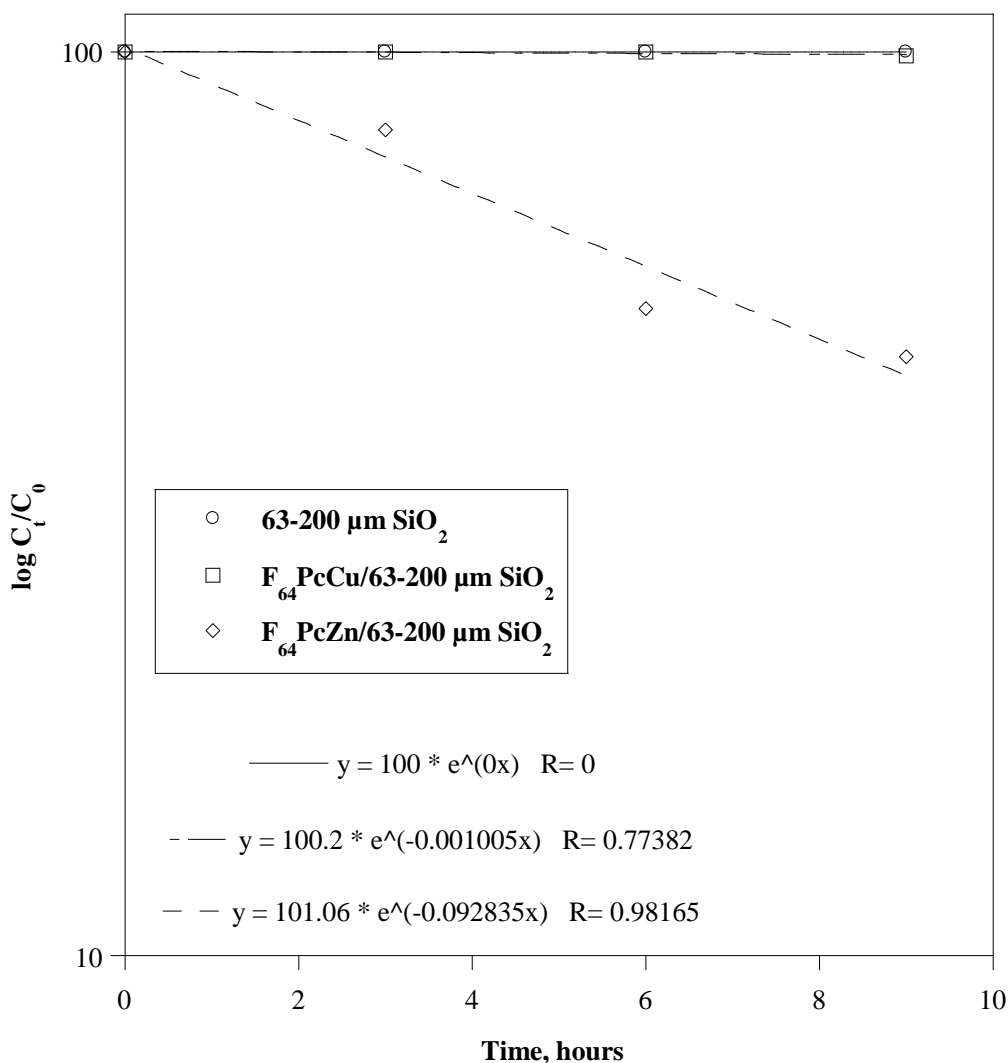


Figure 7. Comparison of photocatalytic efficiency of $F_{64}PcCu/SiO_2$ with $F_{64}PcZn/SiO_2$.

2.3.3. Evaluation of Photostability of F₆₄PcCu and F₆₄PcZn Deposited on SiO₂

To examine the integrity of F₆₄PcCu and F₆₄PcZn deposited on SiO₂ particle after MO photodegradation process, 10 mg of either F₆₄PcCu/SiO₂ or F₆₄PcZn/SiO₂ is added to 5 ml of acetone and the Pc is extracted into acetone by sonicating for 5 min. The UV-Vis absorbance spectra are measured to determine the change in Q band intensity (Figure 8). Results suggest that both F₆₄PcCu/SiO₂ (Figure 8a) and F₆₄PcZn/SiO₂ (Figure 8b) are photochemically robust by showing no change in the main peaks intensities. Here, it is important to remember that the metal center in F₆₄PcM is encapsulated in a refractive organic environment and the strong stabilization of frontier orbitals energy induced by the *i*-C₃F₇ groups disfavors the oxidation of the molecule via electron transfer.¹² Hence, a stable solid-state photocatalyst is thus established.

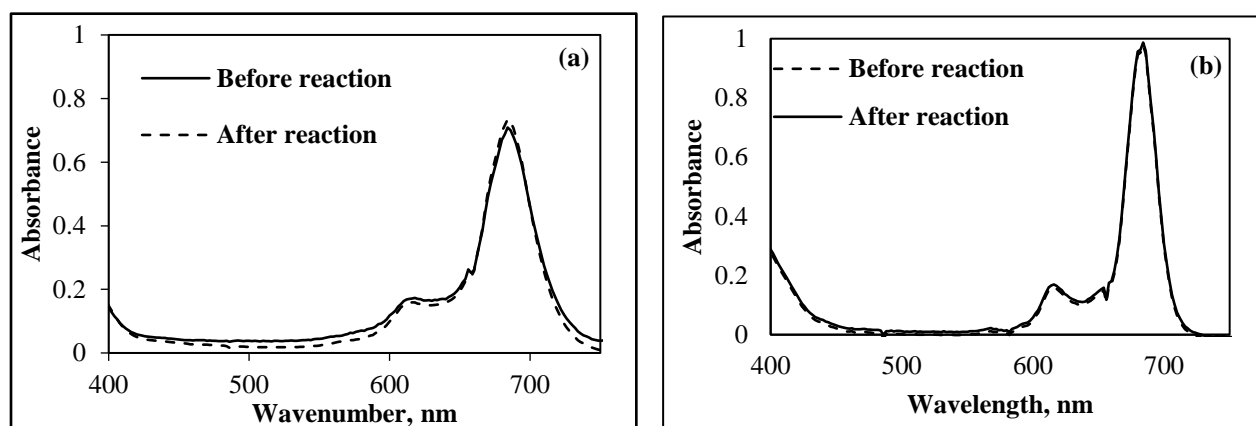


Figure 8. UV-Vis spectra of (a) F₆₄PcCu and (b) F₆₄PcZn extracted using acetone from F₆₄PcCu/SiO₂ and F₆₄PcZn/SiO₂ before and after photodegradation process of MO.

From the results, it can be seen that both F₆₄PcCu/SiO₂ and F₆₄PcZn/SiO₂ composite catalysts can photodegrade MO under visible light illumination. F₆₄PcZn/SiO₂ is 52 times more

efficient as compared to $F_{64}PcCu/SiO_2$. $F_{64}PcZn/SiO_2$ exhibits MO photocatalytic degradation when added at 10 times lesser than the MO concentration.

2.3.4. $F_{64}PcCu/SiO_2$ Versus $F_{64}PcZn/SiO_2$

The MO photodegradation results clearly revealed higher photocatalytic efficiency for $F_{64}PcZn/SiO_2$ as compared to $F_{64}PcCu/SiO_2$. From the literature review it is assumed that the lower photocatalytic efficiency of $F_{64}PcCu$ deposited on SiO_2 is due to the following reason. Having the paramagnetic Cu(II) as a metal center with d^9 electronic configuration, an ultrafast deactivation of initial excited state of the compound might occur. In contrast, Zn(II) is diamagnetic with closed d^{10} electronic configuration. This assumption is supported by the fluorescence spectral data reported by La *et al.*¹⁸ They developed a fluorescent probe based on this concept and showed in their work a fluorescence quenching in the presence of Cu(II) ions in contrast to high intensity fluorescence emission when Zn(II) ions are present. Similarly, in the current study $F_{64}PcCu/SiO_2$ showed less activity which might be due to the ultrafast deactivation of initially excited state of this paramagnetic compound. Further investigations are performed in this thesis only for photoefficient $F_{64}PcZn$ deposited on solid-state matrices rather than $F_{64}PcCu$ which shows a lower photoactivity.

2.3.5. Variation in Catalyst Ratio of $F_{64}PcZn/SiO_2$ Composite Particles

Figure 9 depicts the UV-Vis spectra for MO photodegradation in the presence of $F_{64}PcZn/SiO_2$. The ratio of catalyst added is further reduced to 0.005 mM to 0.1 mM MO.

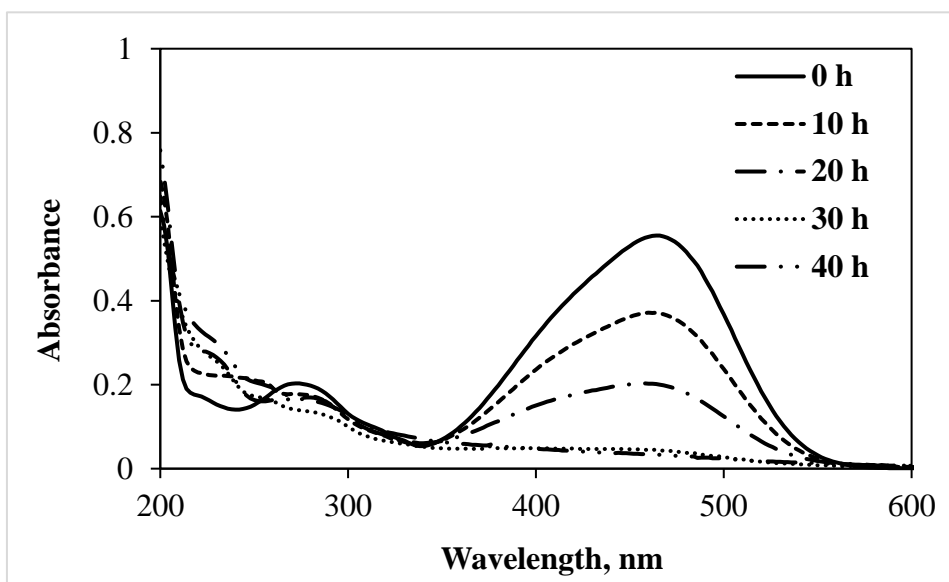


Figure 9. MO photodegradation in the presence of 0.005 mM F₆₄PcZn/SiO₂.

The relative kinetic plots are displayed in Figure 10. SiO₂ exhibits no photocatalytic activity. Even at this ratio of F₆₄PcZn/SiO₂, the absorbance maxima at 464 nm is decreased with irradiation time and disappeared around 30 h suggesting the destruction of -N=N- azo group of MO.¹⁹ Even the peak intensity at 270 nm decreased and new peaks around 230 nm appeared indicating the formation of smaller molecular fragments.^{15,17,20} By comparing the Figures 7 and 10, we can notice nearly a 15% increase in the reaction rate for 0.01 (0.0928 h⁻¹) than 0.005 mM (0.0789 h⁻¹) of F₆₄PcZn/SiO₂.

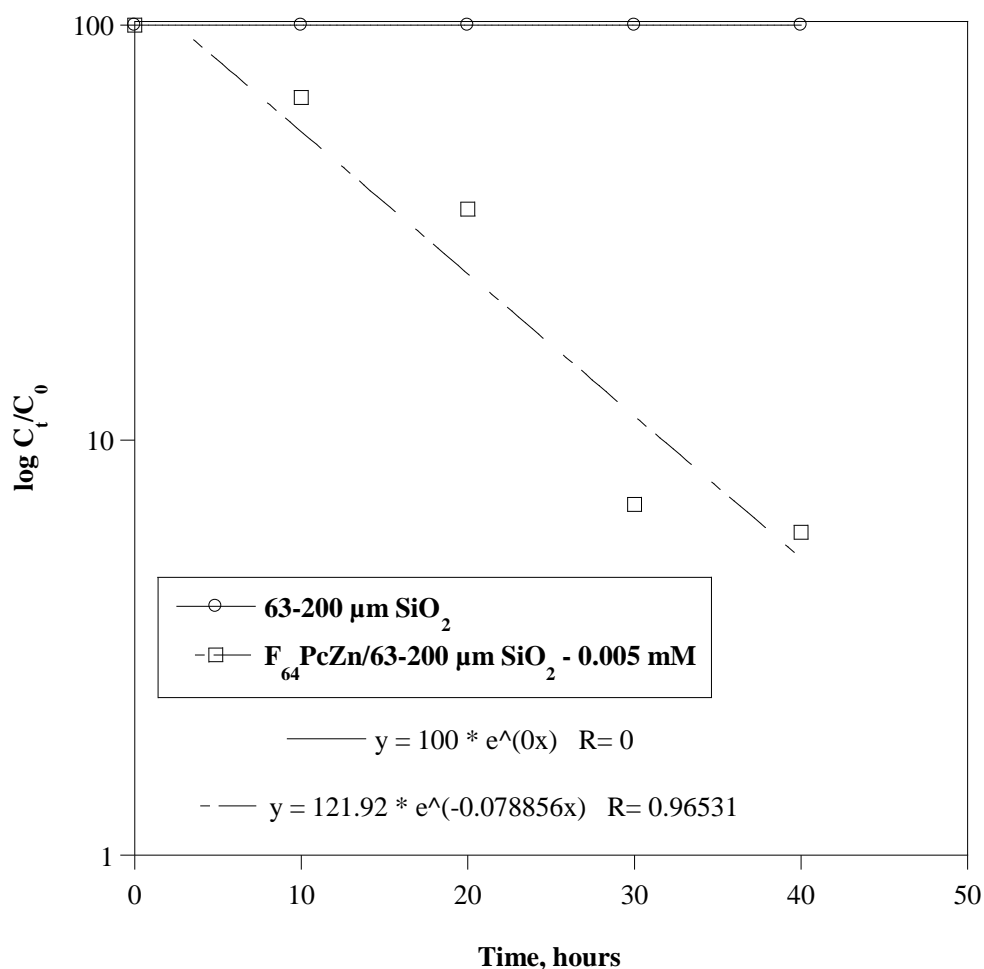


Figure 10. Photocatalytic efficiency of F₆₄PcZn/SiO₂ at lower concentration of 0.005 mM.

Kinetic plots for the degradation of MO.

2.3.6. Influence of Particle Size, Type, Surface Area, and Pore Structure on the Efficiency of Hybrid Photocatalysts

The efficiency of solid-state photocatalysts significantly depends upon their particle sizes in addition to several other factors such as position of band gap edges, porosity, type, surface area etc. Small particle size is a positive factor in hybrid photocatalysts in terms of larger specific surface area. We deposited 3 wt. % (15 mM) of F₆₄PcZn on SiO₂ with various particle sizes and

investigated the change in particle size and related catalytic efficiency. Voronina *et al* reported an increase in the size of the SiO₂ particle after the deposition of phthalocyanines.²⁰ Cobalt (II) sulfo-substituted phthalocyanines are covalently immobilized on SiO₂ matrix due to the interaction of surface hydroxyl groups with sulfo-substituents in the Pc molecules. Using the method of laser diffraction on Analysette 22 Compaq (FRITCH, Germany), they measured the particle sizes in aqueous suspension and noticed that the phthalocyanine immobilized SiO₂ aggregates, resulted in a larger particle size. Ogihara *et al* observed an increase in the particle size of SiO₂ when spray coated with CuPc that lead to increased wettability while they are testing for super hydrophobicity.²¹ In the present investigation, F₆₄PcZn is coated on various smaller size SiO₂ particles to aid the fine distribution of F₆₄PcZn in the aqueous system to improve catalytic efficiency. As a first step, SiO₂ of size 4-12 μm is utilized to deposit F₆₄PcZn and then the initial particle size is further reduced to nanometer scale such as 10-20 nm SiO₂ and 40 nm OX50 SiO₂.

2.3.7. Particle Size Distribution of F₆₄PcZn/SiO₂ Catalysts

Particle size distribution results in de-ionized water for bare SiO₂ and hybrid particles such as F₆₄PcZn/10-20 nm SiO₂ and F₆₄PcZn/OX50 are illustrated in Figure 11. The primary particle size reported by the manufacturer (Evonik, USA) for OX50 is 40 nm according to TEM image analysis. The smaller the particle size, the more pronounced the aggregate formation because of increased surface energy. OX50 readily forms aggregates due to its smaller particle size. In the current investigation the particle sizes are measured in de-ionized water at static conditions, we observed only secondary particle sizes due to agglomeration. The particle sizes measured for SiO₂ and OX50 in de-ionized water are 156 and 165 nm (Figure 11).

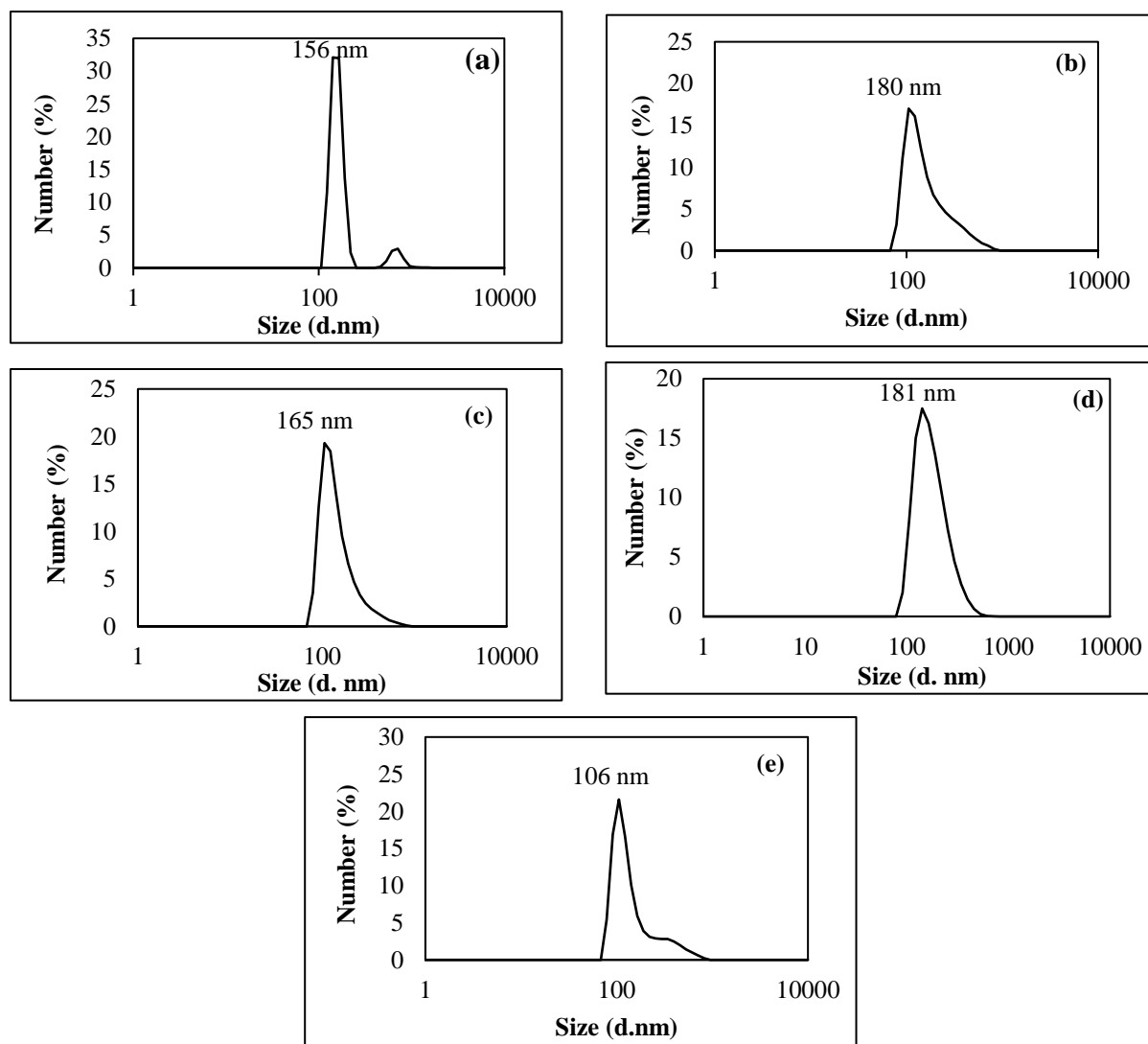


Figure 11. Particle size distribution for (a, b) 10-20 nm SiO₂ and F₆₄PcZn/SiO₂, (c, d) OX50 SiO₂ and F₆₄PcZn/SiO₂ (before photoreaction), (e) OX50 F₆₄PcZn/SiO₂ after photoreaction.

A similar clustering effect is observed for the hybrid catalysts and the particle sizes determined for F₆₄PcZn/10-20 nm SiO₂ and F₆₄PcZn/OX50 SiO₂ are 180 and 181 nm. Since the solution mixture is stirred continuously at 1000 rpm during the photoreaction, the aggregates might be dispersed, the real particle sizes seen under experimental conditions could be even smaller than

the ones reported here, which is measured under static conditions. The particle size of F₆₄PcZn/OX50 SiO₂ was also measured after MO photodegradation reaction. The particle size decreased to 106 nm which could be due to the stirring effect.

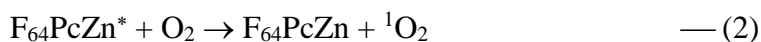
2.3.8. Kinetics Study on Degradation of MO Catalyzed by F₆₄PcZn Deposited on 63-200 μm, 4-12 μm, 10-20 nm and 40 nm SiO₂

The kinetics of MO degradation catalyzed by F₆₄PcZn, F₆₄PcZn/63-200 μm SiO₂, F₆₄PcZn/4-12 μm SiO₂, F₆₄PcZn/10-20 nm SiO₂ and F₆₄PcZn/OX50 (40 nm SiO₂) under illumination of 390,000 lx (~ 3 Suns) visible light are studied and the results are given in Figure 12. The plot of log C_t/C₀ versus time shows a linear dependence with R values of 0.99 for all the catalysts investigated indicating these reactions follow pseudo first order kinetics. F₆₄PcZn is hydrophobic because of the -CF₃ groups in the peripheral positions of the molecule. Dalvi and Rosky investigated the molecular origins of fluorocarbon hydrophobicity in water.²² They claimed that the strong tendency of water to maintain hydrogen bonding network structure at an interface lacking hydrophilic sites leads to greater hydrophobicity for fluorocarbons. Because of the hydrophobicity F₆₄PcZn aggregates in water. Therefore, a low *k* value of 0.01 is obtained when F₆₄PcZn directly added in the MO solution.

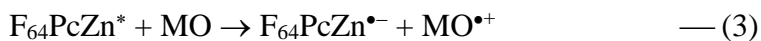
As we can see from Figure 12, a linear increase in the photodegradation rate of MO is observed while decreasing the SiO₂ particle size deposited with the same amount of F₆₄PcZn. The photo-reactivity of the hybrid catalysts increased in the following order: F₆₄PcZn/63-200 μm SiO₂ < F₆₄PcZn/4-12 μm SiO₂ < F₆₄PcZn/10-20 nm SiO₂ < F₆₄PcZn/OX50 (40 nm SiO₂). As the particle size decreases the surface area increases, in this way the F₆₄PcZn molecules can be spread more

on the surface avoiding formation of multiple layers of Pc. It is assumed more number of Pc molecules are exposed to visible light when the SiO₂ particles surface area is larger as in the case of smaller size particles. The results suggest that the photocatalytic efficiency of F₆₄PcZn/SiO₂ hybrids depend on the particle size, pore structure, origin of SiO₂ (F₆₄PcZn/10-20 nm SiO₂ from Sigma-Aldrich < F₆₄PcZn/OX50 40 nm SiO₂ from Evonik) and distribution of F₆₄PcZn on SiO₂.

The mechanism of photocatalysis involves excitation of F₆₄PcZn by absorbing visible light followed by the production of reactive singlet oxygen species (equations 1 and 2) that attacks MO to degrade into smaller fragments.



It has been claimed that the F₆₄PcZn, an electron deficient Pc, can be easily reduced.¹¹ Hence, an electron is transferred from MO to form cation MO^{+•}, which then undergoes degradation as given in equations 3 and 4.



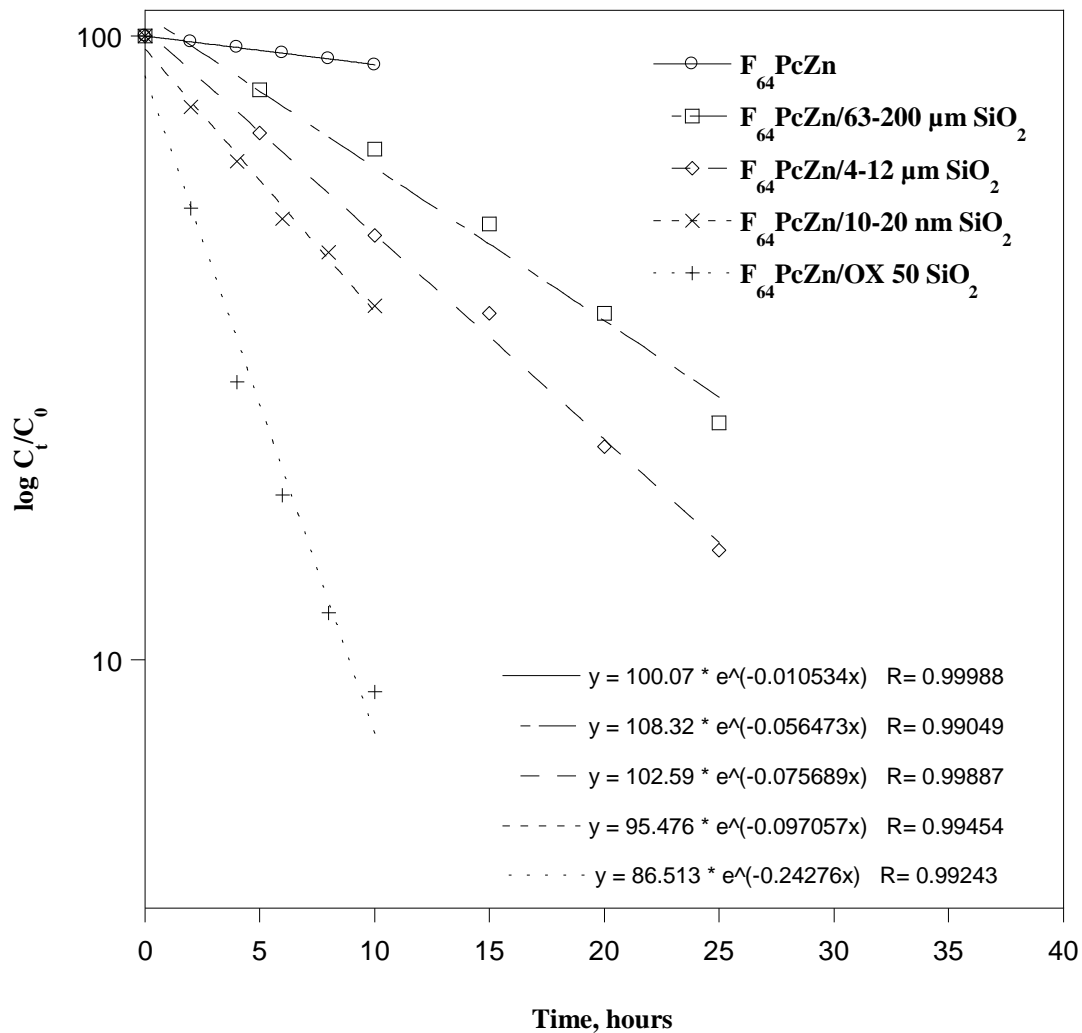


Figure 12. Comparison of MO photodegradation catalyzed by $F_{64}PcZn$, $F_{64}PcZn/63-200 \mu m SiO_2$, $F_{64}PcZn/4-12 \mu m SiO_2$, $F_{64}PcZn/10-20 nm SiO_2$ and $F_{64}PcZn/OX50$ (40 nm SiO_2) under illumination of 390,000 lx visible light.

Among the hybrid photocatalysts, $F_{64}PcZn/OX50$ with the reported particle size of 40 nm SiO_2 from Evonik exhibited 2.5 times higher photoactivity as compared to $F_{64}PcZn/10-20 nm SiO_2$ from Sigma-Aldrich. This could be due to the higher dispersibility and lesser agglomeration of

F₆₄PcZn/OX50 than F₆₄PcZn/10-20 nm SiO₂. This indicates the catalyst distribution, pore structure and origin of SiO₂ greatly affects the hybrid catalyst efficiency. This observation will be discussed in detail in the following fluorescence intensity analysis and particle size measurement sections.

2.3.9. Fluorescence intensity of F₆₄PcZn/10-20 nm SiO₂ and F₆₄PcZn/OX50 catalysts

Figure 13 depicts the fluorescence emission spectra for F₆₄PcZn/10-20 nm SiO₂ in comparison to F₆₄PcZn/OX50. The intense fluorescence peak for F₆₄PcZn deposited on SiO₂ that has a wide bandgap suggests there is no orbital coupling occurs. F₆₄PcZn/OX50 exhibits a wide intense fluorescence peak while F₆₄PcZn/10-20 nm SiO₂ fluorescence intensity is 4.5 times lesser. It is assumed from the results the surface area provided by 10-20 nm SiO₂ for the adsorption of F₆₄PcZn is lesser than OX50. Hence, F₆₄PcZn forms multi-layers when deposited on 10-20 nm SiO₂. The lesser fluorescence intensity for F₆₄PcZn/10-20 nm SiO₂ explains the lower MO photodegradation reaction rate than F₆₄PcZn/OX50.

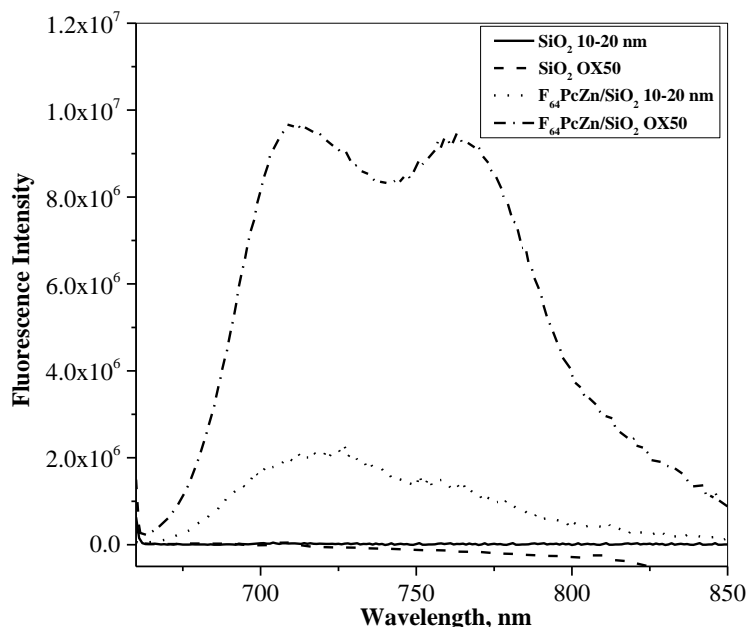


Figure 13. Fluorescence emission spectra for SiO₂ 10-20 nm, SiO₂ OX50, F₆₄PcZn/ SiO₂ 10-20 nm and F₆₄PcZn/OX50 catalysts.

2.3.10. Influence of Oxygen on the Photocatalytic Activity of F₆₄PcZn/SiO₂

Photodegradation studies for MO with the addition of F₆₄PcZn/SiO₂ (4-12 μm) hybrid catalyst is performed in both argon and air under visible light illumination. The experiment in air is also carried out in dark to observe the effect of light in producing reactive singlet oxygen. The molar ratio of MO to catalyst is 10 : 1.

MO degradation reaction in the presence of F₆₄PcZn/SiO₂ (4-12 μm) is initially performed in argon atmosphere for 10 hrs under visible light illumination (Figure 14). No photocatalytic activity is observed. F₆₄PcZn/SiO₂ is active only in air *i.e.*, in the presence of oxygen. To confirm this, the reaction is continued in the presence of air for another 10 hours. MO is effectively

degraded by the catalyst and the bleaching of MO is noticed (Figure 15). In addition, the reaction is also carried out in the presence of air, but in the dark. Again, we observed no reaction. From these results we concluded that the reactive oxygen species formed only in the presence of both air and light.

From the above discussion, we conclude that the rate determining step will be the formation of singlet oxygen ($^1\text{O}_2$) followed by the production of superoxide radical anions $\text{O}_2^{\bullet-}$, $\bullet\text{OOH}$ and $\bullet\text{OH}$. Once $^1\text{O}_2$ is produced, the other steps of daughter radical formation and degradation of pollutants will be faster.

We propose the degradation pathway of MO follows similar mechanism reported by Okte and Yilmaz.²³ The electron excited from the ground state to the excited state of F_{64}PcZn in the presence of light produced $^1\text{O}_2$ and the daughter radicals like $\text{O}_2^{\bullet-}$ and $\bullet\text{OH}$ then attack the azo bond in MO molecule to break down into smaller molecular fragments. Finally, the smaller molecules may oxidize to nontoxic CO_2 and H_2O .²²

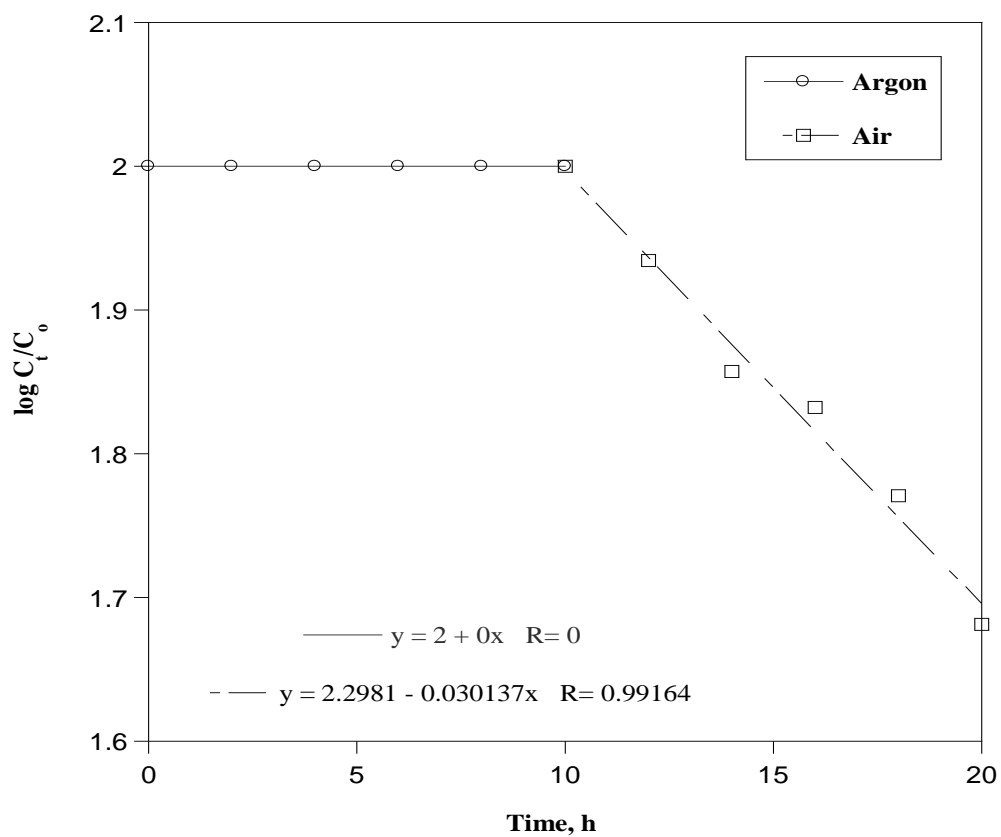


Figure 14. Effect of oxygen: MO photodegradation catalyzed by $F_{64}PcZn/SiO_2$

in argon and air atmospheres.



Figure 15. Decolourization of MO with irradiation time. Aliquotes taken every 2 hours,

from left to right, 0, 2, 4, 6, 8 and 10 hours.¹³

2.3.11. Rhodamine B (RhB) Photodegradation Catalyzed by F₆₄PcZn/SiO₂ 10-20 nm and F₆₄PcZn/SiO₂ OX50

In addition to MO which is an azo dye, the catalytic efficiency of F₆₄PcZn/SiO₂ 10-20 nm and F₆₄PcZn/SiO₂ OX50 in degrading a xanthene dye, RhB, is also examined. This polyaromatic dye is carcinogenic, genotoxic, and mutagenic; because of its stability, it is quite hard to break this molecule into smaller non-toxic fragments.²³

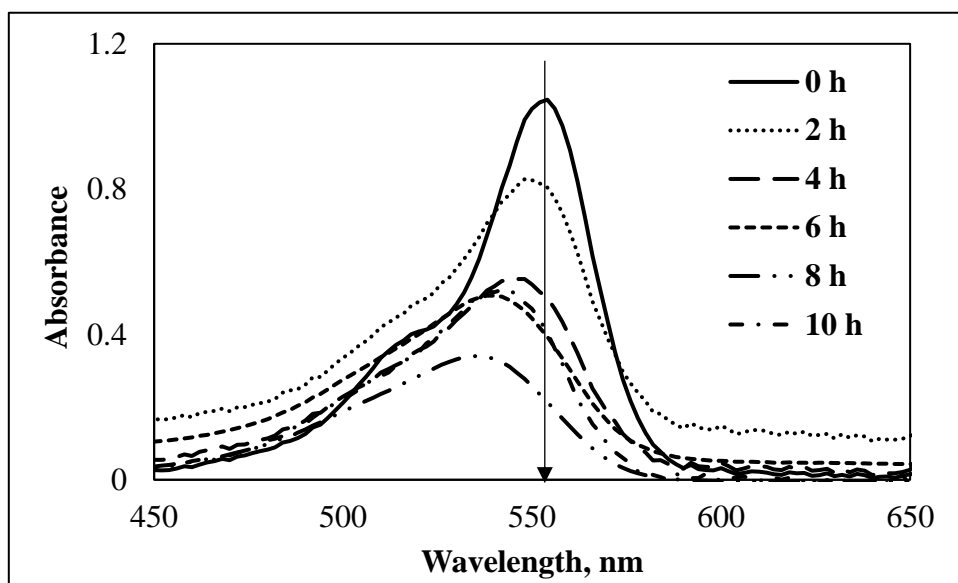


Figure 16. Photodegradation of RhB catalyzed by F₆₄PcZn/OX50.

UV-Vis spectra of RhB photodegradation catalyzed by F₆₄PcZn/OX50 recorded every 2 h up to 10 h is displayed in Figure 16. It can be noticed from the figure, the peak intensity at 554 nm decreased during the course of reaction indicating the destruction of the conjugated structure while a blue shift in the absorbance maximum suggests successive de-ethylation from the aromatic rings, which produces smaller molecular fragments.^{24,25} The shift of wavelength to the blue region

confirms the de-ethylation of aromatic rings is the predominant mechanism involved in the photodegradation process of RhB. This can be clearly explained as follows. If the chromophore of the molecule is destructed, then there will be a drastic decrease in the peak at 554 nm, that corresponded to the chromophore, and several peaks will appear at the lower wavelengths related to the smaller molecular fragments. In this case there would not be any shift in the absorbance maxima. In contrast, here the peak maxima shifted to shorter wavelengths that shows the side groups attached to the chromophore of the molecule are fragmented, but not the chromophore itself.

The rate of decrease in the peak intensity at 554 nm versus time is illustrated in Figure 17 as kinetic plots. The results reveal that the degradation reaction followed first order kinetics. Similar to MO, F₆₄PcZn/OX50 showed a higher photocatalytic activity than F₆₄PcZn/10-20 nm SiO₂. The rate constant *k* is significantly higher, that is 9.4 times, for F₆₄PcZn/OX50. The particle size measurements in Figure 11 suggest similar particle sizes for both F₆₄PcZn/10-20 nm SiO₂ and F₆₄PcZn/OX50 in de-ionized water. But, the matrix 10-20 nm SiO₂ is purchased from Sigma-Aldrich and OX50 is a fumed SiO₂ obtained from Evonik. Since both are obtained from different providers, we are unable to correlate the photodegradation reaction rates directly with the particle size distributions in this case. The reaction rates correlate with the fluorescence peak intensities displayed in Figure 13 for the catalysts F₆₄PcZn/10-20 nm SiO₂ and F₆₄PcZn/OX50.

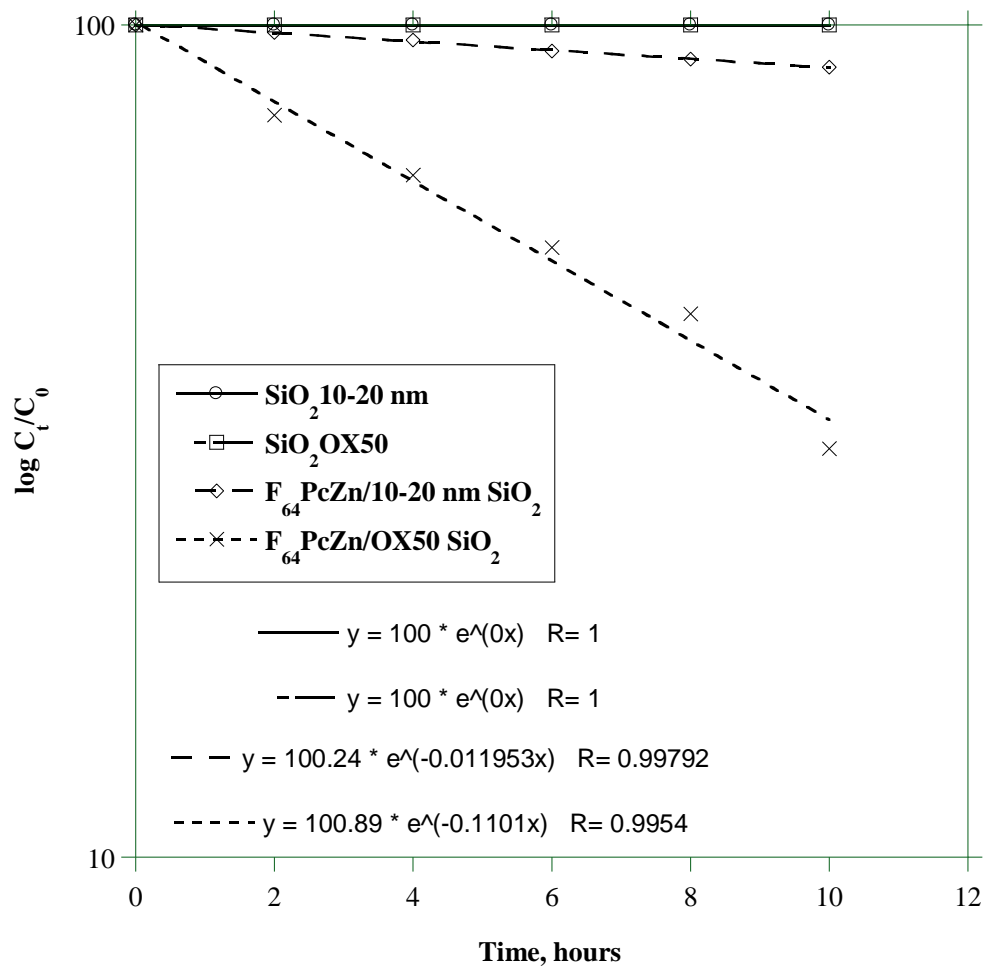


Figure 17. RhB photodegradation catalyzed by F₆₄PcZn/10-20 nm SiO₂ and F₆₄PcZn/OX50 irradiated with visible light.

In addition to particle size effect, the chemical structure of the pollutants (dye molecules: C₁₄H₁₄N₃NaNO₃S (MO) and C₂₈H₃₁ClN₂O₃ (RhB)) also account for the rate of degradation. RhB is a heteropolyaromatic dye, while it may be easier to break the azo bond of MO.²² It can be noticed that the *k* value is 2.2 times higher for MO degradation in comparison to RhB in the case of F₆₄PcZn/OX50.

2.3.12. Mechanism Involved in the Photodegradation Process of Organic Pollutants

Based on the above results we conclude the formation of superoxide radical, $O_2^{\bullet-}$, followed by the daughter radicals like $\bullet OH$ in addition to the formation of $MO^{\bullet+}$ and $F_{64}PcZn^{\bullet-}$ as shown in Figure 18 play a major role in the photodegradation of organic pollutants, for example MO .^{5,26}

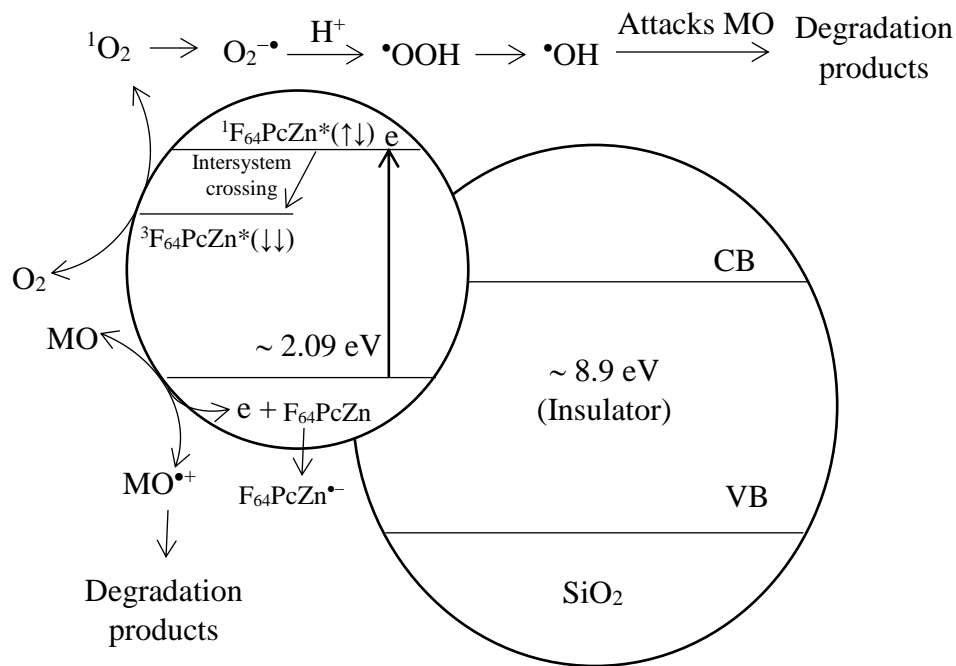
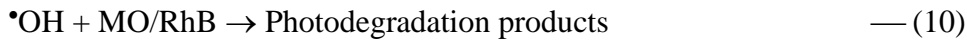
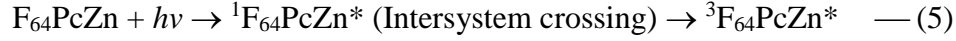


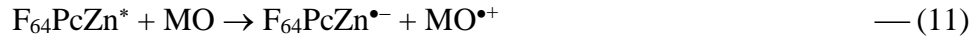
Figure 18. Radical mechanisms involved in the photodegradation of MO catalyzed by $F_{64}PcZn/SiO_2$.

When $F_{64}PcZn/SiO_2$ hybrid catalyst is irradiated with visible light, $F_{64}PcZn$ is excited to a triplet state ($^3F_{64}PcZn^*$) that has 10^3 - 10^7 times longer life than the singlet state ($^1F_{64}PcZn^*$). $^3F_{64}PcZn^*$

reacts with the dissolved oxygen in water via energy transfer to produce singlet oxygen $^1\text{O}_2$. The photoreactions that lead to MO and RhB degradation can be explained as follows.^{5,26}



In addition to this process, the following radical mechanism is also involved in the photoreaction.



Here, the rate limiting step will be the formation of singlet oxygen, $^1\text{O}_2$. Once the $^1\text{O}_2$ is produced the other processes of photodegradation reaction occur faster.

2.3.13. Determination of TOC and TDN for Photodegraded RhB Catalyzed by $\text{F}_{64}\text{PcZn}/\text{SiO}_2$

Figure 19 displays the % of TOC and TDN before and after 10 h of RhB photodegradation catalyzed by $\text{F}_{64}\text{PcZn}/\text{SiO}_2$ 10-20 nm and $\text{F}_{64}\text{PcZn}/\text{OX50}$. We can observe from the figure, the % TOC and % TDN decreased due to RhB photodegradation for both catalysts. But, similar to other

results such as reaction rate and fluorescence intensity, the TOC and TDN are lower for the reaction catalyzed by F₆₄PcZn/OX50.

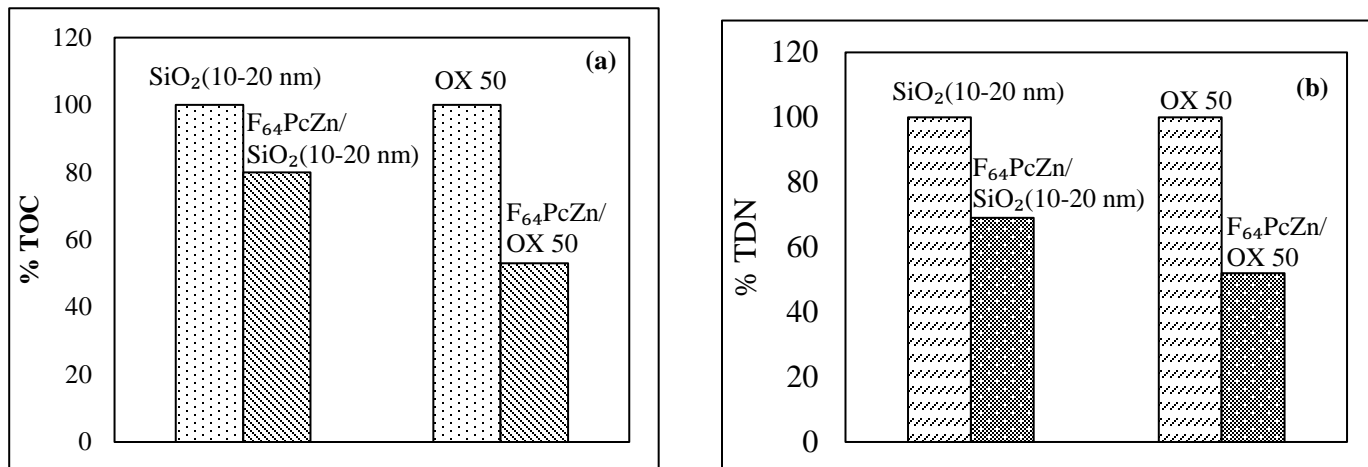


Figure 19. Percentages of (a) TOC and (b) TDN after photodegradation of RhB for 10 h.

F₆₄PcZn/OX50 is more efficient than F₆₄PcZn/SiO₂ 10-20 nm.

The mineralization of organic carbon and nitrogen would lead to the formation of inorganic ions such as COO⁻, NH₄⁺, NO₃⁻ and HCO₃⁻/CO₃²⁻.²⁷ Here it is important to remember the formation of specific ions in high concentrations can affect the pH of water. If water, due to photodegradation reactions, becomes acidic then it may cause issues to both aquatic and human life.^{28,29} It can affect the solubility and toxicity of chemicals and heavy metals in water. So, we check for any changes in the pH before and after photodegradation reaction. When we added 0.01 mM F₆₄PcZn/10-20 nm SiO₂ to MO solution, the pH of the solution changed from 4.1 to 4.2 after photodegradation reaction for 10 h. The pH stayed at 5.0 before and after MO photodegradation reaction with the addition of 0.01 mM F₆₄PcZn/OX50 SiO₂. The results indicate no remarkable variation in pH of the test solution, which may be because a combination of various acidic and basic ions are formed as photodegradation products.

2.3.14. Change in Zeta Potential for F₆₄PcZn/ SiO₂ Catalysts

Table 1 shows the zeta potential obtained for the catalysts investigated in de-ionized water. In general, SiO₂ exhibited negative zeta potential. Mostly silanol groups are present on the surface of SiO₂ in water. After F₆₄PcZn is deposited on the surface, a slight increase in the negative values are observed. This can be related to the perfluoro groups of F₆₄PcZn.³⁰ After photoreaction the zeta potential for F₆₄PcZn/OX50 is still negative as shown in Table 1.

Table 1. Zeta potential for F₆₄PcZn hybrid photocatalysts.

S. No.	Samples	Zeta potential, mV
1	SiO ₂ (10-20 nm)	- 23.6
2	F ₆₄ PcZn/10-20 nm SiO ₂	-27.4
3	OX50 SiO ₂	-31.5
4	F ₆₄ PcZn/OX50	-32.7
5	F ₆₄ PcZn/OX50 - After photoreaction	-29.2

2.3.15. Influence of F₆₄PcZn Molar Concentration on Photo Efficiency and Fluorescence Intensity

As shown in Figure 20, the photoactivity is increased linearly with increasing molar concentration of F₆₄PcZn deposited on SiO₂. In general, under the experimental conditions, silanol groups will be present on the surface of SiO₂ (Figure 21). When F₆₄PcZn is deposited, it can be adsorbed on the surface of SiO₂ through Lewis interactions, that is the interaction between negatively charged Si-O⁻ groups and the central Zn²⁺ ion of Pc, which is more Lewis acidic because of -CF₃ groups at the peripheral positions of the molecule. If more and more F₆₄PcZn is deposited on SiO₂ then these molecules are stacked on the surface of SiO₂ as shown in the Figure 22. These multi layers are stayed together because of the weak van der Waals forces between them.

To understand the photocatalytic activity increase in aqueous solution with increasing amount of F₆₄PcZn deposition on SiO₂ 10-20 nm, fluorescence intensity is measured for these samples. Figure 21 depicts the fluorescence intensity of 0.005, 0.01 and 0.03 mM F₆₄PcZn deposited on SiO₂. The highest intensity fluorescence peak with a shoulder is observed for the lowest amount of 0.005 mM F₆₄PcZn deposition on SiO₂. By increasing the F₆₄PcZn amount to 0.01 mM, the fluorescence intensity dropped randomly. Further increase in F₆₄PcZn deposited amount on SiO₂ to 0.03 mM, resulted in almost complete quenching of fluorescence. These results suggest despite the bulky *i*-C₃F₇ groups too much deposition of F₆₄PcZn leads to packing of this compound in multi-layers that quenches the photocatalytic activity at very high amounts. This study clearly indicates an optimum amount of F₆₄PcZn needs to be deposited on SiO₂ particles to achieve highest catalysis. The catalytic efficiency of the hybrid depends on the surface area of the matrix.

In contrast, the MO degradation kinetics showed linear increase in reaction rate with increasing $F_{64}PcZn$ deposition amount on SiO_2 . As mentioned above the multi-layers of $F_{64}PcZn$ stays together via weak van der Waals forces. The photo reaction mixture is stirred at 1000 rpm during catalytic reaction. $F_{64}PcZn$ desorbs from the surface of SiO_2 and finely dispersed in water because of stirring effect. Note the amount of $F_{64}PcZn$ is very high *i. e.*, 0.03 mM. At this high concentration, $F_{64}PcZn$ is finely divided in the reaction mixture due to stirring, leads to an increase in MO degradation rate. Otherwise the higher amount of $F_{64}PcZn$ on SiO_2 in fact quenches the catalytic activity.

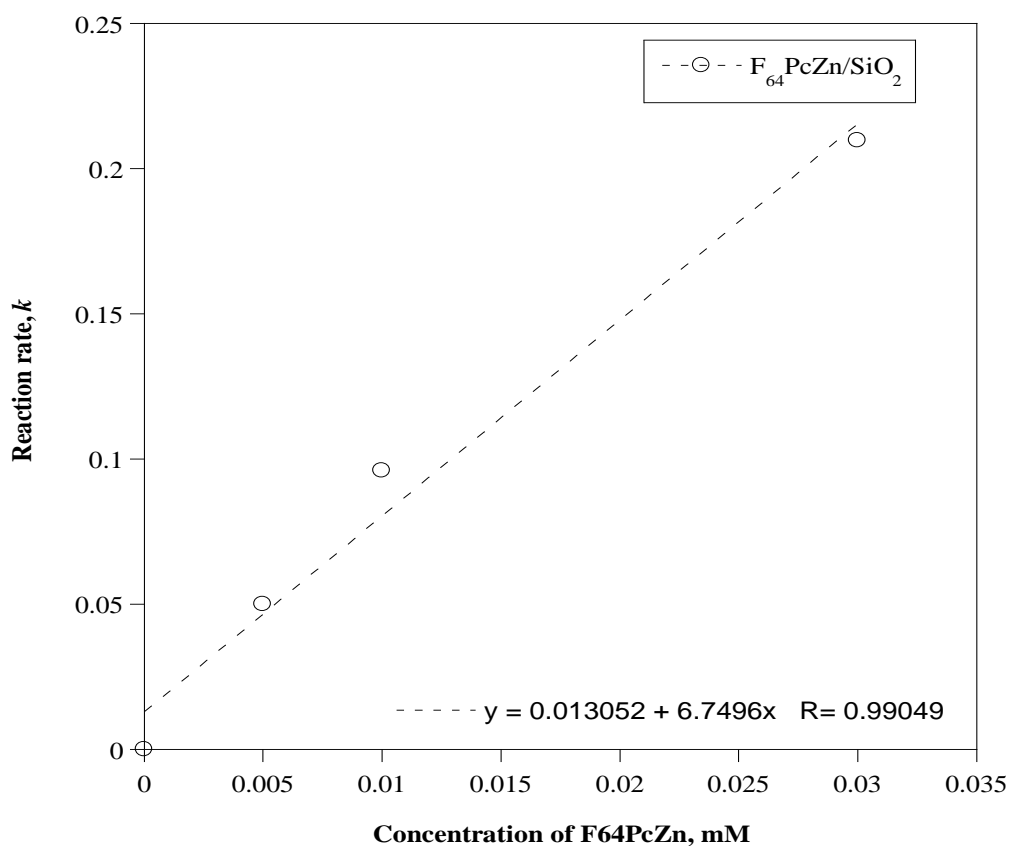


Figure 20. Effect of increasing $F_{64}PcZn$ molar concentration deposited on SiO_2 . Change in reaction rate of MO photodegradation.

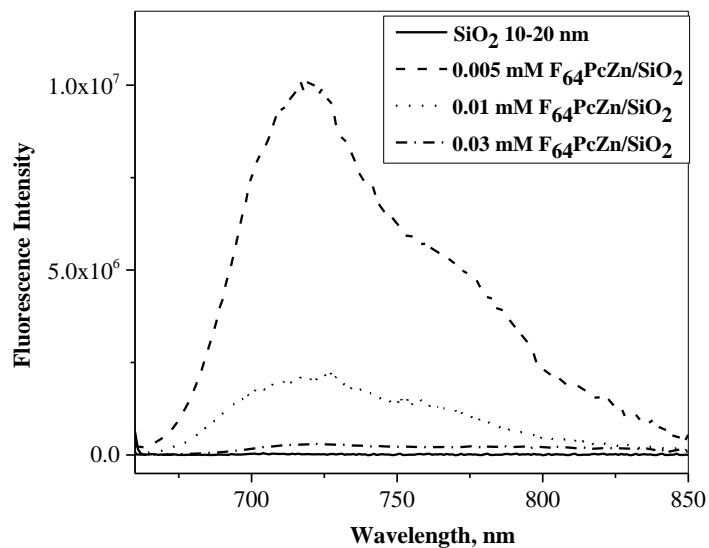


Figure 21. Fluorescence intensity for 0.005, 0.01 and 0.03 mM F₆₄PcZn/SiO₂ catalysts.

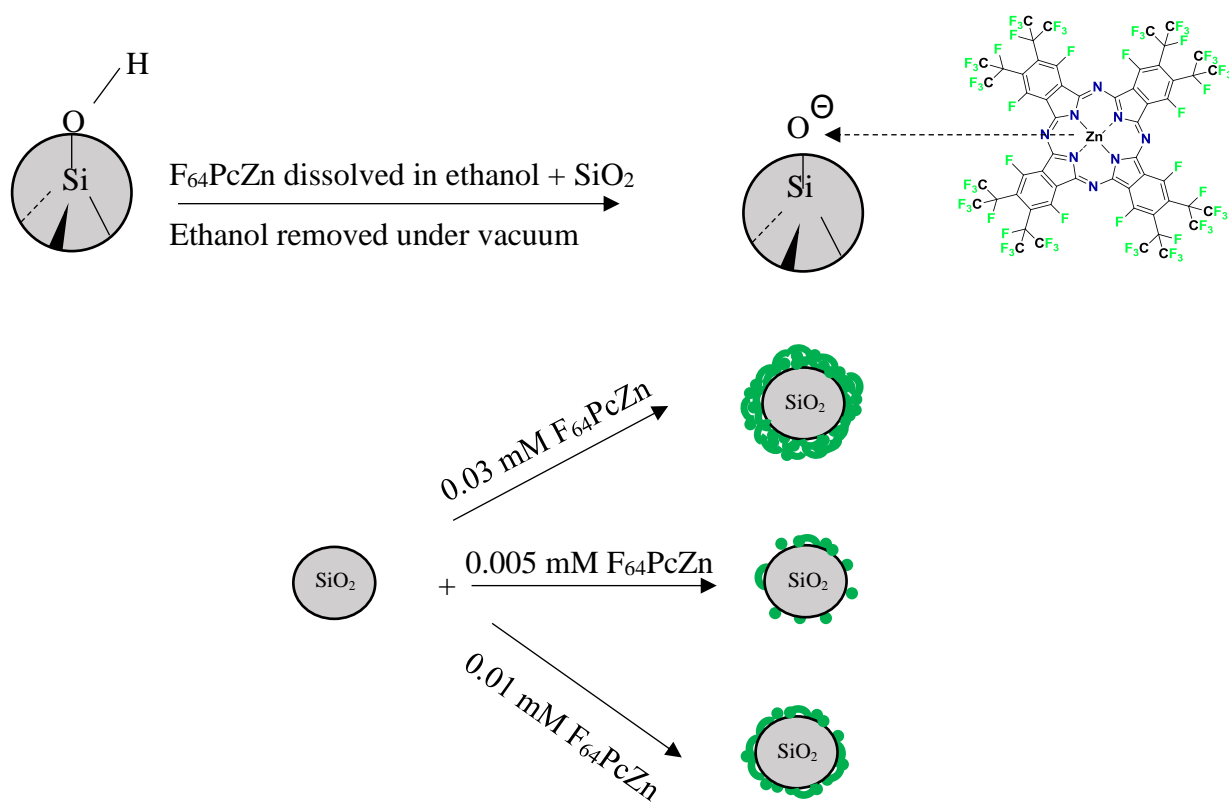


Figure 22. Adsorption of various amount of F₆₄PcZn on SiO₂. Highest amount of F₆₄PcZn forms multi-layer coating on SiO₂.

2.3.16. UV-Vis-NIR Spectral Analysis of Catalysts with Various Amounts of F₆₄PcZn Deposited on SiO₂

To understand the above mechanism of linear increase in reaction rate with increasing amount of F₆₄PcZn deposited on SiO₂, the hybrid catalysts are analyzed using a UV-Vis-NIR spectrophotometer. These results are compared with F₆₄PcZn dissolved in ethanol (Figure 25). For phthalocyanines, the Q band appeared around 600-800 nm which corresponds to the π - π^* transition from the HOMO to the LUMO of Pc²⁻ ring ($\epsilon = 1.7 \times 10^5 \text{ L mol}^{-1} \text{ cm}^{-1}$ in acetone), this is the most intense one accompanied by weaker Soret band or B band ($\epsilon = 3.6 \times 10^4 \text{ L mol}^{-1} \text{ cm}^{-1}$ in acetone) near in the 300-400 nm region.¹² The three-bands in the 200-300 nm region, which are referred to as N, L, and C bands in the order of increasing energy, are together with the B band, sensitive to the central metal. The metal to ligand charge transfer (MLCT) and ligand to metal charge transfer (LMCT) transitions are involved in this spectral region.²⁶ In the case of F₆₄PcZn, these charge transfer transitions are not expected due to d¹⁰ configuration of Zn. The absorption bands in the UV-vis region can be mostly ascribed to π - π^* transitions in F₆₄PcZn.²⁶

The Q and B bands are broader when F₆₄PcZn is deposited on SiO₂ in comparison to the compound dissolved in ethanol. This indicates the aggregation of these molecules on the surface of SiO₂. Yet, there is a linear correlation between the peak intensity and amount of F₆₄PcZn deposited on SiO₂. The peak width increases with increasing the amount of F₆₄PcZn deposited on SiO₂. These results clearly suggest the formation of clumps on the surface of SiO₂ when more and more compound is deposited as explained in the Figure 21. In support of fluorescence quenching at very high amounts of F₆₄PcZn deposited on SiO₂, UV-Vis-NIR spectra suggest aggregation of F₆₄PcZn deposited on SiO₂.

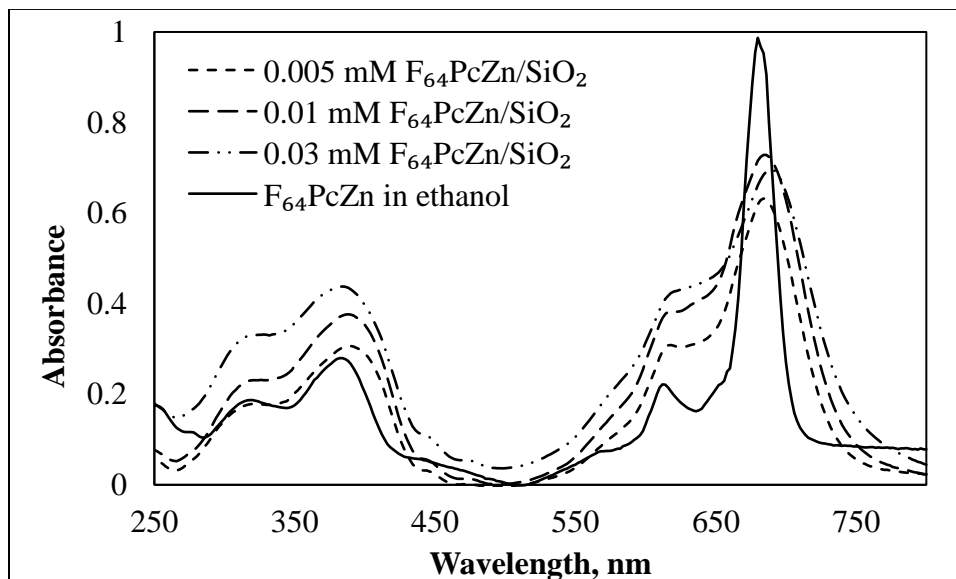


Figure 23. UV-Vis-NIR spectra of F₆₄PcZn deposited on SiO₂ in varying concentrations in comparison with F₆₄PcZn in ethanol.

2.3.17. Hybrid catalyst characterization by XRD analysis

The X-ray diffraction patterns of SiO₂ 10-20 nm and F₆₄PcZn/SiO₂ 10-20 nm are presented in Figure 24. A broad peak around 22 degrees indicates that the SiO₂ is amorphous. The addition of F₆₄PcZn did not change the XRD pattern except a wider peak at 22 deg. This may indicate the amorphous nature of F₆₄PcZn immobilized on SiO₂.

The FWHM decreased after photocatalytic degradation of MO for F₆₄PcZn/SiO₂ in contrast to SiO₂ in which the FWHM increased due to the deposition of MO on the surface. In other words, this observation clearly suggests that MO is photocatalytically degraded on the surface of F₆₄PcZn/SiO₂ particles.

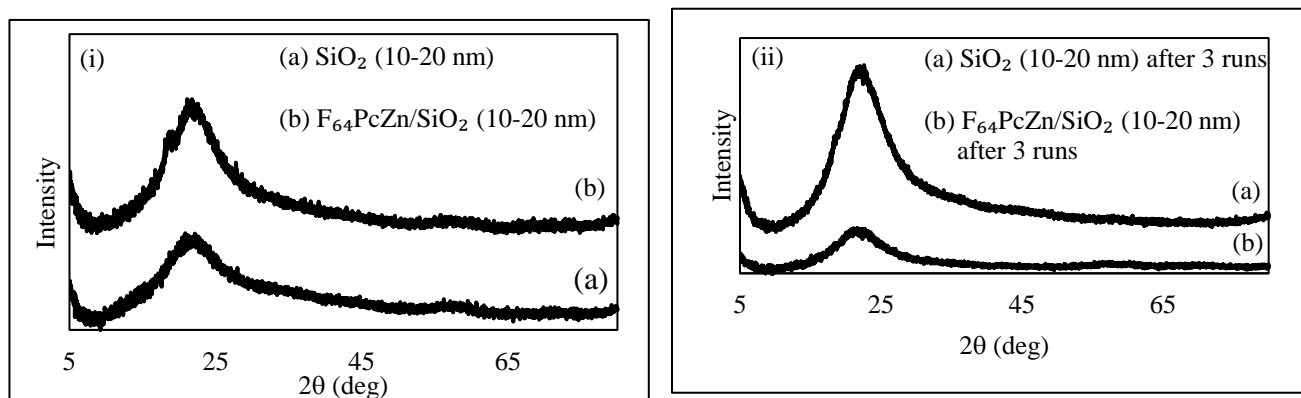


Figure 24. XRD analysis of SiO₂ (10-20 nm) and F₆₄PcZn/ SiO₂ (10-20 nm) (i) before and (ii) after MO photodegradation reaction.

2.3.18. Mode of F₆₄PcZn Adsorption on SiO₂

To verify the mode of F₆₄PcZn adsorption on SiO₂, high-resolution XPS measurements are carried out for F₆₄PcZn, SiO₂ (OX50) and F₆₄PcZn/OX50; the C_{1s}, O_{1s}, Zn_{2p}, F_{1s}, N_{1s} and Si_{2p} core levels are examined. Figure 25 shows the high resolution XPS spectra of C_{1s}, O_{1s}, Zn_{2p}, F_{1s} and N_{1s} for F₆₄PcZn. The C_{1s} spectrum of F₆₄PcZn consists of three main components, that can be clearly distinguished. The peak at 284.82 eV is related to the adventitious carbon. Peak corresponds to the 24 C atoms of four outer benzene rings in the phthalocyanine molecule appeared at 285.9 eV, the peak at the higher binding energy side, *i.e.*, 286.97 eV is ascribed to the 8 pyrrole C atoms in the inner structure of the molecule, while the shallow peak at higher binding energy of 290.56 eV can be explained in terms of $\pi \rightarrow \pi^*$ satellite excitation.³¹ The peak at 288.07 eV can be assigned to C-N bonds and at 289.42 eV is related to the CF groups in the peripheral positions and in the benzene rings, while the strongest peak at 293.34 eV corresponds to the CF₃ groups.³²

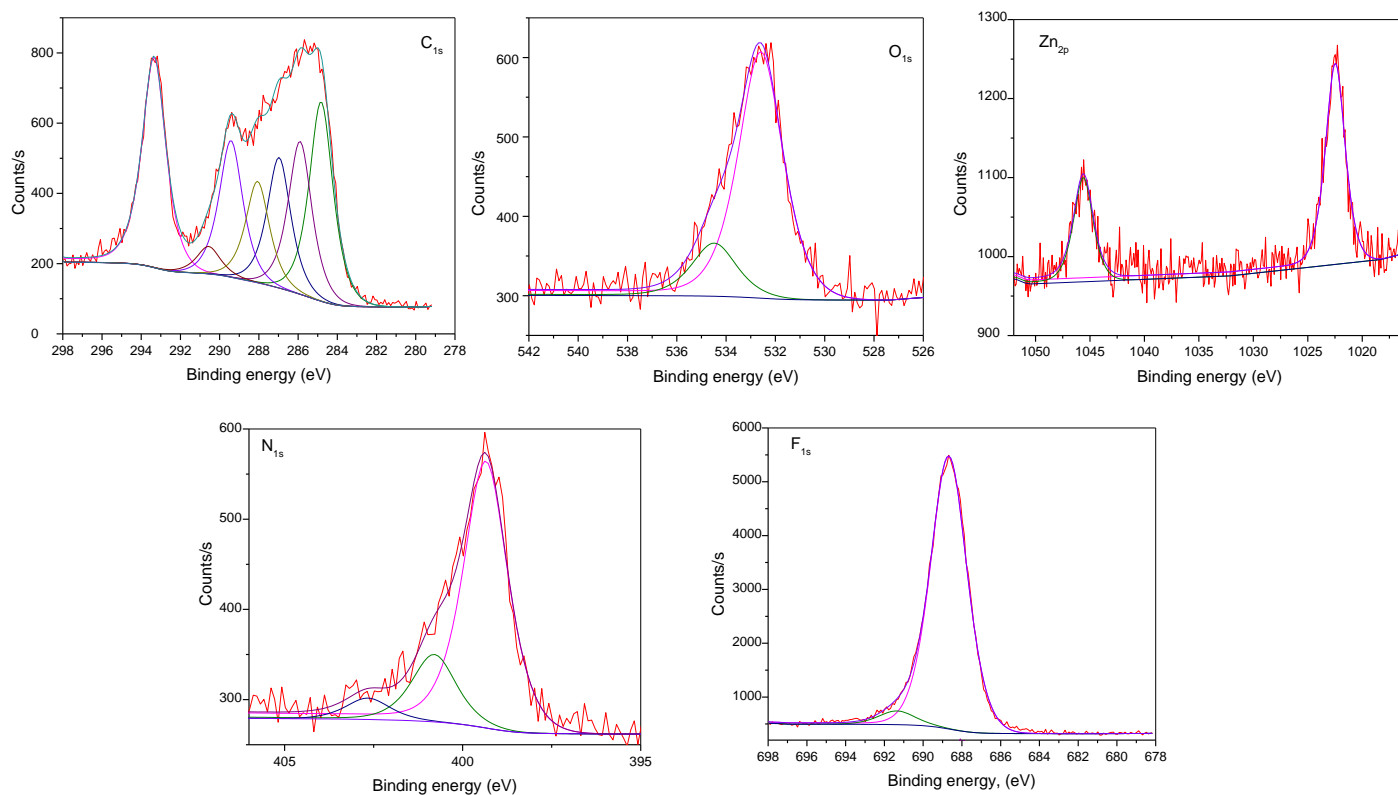


Figure 25. High resolution XPS spectra of C_{1s}, O_{1s}, Zn_{2p}, F_{1s} and N_{1s} for F₆₄PcZn.

The deconvolution of N_{1s} spectrum gives rise to three peaks at binding energies of 399.35, 400.8 and 402.66 eV corresponding to pyridyl N, pyridyl N associated with the central metal atom Zn and pyrrolic N, respectively. In the case of F_{1s} spectrum, the respective peaks at 688.68 and 691.36 eV are attributed to the CF and CF₃ groups.³³ For the central metal atom, a splitting between Zn 2p_{1/2} (1045.61 eV) and Zn 2p_{3/2} (1022.47 eV) equals to 23.1 eV indicates the Zn²⁺ oxidation state for Zn. XPS spectra revealed an O_{1s} spectrum with the peaks at 532.59 and 534.48 eV. It has been reported that in the crystal structure of F₆₄PcZn, in addition to four nitrogen atoms two acetone molecules, are also axially coordinated to Zn because of its high Lewis acidity.¹¹ The

source of oxygen could be water, from moisture, and oxygen, from air, adsorbed on the F₆₄PcZn molecules.

F₆₄PcZn/SiO₂ OX50

The chemical states of SiO₂ and F₆₄PcZn/SiO₂ are examined by XPS. Figure 26a shows the representative survey of XP spectra for SiO₂ and F₆₄PcZn/SiO₂. Figure 26b shows the high resolution XPS spectrum of O_{1s} for SiO₂ and F₆₄PcZn/SiO₂. The deconvolution of the O_{1s} spectrum for SiO₂ gives four peaks at binding energies of 530.89, 531.86, 532.77 and 533.77 eV which can be attributed to adsorbed O, SiO_x, Si-O-H and Si-O-Si.^{34,35} In the case of F₆₄PcZn/SiO₂, the binding energies are shifted to higher values due to the interaction of Si-O⁻ with F₆₄PcZn.

If we consider, in terms of electrostatic interaction, the perfluorinated zinc phthalocyanine should not be adsorbed on the negatively charged SiO₂ nanoparticles because of the repulsive forces. But the electrophilic Zn²⁺ of F₆₄PcZn can interact with the nucleophile Si-O⁻ as displayed in Figure 27. The Zn 2p_{3/2} (Zn 2p_{1/2}) XPS peak is located at 1022.47 (1045.61) eV, with a spin-orbit splitting of 23.1 eV for pure F₆₄PcZn which is attributed to the Zn²⁺.³⁶ For F₆₄PcZn/SiO₂, this peak is observed at 1018.12 (1042.62) eV with the splitting of 24.5 eV. This binding energy shift might be due to the change in chemical environments for F₆₄PcZn that is adsorbed on SiO₂. Thus, the interaction of Zn²⁺ and Si-O⁻ is reflected in the shift of O_{1s} spectrum to higher binding energies in conjunction with the change in spin-orbit splitting of Zn 2p_{3/2} (Zn 2p_{1/2}).

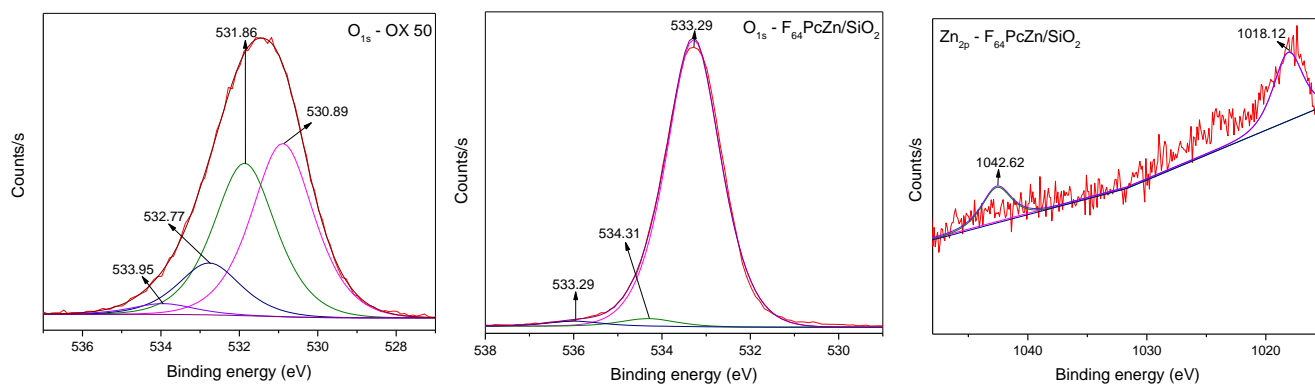
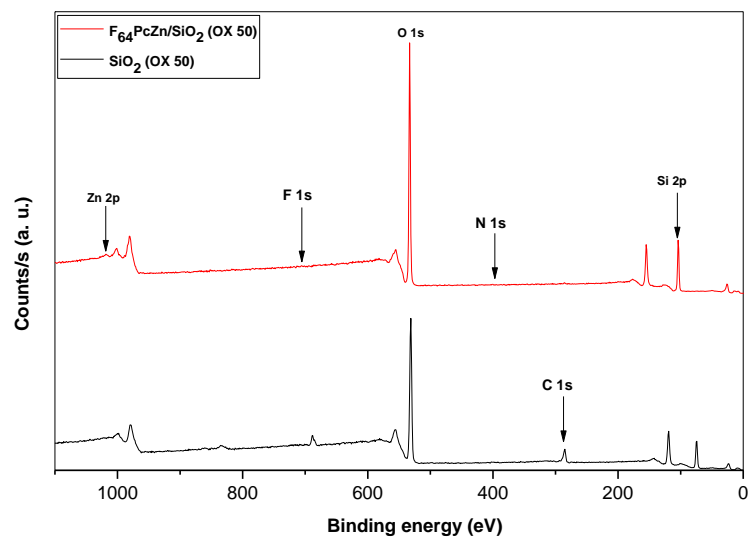


Figure 26. (a) Survey spectra and (b) High resolution XPS spectra of O_{1s} and Zn_{2p} for SiO_2 and $F_{64}PcZn/SiO_2$.

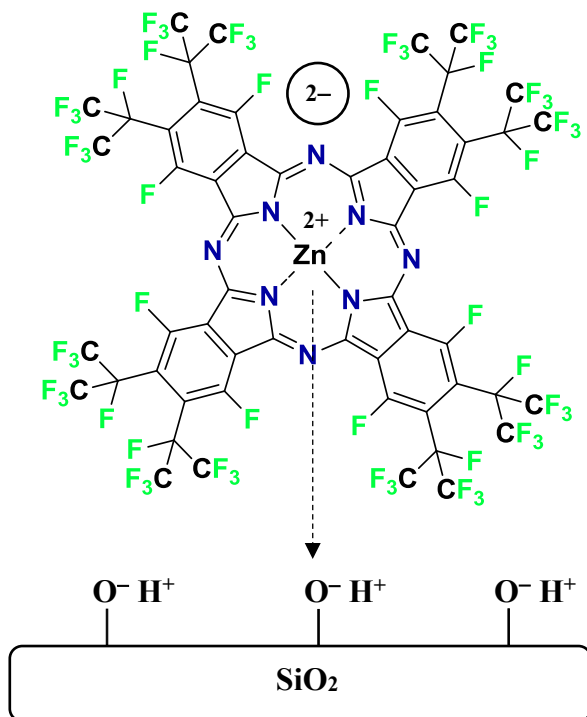


Figure 27. Mode of adsorption of $F_{64}PcZn$ on SiO_2 : Electrostatic interaction of Zn^{2+} and $Si-O^-$ from $F_{64}PcZn$ and SiO_2 , respectively.

2.3.19. Recycling Ability of $F_{64}Pcn/SiO_2$ Hybrid Catalysts

To evaluate the photophysical robustness and adhesion stability of 0.01 mM $F_{64}PcZn/SiO_2$ OX50, repeated cycles of 0.1 mM MO photodegradation reactions are carried out. The reaction rate was monitored at the end of each cycle. The results are given in the Figure 28. It can be found from the results, the catalyst efficiency decreased at the end of the second cycle.

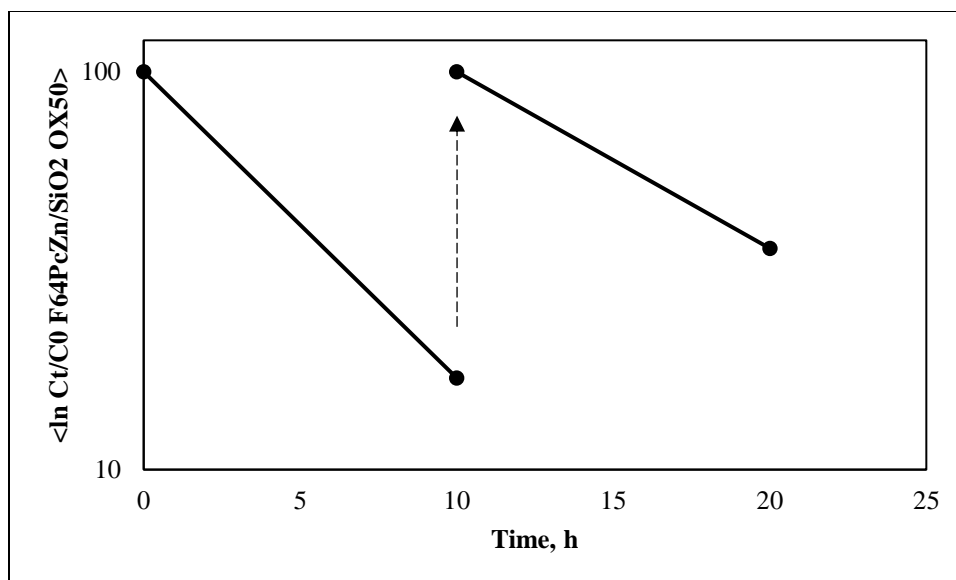


Figure 28. Repeated cycles for MO photodegradation in the presence of $\text{F}_{64}\text{PcZn/OX50}$.

As mentioned in the above discussion, F_{64}PcZn formed clusters on the SiO_2 surface which are adsorbed on the surface via weak van der Waals forces. Since the reaction mixture is mechanically stirred during photodegradation reaction, the weakly adsorbed F_{64}PcZn detached from the SiO_2 surface leading to the loss of catalyst and decrease in the reaction rate. These results suggest, though $\text{F}_{64}\text{PcZn/OX50}$ is an efficient and photophysically stable catalyst, it is not suitable for the reactions in which vigorous mechanical stirring is required.

2.4. CONCLUSIONS

The photoefficiency and photochemical stability of perfluorinated perfluoroalkyl phthalocyanine, F_{64}PcZn deposited on SiO_2 suggest that this solid-state hybrid catalyst can degrade organic contaminants in water. The particle size of SiO_2 plays a vital role, an optimum amount of F_{64}PcZn requires to be deposited to obtain maximum catalytic activity. Too much loading of F_{64}PcZn quenches photoactivity of $\text{F}_{64}\text{PcZn/SiO}_2$. F_{64}PcZn is photochemically stable after catalytic

reactions under visible light irradiation. This observation suggests the molecule can be successfully applied in harsh radical reaction environments. The efficiency of F₆₄PcZn increased with decreasing the particle size of SiO₂ and changing the origin of SiO₂ due to the variation in surface area, pore structure and catalyst distribution. Repeated catalyst cycles indicate that this solid-state catalyst may be more suitable for static conditions rather than dynamic. Wastewater can be pass through a catalyst bed of F₆₄PcZn/SiO₂ to decontaminate from organic pollutants without applying any aggressive mechanical forces.

REFERENCES

- (1) (a) Biffinger, J. C.; Kim, H. W.; DiMagno, G. S. *ChemBioChem*, **2004**, *5*, 622-627. (b) Hugel, H. M.; Jackson, N. *Appl. Sci.* **2012**, *2*, 558-565.
- (2) Bench, B. A.; Brennessel, W. W.; Lee, H. J.; Gorun, S. M. *Angew. Chem. Int. Ed.* **2002**, *41*, 750-754.
- (3) Tsubone, T. M.; Braga, G.; Vilsinski, B. H.; Gerola, A. P.; Hioka, N.; Tessaro, A. L.; Caetano, W. *J. Braz. Chem. Soc.* **2014**, *25*, 890-897.
- (4) Becerra, J. A.; Gonzalez, L. M.; Villa, A. L. *J. Mole. Cat. A Chem.* **2016**, *423*, 12-21.
- (5) Raja, R.; Ratnasamy, P. *Appl. Catal A: Gen.* **1997**, *158*, L7-L15.
- (6) DeOliveira, E.; Neri, C. R.; Ribeiro, A. O.; Garcia, V. S.; Costa, L. L.; Moura, A. O.; Prado, A. G. S.; Serra, O. A.; Iamamoto, Y. *J. Colloid Interface Sci.* **2008**, *323*, 98-104.
- (7) Iliev, V.; Ileva, A.; Bilyarska, L. *J. Mole. Cat. A Chem.* **1997**, *126*, 99-108.
- (8) Wohrle, D.; Thomas, B.; Hundorf, U.; Schulz-Ekloff, G.; Andreev, A. *Macromole. Chem. & Phys.* **1989**, *190*, 961-974.
- (9) Tao, X.; Ma, W.; Li, J.; Huang, Y.; Zhao, J.; Yu, J. C. *Chem. Comm.* **2003**, *0*, 80-81.

- (10) Drozd, D.; Szczubialka, K.; Lapok, L.; Skiba, M.; Patel, H.; Gorun, S. M.; Nowakowska, M. *Appl. Cat. B: Environ.* **2012**, *125*, 35-40.
- (11) Liu, W.; Wang, Y.; Gui, L.; Tang, Y. *Langmuir*, **1999**, *15*, 2130-2133.
- (12) Bench, B. A.; Beveridge, A.; Sharman, W. M.; Diebold, G. J.; Lier, J. E.; Gorun, S. M. *Angew. Chem. Int. Ed.* **2002**, *41*, 747-750.
- (13) Copyright © Karpagavalli Ramji **2018**.
- (14) Sha, Y.; Mathew, I.; Cui, Q.; Clay, M.; Gao, F.; Zhang, X. J.; Gu, Z. *Chemosphere*, **2016**, *144*, 1530-1535.
- (15) Ramakrishnan, R.; Sudha, J. D.; Reena, V. L. *RSC Adv.* **2012**, *2*, 6228-6236.
- (16) Fan, J.; Guo, Y.; Wang, J.; Fan, M. *J. Hazard. Mater.* **2009**, *166*, 904-910.
- (17) Chong, S.; Zhang, G.; Tian, H.; Zhao, H. *J. Environ. Sci.* **2016**, *44*, 148-157.
- (18) La, M.; Hao, Y.; Wang, Z.; Han, G. C.; Qu, L. *J. Anal. Meth. Chem.* **2016**, *1462013*, 6.
- (19) Zhang, Y.; Gao, F.; Wanjala, B.; Li, Z.; Cernigliaro, G.; Gu, Z. *Appl. Cat. B: Environ.* **2016**, *199*, 504-513.
- (20) Voronina, A. A.; Tarasyuk, I. A.; Yu, S. M.; Vashurin, A. S.; Rumyantsev, E. V.; Pukhovskaya, S. G. *J. Non-Crystalline Sol.* **2014**, *406*, 5-10.
- (21) Ogihara, H.; Okagaki, J.; Saji, T. *Langmuir*, **2011**, *27*, 9069-9072.
- (22) Dalvi, V.; Rossky, P. J. *PNAS*, **2010**, *107*, 13603-13607.
- (23) Okte, A. N.; Yilmaz, O. *Appl. Cat. B: Environ.* **2008**, *85*, 92-102.
- (24) Chequer, F. M. D.; Lizier, T. M.; Felicio, R.; Zanoni, M. V. B.; Debonsi, H. M.; Lopes, N. P.; Marcos, R.; Oliveira, D. P. *Toxicology in Vitro*, **2011**, *25*, 2054-2063.
- (25) Pirzada, B. M.; Mehraj, O.; Mir, N. A.; Khan, M. Z.; Sabir, S. *New J. Chem.* **2015**, *39*, 7153-7163.

- (26) Rochkind, M.; Pasternak, S.; Paz, Y. *Molecules*, **2015**, *20*, 88-110.
- (27) Huang, Z.; Zheng, B.; Zhu, S.; Yao, Y.; Ye, Y.; Lu, W.; Chen, W. *Mater. Sci. Semiconductor Process.* **2014**, *25*, 148-152.
- (28) Fang-bai, L. I.; Guo-Bang, G. U.; Guo-Feng, H.; Yun-li, G. U.; Hong-fu, W. *J. Environ. Sci.* **2001**, *13*, 64-68.
- (29) Moore, J. W.; Ramamoorthy, S. *Heavy Metals in Natural Waters: Applied Monitoring and Impact Assessment*, DeSanto, R. S. (eds), Springer-Verlag New York Inc. 1984.
- (30) Johnson, D. B.; Hallberg, K. B. *Sci. Tot. Environ.* **2005**, *338*, 3-14.
- (31) Hwang, T. L.; Lin, Y. K.; Chi, C. H.; Huang, T. H.; Fang, J. Y. *J. Pharm. Sci.* **2009**, *98*, 3735-3747.
- (32) Ottaviano, L.; Nardo, S. D.; Lozzi, L.; Passacantando, M.; Picozzi, P.; Santucci, S. *Surf. Sci.* **1997**, *373*, 318-332.
- (33) Arechederra, R. L.; Artyushkova, K.; Atanassov, P.; Minter, S. D. *Appl. Mater. & Interfaces*, **2010**, *2*, 3295-3302.
- (34) Zhang, F. Y.; Advani, S. G.; Prasad, A. K.; Boggs, M. E.; Sullivan, S. P.; Beebe, T. P. *Electrochim. Acta*, **2009**, *54*, 4025-4030.
- (35) He, P.; Hu, N.; Rusling, J. F. *Langmuir*, **2004**, *20*, 722-729.
- (36) Kim, Y. H.; Lee, D. K.; Cha, G. H.; Kim, C. W.; Kang, Y. C.; Kang, Y. S. *J. Phys. Chem. B*, **2006**, *110*, 24923-24928.

Chapter 3. Enhanced Visible Light Photocatalysis using Perfluoroalkyl Perfluoro Phthalocyanine Zinc/TiO₂ Hybrid Photocatalyst for Water Purification

3.1. INTRODUCTION

The photoactivity of the hybrid catalyst F₆₄PcZn/SiO₂ described in Chapter 2 confirms that an active solid state photocatalytic system can be established based on F₆₄PcZn. In this Chapter photoactive titanium dioxide (TiO₂) is examined as a support instead of photo inactive SiO₂. We expect an enhanced visible light photoactivity by depositing F₆₄PcZn on photoactive TiO₂ solid substrate. TiO₂ nanoparticles P25 and P90 with different particle sizes of 14 and 21 nm, respectively have been investigated as supports in the present study. TiO₂ crystallizes in several polymorphs of which anatase and rutile are more common phases. Anatase has a band gap of 3.2 eV, corresponding to a UV wavelength of 387 nm, while rutile bandgap is 3.0 eV with excitation wavelength that extend into the visible range, 413 nm.¹ In addition to band gap energy, the band alignment is also important while considering photocatalytic properties. If the conduction band minimum (CBM) occurs at the same position in *k*-space as the valence band maximum (VBM), then the energy gap can be directly determined from the optical threshold, for example in the case of rutile (Figure 1a). If the CBM and VBM occur at different points in *k*-space as such in anatase then it is known as indirect band gap (Figure 1b). This situation hinders the electron hole recombination.² The energies of the bands are calculated in *k*-space which is also known as

momentum space. The diagram displayed in Figure 1 is the relation of particle energy E versus the momentum (wave number) k .

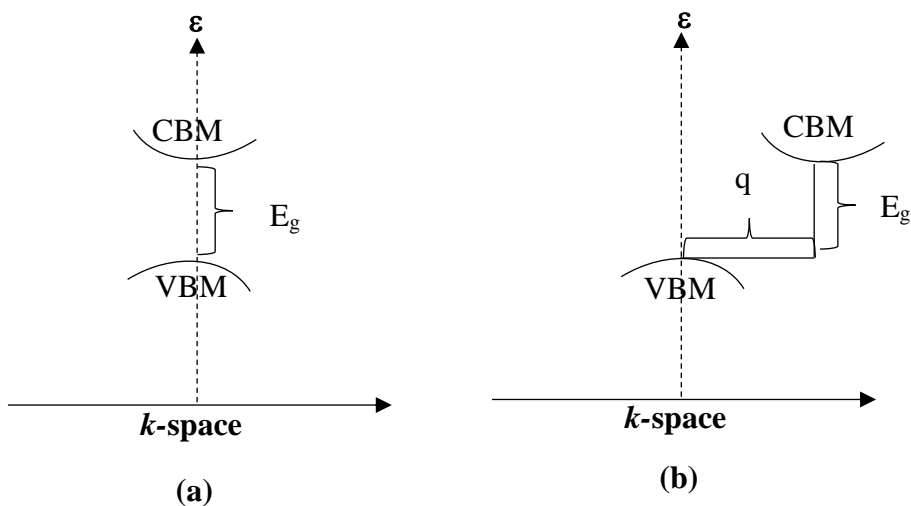


Figure 1. (a) Direct band gap as in rutile and (b) indirect band gap like in anatase.

Energy, ϵ , is plotted against k -space or momentum (wave number) space.

Even though the photo-excitation of rutile extends into the visible light range, it is photocatalytically inactive due to high rates of charge recombination because of the direct band gap.²

P25 and P90 comprise both anatase and rutile phases. The ratio of anatase:rutile in P25 has been reported as 80:20.³ Evonik Degussa claims P25 and P90 have similar composition and physical properties, except the particle size. The photocatalytic efficiency of P25 to oxidize 4-chlorophenol (4-CP) in aqueous effluents has been reported higher than pure anatase and rutile phases under UV irradiation.⁴ P25 and P90 are highly photoactive only with the illumination of

UV light.^{4,5} But the solar energy comprises mostly visible light. Hence efforts have been invested to sensitize TiO₂ under visible light irradiation by depositing phthalocyanine on the surface.

Various phthalocyanines deposited on TiO₂ have been studied by many authors to degrade organic pollutants in water under visible light irradiation.⁶⁻⁹ Guo *et al.* found 2,9,16,23-tetra-nitrophthalocyanine iron(II)/TiO₂ nanofiber heterostructures possess a much higher efficiency to degrade methyl orange (MO) as compared with the use of only H₂O₂ under visible light illumination.⁶ Sevim⁷ impregnated Zn (II) and Co (II) Pcs such as (i) 9(10), 16(17), 23(24)-Tris-(4-ter-butylphenoxy)-2(3)-(4-carboxyphenoxy) phthalocyaninato zinc (II), (ii) 9(10), 16(17), 23(24)-Tris-(4-ter-butylphenoxy)-2(3)-(4-carboxyphenoxy)phthalocyaninato cobalt (II), (iii) 9(10), 16(17), 23(24)-Tris-(4-ter-butylphenoxy)-2(3)-(4-carboxyphenylsulfanyl)-phthalocyaninato zinc (II) and (iv) 9(10), 16(17), 23(24)-Tris-(4-ter-butylphenoxy)-2(3)-(4-carboxyphenylsulfanyl) phthalocyaninato cobalt (II) on TiO₂ to decompose 4-CP under visible light irradiation. They observed 85, 88, 86 and 89 % of 4-CP degradation for the Pc/TiO₂ catalysts (i), (ii), (iii) and (iv). When TiO₂ is added without Pc only 3% of 4-CP degraded. Since visible light is shined, TiO₂ cannot be photoactive because of its wide bandgap energy of 3.2 eV. They claimed the PcM/TiO₂ catalyst is more photoactive than TiO₂ under visible light illumination because the photoexcited PcM injected electrons into the conduction band of TiO₂, thus produced superoxide radicals (O₂^{-•}) to degrade 4-CP. Mesgari *et al.*⁸ reported phthalocyanine ((C₈H₄N₂)₄H₂) modified Fe-doped TiO₂ nanocrystals as visible light sensitive photocatalyst to degrade MO. Like the above-mentioned example, Pc gets excited under visible light illumination and injects electrons into the conduction band of TiO₂. The authors employed Fe-doped TiO₂ because of the charge trapping capability of Fe³⁺ which prevents the recombination of e_{CB}⁻ and h_{VB}⁺ in TiO₂. By trapping electron Fe³⁺ becomes Fe²⁺ that is relatively unstable according to the crystal field theory.

Therefore, Fe^{2+} releases easily electron to become Fe^{3+} . The energy level of $\text{Fe}^{2+}/\text{Fe}^{3+}$ lies close to the level of $\text{Ti}^{3+}/\text{Ti}^{4+}$. Because of this closer proximity, the trapped electron in Fe^{2+} is readily transferred to Ti^{4+} which then combines with O_2 molecule to produce $\text{O}_2^{\bullet-}$ radicals. The authors reported 6 times improvement in the rate constant (k) of MO photodegradation for Pc/TiO_2 compared to bare TiO_2 . Additional one time increase in k is obtained by using Fe doped $\text{Pc}/\text{Fe-TiO}_2$. Iliev and Tomova⁹ investigated the photooxidation of sulfide ion catalyzed by 29H,31H-phthalocyanine (Pc)/ TiO_2 and $\text{Pc}/\text{Al}_2\text{O}_3$ upon irradiation with visible light. Pc/TiO_2 showed 3 times higher photooxidation rate of sulfide ion compared with $\text{Pc}/\text{Al}_2\text{O}_3$. The better photocatalytic activity of Pc/TiO_2 is due to the formation of higher amounts of superoxide radicals ($\text{O}_2^{\bullet-}$). In the case of Pc/TiO_2 both Pc and TiO_2 are photoactive thus produces more $\text{O}_2^{\bullet-}$. But, only Pc is photoactive in $\text{Pc}/\text{Al}_2\text{O}_3$ catalyst. Sun and Xu¹⁰ sensitized TiO_2 with 2,9,16,23-tetracarboxyphthalocyanine aluminum (PcTCAI) to degrade 4-CP using visible light irradiation. They concluded the formation of $\text{PcTCAI}^{\bullet+}$ and $\text{O}_2^{\bullet-}$ radicals lead to the degradation of 4-CP. It is important to notice in all the above-mentioned examples the visible light excited Pc injects electrons from HOMO into the conduction band of TiO_2 to produce reactive radicals under visible light irradiation. In the present investigation we deposited perfluoroalkyl perfluoro phthalocyanine zinc (F_{64}PcZn), which is an electron deficient compound, on TiO_2 .¹¹

In this study, the photocatalytic efficiency and photo stability of F_{64}PcZn deposited on P25 and P90 TiO_2 are investigated. The efficiency of $\text{F}_{64}\text{PcZn}/\text{P25}$ and $\text{F}_{64}\text{PcZn}/\text{P90}$ to degrade model organic pollutants such as methyl orange (MO) and rhodamine B (RhB) under visible light irradiation have been evaluated. We chose to investigate an azo dye (MO) which is a more common pollutant in the aqueous environment. In addition, a more complexly structured xanthene dye (RhB) is selected to examine the efficiency of the studied photocatalysts. The photocatalysts

particle size effect on the pollutant degradation reaction rate is discussed. The mode of adsorption of F₆₄PcZn on P25 and P90 are analyzed using UV-Vis-NIR reflectance spectroscopy and X-ray photoelectron spectroscopy (XPS). The degradation products of RhB are identified via ¹H-NMR, HPLC and LC/MS methods. A possible reaction mechanism pathway is suggested for the photocatalysts P25 and F₆₄PcZn/P25. We further analyzed the photodegradation products of RhB catalyzed by F₆₄PcZn/P25 because of the blue-shift observed in the peak absorbance maxima of UV-Vis spectra after photocatalytic reaction. We are more interested to track the structural changes in RhB accompanying the blue shift.

3.2. MATERIALS AND METHODS

3.2.1. Materials

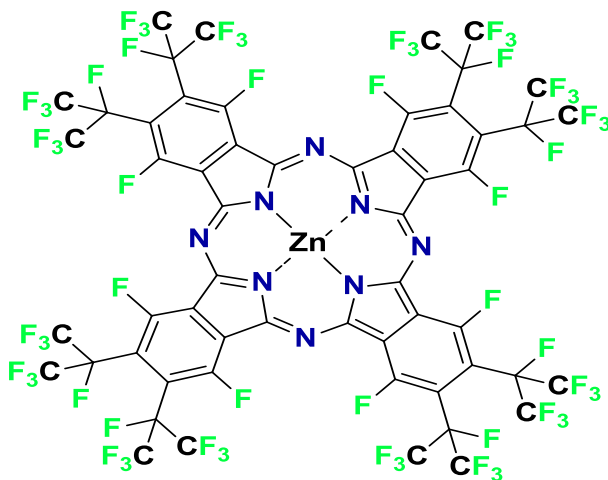
As synthesized F₆₄PcZn¹¹ was deposited on P25 and P90 that were provided as a generous gift by Evonik Degussa, USA. The chemical structure of F₆₄PcZn is illustrated in Figure 2a.¹¹ Methyl orange (MO), rhodamine B (RhB), ethanol and acetone were purchased from Sigma-Aldrich, USA.

3.2.2. Synthesis of F₆₄PcZn/P25 and F₆₄PcZn/P90 Hybrid Catalysts

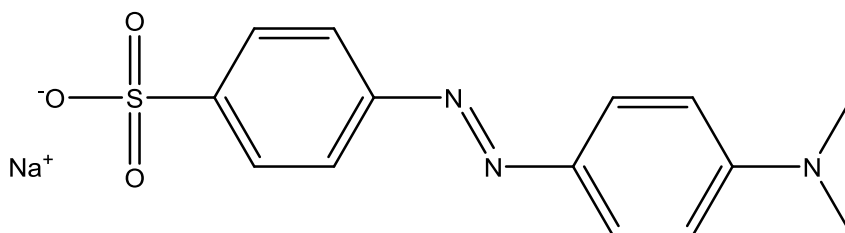
30 mg of F₆₄PcZn was dissolved in ethanol to which 1000 mg of either P25 or P90 TiO₂ was added. The mixture was roto-evaporated to obtain F₆₄PcZn/P25 and F₆₄PcZn/P90 hybrid catalysts. The actual amount of F₆₄PcZn deposited on TiO₂ was determined by extracting back F₆₄PcZn from F₆₄PcZn/TiO₂ using acetone and measuring the concentration using UV-Vis spectroscopy.

3.2.3. Photochemical Reactions

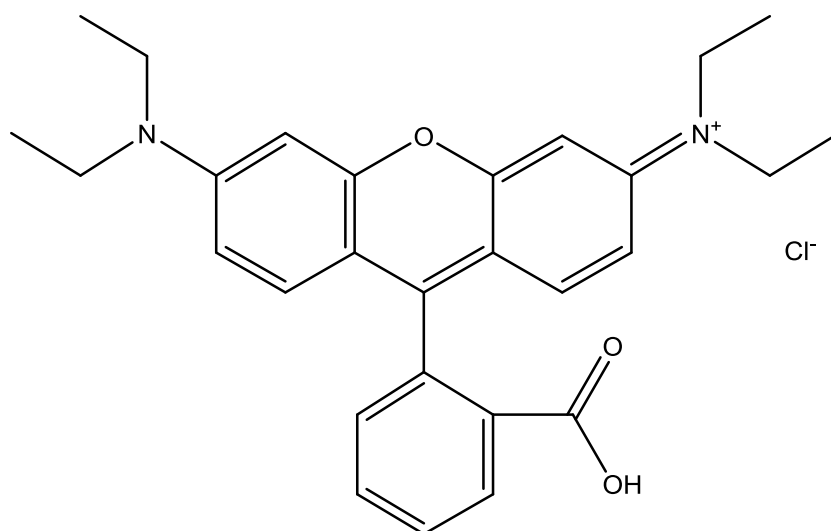
The photocatalytic efficiency of P25, P90, F₆₄PcZn/P25 and F₆₄PcZn/P90 were evaluated by monitoring the change in the concentration of MO and RhB in the presence of catalysts under irradiation of 3 Suns of visible light. The chemical structure of organic model pollutants such as MO and RhB are shown in the Figures 2b and 2c.



(a) Perfluoroalkyl perfluoro phthalocyanine zinc (F₆₄PcZn)



(b) Methyl orange ((E)-4-((4-(dimethylamino)phenyl)diazenyl)benzenesulfonate)



(c) Rhodamine B (*N*-(9-(2-carboxyphenyl)-6-(diethylamino)-3H-xanthen-3-ylidene)-*N*-ethylethaniminium)

Figure 2. Chemical structure of (a) F₆₄PcZn, (b) methyl orange and (c) rhodamine B.

The photoreactions were performed in a reactor vessel kept at constant temperature of 25 °C using a recirculating water bath ((ThermoNeslab-M25). The reaction mixture was stirred at a rate of 1000 rpm using a magnetic stirrer. To perform photoreactions, 50 mL of 0.1 mM MO solution was taken in a photoreactor vessel. The catalyst was added to this solution in the ratio of 10:1 i.e. 0.01 mM of F₆₄PcZn deposited on TiO₂. A visible light with the intensity of 390,000 lx (approx. 3 Suns)¹² was shined on the reactor vessel using a tungsten halogen lamp. The spectral distribution of tungsten halogen lamp used as a light source is given in Figure 3. During the photodegradation process 0.5 mL aliquots of MO was withdrawn every 2 h and diluted 5 times to determine the change in dye concentration using UV-Vis spectrophotometry. For RhB, 0.5 mL aliquot was diluted 10 times to measure the change in concentration using UV-Vis

spectrophotometry. A Hewlett Packard UV-Vis spectrophotometer (8452A diode array) was employed to monitor the change in MO and RhB concentrations.

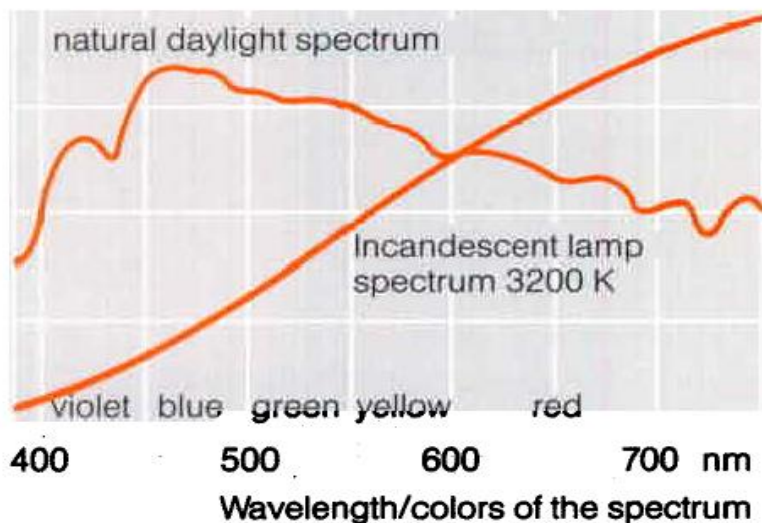


Figure 3. Spectral distribution for the tungsten halogen lamp used as a visible light source

(Copyright © OSRAM SYLVANA Inc. 2001-2017).

3.2.4. Fluorescence Emission Spectral Measurements for H₁₆PcZn, F₁₆PcZn and F₆₄PcZn Deposited on TiO₂

The fluorescence emission spectra were recorded from 660 to 850 nm using a Spex model Fluoromax-3 spectrofluorometer by exciting the H₁₆PcZn, F₁₆PcZn and F₆₄PcZn films coated on P25 TiO₂ and F₆₄PcZn deposited on P90 TiO₂ at the wavelength of 650 nm in the Q-band region.

3.2.5. Photoreaction under UV only, UV +Visible and red-light Irradiations

RhB photodegradation (0.1 mM) catalyzed by P25 and F₆₄PcZn/P25 (0.01 mM) under the influence of lights with different wavelengths like UV, visible and red-lights are investigated. UV

lamp with 6 Watts power was purchased from UVP LLC., CA, USA. The intensity of UV light irradiated was 0.5 mW/cm^2 with the wavelength of 365 nm. A tungsten halogen lamp from Osram, MA, USA was used as a visible light source. The visible light intensity was 390,000 lx, *i.e.*, 57 mW/cm^2 with the wavelengths ranging from 450 to 750 nm. The red LED strip manufactured by 3M, USA was used as a red-light source. The red-light intensity irradiated was 1 mW/cm^2 at the wavelength of 626 nm. The aliquots at different time of intervals were collected to determine the concentration of RhB using UV-Vis spectroscopy.

3.2.6. Photostability of F₆₄PcZn in Comparison to H₁₆PcZn and F₁₆PcZn Deposited on P25 under UV Light Irradiation

The photostability of H₁₆PcZn, F₁₆PcZn and F₆₄PcZn deposited on P25TiO₂ is evaluated by irradiating UV light with the wavelength of 254 nm and intensity of 0.2 mW/cm^2 for 5 h. 100 mg of 0.01 mM H₁₆PcZn/P25, F₁₆PcZn/P25 and F₆₄PcZn/P25 were weighed and dispersed separately in 50 ml of de-ionized water. UV light was shined at the top of the solution surface while stirring the solution at a constant rate using a magnetic stirrer. After 5 h, the Pc/P25 particles were separated and dried at 100 °C for 6 h. Then the Pc was extracted out from the Pc/P25 particles using acetone. The percentage of Pc in acetone before and after UV irradiation of Pc/P25 particles were determined by measuring the absorbance intensity using a UV-Vis spectrophotometer.

3.2.7. Particle Size and Zeta Potential Measurements

The particle size and zeta potential were measured for the studied catalysts in de-ionized water using Zetasizer Nano ZS, Malvern Panalytical, USA. The change in the particle size of P25 and P90 after coating them with F₆₄PcZn have been examined. The surface charge of P25, P90,

F₆₄PcZn/P25 and F₆₄PcZn/P90 were evaluated using zeta potential measurements to understand the interaction between the F₆₄PcZn and the P25 and P90 matrices. Also, zeta potential suggests the available possibilities of adsorption of ionic organic pollutants in water on the surface of catalyst which could enhance the pollutant degradation process.

3.2.8. UV-Vis-NIR Reflectance Spectral Measurements

UV-Vis-NIR reflectance spectra for the studied catalysts were recorded using Perkin-Elmer Lambda 950 UV-Vis-NIR spectrophotometer capable of making measurements in the range of 190 to 3300 nm.

3.2.9. X-ray Photoelectron Spectroscopy Measurements

X-ray photoelectron spectroscopy (XPS) measurements were performed with a Thermo Scientific Spectrometer, USA. All spectra were taken using Al K α micro-focused monochromatized source (1486.6 eV) with a resolution of 0.6 eV. The spot size was 400 μ m and the operating pressure was 5×10^{-9} Pa.

3.2.10. X-ray Diffraction Analysis

X-ray powder diffraction patterns (XRD) were recorded using a Siemens D-500 diffractometer, USA with CuK α radiation source and scintillation counter detector. The XRD patterns were analyzed with the help of JADE XRD analysis software.

3.2.11. ¹H NMR Analysis

RhB photodegradation reactions were carried out in deuterated water (D₂O) catalyzed by P25 and F₆₄PcZn/P25 under oxygen environment for 10 h. The degradation products formed after 10 h were determined using ¹H NMR-500 MHz instrument and ACD/ChemSketch analysis software.

3.2.12. High-Pressure Liquid Chromatography and Liquid Chromatography/Mass Spectrometry Analysis of Photodegradation Intermediate Products

The degradation products of RhB were analyzed using high-pressure liquid chromatography (HPLC) and liquid chromatography/mass spectrometry (LC/MS)–Aliquots were collected for every 2 hours up to 10 hours during the photodegradation reaction. The products were analyzed using a Hewlett-Packard HP100 series HPLC equipped with UV-Vis diode array detector and C₁₈ reverse phase column (150 mm * 4.6 mm ID). Acetonitrile and water were used as mobile phase (60:40, v/v) with the addition of 20 mM H₃PO₄ at pH 3.3. The mobile phase flow rate was maintained at 1 mL/min and the sample injection volume was 5 µL. The mass of intermediate products was determined using a positive ion mode mass spectrum (Hewlett-Packard HP100 series) LC-MSD equipment. The mobile phase used for LC/MS analysis was methanol and water (50:50, v/v) with 0.1% formic acid. The sample injection volume was 1 µL and the mobile phase flow rate was 0.5 mL/min for LC/MS analysis.

3.3. RESULTS AND DISCUSSION

3.3.1. Photodegradation of MO Catalyzed by F₆₄PcZn/P25 under Visible Light Irradiation

Figure 4 exhibits change in the UV-Vis spectra of MO during photodegradation process catalyzed by P25 (Figure 4a) and F₆₄PcZn/P25 (Figure 4b). The absorbance maximum of the main

peak corresponding to the chromophore -N=N- at 464 nm¹³ decreased 16% with the addition of P25. Whereas, F₆₄PcZn/P25 leads to 57% decrease in the peak absorbance maximum providing 3.6 times higher efficiency. The peak intensity around 270 nm which corresponds to π - π transitions of the aromatic rings is decreased when the photoreaction is catalyzed by P25. On the other hand, not only this peak became smaller but few other new peaks around 256 and 232 nm appeared with the addition of F₆₄PcZn/P25 catalyst. Appearance of these new peaks suggests the oxidative decomposition of MO into smaller fragments like sulfanilic acid and aniline.^{14,15} This result confirms the higher photocatalytic efficiency of the hybrid catalyst F₆₄PcZn/P25 as compared to P25.

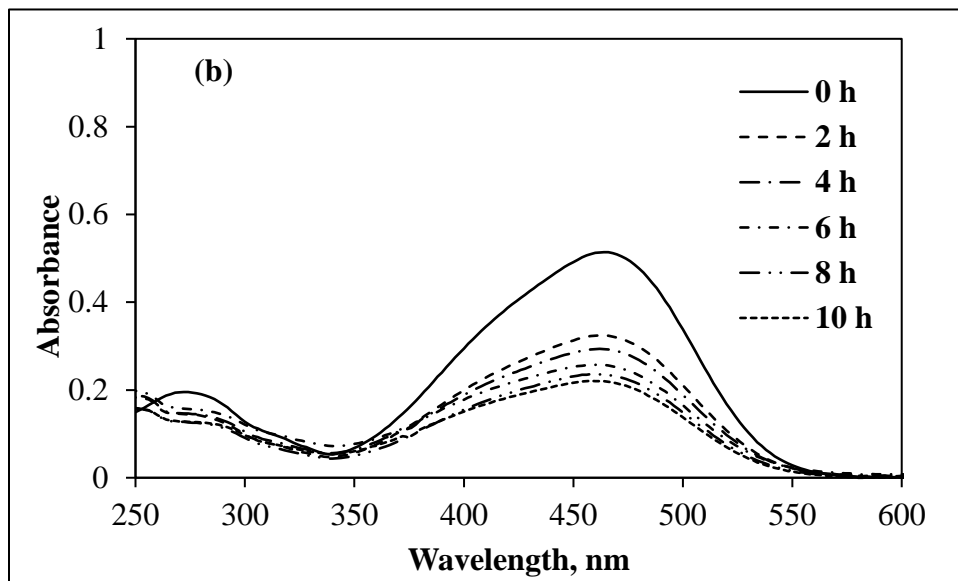
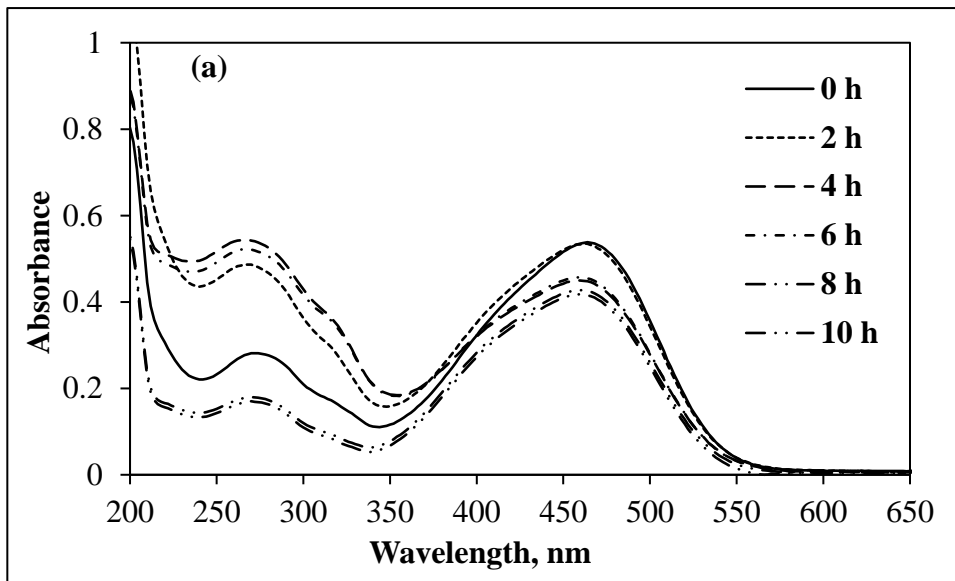


Figure 4. UV-Visible Spectra for the photodegradation of MO catalyzed by

(a) P25 and (b) F₆₄PcZn/P25.

3.3.2. RhB Photodegradation Catalyzed by P25 and F₆₄PcZn/P25 under Visible Light Irradiation

Figures 5a and 5b exhibit RhB photodegradation catalyzed by P25 and F₆₄PcZn/P25 under visible light irradiation. The main peak absorption at $\lambda = 556$ nm that originates from the $n \rightarrow \pi^*$ transition¹⁶ decreased with the addition of both P25 and F₆₄PcZn/P25. But, the decrease is 2.6 times higher for the hybrid catalyst F₆₄PcZn/P25 with a clear hypsochromic/blue shift in the peak absorbance maxima. The peak is blue-shifted from 556 to 532, 502 and 500 nm after 2, 4 and 6 h, respectively for the hybrid catalyst while only a slight blue shift occurred in the presence of P25. The blue shift of peaks observed for F₆₄PcZn/P25 because of the de-ethylation process of RhB that destructs the molecule.¹⁶ Similar blue shift is also found for the addition of F₆₄PcZn/SiO₂ (Chapter 2). To prove the different degradation pathways of RhB catalyzed by P25 and F₆₄PcZn/P25 the products of degradation were analyzed using HPLC and LC/MS. The details are given in the following HPLC and LC/MS section 3.3.2.2.

It is important to mention that the zeta potential of F₆₄PcZn coated P25 particles shifted towards negative values (Table 3) as compared to the uncoated P25 particles. Hence there will be a preferential adsorption of the positively charged ethylamine group of RhB on the surface of the hybrid catalyst F₆₄PcZn/P25. This causes step by step *N*-deethylation of RhB which is reflected in the blue shift of UV-Vis peak absorbance maxima in the case of F₆₄PcZn/P25. After 6 h the peak intensity decreased without further blue-shift suggesting the destruction of chromophore followed by *N*-deethylation (supported by HPLC and LC/MS results presented in the section 3.3.2.2.). These results suggest that the hybrid F₆₄PcZn/P25 is a more efficient photocatalyst than P25 by itself.

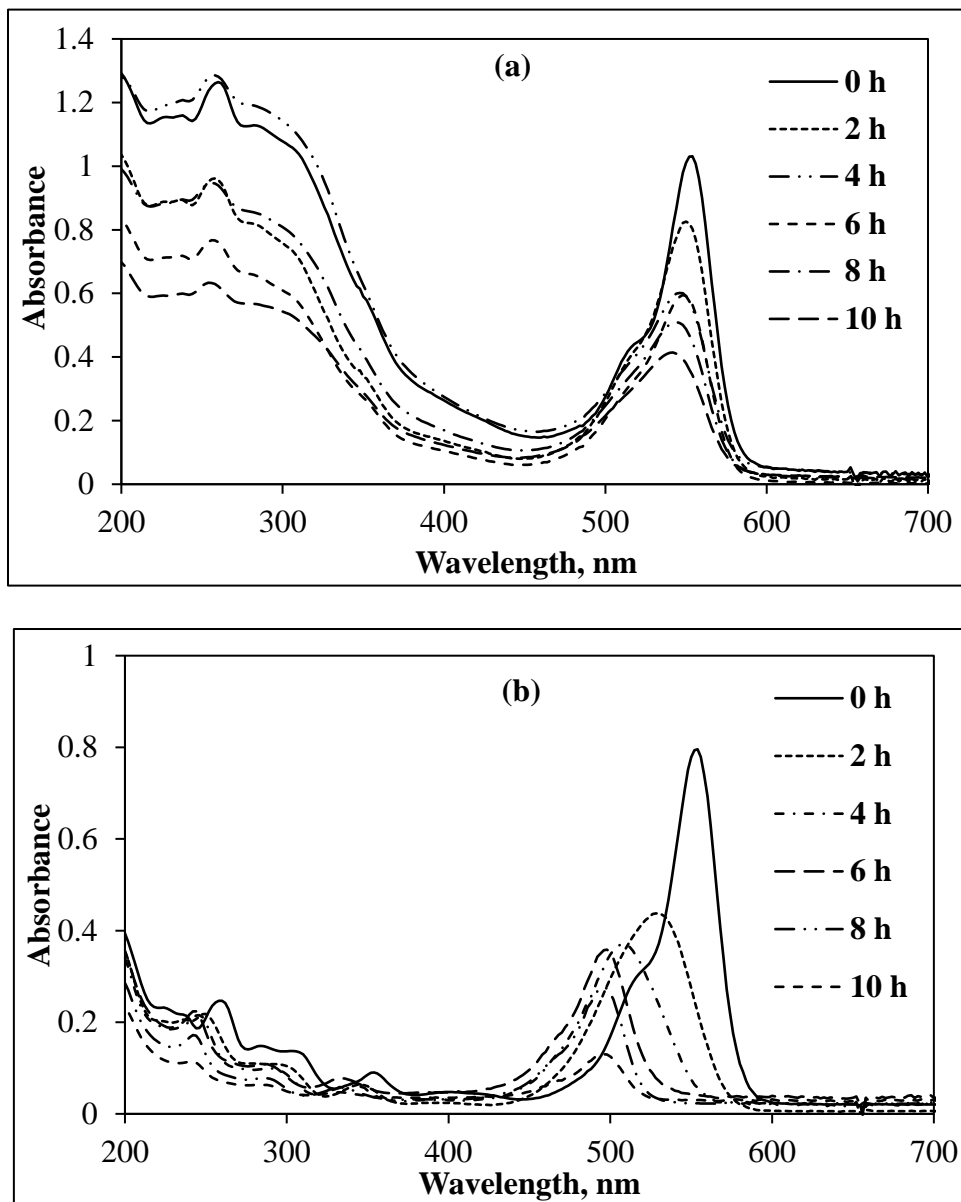


Figure 5. UV-Vis spectra for photodegradation of RhB (a) P25 no hypsochromic/blue shift; (b) F₆₄PcZn/P25 hypsochromic/blue shift.

The above results also suggest the higher capability of F₆₄PcZn/P25 to absorb visible light than P25. The products formed due to *N*-deethylation process followed by the destruction of chromophore will be discussed in the HPLC and LC/MS results section.

After the pollutants degradation reactions, the catalyst F₆₄PcZn/P25 was separated and dried at 100 °C. Then, F₆₄PcZn was extracted using acetone to find the photostability of F₆₄PcZn. The UV-Vis analysis of F₆₄PcZn before and after photoreactions (Figure 6) show F₆₄PcZn is photochemically stable without any difference in the spectral absorbance.

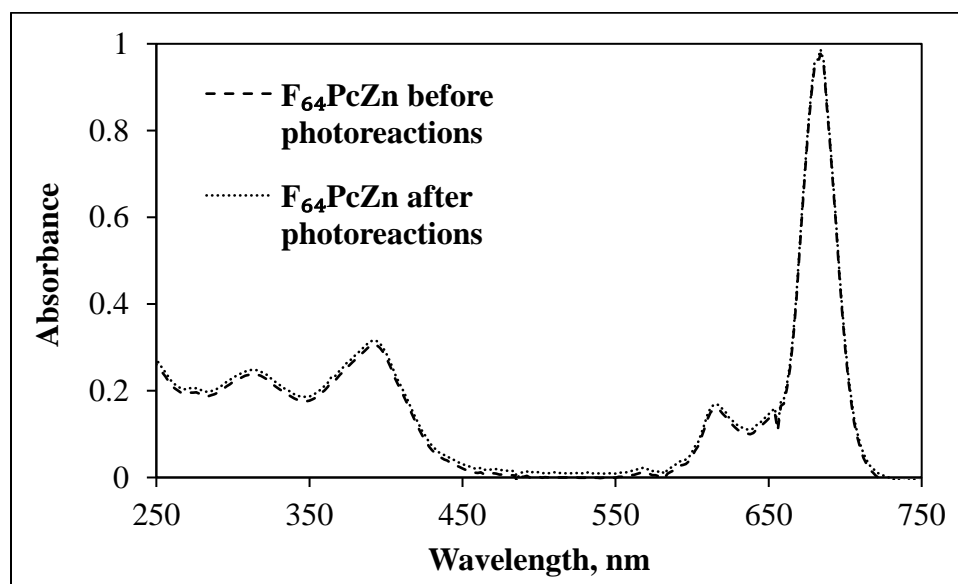


Figure 6. UV-Vis spectra of F₆₄PcZn extracted from F₆₄PcZn/P25 before and after photochemical reaction.

3.3.3. Particle Size Analysis

As shown in our previous results for F₆₄PcZn/SiO₂, an efficient photodegradation processes occurs at an optimum particle size of the catalyst. In general, a smaller particle size would provide a higher specific surface area which in turn increases the number of active surface sites. Many

authors reported a better photocatalytic efficiency for smaller size TiO₂ particles assuming more reactive sites to absorb the molecular pollutants from water.^{17,18} It is noteworthy to mention, TiO₂ works by surface hole transfer, so adsorption is necessary. Whereas F₆₄PcZn generates ¹O₂ which can migrate in to the solution. In this study, we investigated TiO₂ nanoparticles with two different particle sizes, *i.e.*, P25 and P90. The primary particle size of P25 and P90 were determined using tunneling electron microscopy (TEM) by the manufacturer (Evonik, USA) as 21 and 14 nm, respectively. Table 1 displays the mean particle size of P25 and P90 before and after the deposition of F₆₄PcZn which is measured in de-ionized water using a dynamic light scattering method.

Both bare TiO₂ and F₆₄PcZn/TiO₂ aggregate in de-ionized water due to surface charge density and van der Waals forces that lead to secondary particle sizes.¹⁹ The particle sizes measured for P25 and P90 are 79 and 50 nm, respectively in de-ionized water. By depositing F₆₄PcZn on P25 and P90 TiO₂ the particle sizes increased to 91 and 68 nm, respectively. The particle sizes for and F₁₆PcZn/TiO₂ and H₁₆PcZn/TiO₂ are 142 and 459 nm, respectively. The size data suggests the aggregating tendency of F₁₆PcZn and H₁₆PcZn due to π - π stacking of these molecules which might resulted in larger particle sizes.

Table 1. Mean particle size of P25, P90, Pc/P25 and F₆₄PcZn/P90 measured in de-ionized water.

S. No.	Samples	Mean Particle Size (d.nm)
1	P25	79
2	P90	50
3	F ₆₄ PcZn/P25	91
4	F ₁₆ PcZn/P25	142
5	H ₁₆ PcZn/P25	459
6	F ₆₄ PcZn/P90	68

3.3.4. F₆₄PcZn/P90 as Photocatalyst for Photodegradation of MO and RhB

As the quantity of active surface area of photocatalyst directly influence the rates of charge transfer reactions taking place at the surface, the photocatalytic activity of F₆₄PcZn deposited on P90 is investigated as oppose to the one deposited on P25. Figures 7 and 8 exhibit UV-Vis spectra for the photodegradation of MO (Figures 7a and 7b) and RhB (Figures 8a and 8b) catalyzed by P90 and F₆₄PcZn/P90. Results reveal a drastic decrease in the peak absorbance maxima that corresponds to the chromophore for both MO and RhB catalyzed by F₆₄PcZn/P90. It is obvious from the UV-Visible spectral data shown in the Figures 8 and 9 that the hybrid photocatalyst F₆₄PcZn/P90 shows higher efficiency in degrading the organic pollutant dyes than P90 TiO₂.

The fluorinated phthalocyanine extracted before and after photoreactions showed no change in the characteristic peaks for F₆₄PcZn, specifying its robustness even on the surface of TiO₂. P25 and P90 are well known to degrade the organic dyes under irradiation of visible light.

But, our results described the stability of fluorinated phthalocyanine, $F_{64}PcZn$ deposited on P25 and P90, probably because of the “Teflon like” fluorinated structure.

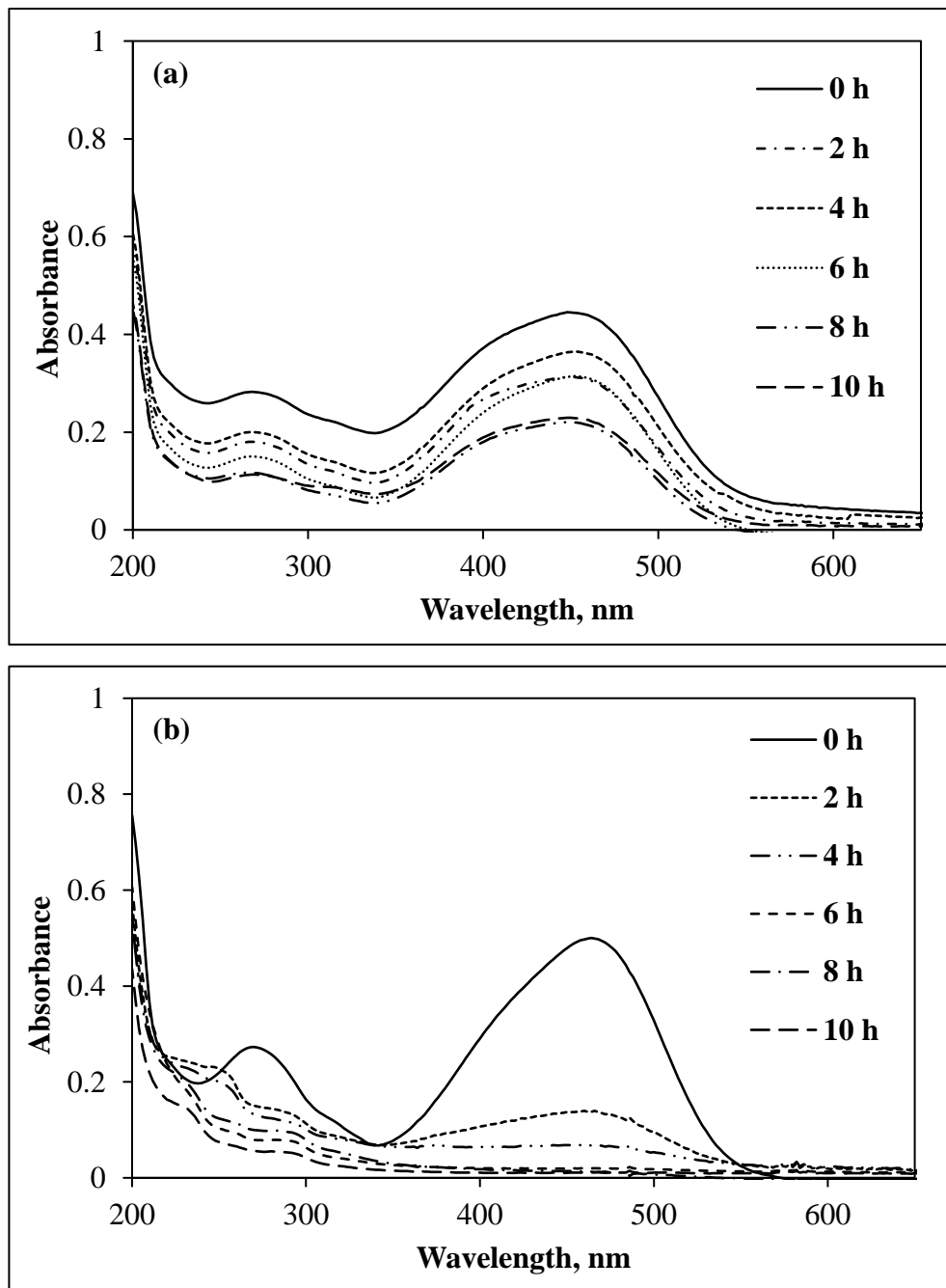


Figure 7. UV-Visible spectra of MO photodegradation with time. (a) P90 and (b) $F_{64}PcZn/P90$.

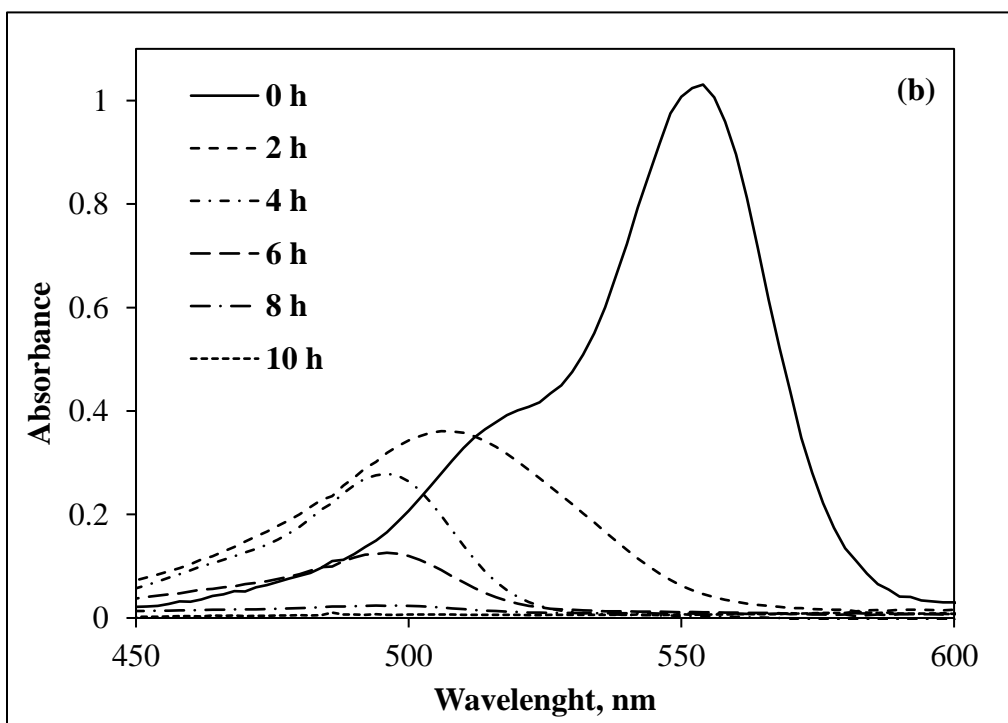
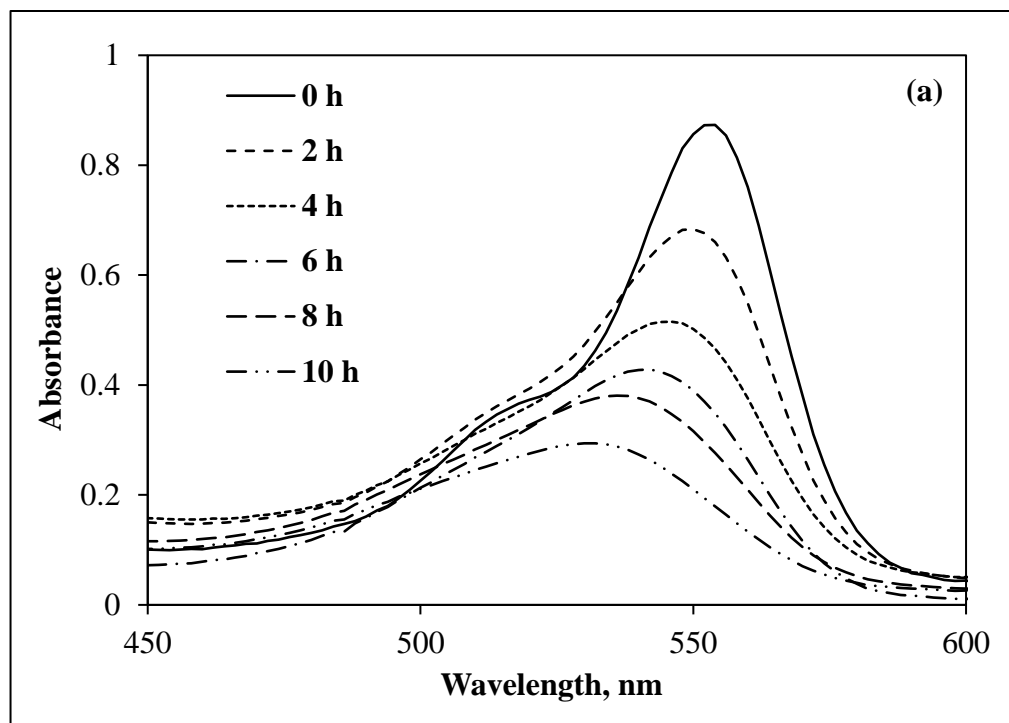


Figure 8. UV-Visible spectra display RhB photodegradation under visible light illumination catalyzed by (a) P90 and (b) F₆₄PcZn/P90. A blue shift in peak absorbance occurred for the reaction catalyzed by F₆₄PcZn/P90.

3.3.5. Kinetic Studies

To further analyze the rates of photodegradation reactions for MO and RhB kinetic models are applied. Figures 9 and 10 show the simulated kinetic plots for MO and RhB photodegradation reactions catalyzed by P25, P90, F₆₄PcZn/P25 and F₆₄PcZn/P90.

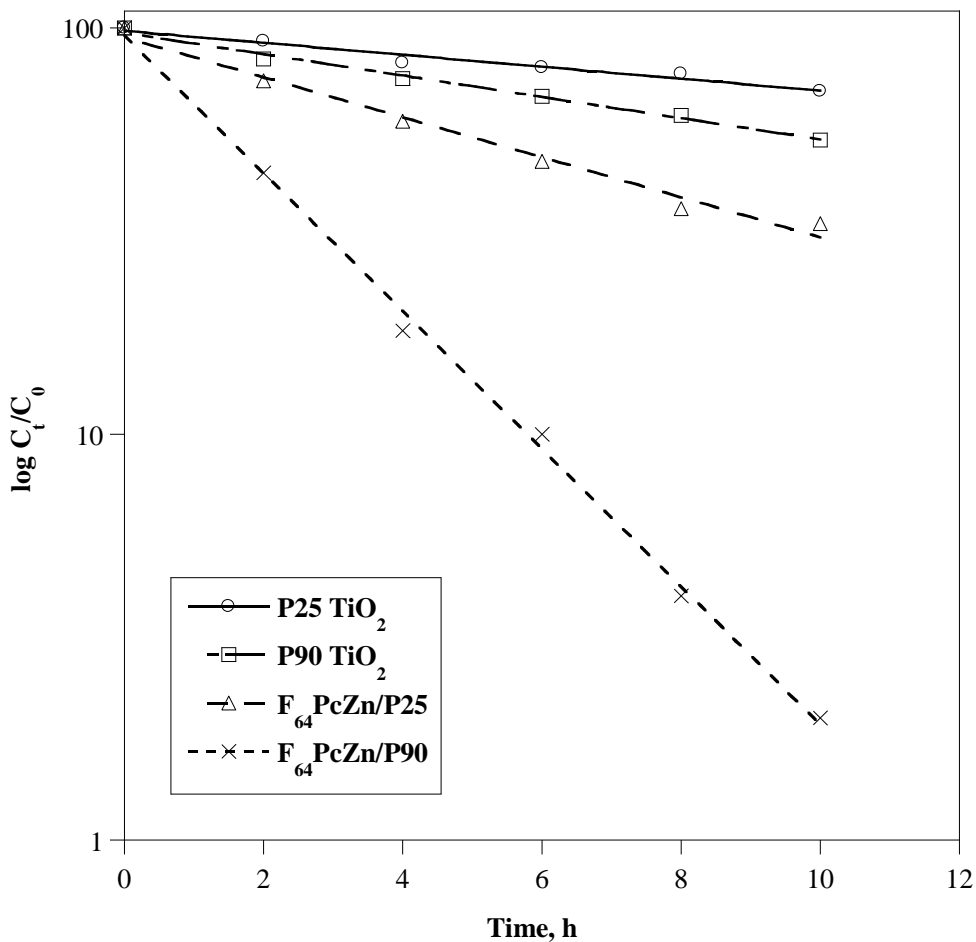


Figure 9. Kinetics plots for MO photodegradation catalyzed by

P25, P90, F₆₄PcZn/P25 and F₆₄PcZn/P90.

A linear fit is obtained while plotting $\ln(C_t/C_0)$ versus time. The results suggest that the reaction rate follows first order kinetics which can be expressed as $\ln[C_t] = -kt + \ln[C_0]$, where C_0

and C_t are the concentrations of MO and RhB solutions at initial and after irradiation of time t . k is the kinetic rate constant. Table 2 depicts k and regression coefficient (R^2) values for bare and $F_{64}PcZn$ loaded TiO_2 particles.

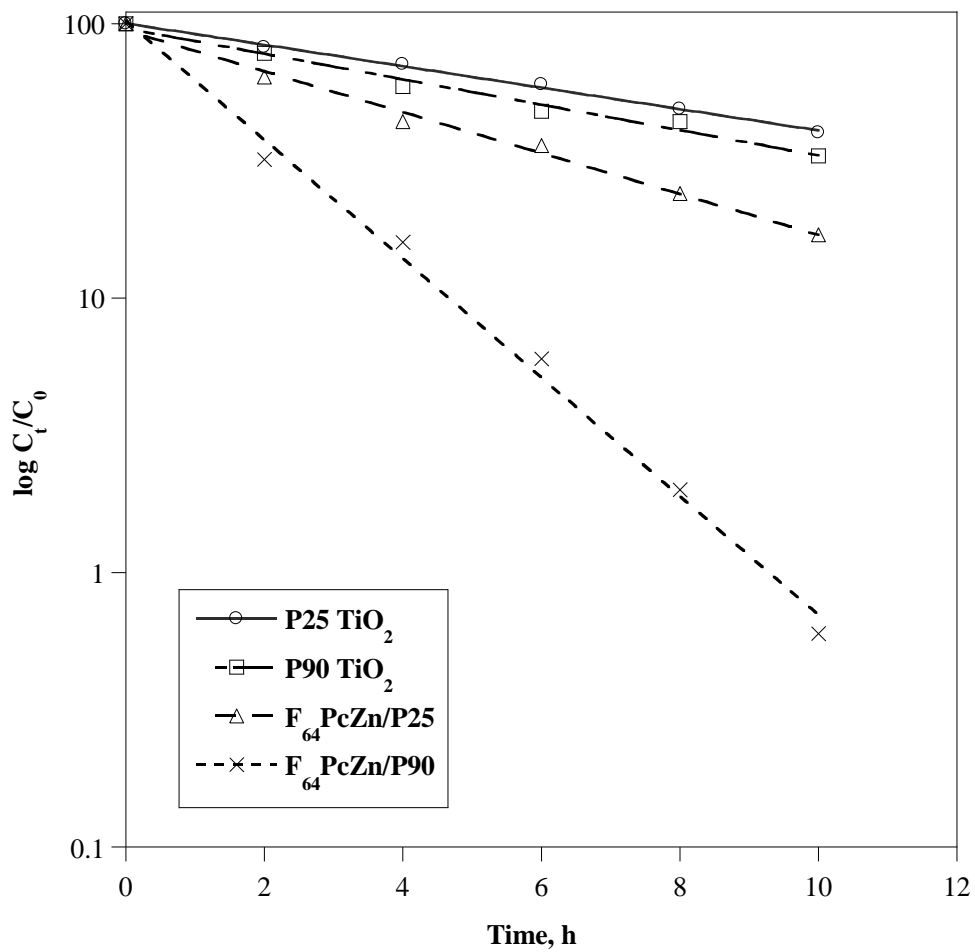


Figure 10. Kinetics plots for RhB photodegradation catalyzed by

P25, P90, $F_{64}PcZn/P25$ and $F_{64}PcZn/P90$.

Table 2. Reaction rate (k) and regression coefficient (R^2) values for the photodegradation reactions.

Catalyst	Reaction				Regression	
	Rate (k $^{1/h}$)		Half-life, $t_{1/2}$ (h)		Coefficient (R^2)	
	MO	RhB	MO	RhB	MO	RhB
P25	0.0339	0.0899	20.44	7.71	0.9808	0.9986
P90	0.0605	0.1067	11.45	6.49	0.9947	0.9932
F ₆₄ PcZn/P25	0.1133	0.1715	6.12	4.04	0.9945	0.9945
F ₆₄ PcZn/P90	0.3906	0.4983	1.77	1.39	0.9994	0.9980

R^2 values for the fitted curves are greater than 0.95, indicating that the photocatalytic degradation process of MO and RhB follows the first order kinetic model. In our study, both MO and RhB photodegradation paths follow first order kinetics, there are several evidences in the literature that these dyes follow first-order kinetics model while using phthalocyanine/TiO₂ as solid-state catalyst.^{8,20,21} The specialty of the current investigation is using a stabilized fluorinated phthalocyanine, F₆₄PcZn, that can withstand in aggressive photochemical environments.

The active supporting substrates, TiO₂ P25 and P90 can photodegrade MO and RhB by irradiating them with a tungsten halogen lamp. It can be noticed from Figure 3 that the tungsten halogen light spectrum contains a small portion of UVA radiation in the range of 320-400 nm (0.87 mW/cm²). According to literature the band gap of P25 is 3.25 eV which can absorb light at 382 nm.^{22,23}

The particle size plays a crucial role in deciding the reaction rate. Table 1 lists the mean particle size of P25, P90, F₆₄PcZn/P25 and F₆₄PcZn/P90 determined in de-ionized water. P90 that has a particle size of 50 nm shows a higher reaction rate than P25 with the secondary particle size of 79 nm (Table 1). More number of dye molecules can interact with the catalyst surface, where it can be degraded, if the surface area is larger. As shown in Table 2, a higher k value is observed for the hybrid F₆₄PcZn/P25 and F₆₄PcZn/P90 catalysts relative to the supporting substrates P25 and P90. These results indicate F₆₄PcZn acts efficiently as a photocatalyst in the solid state while impregnated on solid supports. Both F₆₄PcZn/P25 and F₆₄PcZn/P90 are more efficient than the substrate itself. It can be realized from the results a small addition of photoactivity from P25 and P90 ($k = 0.0339$ and 0.0605 1/h, respectively as listed in Table 2) is involved in the photoactivity of hybrid catalysts. F₆₄PcZn/P25 is 3.2 times more efficient than P25 and F₆₄PcZn/P90 is 7.6 times more active as compared to P90 under visible light irradiation. Comparison of P25 and P90 with F₆₄PcZn/P25 and F₆₄PcZn/P90 gives 1.9 and 4.7 times of improved reaction rates for RhB degradation. It can be noticed that the reaction rates are different for MO and RhB. The degradation rate is lower for the heteropolyaromatic dye *i.e.*, RhB than the azo dye methyl orange.²⁴ The –N=N– azo bond of chromophore can be easily attacked by the hydroxyl radicals, •OH, which could be one of the reasons for the higher degradation rates of MO.²⁴ Here, it is important to remember the photostability of F₆₄PcZn, in which the metal center is encapsulated in a refractive organic environment while the strong stabilization of frontier orbitals energy induced by the *i*-C₃F₇ groups disfavors the oxidation of the molecule via electron transfer. Hence, in this study a stable solid-state photocatalyst which is highly efficient under visible light irradiation is produced. Because of the above-mentioned particle size effect F₆₄PcZn/P90 exhibits a better k value than F₆₄PcZn/P25 as given in Table 2. Maira *et al.* also reported a strong dependence of organic pollutant degradation

rate on both primary and secondary particle sizes of TiO₂.^{25,26} When the surface area is increased for F₆₄PcZn/P90 a larger number of F₆₄PcZn can be exposed to the local environment, hence F₆₄PcZn can absorb most of the visible light shined. Here, we want to mention that the reaction rate increased by increasing the light intensity from 1 Sun to 3 Suns. This shows the fact, the more the number of photons absorbed, the higher the number of excited F₆₄PcZn molecules that produces ROS thus the higher reaction rate k for F₆₄PcZn/P90 than F₆₄PcZn/P25.

3.3.6. Fluorescence emission spectra for F₆₄PcZn deposited on P25 and P90 TiO₂

To understand the catalytic efficiency of F₆₄PcZn deposited on P25 and P90, fluorescence emission spectra were recorded following the excitation at 650 nm (Figure 11). An intense fluorescence peak is observed after depositing F₆₄PcZn on both P25 and P90. The intense fluorescence emission for F₆₄PcZn/P25 suggests in addition to higher catalytic efficiency that there is no charge transfer occurs between TiO₂ P25 conduction band and excited F₆₄PcZn HOMO energy level. Here P25 and F₆₄PcZn separately act as photocatalysts under visible light irradiation. An increase in fluorescence intensity for F₆₄PcZn/P90 than F₆₄PcZn/P25 suggests higher amount of F₆₄PcZn is exposed to the light because of the larger surface area of P90 than P25. This higher fluorescence of F₆₄PcZn/P90 can be correlated to its better catalytic efficiency than F₆₄PcZn/P25. The broadening and splitting of Q-band occur in both F₆₄PcZn/P25 and F₆₄PcZn/P90 due to the agglomeration of F₆₄PcZn deposited on TiO₂.^{27,28}

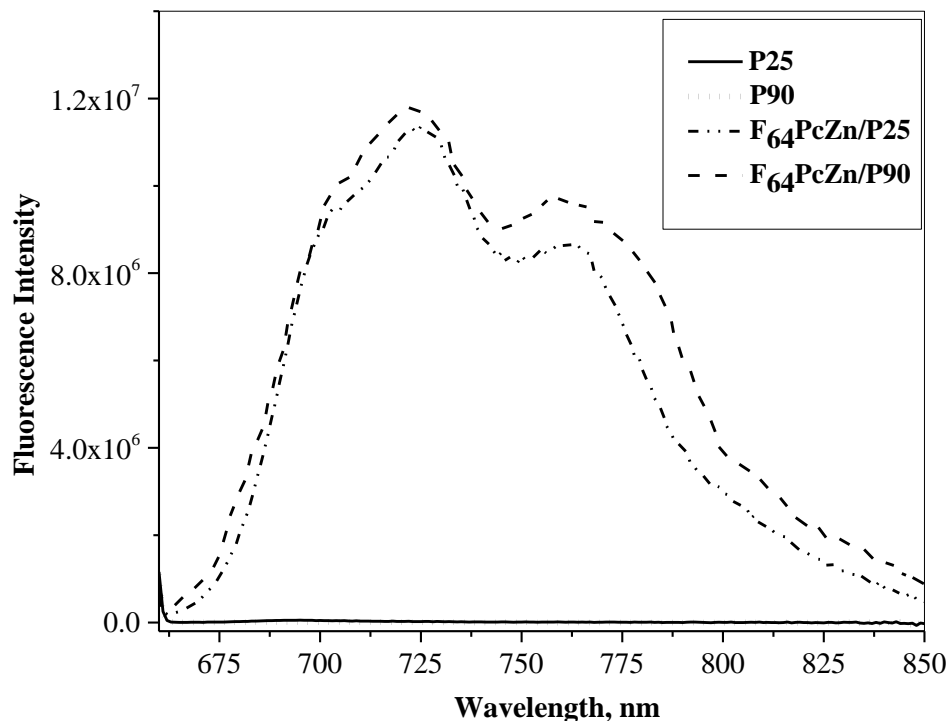


Figure 11. Fluorescence emission spectra of hybrid catalysts $F_{64}PcZn/P25$ and $F_{64}PcZn/P90$ deposited on substrates P25 and P90.

3.3.7. Commercial Phthalocyanines Versus $F_{64}PcZn$

Commercially available phthalocyanines such as $H_{16}PcZn$ and $F_{16}PcZn$ were deposited on P25 to investigate their efficiency as compared to $F_{64}PcZn$. Figure 12 depicts the comparison of reaction rates for $F_{64}PcZn/P25$, $F_{16}PcZn/P25$ and $H_{16}PcZn/P25$ hybrid catalysts. The reaction rates for MO photodegradation are in the following order, $F_{64}PcZn/P25 > P25 > F_{16}PcZn/P25 > H_{16}PcZn/P25$. The higher reactivity of $F_{64}PcZn/P25$ could be related to the greater 1O_2 production than the other Pcs. This conclusion is supported by the fluorescence emission spectra for the hybrid catalysts shown in Figure 13.

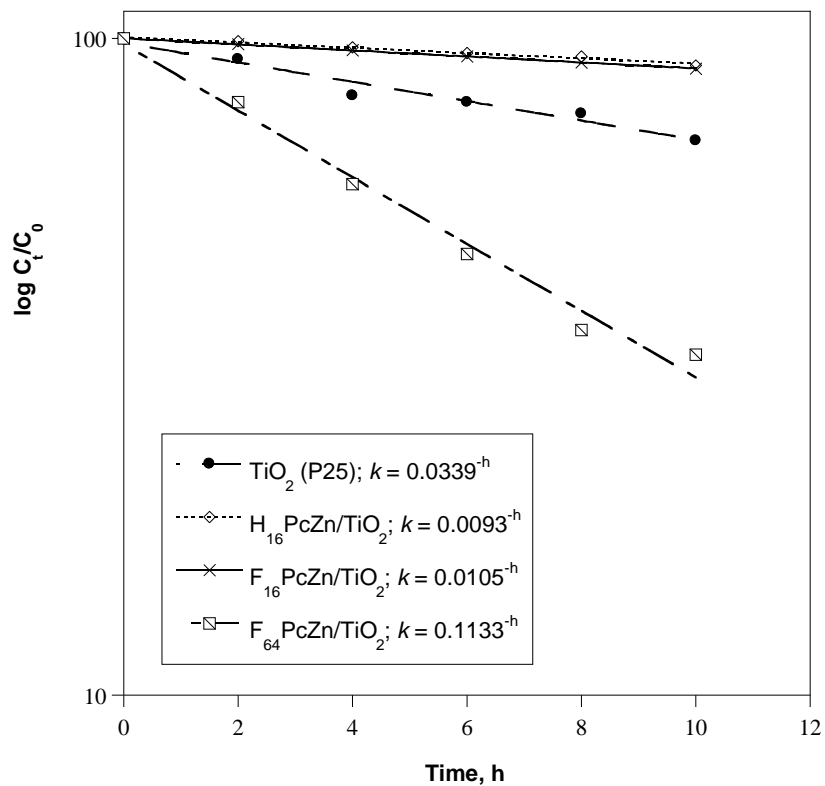


Figure 12. Comparison of MO photodegradation rates between P25,

H₁₆PcZn/P25, F₁₆PcZn/P25 and F₆₄PcZn/P25.

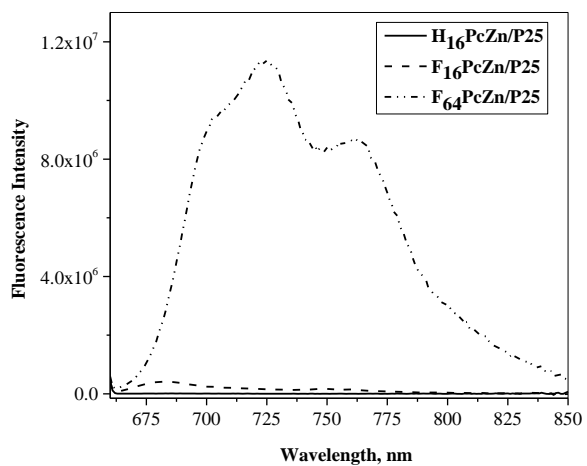


Figure 13. Fluorescence emission comparison for F₆₄PcZn/P25 with H₁₆PcZn/P25

and F₁₆PcZn/P25.

The fluorescence emission intensity is 26 times greater for F₆₄PcZn/P25 than F₁₆PcZn/P25. Whereas, an unnoticeable amount of fluorescence is emitted by H₁₆PcZn/P25 suggesting the π - π stacking of H₁₆PcZn molecules deactivate the excited state. By considering the van der Waals diameters of H₁₆PcZn and F₁₆PcZn molecules, the intermolecular distances could reach ~ 3.4 Å which is consistent with the π - π stacking.¹¹ A lower fluorescence emission from F₁₆PcZn/P25 is also due to the same deactivation of excited molecules rapidly because of π - π molecular stacking effect. This kind of deactivation is hindered in F₆₄PcZn/P25 because of the bulky peripheral -CF₃ groups, hence F₆₄PcZn/P25 shows higher fluorescence, thus greater catalytic efficiency. Previously, a decrease in the excited state lifetimes is reported in solution phase for H₁₆PcZn and F₁₆PcZn as compared to F₆₄PcZn by Beveridge *et al.*²⁹ In the fluorescence spectra of F₆₄PcZn/P25, the broadening and splitting of Q-band in to two peaks at 725 and 763 nm occurs due to agglomeration of F₆₄PcZn deposited on P25. The relation between agglomeration and amount of F₆₄PcZn deposited on P25 will be discussed in the following section.

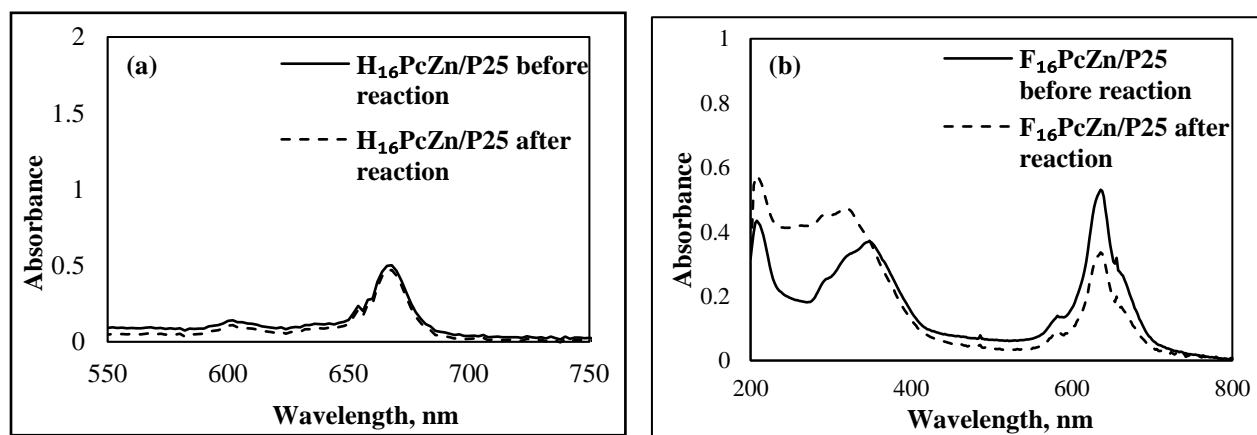


Figure 14. UV-Vis spectra of H₁₆PcZn and F₁₆PcZn extracted from H₁₆PcZn/P25 and F₁₆PcZn/P25 before and after 10 h of MO photodegradation reaction.

Not alone the lower catalytic activity, the photochemical stability of H₁₆PcZn/P25 and F₁₆PcZn/P25 is also not equal to F₆₄PcZn/P25 in the harsh photochemical radical environment due to their C-H bonds which can be attacked by the radicals and photo-oxidized. We observed a slight decrease in the Q-band absorbance for H₁₆PcZn and a noticeable reduction in the Q-band peak intensity of F₁₆PcZn extracted from the hybrids H₁₆PcZn/P25 and F₁₆PcZn/P25 after 10 h of MO photodegradation reaction (Figure 14). This observation suggests P25 is involved in the degradation of these commercial Pcs deposited on the surface in addition to MO degradation. Hence the long time photostability of these commercial Pcs is questionable. The slow bleaching of commercial Pcs is one of the reasons for the lower catalytic activity of the hybrids H₁₆PcZn/P25 and F₁₆PcZn/P25 as compared to bare P25.

3.3.8. Photostability of F₆₄PcZn in Comparison to H₁₆PcZn and F₁₆PcZn Deposited on P25 under UV Light Irradiation

The change in the percentage of 0.01 mM H₁₆PcZn, F₁₆PcZn and F₆₄PcZn deposited on P25 dispersed in de-ionized water under short UV (254 nm) irradiation for 5 h is displayed in Figure 15. The results reveal that 80 and 70 % of H₁₆PcZn and F₁₆PcZn are decomposed by irradiating UV light on H₁₆PcZn/P25 and F₁₆PcZn/P25. Whereas 60% of F₆₄PcZn is degraded when shining short UV light on F₆₄PcZn/P25 dispersed in de-ionized water. These observations suggest a better photostability of F₆₄PcZn than H₁₆PcZn and F₁₆PcZn deposited on P25 TiO₂. Here we want to mention TiO₂ is highly photoactive under short UV light irradiation. Even at this condition 40% of F₆₄PcZn is photochemically stable after 5 h while deposited on P25.

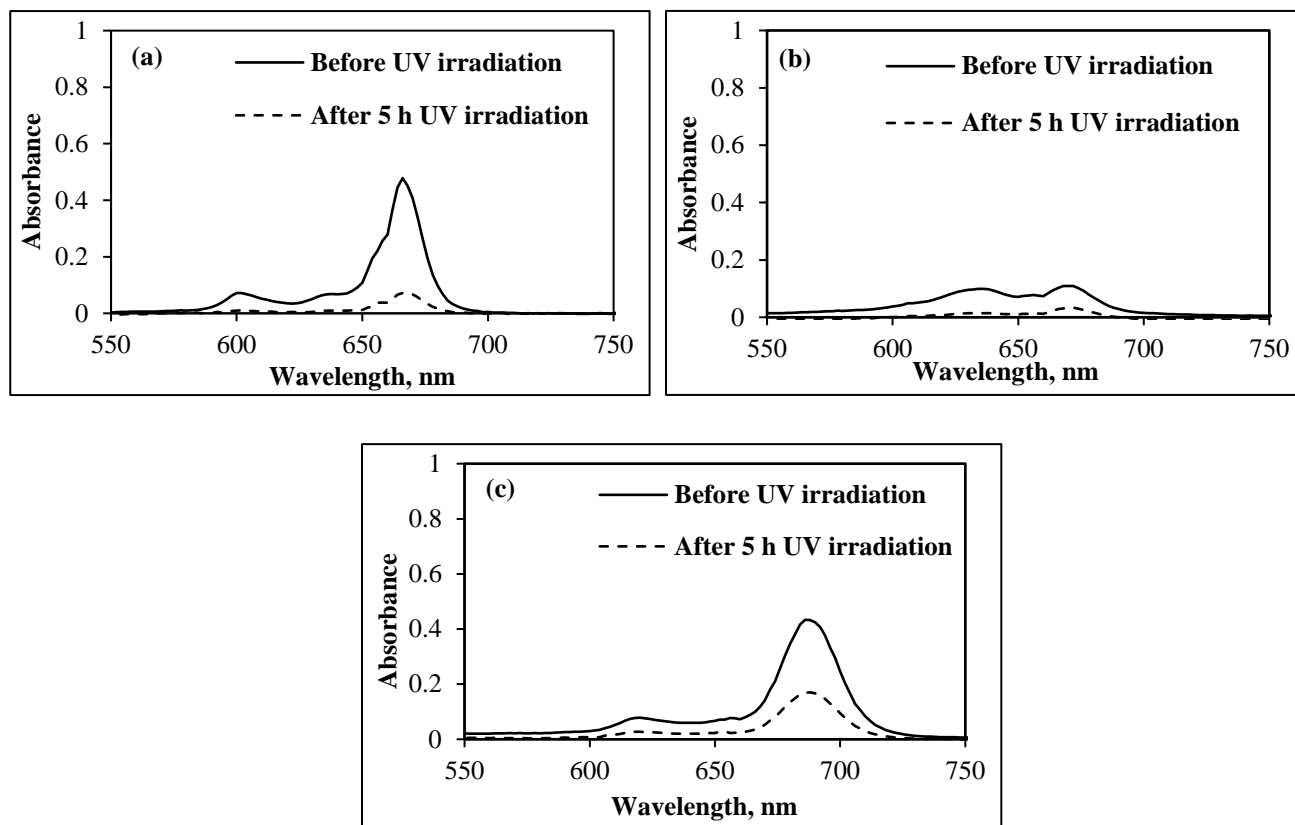


Figure 15. Photostability of (a) H₁₆PcZn, (b) F₁₆PcZn and (c) F₆₄PcZn deposited on P25 under UV (254 nm) light irradiation.

This shows the applicability of F₆₄PcZn/P25 for water decontamination under sunlight irradiation which consists of only 5% long and short UV light. Decomposition of Pcs has been reported in the literature especially under UV light irradiation.^{30,31} Liu *et al* reported decomposition of Pcs deposited on TiO₂ when irradiated with UV light. They found a faster decomposition rate for H₁₆Pc (C₃₂H₁₈N₈) than PcOV (C₃₂H₁₆OV) when H₁₆Pc/TiO₂ and PcOV/TiO₂ were kept under UV illumination.³⁰ Moons *et al.* found intense UV irradiation causes photodegradation of F₆₄PcZn in ethanol solution.³¹ In the current investigation, we observed a slow photodegradation of solid-state F₆₄PcZn deposited on P25.

3.3.9. Zeta Potential Measurement

Zeta potential is measured for the hybrid catalysts in de-ionized water to understand the actual surface charge and the nature of interaction between the hybrid catalysts and the pollutant dye molecules such as MO and RhB. The zeta potential for bare P25 and P 90 have positive values, 9 and 28 mV as shown in Table 3.³²

Table 3. Zeta potential in de-ionized water for TiO₂ and phthalocyanine/TiO₂ catalysts.

S. No.	Samples	Zeta Potential, mV
1	P25	10 ±1
2	P90	29 ±2
3	F ₆₄ PcZn/P25	6 ±1
4	F ₁₆ PcZn/P25	4 ±2
5	H ₁₆ PcZn/P25	10 ±1
6	F ₆₄ PcZn/P90	20 ±1
7	F ₆₄ PcZn/P25 post reaction	-1.5 ±1

Hence it can be concluded at this reaction conditions the negative end of pollutant dye molecules prefer to interact with the TiO₂ surface as shown in Figure 16. In case of MO the SO³⁻ group would easily interact, while for RhB the COO⁻ group will have a preference to interact with TiO₂ surface.³³ The zeta potential is shifted to less positive values after the deposition of fluorinated phthalocyanines F₁₆PcZn and F₆₄PcZn. This indicates the presence of negatively

charged compounds $F_{16}PcZn$ and $F_{64}PcZn$ at the surface of TiO_2 . Similar to this observation, Shimbo *et al.* reported a shift to the negative surface charges after doping fluorine in lead borosilicate glass.³⁴ Biffinger *et al.* argued if the fluorocarbon content of the substrate is increased, positively charged sites will preferentially bind to stabilize the negative end of the C-F dipole.³⁵ As the substrate is highly fluorinated, the pollutant molecules adsorption will be different for $F_{64}PcZn/TiO_2$ as compared to bare TiO_2 (Figure 16). In such cases MO will interact via its positively charged azo nitrogen or dimethyl nitrogen and RhB through its positively charged diethyl nitrogen group.^{36,37} The zeta potential values clearly show that the mode of pollutants adsorption is different for $F_{64}PcZn$ deposited TiO_2 as oppose to bare TiO_2 . This observation can be correlated to the slight blue shift versus an intense blue shift in the RhB UV-Vis peak absorbance maxima catalyzed by TiO_2 and $F_{64}PcZn/TiO_2$.

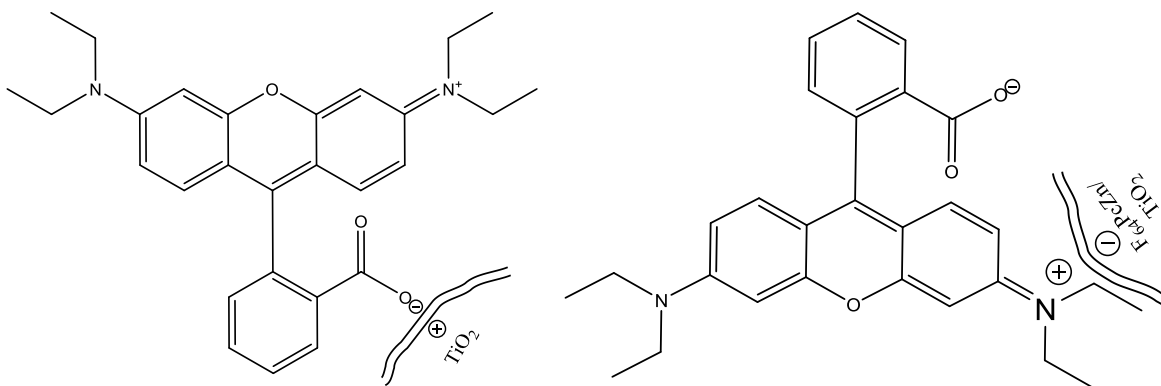


Figure 16. Mode of adsorption of RhB on the surface of TiO_2 and $F_{64}PcZn/TiO_2$.

An elaborate mechanism such as how the different modes of pollutant adsorption resulted in the formation of various degradation products will be discussed in the following HPLC LC/MS

section. The zeta potential for P25 and H₁₆PcZn/P25 are similar. Because of the absence of fluorination of Pc, it has been assumed that the mode of adsorption of MO and RhB will be the same for both P25 and H₁₆PcZn/P25.

3.3.10. Influence of UV-Light, Visible-Light, UV + Visible Light and Red-Light Illumination on Catalysis

RhB photodegradation under the influence of lights with different wavelengths such as UV, visible and red-lights are investigated. The intensity of UV light (at wavelength of 365 nm) irradiated was 0.5 mW/cm². The visible light intensity was the same 390,000 lx, *i.e.*, 57 mW/cm² with the wavelengths ranging from 450 to 750 nm while the red-light intensity irradiated was 1 mW/cm² at the wavelength of 626 nm. Like the other photochemical experiments, aliquots at different time intervals were collected to analyze the concentration of reaction products using UV-Vis spectroscopy.

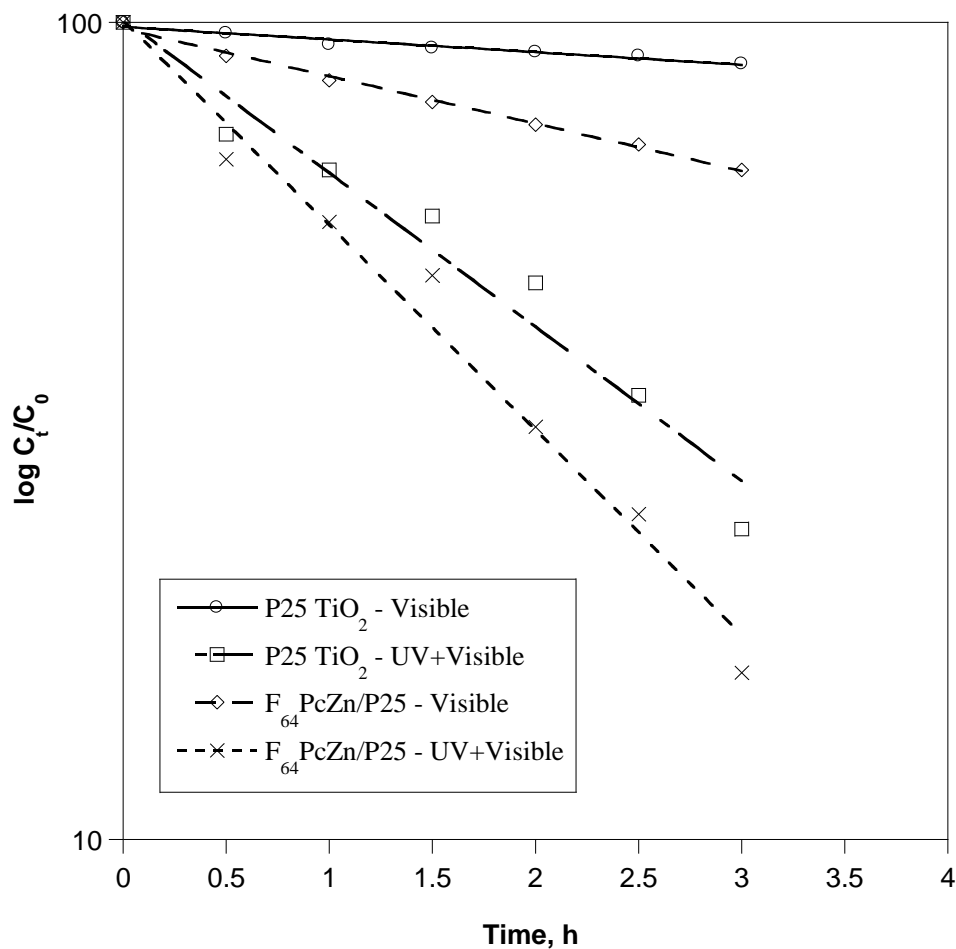


Figure 17. Kinetic plots for the photodegradation of RhB catalyzed by P25 and F₆₄PcZn/P25 upon illumination with only visible light, and with the combination of UV + Visible light.

It can be seen from Figure 18 that the reaction kinetics follows first order. While irradiating with visible light P25 shows lower photoactivity, but the hybrid catalyst is much more active because it can absorb more visible light. While illuminating with UV and visible light F₆₄PcZn/P25 exhibits higher photoactivity than the visible light irradiation because P25 adds up its photoactivity in the combination of UV + Visible light irradiation. Iliev *et al.*³⁸ also observed a higher reaction rate for the photooxidation of oxalic acid using N-doped TiO₂ and Au/N-doped TiO₂ upon

irradiation with the combination of UV-Visible light. The sunlight has 5% of UV light and 95% of visible light.³⁹ By taking advantage of having P25 and P90 as a solid support, F₆₄PcZn/P25 and F₆₄PcZn/P90 can utilize the complete spectrum of solar light to exhibit enhanced photoactivity. Figure 19 displays the UV-Visible spectra for F₆₄PcZn extracted before and after RhB photodegradation reaction under irradiation of UV + Visible light. The reaction was performed for 3 h. Here we extracted F₆₄PcZn from F₆₄PcZn/P25 after stirring to equilibrate the surface of F₆₄PcZn/P25 particles in RhB solution for 30 minutes. Hence the UV-Visible spectra in Figure 18 shows the peaks corresponding to RhB that is adsorbed on F₆₄PcZn/P25 during equilibration process in addition to F₆₄PcZn spectral peaks. It can be seen from the figure that F₆₄PcZn is intact and only RhB degrades under the reaction conditions. This shows that the hybrid catalysts F₆₄PcZn/P25 and F₆₄PcZn/P90 can be applied to decontaminate water efficiently in the water resources in remote areas where the catalyst will utilize only the natural sunlight and air to degrade organic pollutants. We can conclude from these results that the hybrid catalysts F₆₄PcZn/P25 and F₆₄PcZn/P90 will stay robust during long-term practical applications.

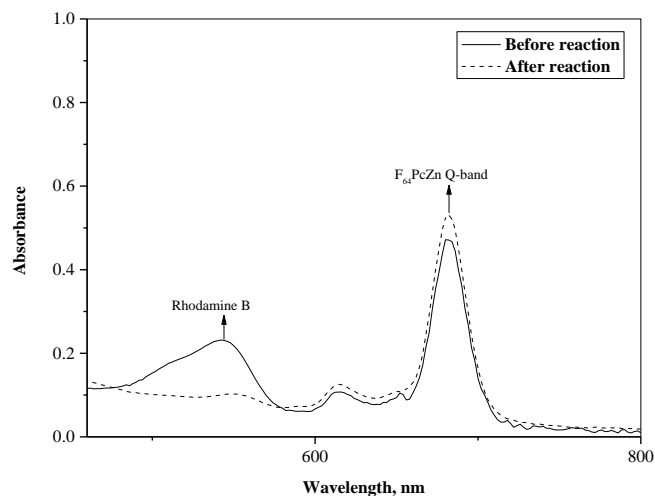


Figure 18. UV-Visible spectra of $F_{64}PcZn$ extracted from $F_{64}PcZn/P25$ after RhB photodegradation using UV + Visible light.

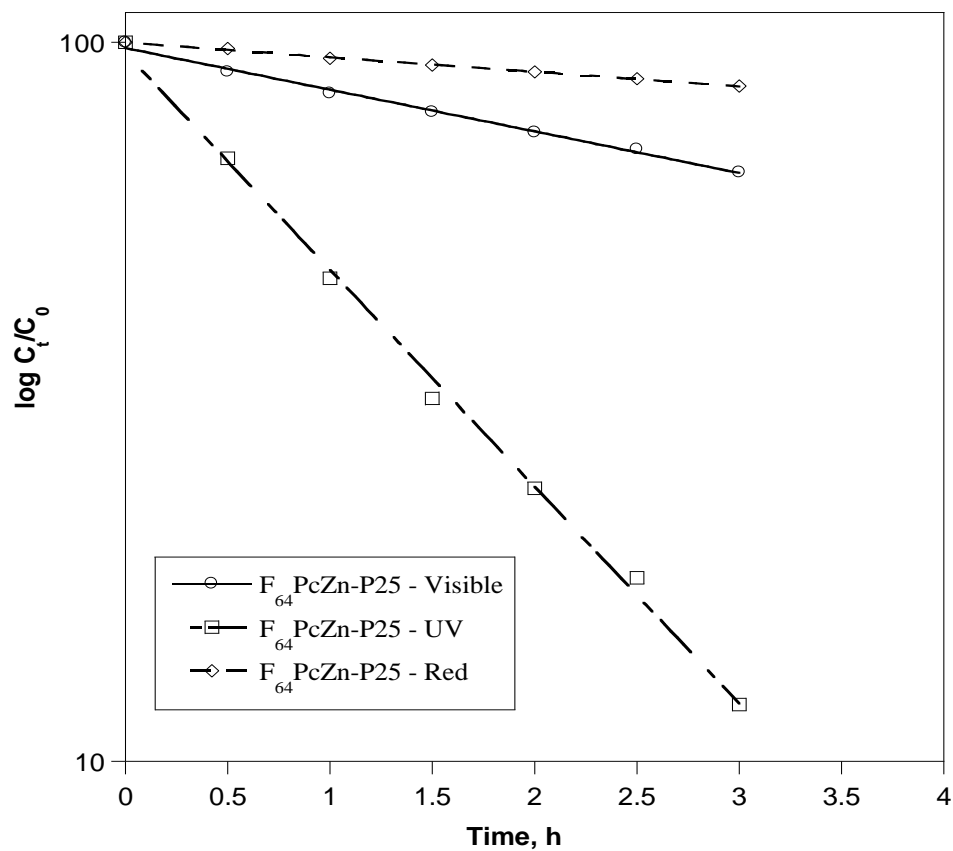


Figure 19. Photodegradation of RhB using $F_{64}PcZn/P25$. Effect of red, visible and UV lights illumination.

Comparison of F₆₄PcZn/P25 efficiency to degrade RhB under irradiation of red, visible and UV lights is shown in Figure 19. F₆₄PcZn is the only component that is active under red-light, and P25 is completely inactive. The results suggest that F₆₄PcZn deposited on P25 at this amount is not very efficient by itself. While shining visible light that has a small portion of UV light both P25 and F₆₄PcZn are active, therefore the RhB degradation rate is increased. But, when the higher energy UV light is shined the RhB degradation rate reached the highest. Under UV light only P25 is active. Because of the higher energy compared to other lights such as visible and red this shows the maximum pollutant degradation rate. But the advantage of using visible light overwhelms this efficiency of UV light due to the availability from natural resources.

Since F₆₄PcZn may show some photoreactivity in the UV region because of the B bands, RhB photodegradation reaction was carried out for 0.1 mM RhB solution catalyzed by 0.01 mM F₆₄PcZn/OX 50 SiO₂ under irradiation of 0.5 mW/cm² intensity of UV light with the wavelength of 365 nm. The experiment was last for 3 h, aliquots were collected every 30 min to follow the concentration of RhB. We noticed there is no change in the concentration of RhB. Comparing the UV-Vis spectra of F₆₄PcZn extracted from F₆₄PcZn/OX 50 before and after photoreaction shows that F₆₄PcZn did not degrade during the photoreaction. This result suggests at this wavelength and intensity of UV irradiation F₆₄PcZn deposited on OX 50 SiO₂ is not effective in degrading RhB.

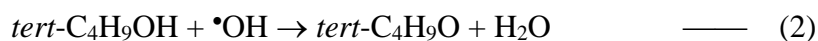
3.3.11. Effect of Visible Light Intensity

The effect of visible light intensity is investigated by applying 130,000 lx light (1 Sun) intensity instead of 390,000 lx (3 suns). A 2/3 reduction in the reaction rate of RhB degradation for F₆₄PcZn/P25 is observed in 5 h. This result suggest RhB can be degraded even in lower light

intensities. This shows the applicability of using F₆₄PcZn/P25 in water purification processes using various light intensities.

3.3.12. Radical Intermediates in the Photoinduced Reactions

Several investigations reported that •OH radicals formed on the surface of TiO₂ by the reaction of photogenerated holes with the surface hydroxyl groups and water are responsible for the photodegradation of organic pollutants.^{6,40-42} To examine the involvement of •OH radicals in the photocatalytic reactions while using P25 and F₆₄PcZn/P25 catalysts, *tert*-butanol is added to the reaction system as a •OH radical scavenger and the rate of RhB photodegradation is monitored. As soon as formed the •OH radicals readily abstract a H-atom from the -CH₃ group or -OH group of *tert*-butanol as given in the equations 1 and 2.



Therefore, the overall RhB photodegradation reaction rate is noticeably decreased in the presence of *tert*-butanol.⁴³ Figure 20 depicts the RhB photodegradation rate catalyzed by P25 and F₆₄PcZn/P25. In this reaction mixture, 4 mL of water is substituted by *tert*-butanol as a •OH radical scavenger.

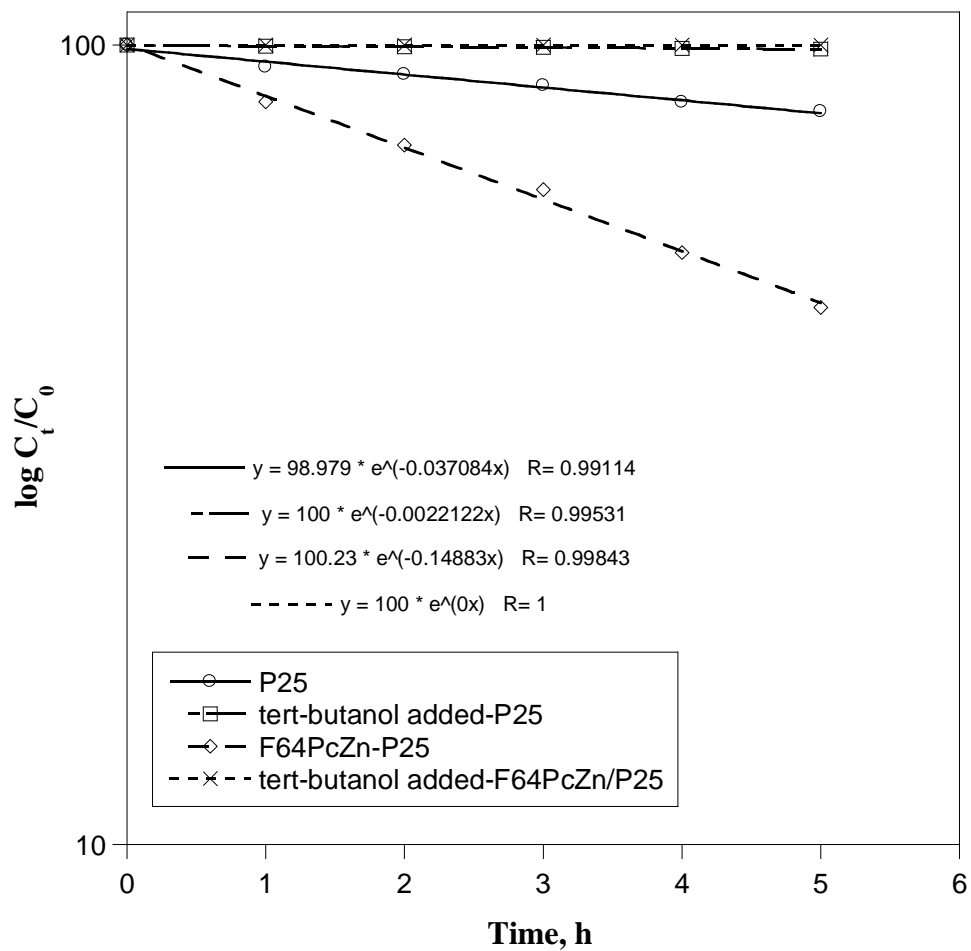


Figure 20. RhB reaction rate under the influence of *tert*-butanol that is added to confirm the role of •OH radical.

When P25 is a catalyst, the RhB degradation reaction is not completely stopped in the presence of *tert*-butanol, rather a 6% of degradation occurred. This shows two different competitive reaction mechanisms are involved when P25 TiO₂ is added as a catalyst. TiO₂ can produce holes under illumination which can directly oxidize RhB. Otherwise, •OH radicals can be produced due to the presence of surface hydroxyl groups at hydrated conditions that degrades RhB.

Our results suggest that there may be approx. 6% of RhB oxidation proceeds via direct hole transfer and the rest occurs because of •OH radicals assisted oxidation reaction.

In contrast, the kinetic plots suggest only •OH radicals pathway is involved in the oxidation of RhB catalyzed by F₆₄PcZn/P25. The degradation reaction rate is decreased to a great extent with the addition of *tert*-butanol (Figure 20). Obviously, •OH radical plays a significant role in the degradation of organic pollutants when F₆₄PcZn/P25 is added as a catalyst. Similar results are reported by Minero *et al.*, they investigated the type of mechanism involved in the oxidation reaction of phenol catalyzed by naked TiO₂ and fluorinated TiO₂/F.⁴⁴ They concluded 10% of the oxidation occurs via the hole transfer mechanism and 90% of phenol oxidation is due to •OH radicals involvement when the reaction is catalyzed by TiO₂. While only •OH radicals pathway is involved in the oxidation of phenol catalyzed by TiO₂/F.

3.3.13. Total Organic Carbon (TOC) and Total Dissolved Nitrogen (TDN) Analysis

The mineralization percentages are calculated using the equation $C_t / C_0 * 100$. The % of total organic carbon (TOC) and total dissolved nitrogen (TDN) before and after photodegradation of RhB catalyzed by P25, P90, F₆₄PcZn/P25 and F₆₄PcZn/P90 are shown in Figure 21. Results suggest a rapid decrease in the percentage of dissolved organic carbon and nitrogen when the RhB photodegradation reaction is catalyzed by the hybrid F₆₄PcZn/P25 and F₆₄PcZn/P90 catalysts. As displayed in Figure 21, a higher percentage of mineralization occurred for the reactions catalyzed by F₆₄PcZn/P90 than F₆₄PcZn/P25. % TOC and % TDN again confirmed the concept that the particles with larger surface area provide higher catalytic efficiency.

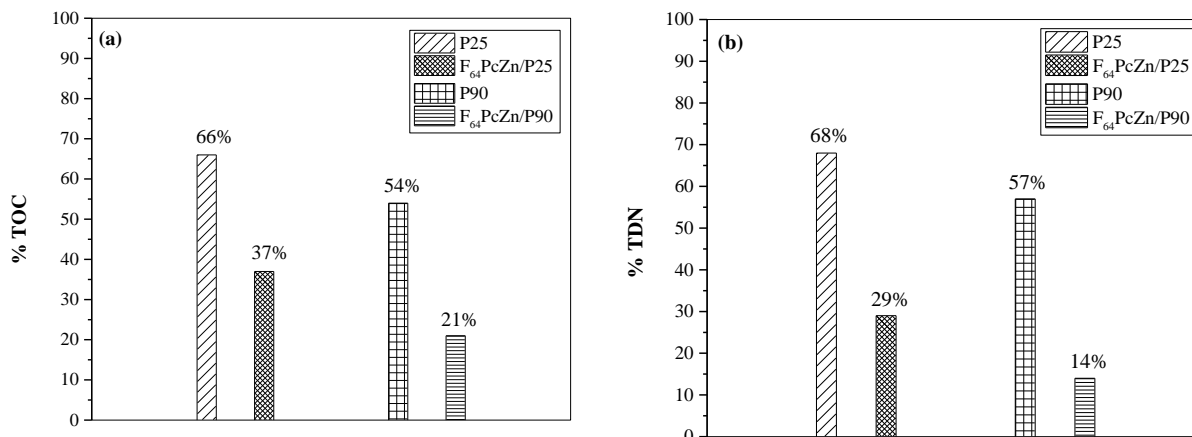


Figure 21. The mineralization of RhB catalyzed by P25, P90, F₆₄PcZn/P25 and F₆₄PcZn/P90.

(a) % of total dissolved carbon (TOC) and (b) % of total dissolved nitrogen (TDN).

F₆₄PcZn/P90 is the most efficient catalyst among the solid-state photocatalysts investigated. A 21% of TOC is obtained for this photocatalyst, indicating the smaller organic fragments are still present in the solution. We assume prolonged exposure to visible light may remove most of these organic degradation products. Being a xanthene dye, RhB has two N- groups, the studied catalysts are able to destruct the molecule as indicated by the decrease in the TOC and TDN values. The mineralization of organic carbon leads to the formation of soluble carboxylate ions (COO⁻) and carbon dioxide (CO₂) gas.^{45,46} The photooxidation of N- groups causes the formation of inorganic ions such as nitrates (NO₃⁻), nitrites (NO₂⁻) ammonium ions (NH₄⁺) and ammonia (NH₃) gas.^{45,46} We have determined the pH of the test solutions before and after photocatalytic reactions to check for any variation.

3.3.14. pH Determination

Table 4 displays the pH of RhB solution before and after photodegradation process catalyzed by P25, P90, F₆₄PcZn/P25 and F₆₄PcZn/P90. The values suggest that there is no much change in the pH of the solution which could be an advantage of using these F₆₄PcZn deposited hybrid catalysts to clean water in remote areas using sunlight.

Table 4. pH of the Test Solutions Before and After Photoreaction.

S. No.	Photocatalyst	pH Before Photoreaction (0 h)	pH After Photoreaction (10 h)
1	P25	4.1	4.1
2	P90	4.1	4.1
3	F ₆₄ PcZn/ P25	4.2	4.1
4	F ₆₄ PcZn/ P90	4.3	4.3

3.3.15. Effect of F₆₄PcZn amount deposited on P25

Various amounts of F₆₄PcZn was deposited on P25 with the scope of absorbing more visible light that could increase the efficiency of F₆₄PcZn/P25. Results given in Table 5 for the photodegradation of MO confirmed an increase in the efficiency with increasing loading amount of F₆₄PcZn on P25. The reaction rate k linearly increased from 0.034 to 0.106 with increasing the amount of F₆₄PcZn deposited on P25 from 0 mM to 0.01 mM while keeping the MO concentration constant as 0.1 mM. This could be explained by the efficiency to absorb larger intensities of light which is discussed in the following section, fluorescence intensity measurements for F₆₄PcZn/P25 with different deposition amounts of F₆₄PcZn.

Table 5. Reaction Rate (k) and Half-life ($t_{1/2}$) for F₆₄PcZn/P25 with Different Deposition Amounts of F₆₄PcZn.

S. No.	Amount of F ₆₄ PcZn		Reaction Rate (k) h ⁻¹	Half-life ($t_{1/2}$) h
	Deposited on P25 (mM)			
1	0		0.034	20.2
2	0.002		0.044	15.8
3	0.003		0.054	12.8
4	0.007		0.083	8.4
5	0.01		0.106	6.5

3.3.16. Change in Fluorescence Intensity with F₆₄PcZn Deposition Amount on P25

The change in fluorescence intensity with increasing amount of F₆₄PcZn deposited on P25 is displayed in Figure 22. At lower F₆₄PcZn deposition amounts, a single fluorescence peak with a shoulder is appeared. For example, when 0.002 and 0.003 mM F₆₄PcZn is deposited on P25 a fluorescence peak centered at 718 nm with a shoulder around 779 nm is observed. Whereas by increasing the depositing amount of F₆₄PcZn to 0.007 mM the fluorescence intensity increased by 1.3 times, but the peak became broader. Again, with the increase in F₆₄PcZn deposition amount to 0.01 mM, further broadening of the peak and a clear split in the peak with the peak maxima of 724 and 763 nm are observed. This broadening and peak splitting occur due to the agglomeration of F₆₄PcZn on the surface of P25. Phthalocyanines generally form face-to-face oriented H-aggregates and side-by-side oriented J-aggregates.⁴⁷⁻⁴⁹ J-aggregates are known to be fluorescent whereas H-

aggregates are non-fluorescent.⁴⁷⁻⁴⁹ It can be understood from the broad and split Q-band, F₆₄PcZn randomly formed aggregates on P25 by increasing the F₆₄PcZn deposition amount.

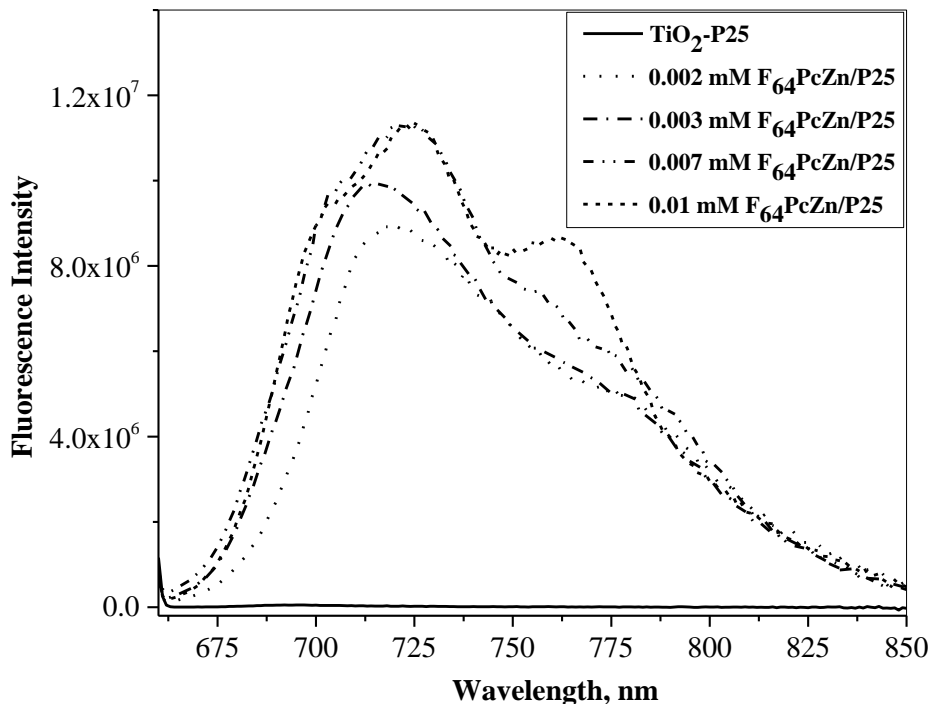


Figure 22. Change in fluorescence intensity with increasing amount of F₆₄PcZn deposited on P25.

The fluorescence intensity results suggest an optimum amount of Pc should be deposited on TiO₂ to obtain maximum catalyst reactivity, by increasing the deposition amount further would lead to aggregation of Pc with no improvement in the catalyst activity. In another view point the thicker coating may result in the desorption of Pc from the surface of TiO₂ because the interaction between the molecules of F₆₄PcZn is very weak.

3.3.17. Light Absorption Efficiency of F₆₄PcZn/P25 with Varying Amounts of F₆₄PcZn: Evaluation using UV-Vis-NIR Spectral Measurements

Figure 23 depicts the UV-Vis-NIR spectra for solid state P25, F₆₄PcZn/P25 with various amounts of F₆₄PcZn deposited on P25 and F₆₄PcZn in ethanol solution. The Q band due to π - π^* transitions is observed at 682 nm for F₆₄PcZn in ethanol solution while 688 nm for solid state 0.01 mM F₆₄PcZn/P25. A slight red shift and Q-band peak broadening is an indication of multiple interactions between adjacent molecules while moving from the single molecule solution phase to the condensed phase.⁵⁰ In addition, the B band located at 392 nm for F₆₄PcZn is replaced by a strong and broad absorption band ranging from 200 to 450 nm for F₆₄PcZn/P25, looks like a combined band of TiO₂ and F₆₄PcZn. The absorption characteristics of both F₆₄PcZn and TiO₂ moieties are clearly displayed for F₆₄PcZn/P25 hybrids. The large coverage of the solar spectrum from UV to near IR region render the hybrid catalyst F₆₄PcZn/P25 useful light harvesting material. The higher photoactivity of the hybrid catalyst F₆₄PcZn/P25 with increasing amount of F₆₄PcZn deposition may be because of the higher light harvesting efficiency.

The variation of Q-band absorbance maxima with different amounts of F₆₄PcZn deposited on P25 is displayed in Figure 23b. An increase in the Q-band absorbance intensity with deposition amount of F₆₄PcZn suggest π - π molecular stacking is limited because of the bulky peripheral -CF₃ groups in F₆₄PcZn.

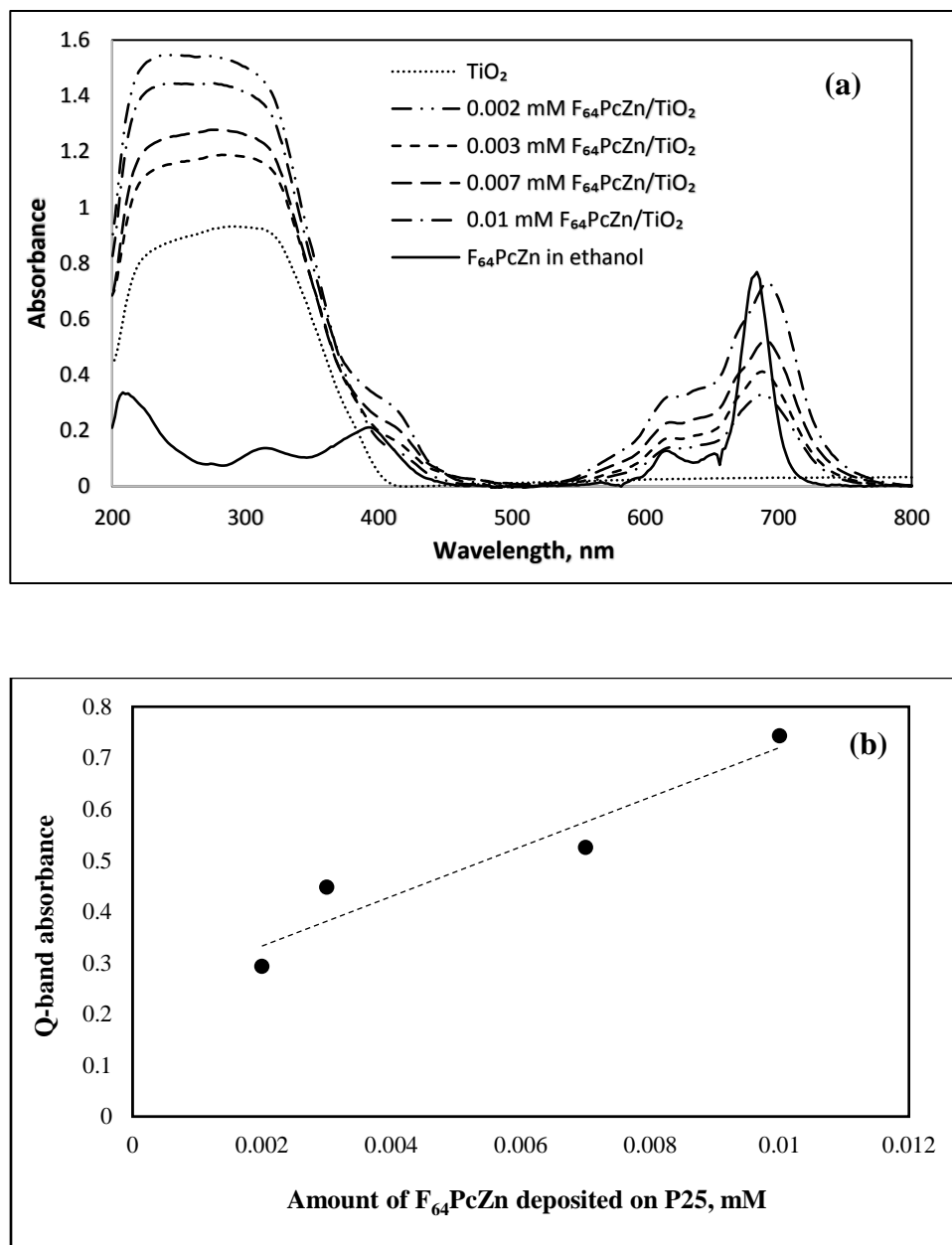


Figure 23. (a) UV-Vis-NIR spectra for P25 and $\text{F}_{64}\text{PcZn}/\text{P25}$ with different amounts of F_{64}PcZn deposited on 25. (b) Plot of Q-band absorption intensities with increasing amounts of F_{64}PcZn deposited on P25.

3.3.18. Adsorption of Pcs on P25: X-Ray Photoelectron Spectroscopy (XPS) Analyses

To reveal the mode of $F_{64}PcZn$ adsorption on TiO_2 , high-resolution XPS analyses are performed for $F_{64}PcZn$, P25 TiO_2 and $F_{64}PcZn/P25$. In addition, $H_{16}PcZn/P25$ and $F_{16}PcZn/P25$ are characterized using XPS analyses as a comparison to $F_{64}PcZn/P25$. The C 1s, O 1s, Zn 2p, F 1s, N 1s, Ti 2p and Si 2p core levels are examined.

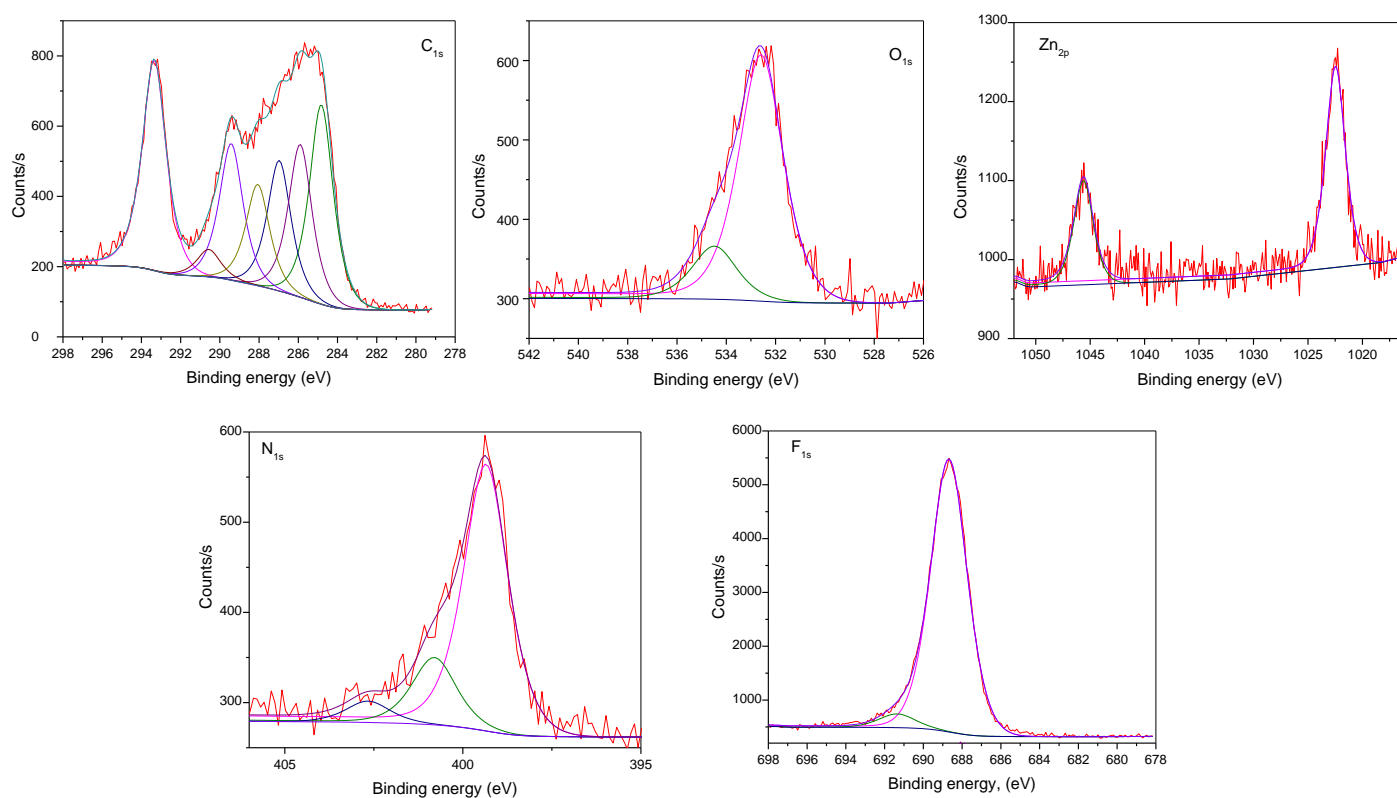


Figure 24. High resolution XPS spectra of C 1s, O 1s, Zn 2p, F 1s and N 1s for $F_{64}PcZn$.

Typical XPS spectra of C 1s, O 1s, Zn 2p, F 1s and N 1s for $F_{64}PcZn$ are shown in Figure 24. The details are discussed in Chapter 2. These spectra are included here to understand the changes in binding energy values when $F_{64}PcZn$ is deposited on P25. The survey of XP spectra for

P25 and F₆₄PcZn/P25 are shown in Figure 26. The peaks corresponding to N 1s, F 1s and Zn 2p appeared for F₆₄PcZn/P25 confirm the adsorption of F₆₄PcZn on TiO₂ nanoparticles.

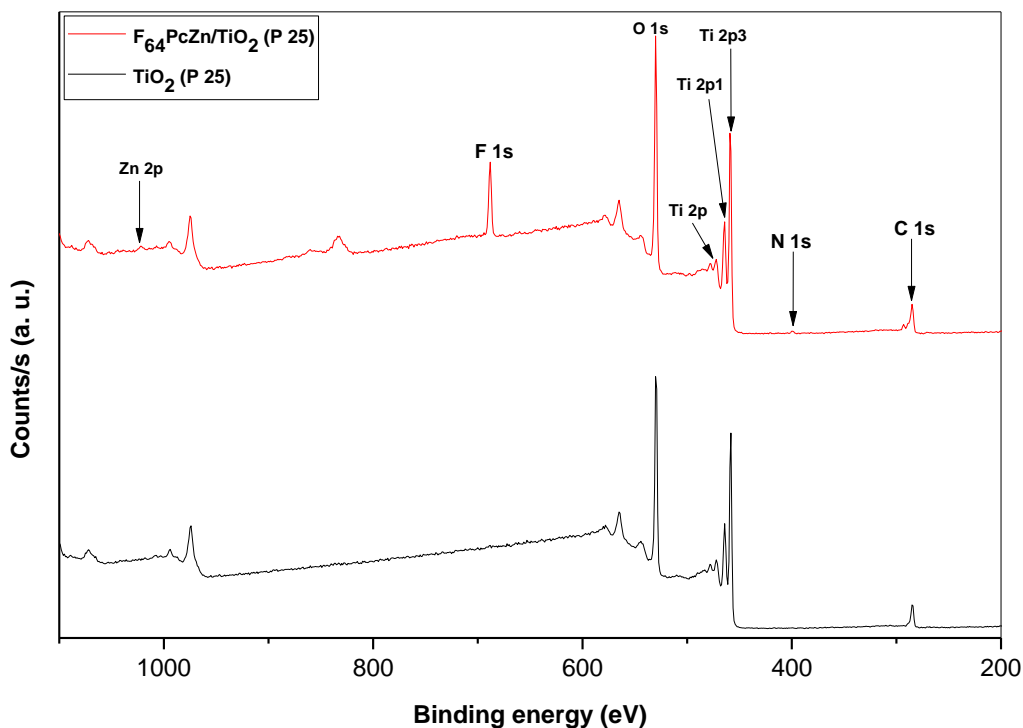


Figure 25. XP survey spectra for P25 and F₆₄PcZn/P25.

As shown in Table 6, the spin-orbit splitting of Ti 2p_{3/2} and Ti 2p_{1/2} are 5.73 and 5.64 eV for P25 and F₆₄PcZn/P25, respectively. The spin-orbit splitting varies with the chemical environment of Ti. It is understandable from Table 6 that the spin-orbit splitting is different for H₁₆PcZn/P25, F₁₆PcZn/P25 and F₆₄PcZn/P25 such as 6, 6.6, 5.64 eV. This change in spin-orbit splitting explicitly shows the change in chemical environment of Ti in TiO₂ due to the adsorption of the Pcs such as H₁₆PcZn, F₁₆PcZn and F₆₄PcZn on the surface.^{51,52}

Table 6. Core Level Binding Energies of Elements.

Elements	Binding Energy (eV)				
	TiO ₂	F ₆₄ PcZn/TiO ₂	F ₆₄ PcZn	F ₁₆ PcZn/TiO ₂	H ₁₆ PcZn/TiO ₂
Ti _{2p3/2}	458.64	458.97	-	457.76	458.73
Ti _{2p1/2}	464.37	464.61	-	464.36	464.73
Zn _{2p3/2}		1021.88	1022.47	1022.84	1021.73
Zn _{2p1/2}		1044.98	1045.61	1045.79	1044.74
O _{1s}	529.88	530.19	-	530.58	529.98
	531.72	532.04	-	533.34	531.49
	-	541.23	-	533.64	532.16
	-	-	-	535.69	-
N _{1s}	-	399.01	399.35	399.42	398.42
	-	400.91	400.8	400.87	400.19
	-	-	402.66	403.03	-
F _{1s}	-	688.5	688.68	688.57	-
	-	684.01	691.36	689.53	-
	-	-	-	690.97	-

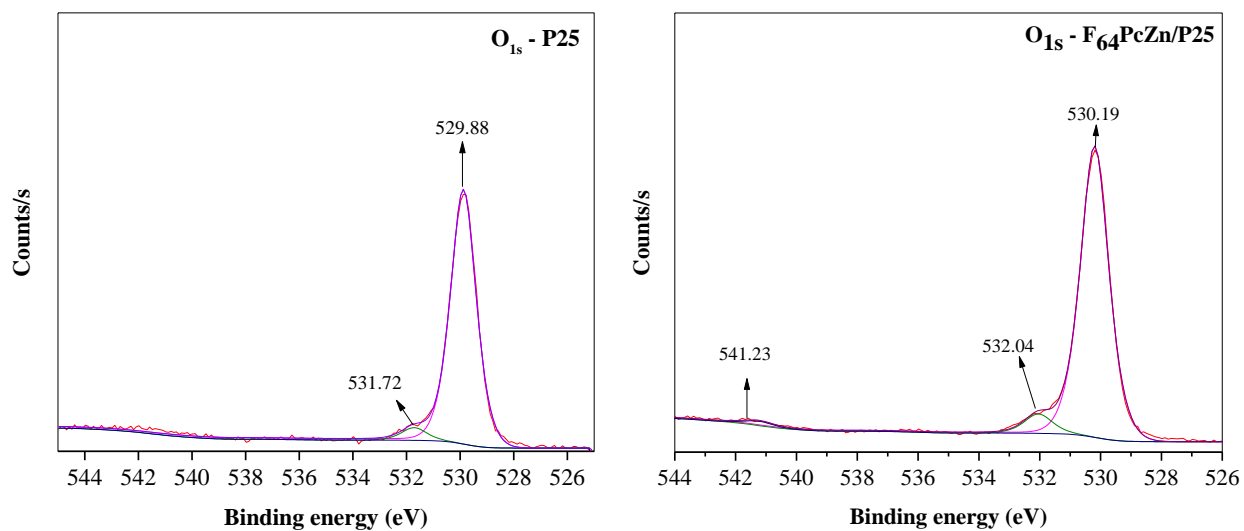


Figure 26. Deconvoluted O 1s spectra for P25 TiO_2 and $F_{64}PcZn/P25$.

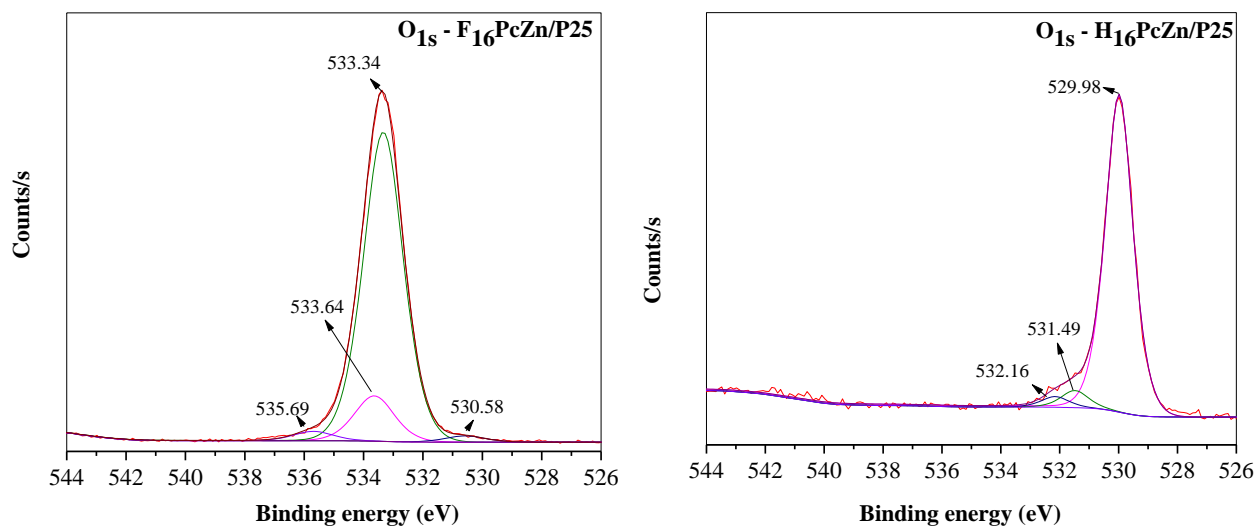


Figure 27. Deconvoluted O 1s spectra for $F_{16}PcZn/P25$ and $H_{16}PcZn/P25$.

Figure 26 depicts the O 1s spectra for TiO₂ and F₆₄PcZn/P25. The peak at 530 eV is due to the adsorbed oxygen from ambient environment. The peak at the BE of 532 eV with the FWHM of 1.1 eV is ascribed to the oxygen content of TiO₂. When F₆₄PcZn is deposited on P25, a new peak appeared at 541.2 eV in the O 1s spectrum at the higher energy side of the oxygen content peak. We can notice that the FWHM of O 1s peaks that correspond to adsorbed atmospheric oxygen and oxygen content of TiO₂ do not seem to change for both the samples P25 and F₆₄PcZn/P25. These observations suggest that the O 1s peak at higher BE is associated to the coordination of perfluorinated organic carbon in -CF₃ of F₆₄PcZn with the hydroxyl O of TiO₂.^{53,54}

Figure 27 displays the O 1s spectra for H₁₆PcZn/P25 and F₁₆PcZn/P25. These spectra are recorded to analyze the way H₁₆PcZn and F₁₆PcZn interacts with the hydroxyl O of TiO₂ in comparison to F₆₄PcZn. In the case of H₁₆PcZn/P25 the deconvoluted spectra depicts peaks at 529.98 and 531.49 eV that correspond to adsorbed oxygen from the atmosphere and the bulk oxygen of TiO₂, respectively. The peak at 532.16 is related to the interaction of organic carbon of H₁₆PcZn with the O of TiO₂ surface hydroxyl groups. If we look at the O 1s spectra for F₁₆PcZn/P25, the deconvolution of the high-resolution spectra gives rise a peak at 530.58 eV that correlates to the adsorbed oxygen and water from moisture in the atmosphere.⁵⁵ The peak at 533.34 eV is related to the oxygen content of P25 TiO₂. The peaks at higher binding energy values of 533.64 and 535.69 eV are assigned to the interaction of the O of surface hydroxyl groups of TiO₂ with the organic carbons without (C--O) and with fluorination (O--C-F).^{55,56} It can be noticed that the O 1s spectra show peaks at higher binding energy values for the interactions of organic C-C, C-F and C-F₃ in the increasing order of 533.64, 535.69 and 541.2 eV due to the higher electronegativity of fluorine atom.

The results from O 1s spectra concludes that F₆₄PcZn adsorbs via -CF₃ groups to the surface hydroxyl group of P25. Whereas H₁₆PcZn interacts with the surface hydroxyl group of P25 through -CH group and F₁₆PcZn adsorbs on P25 by means of -CH and -CF groups.

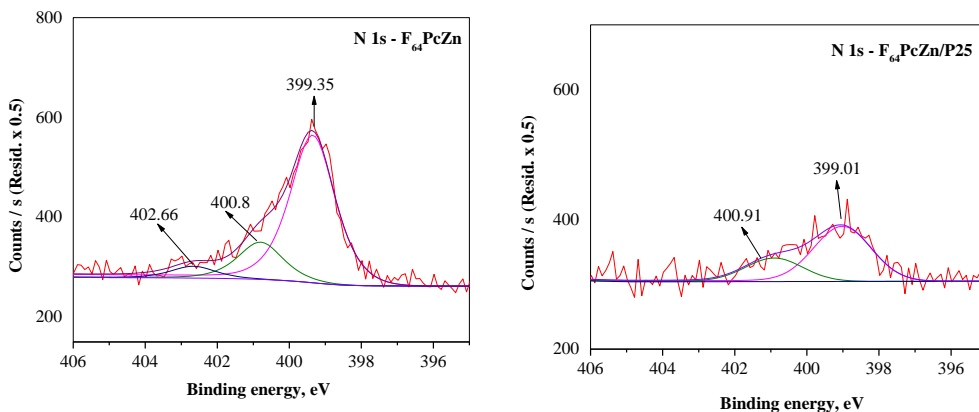


Figure 28. High resolution XPS spectra: N 1s spectra for F₆₄PcZn and F₆₄PcZn/P25.

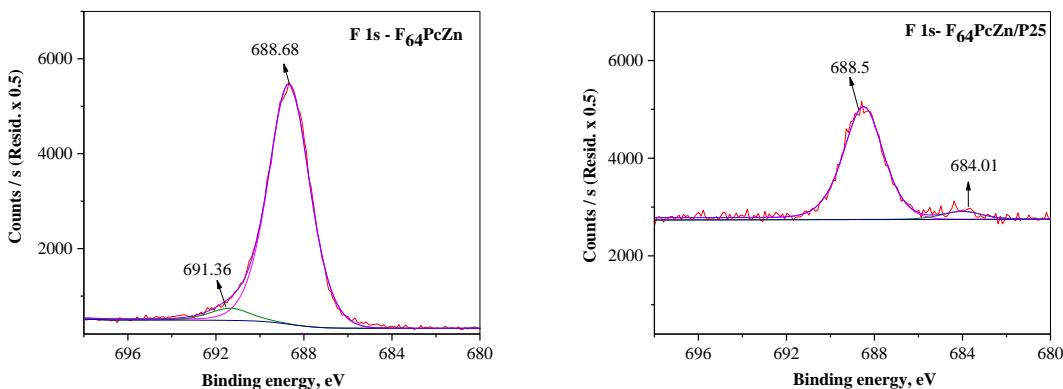


Figure 29. High resolution XPS spectra: F 1s spectra for P25 TiO₂ and F₆₄PcZn/P25.

The deconvolution of N 1s spectrum of F₆₄PcZn gives rise to three peaks at binding energies of 399.35, 400.8 and 402.66 eV corresponding to pyridyl N, pyridyl N associated with

the central metal atom Zn and pyrrolic N, respectively (Figure 24). N 1s peak that corresponds to the pyridyl N coordinated to the central metal atom Zn is observed at 400.91 eV for F₆₄PcZn/P25 (Figure 28). The slight broadening of full-width half maximum (FWHM) of this peak by 0.4 eV indicates the interaction of F₆₄PcZn with TiO₂ via central Zn atom. The change in the binding energy of pyridyl N bound to metal has been reported in literature as due to different chemical environments.⁵⁷ There is no much change in the F 1s spectra for -CF groups however the binding energy shifts to lower values by 7.4 eV for -CF₃ groups (Figure 29). Mitsuya and Sato⁵⁸ observed this kind of decrease in F 1s binding energy while investigating the chemisorption of perfluoroalkyl molecules such as 3-perfluorohexyl-1,2-epoxypropane (C₉H₅F₁₃O), perfluorodecanoic acid (C₁₀HF₁₉O₂), 2-(perfluorooctyl)ethanol (C₅H₁₀F₁₇O), 2-(perfluorohexyl)ethanol (F(CF₂)₆CH₂CH₂OH) and 2-(perfluorobutyl)ethanol (C₆H₅F₉O) onto Si (111) surfaces. Core peaks from long perfluoroalkyl chains shift to lower BE with increasing surface coverage. They concluded the shift as the relaxation of core electron levels derived from a close molecular packing in the adsorbate layer on the surface. Hence, we concluded the lower binding energy shift in F 1s peak corresponding to -CF₃ groups could be due to electron relaxation energy caused by the closely packed F₆₄PcZn on P25. It is important to notice this kind of BE shift is observed only for the -CF₃ groups and not for -CF groups of F₆₄PcZn.

It can be concluded from the XPS results that F₆₄PcZn adsorbed on P25 surface binds via the interaction between central Zn²⁺ metal atom and peripheral -CF₃ group of F₆₄PcZn with the O atom of TiO₂ surface hydroxyl group (Figure 30). Mathew *et al.* reported the interaction of TiO₂ surface hydroxyl O with the F atoms at the peripheral position of porphyrin containing an electron-donating diarylamino group at the meso-position and a strongly electron-withdrawing 4-carboxy-2,3,5,6-tetrafluorophenylethynyl anchoring group at the opposite meso-position (ZnPF).⁵⁹

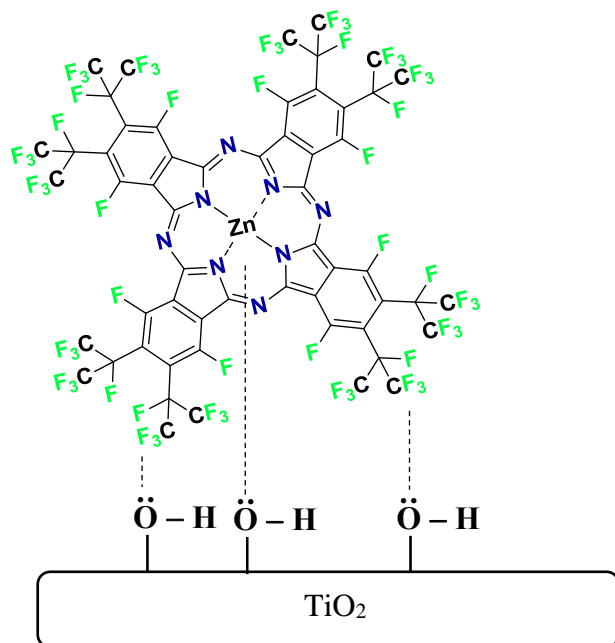


Figure 30. Proposed mode of interaction: F₆₄PcZn deposited on P25.

In our case, the central Zn²⁺ metal atom also interacts with TiO₂ surface in addition to -CF₃ group due to high Lewis acidity of Zn²⁺ because of the substitution of -CF₃ groups at the peripheral position of F₆₄PcZn. The Zn 2p_{3/2} and Zn 2p_{1/2} spin-orbit splitting (23.1 eV) corresponds to Zn²⁺ for all Pcs adsorbed on P25. A clear change in peak binding energy and full-width half maximum is observed for pyridyl N coordinated to central Zn²⁺ atom of F₆₄PcZn/P25 as compared to pure F₆₄PcZn. These observations lead to a conclusion the F₆₄PcZn binds with TiO₂ via -CF₃ group and central Zn²⁺ metal atom. This assumption is based on the XPS studies only. There may be several other techniques available to support this conclusion.

We observed interaction between -CH organic carbon of H₁₆PcZn and P25 for H₁₆PcZn/P25 catalyst. The XPS results for F₁₆PcZn/P25 shows binding of -CH and -CF organic

carbons of F₁₆PcZn on P25. More detailed study is required to reach a conclusion on adsorption for these catalysts, H₁₆PcZn/P25 and F₁₆PcZn/P25.

3.3.19. Characterization of F₆₄PcZn/P25 Before and After Photocatalytic Reactions using X-Ray Diffraction (XRD) Analysis

XRD patterns are similar for both P25 and F₆₄PcZn/P25 as depicted in Figure 31. Because of high intensity peaks of TiO₂ the related peaks for phthalocyanine are not observed. But, the XRD data was used to calculate the primary particle size of catalyst particles before and after photoreaction (Table 7).⁶⁰ The primary particle size calculated for P25 before photocatalytic reaction is 19.8 nm. F₆₄PcZn/P25 particle size is slightly higher, 20.1 nm. The reported primary particle size for P25 by Evonik Degussa is 21 nm. A slight decrease in the particle sizes determined after the photocatalytic reactions could be related to the mechanical stirring effect, because the kinetic studies are performed under constant stirring. This means more uncoated P25 surface may be exposed at the end than the initial stages of the photoreaction.

Table 7. Particle Sizes Determined from XRD Patterns of P25 and F₆₄PcZn/P25.

S. No.	Catalysts	Size (nm)
1	P25	19.8
2	P25 - after 3 runs	18.2
3	F ₆₄ PcZn/P25	20.1
4	F ₆₄ PcZn/P25 - after 3 runs	19.8

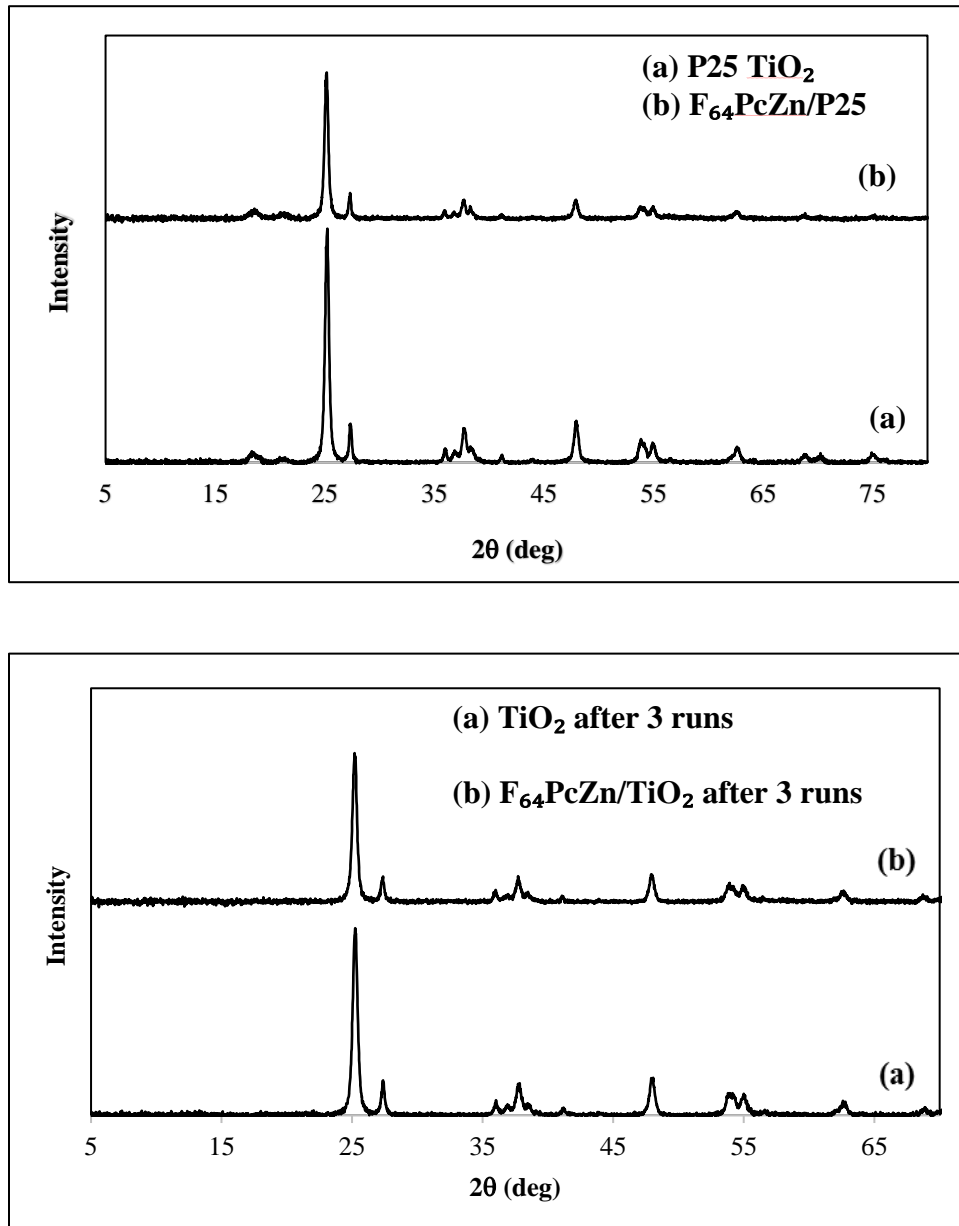


Figure 31. XRD patterns for P25 and F₆₄PcZn/P25 before and after 3 runs of MO photodegradation reactions. One run lasts for 10 h.

3.3.20. NMR Analysis of RhB Photodegradation Products

To identify the degradation products $^1\text{H-NMR}$ spectra was recorded before and after 10 h of photodegradation process for RhB catalyzed by P25, $\text{F}_{64}\text{PcZn/P25}$. Figure 32 shows the $^1\text{H-NMR}$ proton assignments in the chemical structure of RhB.

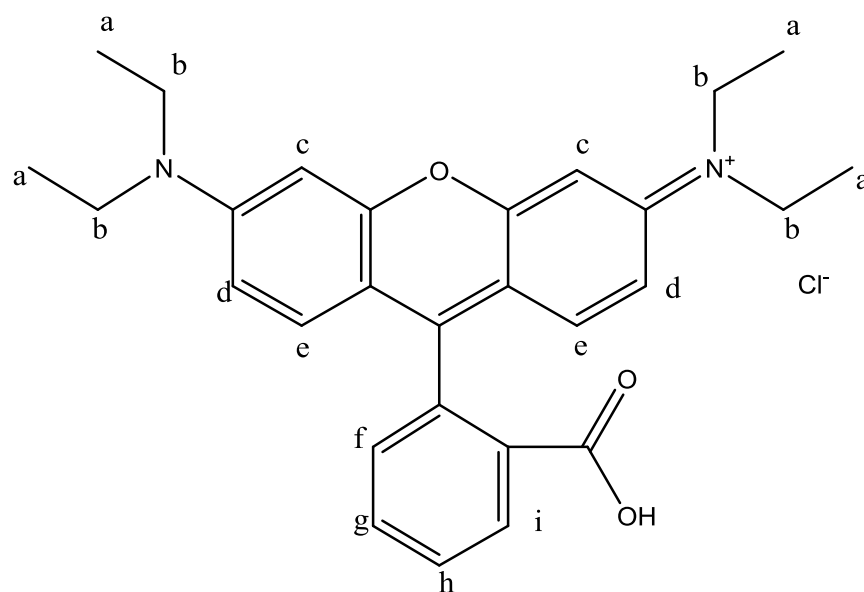


Figure 32. Proton assignments in the molecular structure of RhB.

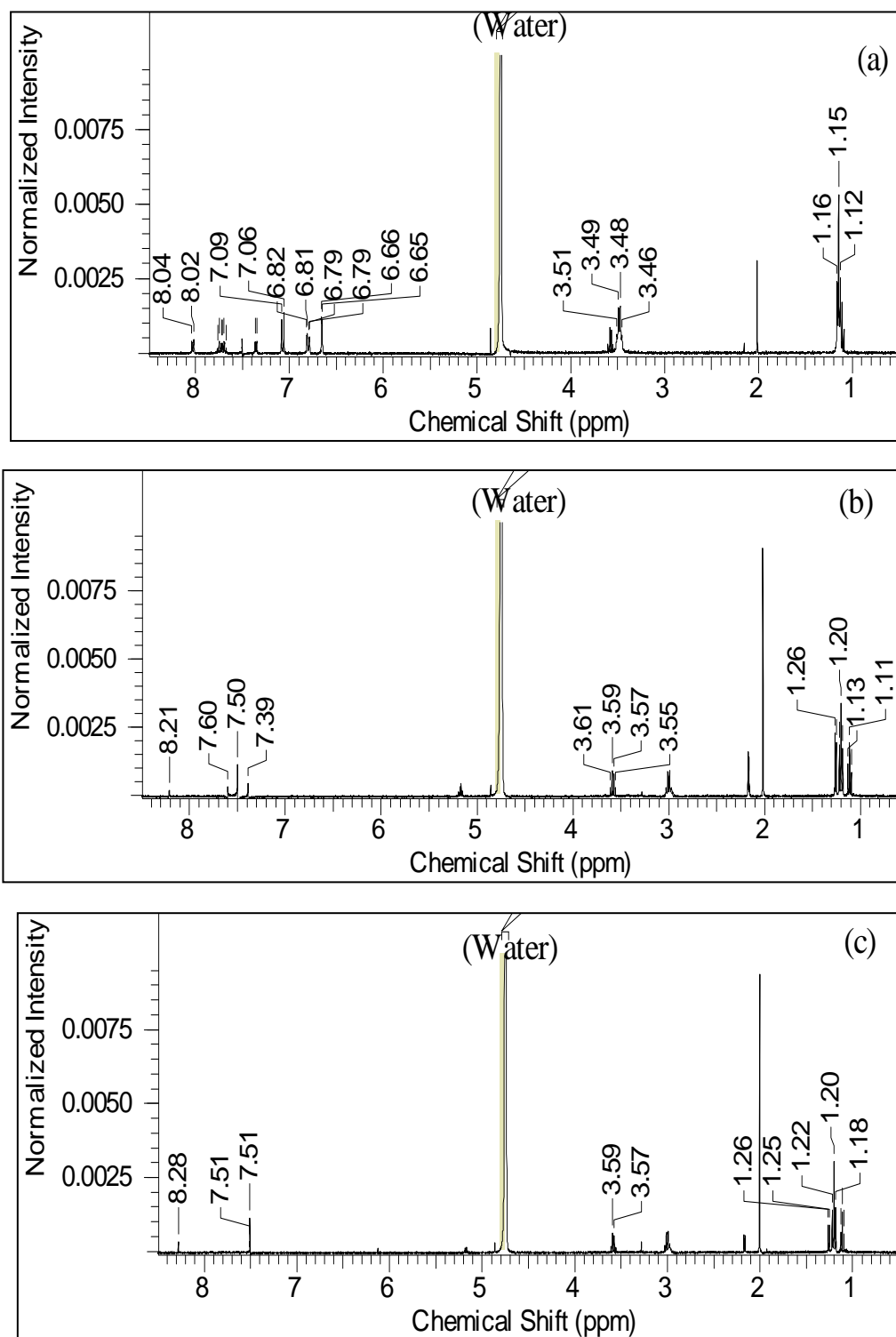


Figure 33. $^1\text{H-NMR}$ spectra for RhB in D_2O . (a) before photoreaction, (b) photodegradation catalyzed by P25 and (c) photodegradation reaction catalyzed by $\text{F}_{64}\text{PcZn/P25}$.

Figure 33a shows the $^1\text{H-NMR}$ spectrum for RhB before photoreaction which include the alkyl group protons around 1 to 3 ppm and the aromatic protons at a greater chemical shift, from 6.6 to 8.5 ppm.⁶¹ Figure 33b exhibits $^1\text{H-NMR}$ spectrum for the degradation products formed after 10 h reaction catalyzed by P25. The peaks related to CH_3 and CH_2 of *N*-diethyl groups are observed around 1.08 to 1.14 ppm and 3.55 to 3.61 ppm, respectively. The integration of these peaks revealed a 50 % reduction in the intensities for the peaks assigned to $-\text{CH}_3$ group of *N*-diethyl fragment. The protons assigned as c, d and e disappeared suggesting the photooxidation and destruction of the aromatic ring consisting of these protons into smaller molecular fragments.⁶² The peaks related to the sites f, g and i are still observed but these peaks showed up as singlet instead of either doublet or triplet. This result reveal loss of these protons due to photooxidation reaction. It can be concluded from the results the aromatic ring structure is destructed, the appearance of f, g and i proton peaks suggest benzoic acid might be one of the degradation products.

After the photodegradation of RhB catalyzed by $\text{F}_{64}\text{PcZn/P25}$ (Figure 33c), the relative peak intensity for CH_3 (1.09-1.11 ppm) and CH_2 (3.57-3.59) groups in *N*-diethyl fragment rapidly decreased. The peak integration reveals 88% reduction in the *N*-diethyl fragment which suggest *N*-deethylation is the predominant pathway of RhB photodegradation catalyzed by $\text{F}_{64}\text{PcZn/P25}$. This result is supported by the blue shift of absorbance maxima in the UV-Vis spectra. The peaks correspond to aromatic protons disappeared except the ones for g and i. There are other new peaks appeared at lower field suggest the formation of molecular fragments from the degradation of aromatic ring structure of RhB.

3.3.21. HPLC and LC/MS Analysis of Photodegradation Products of RhB Catalyzed by P25 and F₆₄PcZn/P25

Figure 34 displays the HPLC chromatograms for RhB photodegradation products formed after 0, 2, 4, 6, 8 and 10 hours of photoreactions catalyzed by P25 and F₆₄PcZn/P25. The comparison of relative peak areas for the produced degradation products catalyzed by P25 and F₆₄PcZn/P25 (Figure 35) suggest the degradation pathways may be different for these catalysts which is discussed in detail as follows. The chromatogram pattern of RhB before photoreaction, that is at 0 h in Figure 34, shows a major peak at retention time of 10.6 min with the highest peak area.⁶³ The analogous MS data corresponds to 0 h look similar for both P25 and F₆₄PcZn/P25 as displayed in the Figures 36 and 37 showing a major peak at the *m/z* value of 443.5 which is related to RhB without Cl⁻ ion.^{63,64} This molecular structure is given in Table 8, S. No. 1. Literature review on the photodegradation products of RhB suggests the initial formation of four major components related to *N*-deethylation of RhB which are shown as A, B, C and D in Figure 35 corresponding to *N,N*-diethyl-*N*-ethyl-rhodamine (A), *N,N*-diethyl-rhodamine (B), *N*-ethyl-rhodamine (C) and rhodamine (D).⁶³⁻⁶⁵ The molecular structures of A, B, C and D are illustrated in Table 8, S. No. 2 to 5. It has been reported that this kind of *N*-deethylation is a predominant process when RhB adsorbed on the photocatalyst via its -N[⊕] of diethyl amino group. A negatively charged photocatalyst surface facilitates the adsorption of -N[⊕] of diethyl amino group of RhB while the carboxylate group, -COO⁻, of RhB will interact with the photocatalyst if the surface charge is positive.

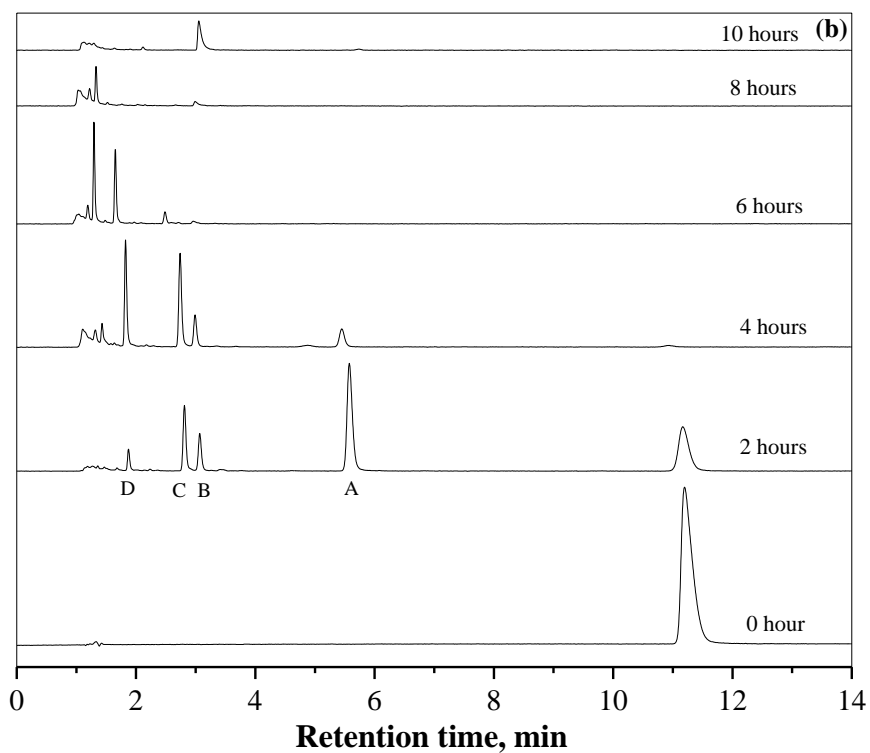
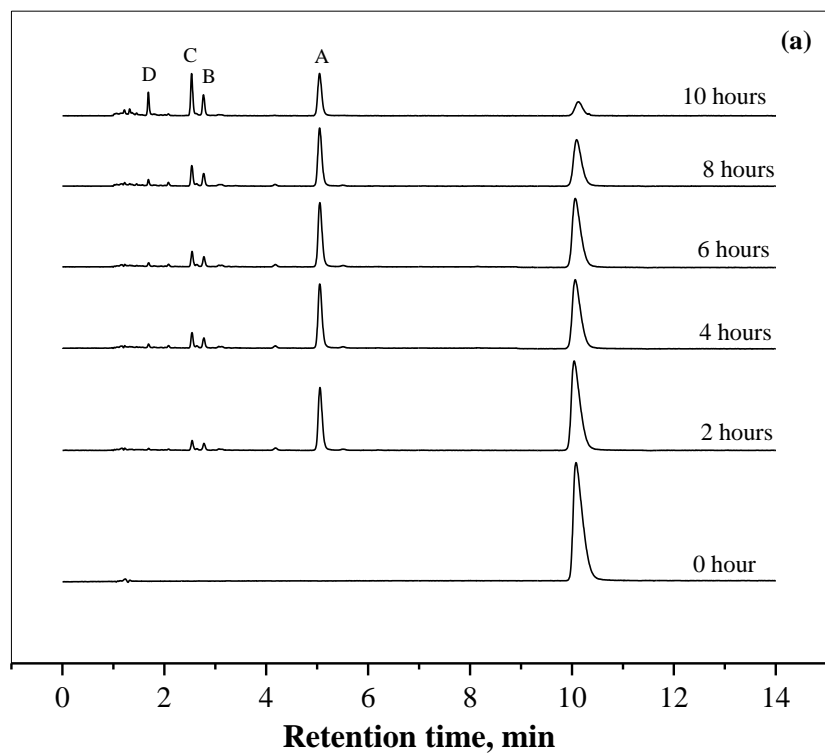


Figure 34. Comparison of HPLC chromatograms obtained for the degradation products of RhB catalyzed by (a) P25 and (b) F₆₄PcZn/P25.

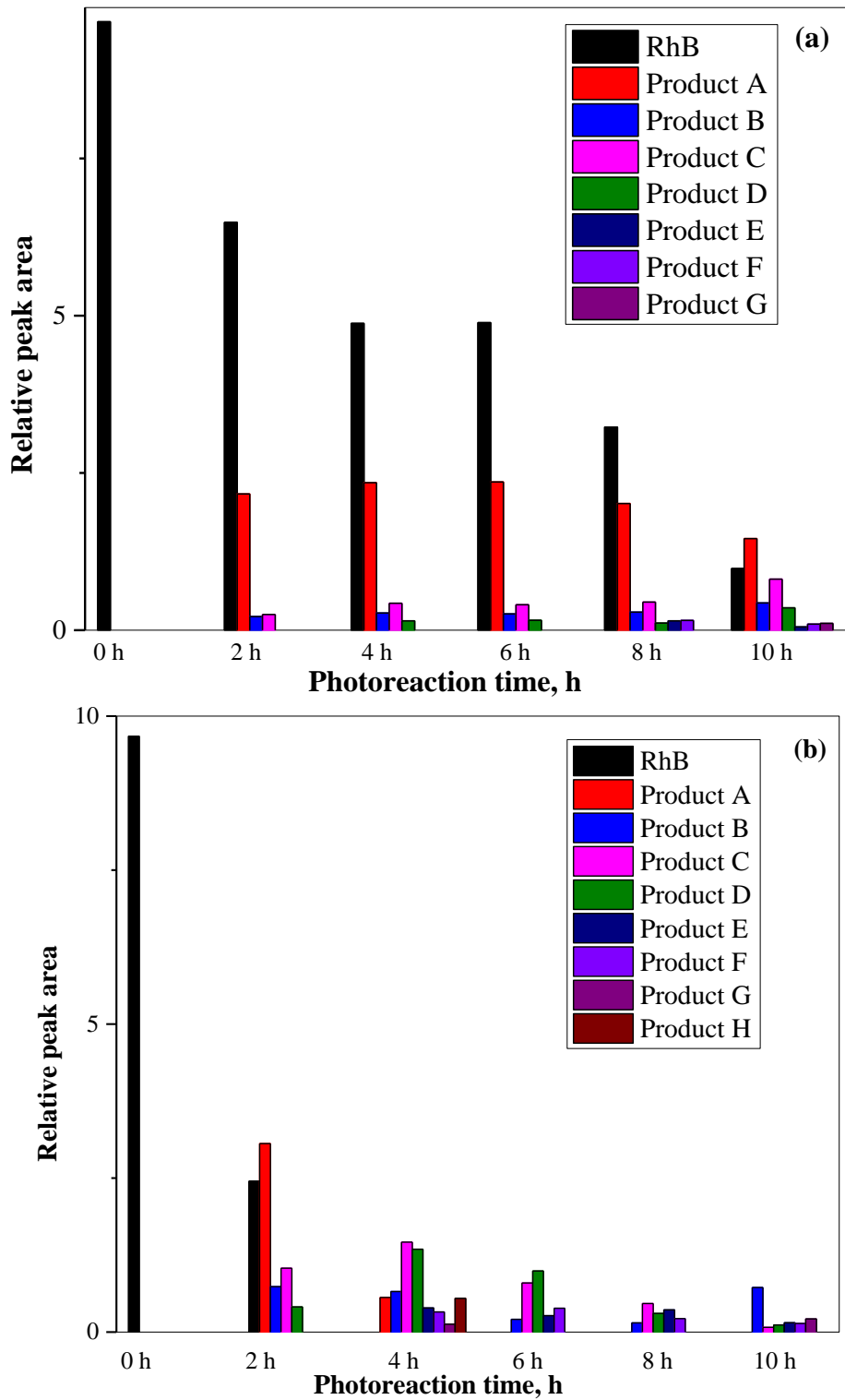


Figure 35. Relative peak area determined from the above displayed HPLC chromatograms;

(a) P25 and (b) F₆₄PcZn/P25.

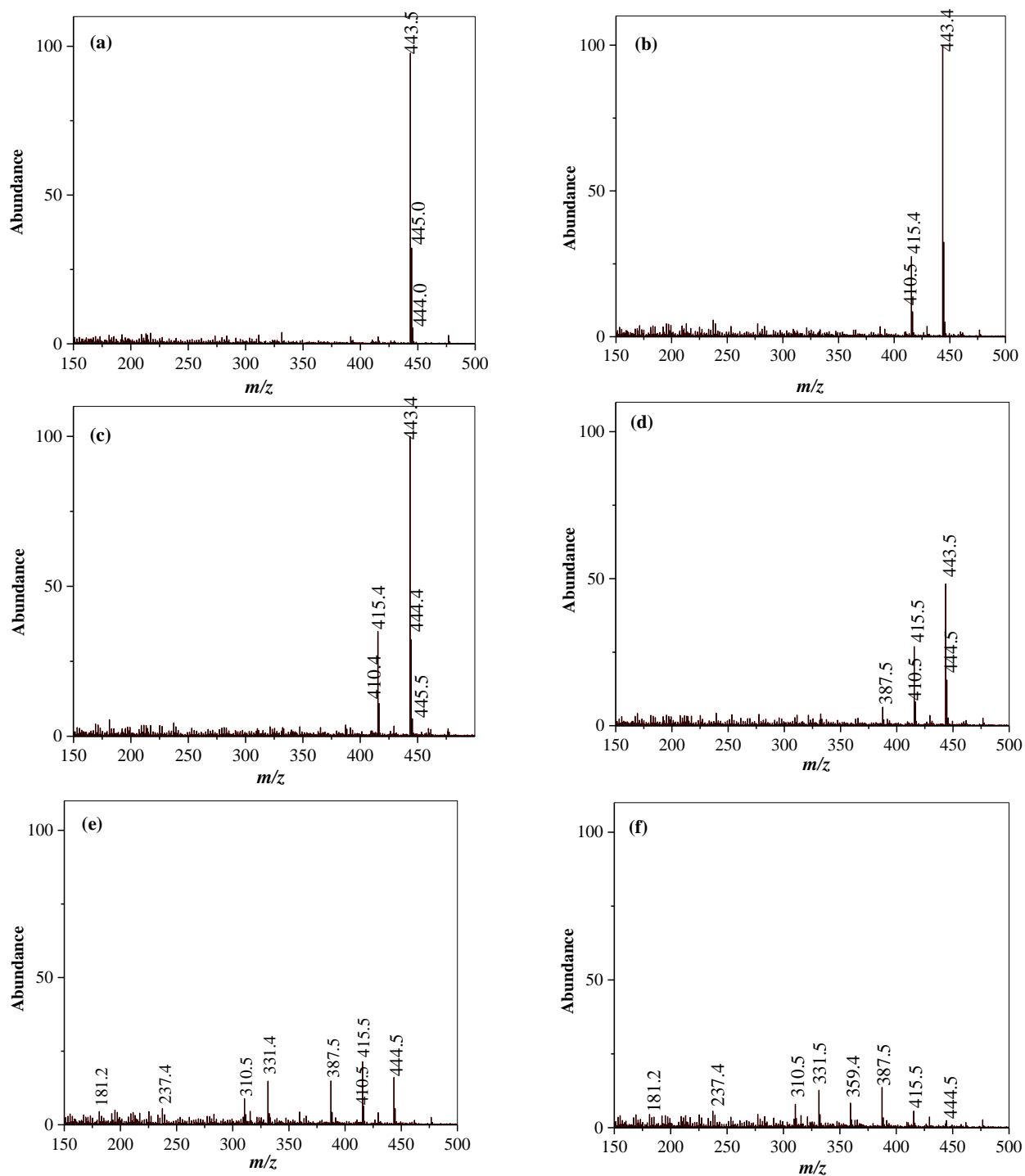


Figure 36. MS results obtained for the degradation products formed after (a-f) 0, 2, 4, 6, 8 and 10 hours of RhB photodegradation for P25.

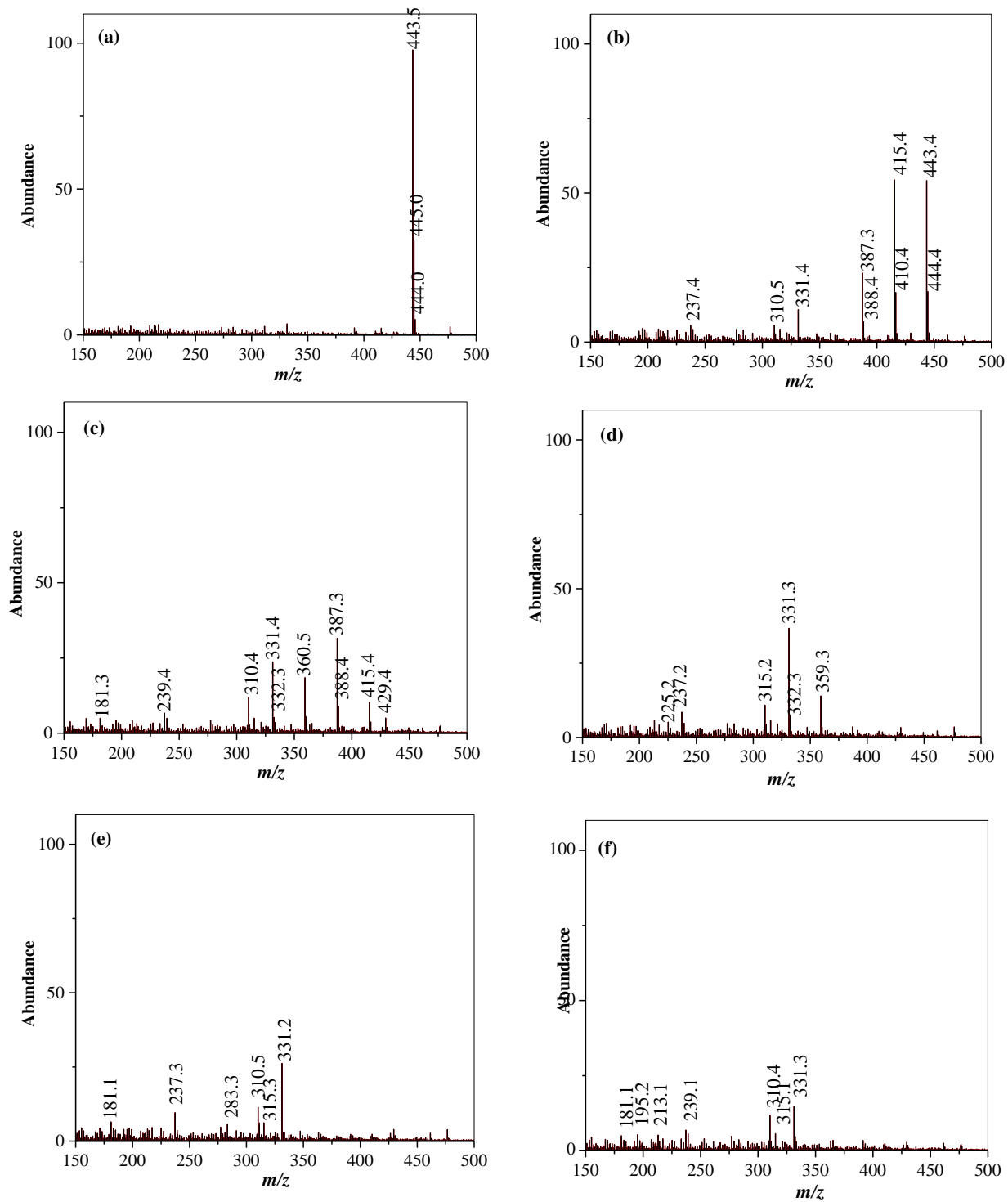
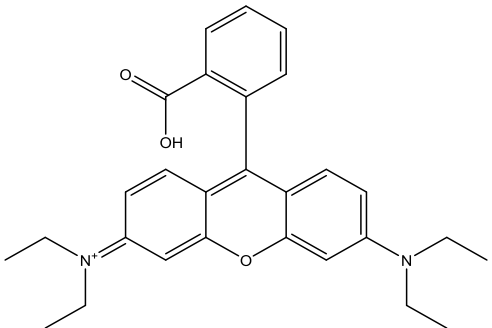
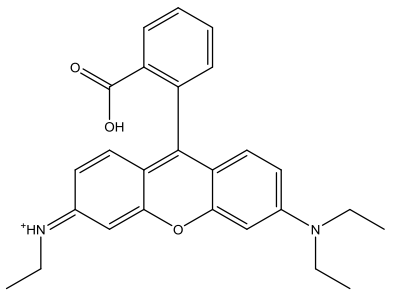
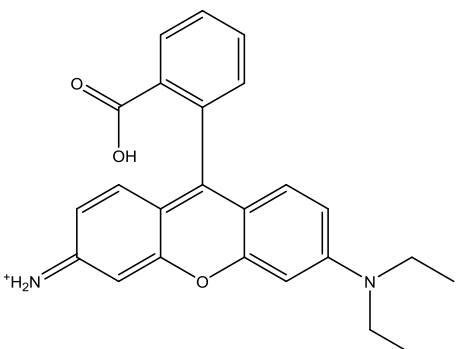
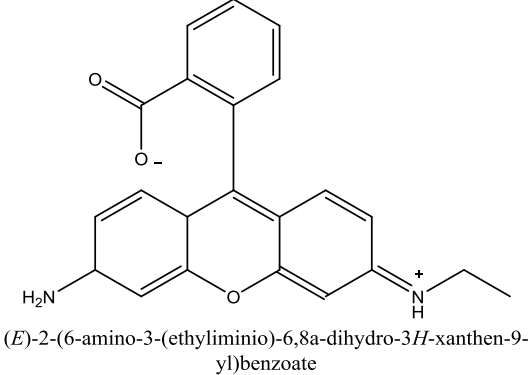
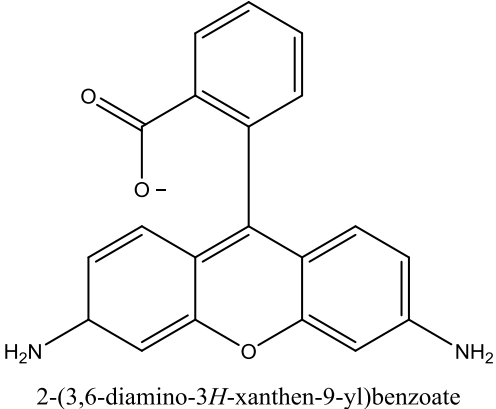


Figure 37. MS for the degradation products formed after (a-f) 0, 2, 4, 6, 8 and 10 hours of RhB photodegradation catalyzed by $F_{64}PcZn/P25$.

Table 8. Products of *N*-deethylation of RhB (1). *N, N*-diethyl-*N*-ethyl-rhodamine (2), *N, N*-diethyl-rhodamine (3), *N*-ethyl-rhodamine (4) and Rhodamine (5)

S. No.	<i>m/z</i> (amu)	Molecular Structure
1 ⁶³⁻⁶⁵	443.23 (100.0%) 444.24 (30.3%) 445.24 (2.7%)	 <p><i>N</i>-(9-(2-carboxyphenyl)-6-(diethylamino)-3<i>H</i>-xanthen-3-ylidene)-<i>N</i>-ethylethanaminium</p>
2 ⁶³⁻⁶⁵	415.20 (100.0%) 416.20 (28.1%) 417.21 (2.7%)	 <p>(<i>Z</i>)-<i>N</i>-(9-(2-carboxyphenyl)-6-(diethylamino)-3<i>H</i>-xanthen-3-ylidene)ethanaminium</p> <p><i>N, N</i>-diethyl-<i>N</i>-ethyl-rhodamine (Product A)</p>
3 ⁶³⁻⁶⁵	387.17 (100.0%) 388.17 (26.0%) 389.18 (2.7%)	 <p>9-(2-carboxyphenyl)-6-(diethylamino)-3<i>H</i>-xanthen-3-iminium</p> <p><i>N, N</i>-diethyl-rhodamine (Product B)</p>

S. No.	<i>m/z</i> (amu)	Molecular Structure
4 ⁶³⁻⁶⁵	360.15 (100.0%)	 <p>(<i>E</i>)-2-(6-amino-3-(ethyliminio)-6,8a-dihydro-3<i>H</i>-xanthen-9-yl)benzoate</p> <p><i>N</i>-ethyl-rhodamine (Product C)</p>
	361.15 (23.8%)	
	362.15 (2.7%)	
5 ⁶³⁻⁶⁵	331.11 (100.0%)	 <p>2-(3,6-diamino-3<i>H</i>-xanthen-9-yl)benzoate</p> <p>Rhodamine (Product D)</p>
	332.11 (21.6%)	
	333.12 (2.2%)	

HPLC data illustrated in Figure 34 shows higher photocatalytic efficiency of hybrid catalyst F₆₄PcZn/P25 against bare P25. Though P25 can degrade RhB, the peak related to RhB at 10.6 min can be recognized even after 10 h of photoreaction. The peak appeared with *m/z* of 444.5 atomic mass unit (amu) until 10 h in the MS data supports this observation (Figure 36). Among the *N*-deethylated products, a major amount of product A, *N,N*-diethyl-*N*-ethyl-rhodamine, at *m/z*

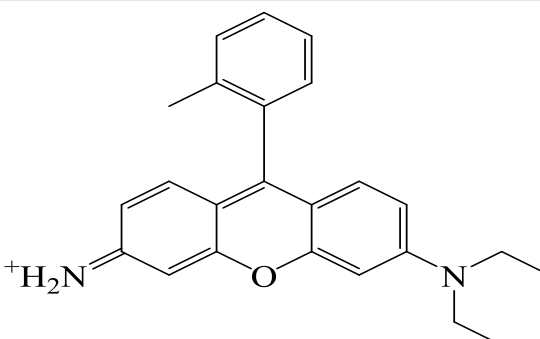
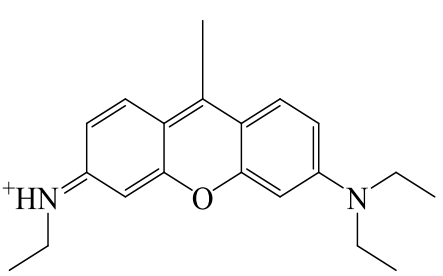
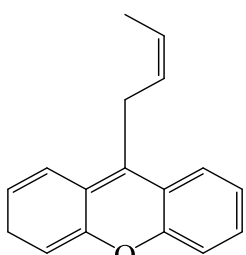
value of 415.4 is formed while the other *N*-deethylated products are produced in minimum quantities.

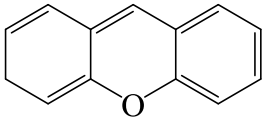
For example, after 2 h 27% of *N*-deethylated products are formed in which product A constitutes 22%. After 4 and 6 h a small increase in the percentage, *i.e.*, 33% of *N*-deethylated products is observed. In these cases, products B, C and D are formed in smaller amounts (Figure 35) related to *N,N*-diethyl-rhodamine, *N*-ethyl-rhodamine and rhodamine. The percentage of *N*-deethylated products decreased to 31% and 29% while many other smaller molecular fragments are formed at the lower retention times of 8 and 10 h as shown in the chromatogram. The corresponding MS data supports the above results. From the MS data the molecular fragments formed are constructed using ChemDraw Professional 16.0 software and are listed in Tables 8-10. Citations are included for these structures wherever possible. The structure of products A, B, C and D are shown in Table 8. The percentages of products formed stated above are determined from the peak areas of chromatograms using Origin software. From the type of photodegradation products formed we can assume the mode of adsorption of RhB on the surface of P25 catalyst and the following degradation process under visible light irradiation. Table 9 depicts the photodegraded molecular fragments of RhB, if it is attacked at the -COO^- group because of the electrostatic interaction between -COO^- and the positively charged surface of P25. We must remember that the zeta potential of P25 determined in de-ionized water is positive (Table 3). MS results (Figure 36) indicate the formation of products E, F, G and H when P25 is a photocatalyst.⁶³⁻
⁶⁶ These intermediates formed due to the destruction of RhB indicate the adsorption of this dye molecule via -COO^- group and the attack of $\text{h}^\oplus / \text{OH}^\bullet$ radicals on the nearby groups. Figure 38 depicts the plausible mechanism of adsorption of RhB on P25 and attack of $\text{h}^\oplus / \text{OH}^\bullet$ radicals on the nearest -COO^- group and the nearby *N*-diethyl group.

The chemical structure of products E, F, G and H formed confirm the attack of $h^{\oplus} / OH^{\bullet}$ radicals on the COO^{-} group of RhB. In addition, as displayed in Figure 39, the $h^{\oplus} / OH^{\bullet}$ radicals can attack the nearby *N*-diethyl group. This describes the formation of product A as one of the major destruction components (Figures 34a and 35a). In the above Table 9 product F is missing; the molecular structure of this product is given in Table 10. Only *N*-deethylation process can lead to the formation of product F. The absence of product F in the MS spectra when P25 is a catalyst proves the initial attack of $h^{\oplus} / OH^{\bullet}$ radicals on the COO^{-} group and the nearby *N*-diethyl group.

The above mentioned RhB degradation pathway with the addition of TiO_2 catalyst is also supported by the 1H -NMR spectrum of RhB after 10 h photodegradation catalyzed by P25 displayed in Figure 33b. The photodegradation products of RhB catalyzed by P25 revealed there is only 50% reduction of *N*-diethyl hydrogens after 10 h of reaction while many aromatic hydrogens disappeared suggesting the preferential destruction of the aromatic chromophore. The formation of (*z*)-9-(but-2-en-1-yl)-3H-xanthene could be attributed to the destruction of chromophore that occurs at the early stages because of the way of RhB adsorption on P25. The byproduct 3H-xanthene related to m/z 181.2 also confirmed the chromophore destruction.^{67,68}

Table 9. Molecular Structure of the Photodegradation Products Formed due to the Removal of Carboxylic Acid Functional Group.

S. No.	<i>m/z</i> (amu)	Molecular Structure
1 ⁶³⁻⁶⁶	357.20 (100%)	 <p>6-(diethylamino)-9-(<i>o</i>-tolyl)-3<i>H</i>-xanthen-3-iminium (Product E)</p>
	358.20 (26%)	
	359.20 (2.7 %)	
2 ⁶³⁻⁶⁶	309.20 (100.0%)	 <p><i>N</i>-(9-(2-carboxyphenyl)-6-(diethylamino)-3<i>H</i>-xanthen-3-ylidene)-<i>N</i>-ethylethanaminium (Product G)</p>
	310.20 (22.7%)	
	311.20 (2.5%)	
3 ⁶³⁻⁶⁸	236.12 (100%)	 <p>(<i>Z</i>)-9-(but-2-en-1-yl)-3<i>H</i>-xanthene (Product H)</p>
	237.12 (18.4%)	
	238.13 (1.6%)	

S. No.	<i>m/z</i> (amu)	Molecular Structure
4 ⁶³⁻⁶⁸	182.07 (100%) 183.08 (14.1%)	 <p>3<i>H</i>-xanthene</p> <p>(Product I)</p>

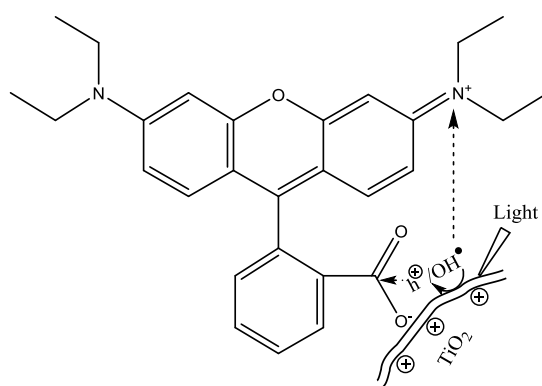


Figure 38. Mode of RhB adsorption on TiO₂ and cleavage of nearby bonds by h[⊕] / OH[•] radicals.

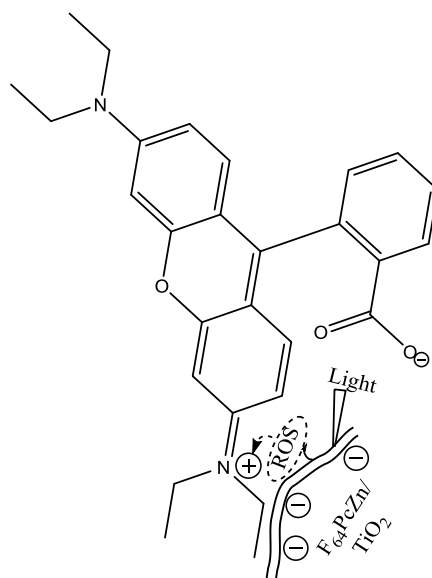


Figure 39. *N*-deethylation of RhB dominates for F₆₄PcZn/P25 photocatalyst.

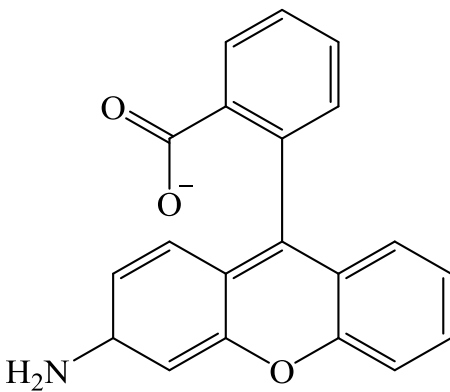
HPLC chromatograms displayed in Figure 34b and the corresponding peak areas plotted in Figure 35b for RhB photodegradation catalyzed by F₆₄PcZn/P25 suggest the occurrence of initial *N*-deethylation process before the destruction of chromophore. In contrast to P25, the peak related to RhB at retention time around 11.2 min drastically decreased indicating the higher photocatalytic efficiency of F₆₄PcZn/P25 than bare P25. These results are further supported by the UV-Vis spectral observations. After 2 h of photoreaction 54% of *N*-deethylated products are formed as oppose to 27% formed in the presence of P25. As the photoreaction proceeds the intensity of the RhB major peak is reduced in the HPLC profile, thus the corresponding *m/z* 443.5 peak in the MS data also decreased.

The peak area plotted in Figure 35b shows the formation of A, B, C and D after 2h of photoreaction onwards. The related MS spectra depicted in the Figure 34 reveal *m/z* values of 415.4, 387.3, 360.5 and 331.4 corresponding to *N*-deethylated structures A, B, C and D (Table 8, S. No. 2-5).⁶³⁻⁶⁵ In the MS spectra the peak related to C is not obvious after 2 h of photoreaction but it is visible after 4 h. A *m/z* peak at 315.2 starts appearing from 6 h until 10 h. The corresponding molecular structure predicted is shown in Table 10. As mentioned above this product did not appear as one of the degradation products when P25 is a catalyst. The appearance of 2-(3-amino-3H-xanthen-9-yl)benzoate confirms the mode of RhB adsorption and the following degradation pathway is different for the hybrid catalyst F₆₄PcZn/P25. Several other weak peaks with *m/z* 310.5 and 237.4 related to deamination of D (2-(3H-xanthen-9-yl)benzoate) and ring opening of chromophore ((*z*)-9-(but-2-en-1-yl)-3H-xanthene) are also appeared (Table 9).⁶³⁻⁶⁸

The hypsochromic (blue) shift observed in the UV-Vis absorption spectra (Figure 5b) associated to the *N*-deethylation process of RHB catalyzed by F₆₄PcZn/P25 is confirmed by the HPLC and MS results. After 6 h the peak for product A disappeared, the related MS shows *m/z* at

359.3, 331.3, 315.2 and 237.2. The associated structures are listed in the Table 9 and 10. The m/z values obtained for 10 h reveal a weak signal at 331.3. The disappearance of other peaks with higher m/z values suggest the completion of *N*-deethylation process. The m/z peaks at 239.1, 195.2 and 181.1 associated to smaller molecular fragments⁶⁶⁻⁶⁸ supports the UV-Vis spectral observation in which the peak maxima at 556 nm drastically decreased and new peaks start appearing at lower wavelengths.

Table 10. Confirmation of Predominant *N*-deethylation of RhB catalyzed by F₆₄PcZn/P25.

S. No.	m/z (amu)	Molecular Structure
1 ⁶³⁻⁶⁶	316.10 (100.0%)	
	317.10 (21.6%)	
	318.10 (2.2%)	
		2-(3-amino-3 <i>H</i> -xanthen-9-yl)benzoate (Product F)

A major difference in the ratio of *N*-deethylated products formed can be realized in the presence of F₆₄PcZn/P25 as compared to P25. The peak areas determined from the chromatograms clearly indicate the greater ratio of *N*-deethylated products formed in the presence of F₆₄PcZn/P25 (Figure 35b). The percentage of *N*-deethylated products A to D gradually decreased from 54% to

39%, 22% and 9% after every two hours of photoreaction. Several smaller molecular fragments are appeared as the photodegradation process duration is extended. The production of higher concentrations of *N*-deethylated products and their gradual decrease can be related to the blue shift along with the decrease in the absorbance of peak maxima in UV-Vis spectral measurements.

The preferential *N*-deethylation process of RhB can be related to the mode of its adsorption on the hybrid photocatalyst. From the zeta potential measurements reported in section 3.3.9. it can be seen a positive value for P25 in de-ionized water and a shift to lower values when F₆₄PcZn is being added, due to the fluorine groups at the peripheral positions of the Pc. This means P25 has negatively charged F₆₄PcZn deposited at the surface. Therefore, the positively charged ethylamine group of RhB preferred to adsorb on the surface of F₆₄PcZn/P25 in contrast to P25 where the surface is positively charged hence the carboxylic acid group of RhB has preferential adsorption.^{63,66} Since the photogenerated radicals attack the nearest groups, it initially attacks the auxochrome instead of chromophore of RhB when catalyzed by F₆₄PcZn/P25. Previously, even the XPS analyses suggest the adsorption of F₆₄PcZn on P25 which renders F₆₄PcZn/P25 more negative that leads to a different mode of adsorption of RhB as shown in Figure 40. Thus, the photodegradation pathway is different for RhB catalyzed by F₆₄PcZn/P25 as compared to P25.

3.3.22. Photostability of F₆₄PcZn Deposited on TiO₂

As a heterogeneous photocatalyst, F₆₄PcZn/TiO₂ can be separated by simple filtration and used for several number of photocatalytic reactions. Figure 40 shows the results of reusing F₆₄PcZn/P25 and F₆₄PcZn/P90 to catalyze MO photodegradation process for five consecutive cycles in which each cycle lasts for 10 h. From the results, it is obvious that the photocatalyst did

not show any loss in photoactivity after 5 consecutive cycles which confirms the photochemical stability of F₆₄PcZn deposited on TiO₂.

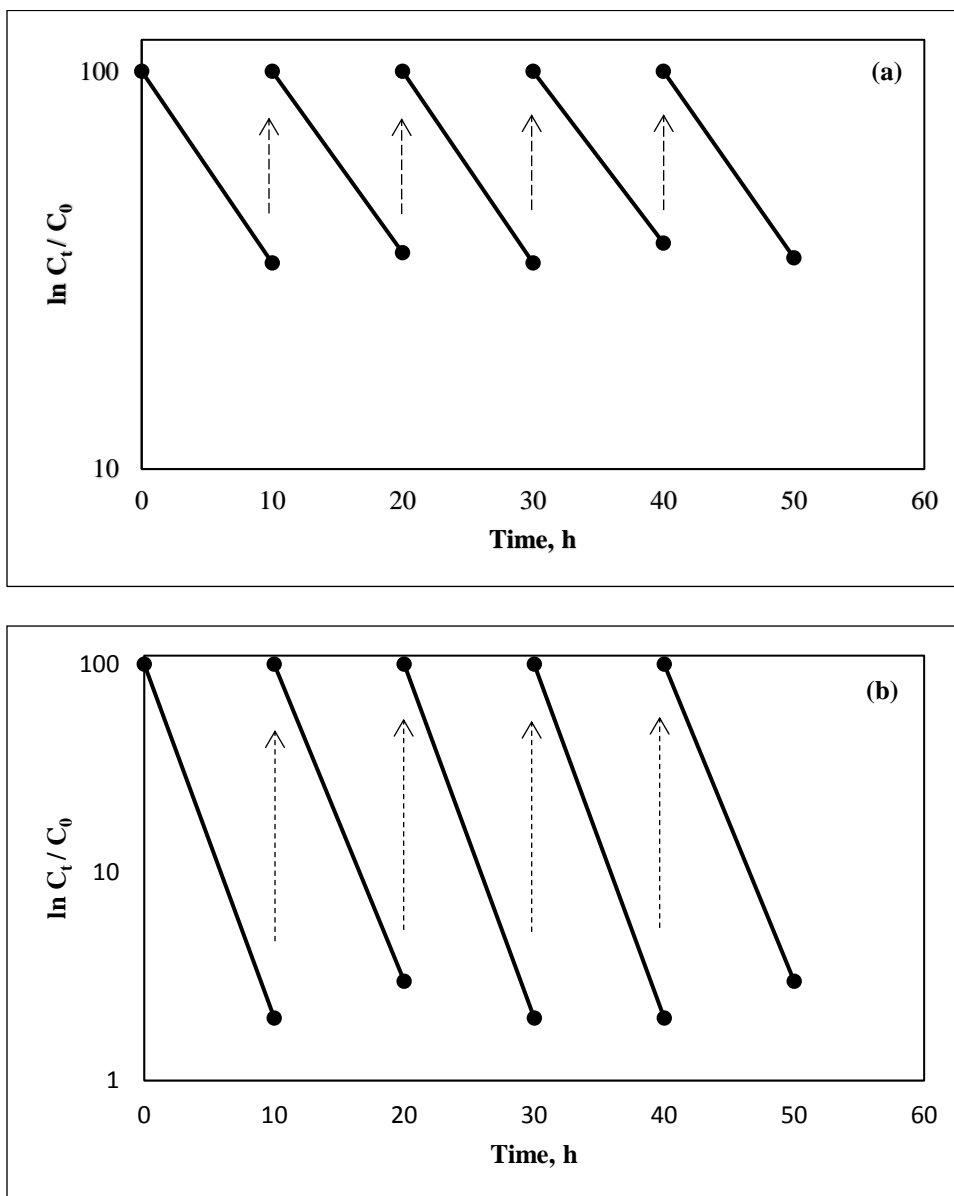


Figure 40. Five recycles of (a) F₆₄PcZn/P25 and (b) F₆₄PcZn/P90 for MO photodegradation reactions.

To confirm the photostability, F₆₄PcZn has been extracted from F₆₄PcZn/P25 using acetone that is used for 5 consecutive cycles of photoreactions. Comparison of UV-Vis spectra for unused and used catalyst suggests that there is no change in the Q band and B band intensities. Figure 41 displays the UV-Vis spectra of F₆₄PcZn deposited on P25 extracted back before and after 5 consecutive cycles of photoreactions. It can be found from the figure bleaching did not occur, revealing the high photostability of F₆₄PcZn in aggressive radical environment because of the -CF₃ groups substituted in the peripheral positions.

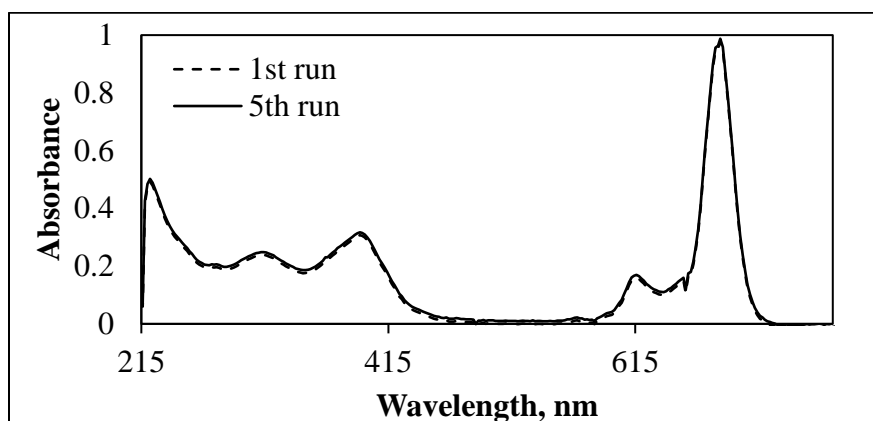


Figure 41. UV-Vis spectra of F₆₄PcZn extracted from F₆₄PcZn/P25 before and after 5 consecutive cycles of photoreactions.

3.4. CONCLUSIONS

F₆₄PcZn deposited on TiO₂ solid supports such as P25 and P90 effectively degrade organic pollutants in water under visible light irradiation. Kinetic plots suggest that the reaction rate follows first order. The particle size plays a vital role in deciding the efficiency of photocatalyst. Reaction rate increases with decreasing particle size due to interaction of more number of pollutant

molecules with particles having larger specific surface area. As a result, F₆₄PcZn/P90 is more efficient in degrading organic pollutants like MO and RhB than F₆₄PcZn/P25. Fluorescence intensity measurements suggest the catalyst is more efficient at an optimum amount of F₆₄PcZn deposited on TiO₂. By increasing the F₆₄PcZn deposition amount initially increases the fluorescence but after certain point fluorescence peak broadening and splitting occurs because of agglomeration of F₆₄PcZn. F₆₄PcZn readily adsorbs on the positively charged surface of P25 and P90, electronegativity of fluorine plays a significant role in the adsorption of perfluoroalkyl perfluorinated phthalocyanine zinc, F₆₄PcZn. Moreover, XPS analyses depict the adsorption of F₆₄PcZn on P25 via interactions between the peripheral -CF₃ group in addition to central Zn²⁺ metal of F₆₄PcZn and the surface hydroxyl group of TiO₂. Kinetic study did not show any synergism in the reaction rate for F₆₄PcZn/P25 and F₆₄PcZn/P90. Fluorescence intensity suggests that there is no electron transfer occurs between the excited state F₆₄PcZn HOMO energy level and the TiO₂ conduction band. Thus, photocatalytic activity obtained is a simple addition of efficiency provided by TiO₂ and F₆₄PcZn. TOC and ¹H-NMR analyses of MO and RhB solutions after photoderadation catalyzed by F₆₄PcZn/P25 under visible light irradiation confirms the degradation of azo and xanthene dyes into smaller molecular fragments. The photocatalytic efficiency of F₆₄PcZn/P25 irradiated with UV, visible and red lights suggest that the hybrid catalyst is able to absorb a wide range of light spectrum. Thus, making this catalyst useful in decontaminating organic pollutants in water resources even in remote areas utilizing only sunlight and air. UV-Vis spectra indicate a hypsochromic shift of RhB chromophore peak when catalyzed by F₆₄PcZn/P25 but not for P25. HPLC and LC/MS analyses of degradation products indicate that the RhB degradation pathway is different for these catalysts. Because of the variation in the surface charges of F₆₄PcZn/P25 and bare P25, as a zwitterion different functional groups of RhB interacts with the

catalysts. Our investigation suggests the hybrid catalyst is very effective in degrading organic pollutants without any significant pH change. This finding is important because making environment acidic while degrading organic compounds will affect the aqua life. F₆₄PcZn/P25 and F₆₄PcZn/P90 are photochemically stable and reusable as a catalyst for several times to decontaminate water from organic pollutants. F₆₄PcZn is more robust compared to commercial Pcs such as H₁₆PcZn and F₁₆PcZn. The stability test under illumination of UV radiation suggests F₆₄PcZn deposited on P25 will not be bleached for a longer run when used under sunlight. When using F₆₄PcZn/P25 and F₆₄PcZn/P90 catalysts, hydroxyl radicals are primarily involved in the degradation process of organic pollutants. Photostability tests proved the catalysts F₆₄PcZn/P25 and F₆₄PcZn/P90 are photochemically stable in this aggressive radical environment. Thus, a stable solid state photocatalyst has been produced which can efficiently photodegrade organic pollutants in water using renewable resources.

REFERENCES

- (1) Tan, L. L.; Ong, W. J.; Chai, S. P.; Mohamed, A. R. *Chem. Commun.* **2014**, *50*, 6923-6926.
- (2) New and Future Developments in Catalysis: Catalysis by Nanoparticles, Editor: Suib, S. L. Publisher: Newnes, **2013**, 212-244.
- (3) Nazarkovsky, M.A.; Gunko, V.M.; Wojcik, G.; Czech, B.; Sobieszek, A.; Zieba, J. S.; Janusz, W.; Skwarek, E. *Chem. Phy. & Technol. Surf.*, **2014**, *5*, 421-437.
- (4) Apopei, P.; Catrinescu, C.; Teodosiu, C.; Royer, S. *Appl. Cataly. B: Environ.*, *160–161*, **2014**, 374–382.

- (5) Doudrick, K.; Monzon, O; Mangonon, A; Hristovski, K.; Westerhoff, P. *J. Environ. Eng.* © ASCE. **2012**, Aug, 852-861.
- (6) Guo, Z.; Chen, B.; Mu, Zhang, J.; Zhang, M.; Zhang, Z.; Wang, J.; Zhang, X.; Sun, Y.; Shao, C.; Liu, Y. *J Hazard. Mater.* 219 - 220, **2012**, 156 - 163.
- (7) Sevim, A. M. *J. Organometallic Chem.* **2017**, 832, 18-26.
- (8) Mesgari, Z.; Gharagozlou, M.; Khosravi, A.; Gharanjig, K. *Spectrochim. Acta Part A: Mole. & Biomole. Spectros.* **2012**, 92, 148-153.
- (9) Iliev, V.; Tomova, D. *Cataly. Commun.* **2002**, 3, 287–292.
- (10) Sun, Q.; Xu, Y. *J. Phys. Chem. C* **2009**, 113, 12387–12394.
- (11) Bench, B. A.; Beveridge, A.; Sharman, W. M.; Diebold, G. J.; Lier, J. E.; Gorun, S. M. *Angew. Chem. Int. Ed.* **2002**, 41, 748-750.
- (12) Lingfors, D.; Volotinen, T. *Opt. Express.* **2013**, 21, A642-A655.
- (13) Ramakrishnan, R.; Sudha, D. J.; Reena, V.L. *RSC Adv.* **2012**, 2, 6228-6236.
- (14) J. Gu, S. Kan, Q. Shen, J. Kan, *Int. J. Electrochem. Sci.* **2014**, 9, 6858 - 6869.
- (15) Organic Spectroscopy: Principles and Applications, Author: Jag Mohan, CRC Press, 2004, ISBN 0849339529, 9780849339523, Page 168.
- (16) Pirzada, B. M.; Mehraj, O.; Mir, N. A.; Khan, M. Z.; Sabir, S. *New J. Chem.* **2015**, 39, 7153-7163.
- (17) Hao, W. C.; Zheng, S. K.; Wang, C.; Wang, T. M. *J. Mater. Sci. Lett.* **2002**, 21, 1627-1629.
- (18) Jang, H. D.; Kim, S. K.; Kim, S. J. *J. Nanopart. Res.* **2001**, 3, 141-147.
- (19) Lin, H.; Huang, C.P.; Li, W.; Ni, C.; Shah, S. I.; Tseng, Y. *Appl. Cataly. B: Environ.* **2006**, 68, 1–11.
- (20) Wilhelm, P.; Stephan, D. *J. Photochem. & Photobiol. A: Chem.* **2007**, 185, 19-25.

- (21) Wu, J. M.; Zhang, T. W. *J. Photochem. & Photobiol. A: Chem.* **2004**, *162*, 171-177.
- (22) Wang, G.; Xu, L.; Zhang, J.; Yin, T.; Han, D. *Int. J. Photoener.* **2012**, *Article ID 265760*, Maira, 1-9.
- (23) Tan, L.; Ong, W.; Chai, S.; Mohamed, A. R. *Chem. Commun.* **2014**, *50*, 6923-6926.
- (24) Hosseinnia, A.; Keyanpour-Rad, M.; Pazouki, M. *World Appl. Sci. J.* **2010**, *8*, 1327-1332.
- (25) Maira, A. J.; Yeung, K. L.; Lee, C. Y.; Yue, P. L.; Chan, C. K. *J. Cat.* **2000**, *192*, 185-196.
- (26) Maira, A. J.; Yeung, K. L.; Soria, J.; Coronado, J. M.; Belver, C.; Lee, C. Y.; Augugliaro, *Appl. Cat. B: Environ.* **2001**, *29*, 327-336.
- (27) El-Nahass, M. M., Farag, A. M., Abd El-Rahman, K. F., Darwish, A. A. A., *Opt. Laser Technol.* **2005**, *37*, 513-523.
- (28) Gomez, A. R.; Sanchez-Hernandez, C. M.; Fleitman-Levin, I.; Arenas-Alatorre, J.; Alonso-Huitron, J. C.; Vergara, M. E. S. *Materials*, **2014**, *7*, 6585-6603.
- (29) Beveridge, A. C.; Bench, B. A.; Gorun, S. M.; Diebold, G. J. *J. Phys. Chem. A* **2003**, *107*, 5138-5143.
- (30) Liu, W.; Wang, Y.; Gui, L.; Tang, Y. *Langmuir*, **1999**, *15*, 2130-2133.
- (31) Moons, H.; Loas, A.; Gorun, S. M.; Doorslaer, S. V. *Dalton Trans.*, **2014**, *43*, 14942-14948.
- (32) Basic characteristics of aerosil fumed silica, *Technical Bull. Fine Part. 11*, **2006**, TB11-1-(7/2006).
- (33) Wilhelm, P.; Stephan, D. *J. Photochem. Photobio. A: Chem.* **2007**, *185*, 19-25.
- (34) Shimbo, M.; Furukawa, K.; Tanzawa, K.; Higuchi, T. *IEEE Transactions on Electron Dev.* **1988**, *35*, 124-128.
- (35) Biffinger, J. C.; Kim, H. W.; DiMagno, S. G. *ChemBioChem*, **2004**, *5*, 622-627.

- (36) Cheng, F.; Zhao, J.; Hidaka, H. *Int. J. Photoenergy*, **2003**, *5*, 209-217.
- (37) Yu, K.; Yang, S.; He, H.; Cheng, S.; Gu, C.; Ju, Y. *J. Phys. Chem. A*, **2009**, *113*, 10024-10032.
- (38) Iliev, V.; Tomova, D.; Rakovsky, S. *Desalination*, **2010**, *260*, 101-106.
- (39) Li, Y.; Zhang, H.; Guo, Z.; Han, J.; Zhao, X.; Zhao, Q.; Kim, S. *Langmuir*, **2008**, *24*, 8351-8357.
- (40) Mele, G.; Lopez, E.; Palmisano, L.; Dyrda, G.; Slota, R. *J. Phys. Chem. C* **2007**, *111*, 6581-6588.
- (41) Wang, Z.; Mao, W.; Chen, H.; Zhang, F.; Fan, X.; Qian, G. *Cataly. Commun.* **2006**, *7*, 518-522.
- (42) Dvoranova, D.; Barbierikova, Z.; Brezova, V. *Molecules* **2014**, *19*, 17279-17304.
- (43) Batista, P. S.; Souza, D. R.; Maximiano, R. V.; Neto, N.; Machado, A. *J. Mater. Sci. Res.* **2013**, *2*, 82-95.
- (44) Minero, C.; Mariella, G.; Maurino, V.; Vione, D.; Pelizzetti, E. *Langmuir*, **2000**, *16*, 8964-8972.
- (45) Ljubas, D.; Smoljanic, G.; Juretic, H. *J. Environ. Mgmt.* **2015**, *161*, 83-91.
- (46) Vahatalo, A. V. *Encyclopedia of Inland Waters*, Publisher: Elsevier BV, **2009**, 761-773.
- (47) Snow, A. W. Phthalocyanine aggregation. *The Porphyrin Handbook*, Kadish, K. M.; Guillard, R.; Smith, K. M., Eds., Academic Press: New York, **2002**, *17*, 129– 173.
- (48) El-Nahass, M. M., Farag, A. M., Abd El-Rahman, K. F., Darwish, A. A. A., *Opt. Laser Technol.* **2005**, *37*, 513–523.
- (49) Kotiaho, A.; Lahtinen, R.; Efimov, A.; Metsberg, H.; Sariola, E.; Lehtivuori, H.; Tkachenko, N. V.; Lemmetyinen, H. *J. Phys. Chem. C*, **2010**, *114*, 162-168.

- (50) Kadish, K. M.; Smith, K. M. Guilard, R. The Porphyrin Handbook, *Phthalocyanines: Properties and Materials*, Academic Press, 17, 2003.
- (51) Yu, Y.; Wang, J.; Li, W.; Zheng, W.; Cao, Y. *Cryst. Eng. Comm.* **2015**, 17, 5074-5080.
- (52) Rodriguez, J. A.; Hrbek, J. *J. Chem. Phys.* **1992**, 12, 9427-9439.
- (53) Spadavecchia, J.; Methivier, C.; Landoulsi, J.; Pradier, C. M. *ChemPhysChem*, **2013**, 14, 2462-2469.
- (54) Knut, R.; Lindblad, R.; Grachev, S.; Faou, J. Y.; Gorgoi, M.; Rensmo, H.; Sondergard, E.; Karis, O. *J. Appl. Phys.* **2014**, 115, 043714-1-043714-7.
- (55) Desimoni, E.; Brunetti, B.; *Chemosensors*, **2015**, 3, 70-117.
- (56) Yun, S. M.; Kim, J. W.; Jung, M. J.; Nho, Y. C.; Kang, P. H.; Lee, Y. S. *Carbon Letters*, **2007**, 8, 292-298.
- (57) Arechederra, R. L.; Artyushkova, K.; Atanassov, P.; Minter, S. D. *Appl. Mater. & Interfac.* **2010**, 2, 3295-3302.
- (58) Mitsuya, M.; Sato, N. *Langmuir*, **1999**, 15, 2099-2102.
- (59) Mathew, S.; Iijima, H.; Toude, Y.; Umeyama, T.; Matano, Y.; Ito, S.; Tkachenko, N. V.; Lemmetyinen, H.; Imahori, H. *J. Phys. Chem. C*, **2011**, 115, 14415-14424.
- (60) Dai, S.; Wu, Y.; Sakai, T.; Du, Z.; Sakai, H.; Abe, M. *Nanoscale Resear. Lett.* **2010**, 5, 1829-1835.
- (61) Cherian, S.; Wamser, C. *J. Phys. Chem. B* **2000**, 104, 3624-3629.
- (62) Jing-yi, L. I.; Wan-hong, M. A.; Peng-xiang, L. E. I.; Jin-cai, Z. *J. Environ. Sci.* **2007**, 19, 892-896.
- (63) Chen, F.; Zhao, J.; Hidaka, H. *Int. J. Photoener.* **2003**, 5, 209-217.
- (64) Sabatini, F.; Giugliano, R.; Degano, I. *Microchem. J.* **2018**, 140, 114-122.

- (65) Zhang, Z.; Wen, X.; Deng, K.; Zhang, B.; Lv, K.; Sun, J. *Catal. Sci. Technol.* **2013**, *3*, 1415-1422.
- (66) Yu, K.; Yang, S.; He, H.; Sun, C.; Gu, C.; Ju, Y. *J. Phys. Chem. A* **2009**, *113*, 10024-10032.
- (67) Liu, T.; Wang, L.; Lu, X.; Fan, J.; Cai, X.; Gao, B.; Miao, R.; Wang, J.; Lv, Y. *RSC Adv.* **2017**, *7*, 12292-12300.
- (68) Natarajan, T. S.; Thomas, M.; Natarajan, K.; Bajaj, H. C.; Tayade, R. J. *Chem. Eng. J.* **2011**, *169*, 126-134.

SUPPLEMENTARY MATERIAL

ABSTRACT

We investigated the potential of using wide band-gap particles such as SiO₂ and TiO₂ as supports for perfluoroalkyl perfluoro phthalocyanine, F₆₄PcZn. Moving forward, we want to pursue substrates with narrow band-gap energy in the assumption of establishing orbital coupling as well as synergistic photocatalytic activity. Hence, we chose NiO particles as supporting substrate for F₆₄PcZn. The photodegradation and fluorescence experimental results suggest fast quenching of F₆₄PcZn excited state when deposited on NiO. Further characterization of the hybrid F₆₄PcZn/NiO is required to understand the fast quenching of F₆₄PcZn excited state deposited on NiO. Therefore, this work is included as a supplementary material in the Thesis.

In addition to using micro to nano size particles, we examined polymer membranes namely polytetrafluoroethylene (PTFE), polyethersulfone (PES) and polypropylene (PP) as supports for F₆₄PcZn. Initially, we examined the catalytic efficiency of F₆₄PcZn/polymer membrane prepared using a simple dip coating method. To improve the adhesion of F₆₄PcZn on the membrane surface, we functionalized the PP membrane via acid treatment. Even though the results suggested a better adhesion of F₆₄PcZn on the functionalized PP membrane, additional characterization is required to understand the mode of adsorption of F₆₄PcZn on the membrane surface. Hence, the work on F₆₄PcZn/polymer membrane is also added as a supplementary material in this Thesis.

Chapter 4. NiO as a Supporting Matrix for Perfluoroalkyl

Perfluoro Phthalocyanine

4.1. INTRODUCTION

In the Chapters 2 and 3 we evaluated SiO₂ and TiO₂ nanoparticles as supporting matrices for F₆₄PcZn. In continuation to look for a solid-state support that can successfully establish orbital coupling and electron communication with F₆₄PcZn, we examined NiO as a support for F₆₄PcZn. NiO is a *p*-type semiconductor with bandgap energy of 3.9 eV *i.e.* 317 nm.^{1,2} NiO was deposited on semiconductor surfaces to act as a reduction site.³ Recently, H₁₆PcCo was deposited on NiO and characterized using photoluminescence spectra for detecting possible orbital coupling. Fluorescence quenching is observed for H₁₆PcCo/NiO, the authors claimed an orbital coupling between H₁₆PcCo and NiO lead to the quenching of fluorescence.⁴ In the current study, we investigated F₆₄PcZn/NiO to obtain synergistic photocatalytic effect under visible light irradiation through establishing orbital coupling between the matrix and the Pc.

4.2. MATERIALS AND METHODS

The perfluoroalkyl perfluorinated phthalocyanines with Cu and Zn central metal atoms (F₆₄PcCu and F₆₄PcZn) were synthesized by the members of our research group using an already reported method⁵ and provided for this investigation. NiO was purchased from Sigma-Aldrich, USA. To prepare the hybrid catalyst, F₆₄PcZn was dissolved in ethanol and NiO was added to it.

This mixture was roto evaporated to get a dry $F_{64}PcZn/NiO$ powder. The hybrid catalyst thus obtained was dried at 100 °C for 6 hours and then used for photocatalytic reactions. The same procedure was followed to synthesize $H_{16}PcZn/NiO$, $F_{16}PcZn/NiO$ and $F_{64}PcCu/NiO$. Photodegradation reactions of methyl orange (MO) catalyzed by $F_{64}PcZn/NiO$, $H_{16}PcZn/NiO$, $F_{16}PcZn/NiO$ and $F_{64}PcCu/NiO$ were performed under visible light irradiation. A tungsten halogen lamp was used as a visible light source. Figure 1a displays the light spectrum of tungsten halogen lamp. The wavelengths of its emission spectra are in the range of 400 to 700 nm as reported by the manufacturer. As mentioned previously in the Chapter 3.3.5, a small portion of UVA light in the range of 320 - 400 nm is included in the emission spectra of the tungsten halogen lamp. The UVA light intensity was determined using a light meter as 0.87 mW/cm^2 . The ratio of catalyst added to MO was maintained constant for all the reactions at 0.01:0.1 mM. The change in MO concentration during photodegradation reaction was followed using UV-Vis spectral measurements (Perkin Elmer, USA). Fluorescence emission spectra were recorded for the hybrid catalysts from 660 to 850 nm after excitation at 650 nm using a Spex model Fluoromax-3 spectrofluorometer.

4.3. RESULTS AND DISCUSSION

Figure 1b demonstrates the kinetics of MO photodegradation reaction follow first-order for $H_{16}PcZn/NiO$ and $F_{16}PcZn/NiO$. The corresponding reaction rates (k) are listed in Table 1. MO did not degrade when catalyzed by NiO, $F_{64}PcZn/NiO$ and $F_{64}PcCu/NiO$ under visible light irradiation. A small amount of MO photodegradation is noted for the reactions catalyzed by $H_{16}PcZn/NiO$ and $F_{16}PcZn/NiO$, with the reaction rates of 0.0026 and 0.0041 h^{-1} . However, the data for $H_{16}PcZn/NiO$ is noisy.

Since NiO can only absorb longer wavelength UV light, we are not able to see any photocatalytic activity under visible light illumination. To understand the zero degradation reaction rates for MO catalyzed by F₆₄PcZn/NiO and F₆₄PcCu/NiO, fluorescence measurements are performed. As displayed in Figure 2, a low fluorescence intensity is observed for all the Pcs deposited on NiO. The fluorescence intensities obtained at the wavelength of 710 nm for H₁₆PcZn/NiO, F₁₆PcZn/NiO and F₆₄PcZn/NiO are 6.8x10³, 9.9x10³ and 2.0x10⁴ counts per second (cps). When F₆₄PcZn is deposited on SiO₂ and TiO₂ an intense fluorescence peak is observed, this is because there is no electron transfer between the HOMO orbital of excited F₆₄PcZn and the conduction band of SiO₂ and TiO₂. For example, the fluorescence intensities observed for the catalysts F₆₄PcZn/P90 and F₆₄PcZn/OX50 are 1.1x10⁷ and 9.7x10⁶ cps, respectively. The results of F₆₄PcZn/NiO indicate an electron is transferred from the conduction band of excited NiO into the singly-occupied HOMO of excited F₆₄PcZn, followed by the opposite transfer from the singly-occupied LUMO of excited F₆₄PcZn to NiO is assumed to rapidly return the excited phthalocyanine to its singlet-ground state and thus block the inter-system crossing process necessary to produce singlet oxygen (¹O₂). Here, we want to mention a small portion of UVA light in the range of 320-400 is included in the emission spectra of tungsten halogen lamp. This could lead to the contribution of NiO in photo reactivity. The results also demonstrate the aggregation of Pc could affect the electron transfer. An electron from NiO might not be transferred to the top layer of Pc in the cases of H₁₆PcZn/NiO and F₁₆PcZn/NiO due to tight packing/aggregation of these Pcs on NiO surface. Therefore, a small amount of MO photodegradation is obtained for reactions catalyzed by H₁₆PcZn/NiO and F₁₆PcZn/NiO. But, due to the non-aggregating character of F₆₄PcZn⁵ the electrons from NiO can be easily transferred to all the Pc molecules. Hence, the

MO photodegradation is completely dropped down to zero for reactions catalyzed by $F_{64}PcZn/NiO$ and $F_{64}PcCu/NiO$.

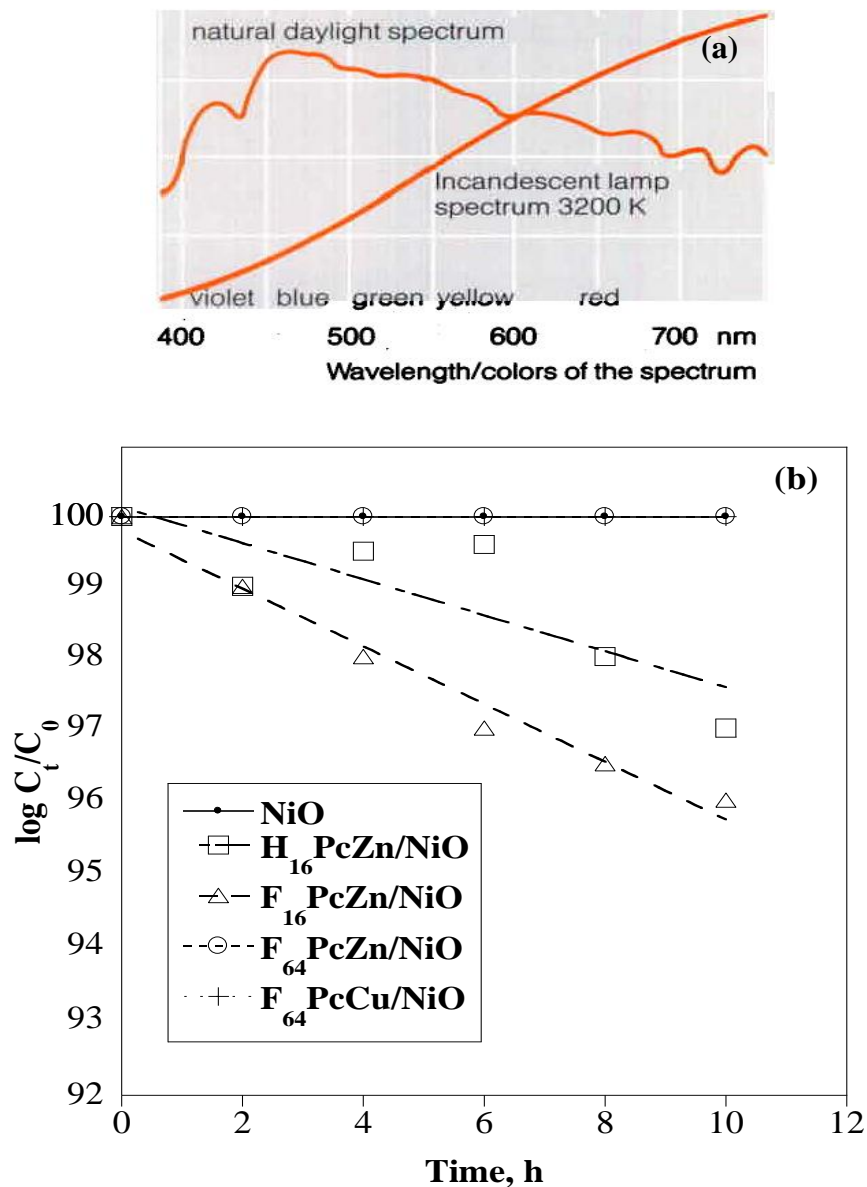


Figure 1. (a) Spectral distribution for the tungsten halogen lamp used as a visible light source (Copyright © OSRAM SYLVANA Inc. 2001-2017). (b) Plots of time-dependent MO photodegradation catalyzed by NiO , $F_{64}PcZn/NiO$, $H_{16}PcZn/NiO$, $F_{16}PcZn/NiO$ and $F_{64}PcCu/NiO$ under visible light irradiation.

Table 1. Reaction rates (k) for MO photodegradation catalyzed by F₆₄PcZn/NiO, H₁₆PcZn/NiO, F₁₆PcZn/NiO and F₆₄PcCu/NiO.

Catalyst	Reaction rate, k (1/h)
NiO	0
H ₁₆ PcZn/NiO	0.0026
F ₁₆ PcZn/NiO	0.0041
F ₆₄ PcZn/NiO	0
F ₆₄ PcCu/NiO	0

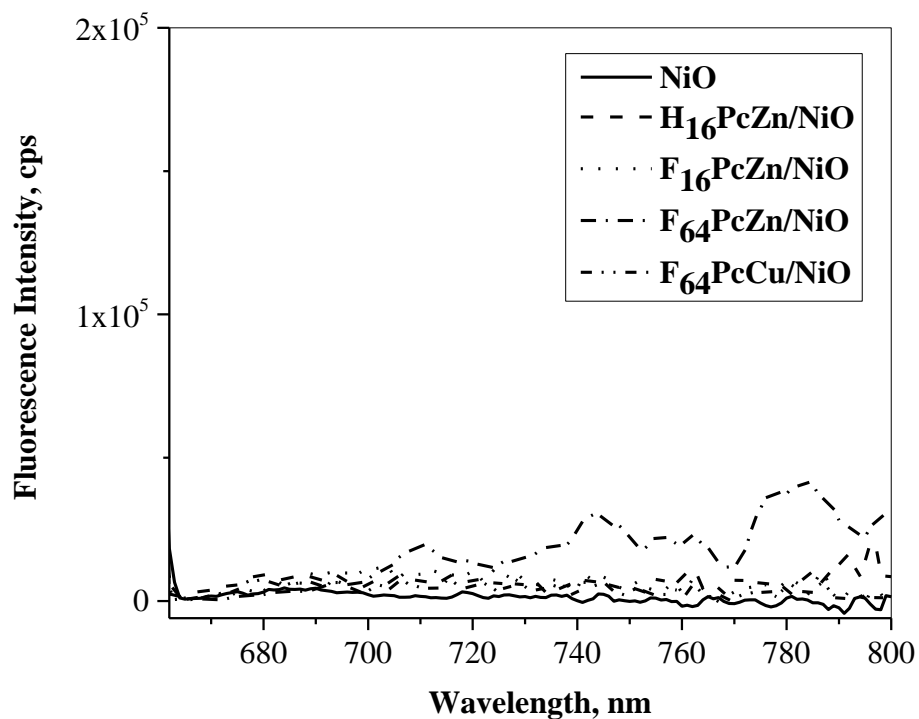


Figure 2. Fluorescence emission intensity for NiO, F₆₄PcZn/NiO, H₁₆PcZn/NiO, F₁₆PcZn/NiO and F₆₄PcCu/NiO catalysts.

To prove that $F_{64}PcZn$ deposited on NiO is unaffected by reactive radicals during catalytic reaction, $F_{64}PcZn$ was extracted using acetone from $F_{64}PcZn/NiO$ after MO photocatalytic reaction and the UV-vis absorption intensity compared with the one before using for photoreaction. The UV-Vis absorption intensities corresponding to Q band and B band are the same (Figure 3), suggesting $F_{64}PcZn$ is chemically intact and the electron transfer from NiO to $F_{64}PcZn$ may be the reason for zero MO photodegradation reaction rate.

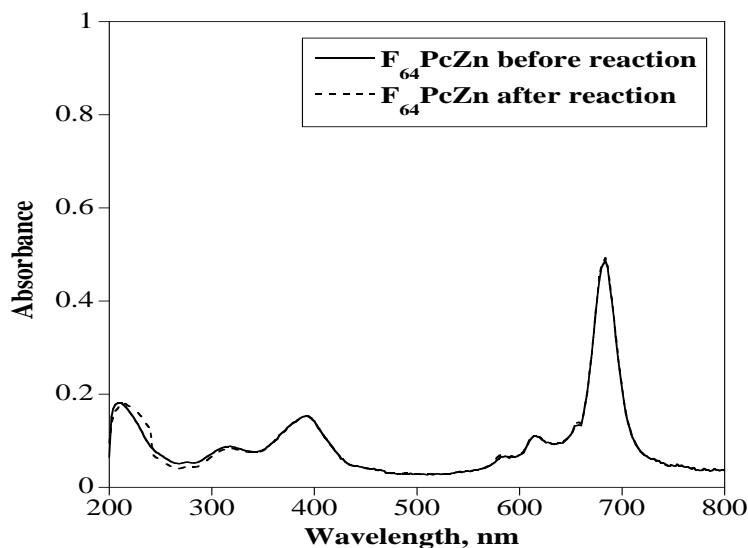


Figure 3. UV-Vis spectra of $F_{64}PcZn$ extracted from $F_{64}PcZn/NiO$ before and after photocatalytic reaction. $F_{64}PcZn$ structure is unaffected by the catalytic reaction.

4.4. CONCLUSIONS

The orbitals coupling is established between $F_{64}PcZn$ and NiO matrix in contrast to other SiO_2 and TiO_2 matrices, as suggested by the very low fluorescence intensity of hybrids $F_{64}PcZn/NiO$ and $F_{64}PcCu/NiO$. An electron transfer from the conduction band of excited NiO

into the singly-occupied HOMO of excited F₆₄PcZn, followed by the opposite direction transfer from the singly-occupied LUMO of excited F₆₄PcZn to NiO is assumed to rapidly return the excited phthalocyanine to its singlet-ground state and thus block the inter-system crossing process necessary to produce singlet oxygen.

To confirm the above-mentioned assumption of excited state quenching of F₆₄PcZn while deposited on NiO, additional investigations and characterization of the hybrid F₆₄PcZn/NiO are required. Therefore, the results and discussion of the hybrid F₆₄PcZn/NiO is included in this Thesis as a supplementary material.

REFERENCES

- (1) Niedermeier, C. A.; Rasander, M.; Rhode, S.; Kachkanov, V.; Zou, B.; Alford, N.; Moram, M. A. *Sci. Rep.* **2016**, *6*:31230, 1-9.
- (2) Dwyer, P.; Vander Valk, R.; Kelty, S. *MRS Proceedings*, **2015**, *593*, Mrss 15-2134167.
Doi: 10.1557/opl.2015.593.
- (3) Maeda, K.; Domen, K. *J. Phys. Chem. Lett.* **2010**, *1*, 2655-2661.
- (4) Sheena, P. A.; Priyanka, K. P.; Sreedevi, A.; Varghese, T. *J. Nanostructure Chem.* **2018**, *8*, 207-215.
- (5) Bench, B. A.; Beveridge, A.; Sharman, W. M.; Diebold, G. J.; Lier, J. E.; Gorun, S. M. *Angew. Chem. Int. Ed.* **2002**, *41*, 747-750.

Chapter 5. Zinc Perfluoroalkyl Perfluoro Phthalocyanine Impregnated Polymer Membranes for Water Purification

5.1. INTRODUCTION

Clean water, essential to human life, is in increasing demand due to population and industrialization increase as well as decrease in available fresh water resources because of pollution. Organic dye compounds, present, for example, in textile effluents are one of the major sources of water pollution owing to their limited biodegradability, toxicity and potential carcinogenic risks.¹ Before certifying water for public consumption or for reuse in industries or for discharge in surface watercourses it is critically important to degrade the organic pollutants. This effort currently requires the use of sophisticated cleaning up methodologies and energy consumption.

Adsorption and microbiological degradation are the two major, traditional methods employed for the removal of synthetic dyes from wastewater.^{2,3} One of the known limitations of the adsorption method is the secondary pollution from adsorbent regeneration.⁴ Since synthetic dyes are very stable, microbiological degradation is less efficient. Consequently, it is crucial to develop efficient as well as cost effective methods for wastewater treatment.

Membrane technology has been widely used in water treatment processes.^{5,6} New, emerging water treatment technologies coupled photocatalytic reaction with membrane separation.^{7,8} In this method a photocatalyst is either suspended in water and filtrated by the membrane or incorporated within the membrane.⁹ TiO₂ is the major photocatalyst used,¹⁰ but it is

only responsive to ultraviolet (UV) irradiation due to its large band gap. But, under UV illumination light induced degradation of polymer occurs. This lead to the loss of tensile strength upon exposure to UV radiation which limits the use of organic polymer membranes,^{11,12} leaving only inorganic membranes as an alternative. Inorganic membranes have the advantage of withstanding in harsh chemical environments, but they are expensive and fragile.^{13,14} Cheryan and Rajagopalan reviewed the potential of applying membranes to treat oily wastewater and the possible pitfalls.¹⁵

To overcome the above-mentioned disadvantages, in the present study a stable organic photocatalyst which responds to visible light excitation, a non-planar zinc perfluoro phthalocyanine ($F_{64}PcZn$), is incorporated into the polymer membranes, namely polytetrafluoroethylene (PTFE), polyethersulfone (PES) and polypropylene (PP) via a simple dip-coating technique. The photocatalytic efficiency of $F_{64}PcZn$ is investigated, with the scope of using it as a catalyst with a membrane in aggressive environments that include reactive oxygen species (ROS), useful for the potential degradation of refractive pollutants, including dyes. Several papers have been published on the crystal structure, photophysical and chemical properties of $F_{64}PcZn$.^{16,17} It has also been reported that $F_{64}PcZn$ is photochemically active upon illumination with radiation in the visible region, besides being structurally robust due the presence of perfluoroalkyl groups located at the peripheral positions.¹⁸ Furthermore, it has been shown that the $F_{64}PcZn$ catalyst broadens the reactivity spectrum of known phthalocyanine catalysts, while the perfluoroalkyl substituents suppress its nucleophilic, electrophilic and radical degradation pathways.¹⁹ The favorable properties can be extended to the degradation of biomolecules,²⁰ the general reactivity pathway involving the possible photoreduction and/or light-induced triplet-state formation, $F_{64}PcZn$ being demonstrated to be a "single-site" catalyst.²¹ The hybrid polymer

membranes are tested for their efficiency in degrading organic pollutants under visible light irradiation.

The most widely used membrane technologies in water treatment are microfiltration, ultrafiltration, nanofiltration and reverse osmosis, listed in the descending order of pore sizes. Microporous membranes are used for processes such as microfiltration and ultrafiltration. In general, microfiltration membranes can separate particles between 0.1 and 10 μm and capable of removing suspended solids, bacteria and protozoa.²² Several polymers have been used as supports for photocatalysts. These include polymers such as polyamide, polyvinylidene fluoride (PVDF), polysulfone (PSf), polyethersulfone (PES), sulfonated polyethersulfone (SPES), polyurethane (PU), polyethylene terephthalate (PET), polyester, polyacrylonitrile (PAN) and polytetrafluoroethylene (PTFE).^{23,24} Here, we investigated PTFE and PES membranes with micrometer pore sizes as supporting matrices.

Polypropylene filters are attractive because of their low cost, good mechanical strength, and chemical and thermal resistance. Their disadvantage, if one considers supported catalysis technology is the inability to form bonds stronger than van der Waals due to their chemically non-functionalized surface. Thus, F_{64}PcZn catalyst may exhibit low adhesiveness and therefore leached in the environment as well as result in the formation of surface catalyst aggregates. Even though F_{64}PcZn may aggregate, it is important to remember this will not result in loss of excitation, unlike F_{16}PcZn because of the presence of peripheral bulky perfluoroalkyl groups that prevent π - π stacking. The aggregates exhibit low surface area relative to the potential "single-site" type catalytic efficiency and thus non-optimal catalytic reactivity. It would be, therefore, beneficial to modify the polymer surface to allow the possibility of ionic or covalent bond formation between the membrane and the Pc.

A thorough literature search revealed that the poor attachment of chitosan to commercial polypropylene textiles has been resolved after treatment of the support with sulfuric acid (H_2SO_4).²⁵ The acid treatment produced sulfonic acid groups at the polypropylene membrane surface. Chitosan is a polysaccharide containing D-glucosamine units and thus positively charged free amino groups. The amino groups of chitosan interact with the sulfonic acid groups at the surface of acid treated polypropylene membrane leading to strong adsorption of chitosan. In our case, F_{64}PcZn also consists of nitrogen functionalities, namely the heterocyclic aza-bridging groups. These groups are believed to be responsible for the dissolution of water insoluble Pc in concentrated H_2SO_4 via their protonation.²⁶ Notably, the Pc is not decomposed by the acid.^{26,27} Thus, in our case, sulfonic groups present at the surface of polypropylene polymer membrane may interact both with the aza-nitrogens and with the F_{64}PcZn metal center because of the Lewis acidity. Matos *et al* showed a strong adsorption of cationic methylene blue on H_2SO_4 treated polypropylene due to the interaction with the sulfonic acid groups at the surface.²⁸

In this study, the chemically inert polypropylene membrane surface is modified via chemical treatment with H_2SO_4 . Sulfonic acid groups are formed on the polypropylene surface via electrophilic addition of $-\text{SO}_3\text{H}$.²⁸ The chemically modified polypropylene with sulfonic groups, $-\text{SO}_3\text{H}$, can easily form surface anions. These groups are normally not strong metal ions binders, but in our case the Zn^{2+} center of F_{64}PcZn exhibits a strongly, enhanced Lewis acidity due to the electronegativity of the fluorine groups. A similar Lewis-acidity enhancement was noticed in the case of the isostructural F_{64}PcCo , the metal center being unusually electron poor and thus able to oxidize acidic thiols.^{16,19} Thus, the sulfonic group may coordinate with the metal center of F_{64}PcZn leading to its anchoring on the surface as individual, "single-site" molecules.

The photocatalytic efficiency of F₆₄PcZn/functionalized polypropylene membrane (F₆₄PcZn/FPP) is investigated using methyl red as a model organic dye. The photodegradation rates of methyl red under visible light, white light and red-light irradiations, for F₆₄PcZn/FPP membrane with various F₆₄PcZn loading densities is reported. The stability in terms of chemical and structural robustness after photoreactions is evaluated.

5.2. MATERIALS AND METHODS

5.2.1. Materials

Polytetrafluoroethylene (PTFE) and polyethersulfone (PES) membrane filters both with 20 µm pore size and polypropylene (PP) membrane filter with 5 µm pore size (PMA series) were purchased from Sterlitech Corporation, USA and provided as a gift by Graver Technologies, USA, respectively. F₆₄PcZn was used as provided by Dr. Gorun's research group, SHU, USA. Sulfuric acid, methyl orange (MO) and methyl red (MR) were purchased from Sigma-Aldrich. De-ionized water was used to prepare the test solutions.

5.2.2. Development of Hybrid F₆₄PcZn Incorporated Polymer Membranes

PES and PTFE membrane filters were impregnated with F₆₄PcZn using the following procedure. There were 3 layers present in the PP membrane, all made up of polypropylene. The top 2 layers are protective layers to the central polymer membrane. So, only the middle polymer membrane layer was coated with F₆₄PcZn as follows. 11 mg of F₆₄PcZn was dissolved in 3 ml ethanol and the membrane was placed in the solution. Most of the solution was absorbed by the

membrane due to capillary force. The membranes were completely air dried by evaporating ethanol at room temperature. The weight of membranes before and after dip coating was measured to determine the amount of F₆₄PcZn loaded on the membranes. The loading density of F₆₄PcZn obtained following this procedure was 0.4 μmol/cm². Figure 1 shows the optical images of all the three membranes investigated, F₆₄PcZn/PES, F₆₄PcZn/PTFE and F₆₄PcZn/PP (only middle layer loaded with F₆₄PcZn, the outer layers were left uncoated).

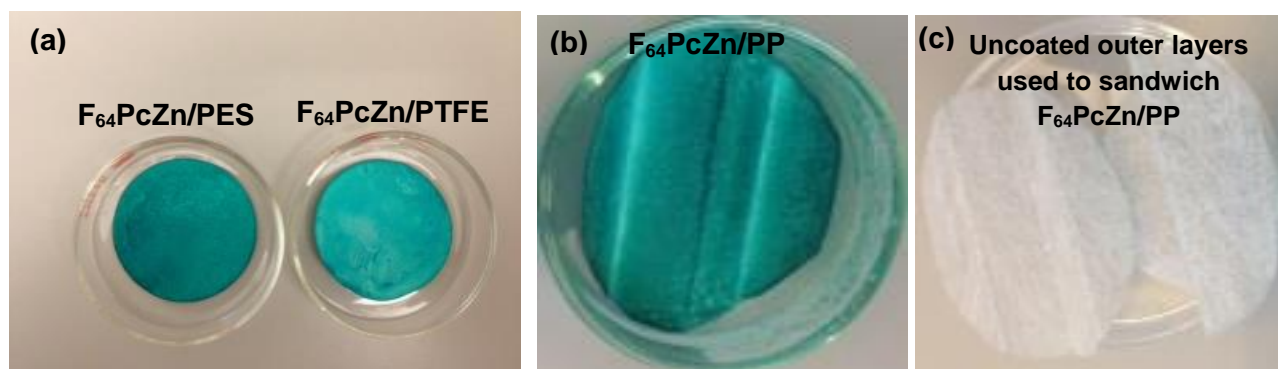


Figure 1. Optical images of (a) F₆₄PcZn/PES, F₆₄PcZn/PTFE, (b) F₆₄PcZn/PP (middle layer) and (c) the outer uncoated layers used to sandwich F₆₄PcZn/PP membrane (© Karpagavalli Ramji, 2018).

5.2.3. Surface Modification of Polypropylene Membrane: Functionalized Polypropylene Membrane

Polypropylene membranes were cut into circles with the area of ~ 20.1 cm². The membranes were treated with 100 mL of sulfuric acid at 100 °C for 1 h. Next, the membranes were thoroughly washed with de-ionized water until the pH of the effluent was neutral and then air

dried. Thus, produced sulfonated polypropylene membranes, mentioned hereafter as functionalized polypropylene membranes (FPP), are shown in Figure 2. The sulfonated polypropylene membrane was characterized using infrared spectroscopy (IR). KBr pellets were made for the test materials to record IR spectra on Nicolet 4700 FT-IR spectrophotometer from Thermo Electron Corporation, USA and the data was processed using OPUS software (Bruker). To prepare KBr pellet, 2 mg of polymer membrane and 200 mg of KBr were added into an agate mortar and ground finely to make a homogenous mixture. The polymer/KBr mixture was transferred to the mini-press to make the pellet. The mixture was evenly distributed in the mini-press and closed tightly to make the KBr pellet. This pellet was transferred to the IR spectrophotometer for analysis.

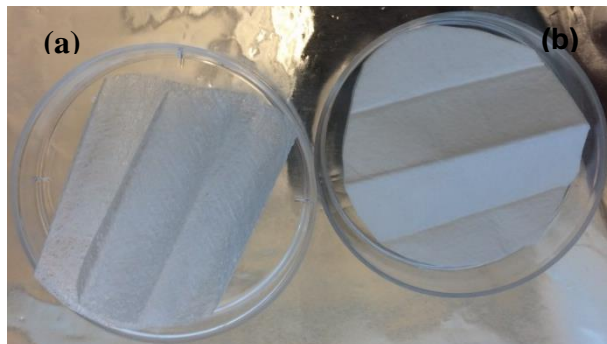


Figure 2. Polypropylene membranes functionalized with sulfonic acid groups. (a) FPP outer protecting layers and (b) FPP inner membrane layer (© Karpagavalli Ramji, 2018).

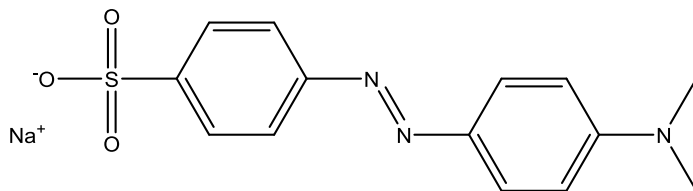
5.2.4. Incorporation of F₆₄PcZn into Functionalized Polypropylene Membrane

F₆₄PcZn was incorporated using three different concentrations of starting solutions to investigate the rate of the photocatalytic reaction as a function of catalyst loading. The loading

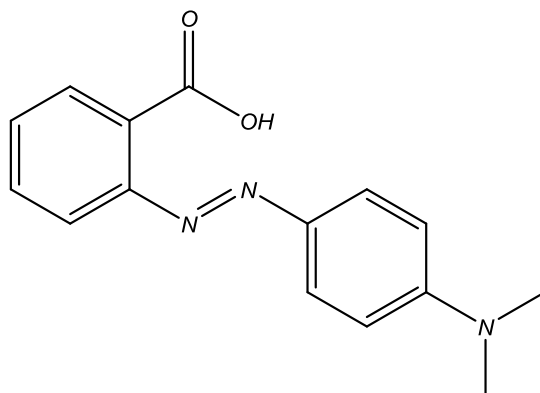
density of F₆₄PcZn was 0.08, 0.4 and 0.8 μmol/cm². The required amount of F₆₄PcZn was dissolved in ethanol and the FPP membrane was immersed in this solution. F₆₄PcZn incorporated FPP membrane was obtained by evaporating ethanol at room temperature. The amount of F₆₄PcZn loading on the membrane was determined by weighing the membrane before and after the deposition of F₆₄PcZn.

5.2.5. Photodegradation Measurements

Photocatalytic efficiency of F₆₄PcZn/PES, F₆₄PcZn/PTFE and F₆₄PcZn/FPP membranes were examined using methyl orange (MO) and methyl red (MR) as model pollutants. The chemical structures of MO and MR are illustrated in Figure 3. In the case of MO, the change in UV-Vis peak absorbance observed in the range of 350 to 550 nm was monitored. For MR spectral changes were monitored in the 400 to 600 nm region, where the pH-indicating chromophore is located. In the case of F₆₄PcZn/FPP, the F₆₄PcZn coated middle layer was sandwiched between the uncoated outer layers (shown in Figure 2a) while performing the photodegradation reactions.



(a) *(E)*-4-((4-(dimethylamino)phenyl)diazenyl)benzenesulfonate,
Methyl Orange



(b) 2-(*N,N*-dimethyl-4-aminophenyl) azobenzenecarboxylic acid,
Methyl Red

Figure 3. The molecular structures of (a) MO and (b) MR.

MO and MR are azo dyes used extensively as an indicator of water acidity, including in ASTM D1067: Standard Test Method for Acidity or Alkalinity of Water". As an example, the variation in the color of MR at different pH is displayed in Figure 4. MR is only slightly soluble in water. The MR solution (0.01 mM) is prepared by adding the solid MR to deionized water and boiling the mixture while stirring. The solution is then cooled down to room temperature before running the photodegradation reactions.

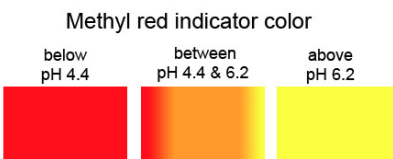


Figure 4. The colors of MR versus pH (© Karpagavalli Ramji, 2018).

To perform the MO photodegradation process under static conditions, 200 mL of 1 μ M MO solution was added to the funnel of the filtration system. The flow rate of MO solution was 0.03 mL/min for F₆₄PcZn/PES and F₆₄PcZn/PP membranes and 0.09 mL/min for F₆₄PcZn/PTFE membrane. UV-Vis spectrophotometry was employed to determine the concentration of MO before and after photodegradation.

5.2.6. Dynamic Flow Measurements

A recirculation system was used for the dynamic flow of reaction solution. The filtration device was loaded with the F₆₄PcZn/FPP membrane. This filtration device is made up of borosilicate glass. It is well known that borosilicate glass cuts off the wavelengths below 300 nm.²⁶ Here we are interested only in visible light irradiation, not UV light. As shown in Chapters 2 and 3, we used a tungsten halogen lamp to irradiate the filter membranes with visible light of wavelengths ranging from 400 to 700 nm. The intensity of the visible light was 130,000 lx (~ 1 Sun) used for 1 μ M MO/MR solutions. In MR degradation experiments, 200 ml of 10 μ M dyes were irradiated using 3 Suns of visible light, *i.e.*, 390,000 lx. The visible light from the tungsten halogen lamp covers the wavelengths ranging from 400 to 700 nm. LEDs were also employed as

light source to compare the photo efficiency of F₆₄PcZn/FPP membrane under red and white lights illumination. LEDs were provided by U. S. Army Corps of Engineers' Vicksburg District, Vicksburg, MS. The red-light LED has a peak emission at 626 nm and white light LEDs emit from 400 to 700 nm. The light intensities of white and red LEDs are 80,000 and 20,000 lx, respectively. In all these studies, light reaches the membrane surface through the glass filtration funnel which is made up of borosilicate glass. We employed light wavelengths above 400 nm.

For dynamic flow experiments, the test solution was added to the filtration device and maintained in a continuous flow at a rate of 200 mL/min using a Cole Palmer pump. UV-Vis spectrophotometry was employed to measure the concentration of test solution before and after illumination.

5.2.7. Structural integrity of F₆₄PcZn/PP Membrane after MR Photodegradation

The structural integrity of F₆₄PcZn/PP membrane was analyzed using IR spectroscopy after MR photodegradation reaction for 15 h in dynamic reaction conditions. KBr pellet was prepared following the procedure mentioned in section 5.2.3 to measure IR spectra for PP and F₆₄PcZn/PP membranes. The spectra were recorded on a Nicolet 4700 FT-IR spectrometer from Thermo Electron Corp., USA. The data was processed using OPUS software.

5.2.8. Microstructural Characterization using Optical and Scanning Electron Microscopy

The membranes before and after MO photodegradation process were analyzed using an optical microscope (Nikon Instruments Inc., USA) and a scanning electron microscope (LEO1525,

Carl Zeiss SMT AG, Germany) to investigate any changes in the microstructure after photodegradation reaction.

5.2.9. Hydrophobicity of F₆₄PcZn Incorporated PTFE Membrane

The hydrophobicity of uncoated PTFE and coated F₆₄PcZn/PTFE membrane was analyzed through dynamic water contact angle measurements. The advancing and receding contact angles for water and hexadecane were measured using Rame-Hart contact angle goniometer equipped with a Motic 100 digital camera.

5.3. RESULTS AND DISCUSSION

The chemical structure of PTFE, PES and PP membranes are given below in Figure 5. Both F₆₄PcZn as well as PTFE are fluorinated compounds, because of the low intermolecular interactions of fluorinated compounds, the physical adsorption of F₆₄PcZn on PTFE membrane may be weak. In contrast, PES has diphenylene sulfone repeating units -(O=S=O) in the molecular structure. The oxygen atoms in the -(O=S=O) groups have two unshared electrons.^{26,27} Therefore, Lewis acidic metal center of F₆₄PcZn can interact in a better way with the oxygen attached to the sulfur atom.

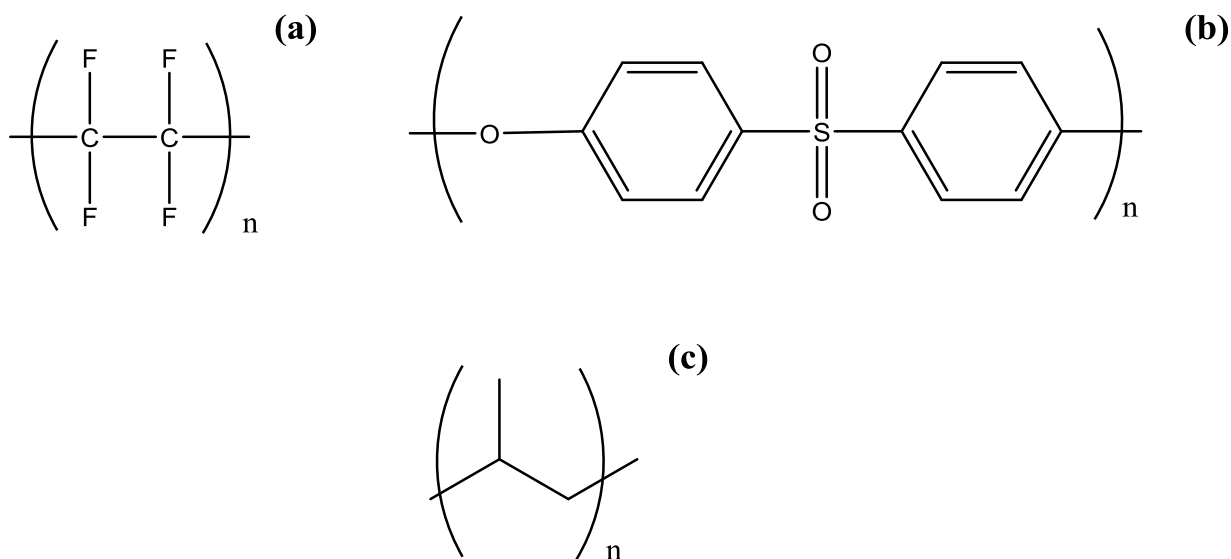


Figure 5. Chemical structure of (a) PTFE, (b) PES and (c) PP.

5.3.1. Microstructure of F₆₄PcZn Loaded PTFE, PES Membranes

Figure 6 and 7 depict optical and SEM micrographs of F₆₄PcZn loaded PTFE and PES membranes in comparison to the bare membranes. It can be seen from the micrographs F₆₄PcZn precipitated out on PTFE membrane and deposited as clumps on the membrane surface while an even layer of F₆₄PcZn coating is formed on the PES membrane. This observation suggests poor interaction between fluorinated PTFE and F₆₄PcZn compounds. A better adsorption of F₆₄PcZn on PES membrane could be due to the -(O=S=O) group, that has oxygen atoms with unshared electrons,^{26,27} in the chemical structure of PES. Because we observed a better interaction of F₆₄PcZn with PES while investigating F₆₄PcZn loaded PP membranes for photoactive filter applications, we modified the PP membrane surface with sulfonic acid groups which is explained in later sections of this Chapter.

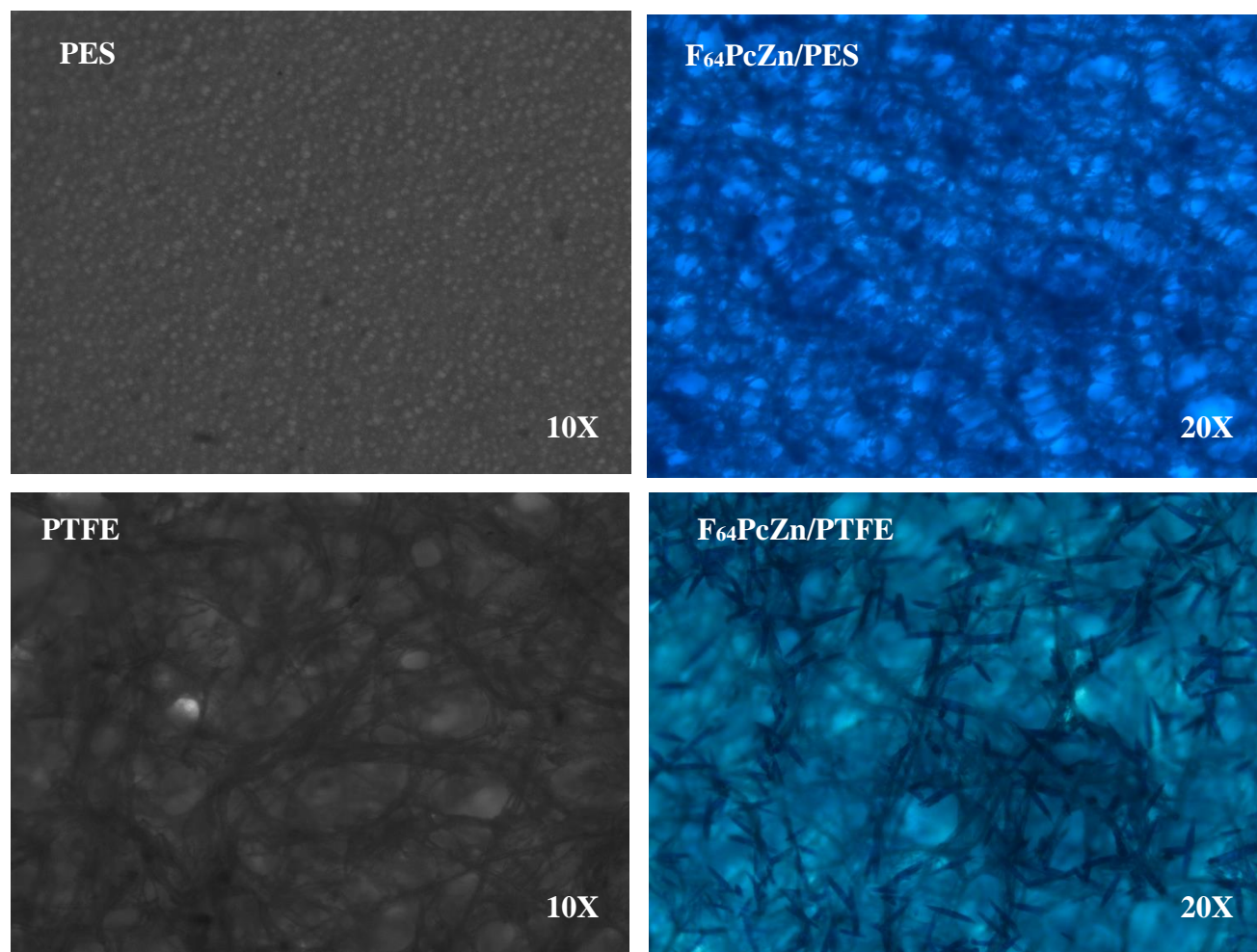


Figure 6. Optical micrographs of PES, PTFE, F₆₄PcZn/PES, and F₆₄PcZn/PTFE filter membranes. F₆₄PcZn impregnated membranes fluorescent under light.

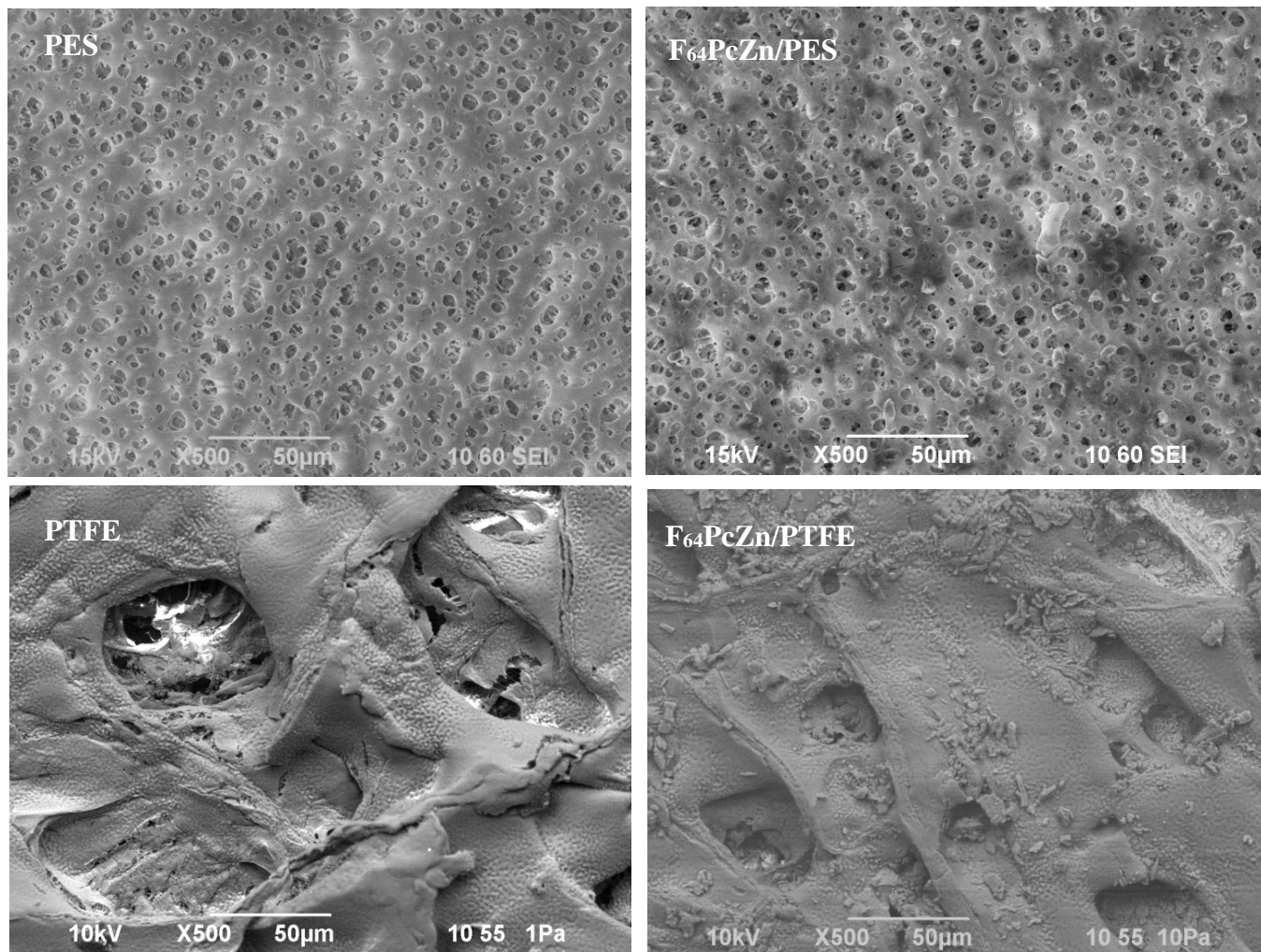


Figure 7. SEM micrographs of bare PES, PTFE and F₆₄PcZn deposited membranes such as F₆₄PcZn/PES and F₆₄PcZn/PTFE.

5.3.2. Contact Angle Measurements for F₆₄PcZn Coated PTFE

Water and hexadecane contact angles (CAs) for the PTFE and F₆₄PcZn/PTFE membranes are determined to monitor the polar and chemical heterogeneity of the surfaces. Water CA for PTFE and F₆₄PcZn/PTFE membranes are 149° and 118°. Hexadecane CA for PTFE and

F₆₄PcZn/PTFE membranes are 55° and 44°. CA hysteresis is calculated from the difference between the advancing and receding angles. The advancing angle refers to the maximum angle associated with adding water/hexadecane volume while receding angle corresponds to the smallest possible angle upon removing volume.²⁸ An increase in water CA hysteresis from 59° to 66° and a decrease in hexadecane CA hysteresis from 48° to 38° for F₆₄PcZn/PTFE compared to bare PTFE membrane suggest the following. The increase in water CA hysteresis can be explained by the deposition of uneven clumps of F₆₄PcZn on the filter membrane as revealed by the SEM micrograph, an effect which could increase the surface roughness of the membrane.²⁹ Hexadecane CA hysteresis is more sensitive to the nonpolar character of the surface. Hexadecane CA hysteresis decreased due to the increase in perfluoroalkyl group content by depositing F₆₄PcZn on the surface. Schmidt *et al* showed similar hexadecane CA hysteresis decrease due to increase in perfluoroalkyl groups in polymer coatings and suggested this property can help in resisting marine biofouling.³⁰ Hence, we assume the chemical properties of F₆₄PcZn would be advantageous while deposited on polymer membranes for wastewater treatment.

5.3.3. F₆₄PcZn/PTFE and F₆₄PcZn/PES Membranes: Photodegradation of MO

Figure 8 illustrates the comparison of photocatalytic ability of F₆₄PcZn/PTFE and F₆₄PcZn/PES membranes to degrade 1 μM MO under irradiation with 130,000 lx visible light. Higher percentage of MO photodegradation is observed in the case of F₆₄PcZn/PES than F₆₄PcZn/PTFE, *i.e.*, 27% as compared to 16%. In both cases F₆₄PcZn is not found in the filtrate. This could be either F₆₄PcZn coatings on the membrane did not come off or if desorbed from the membrane F₆₄PcZn might be filtered out by the frit of the filtration device. We were able to see

F₆₄PcZn on the frit surface after the MO photodegradation reaction especially higher amount when F₆₄PcZn/PTFE membrane is placed. The higher photoactivity of F₆₄PcZn/PES membrane could be due to many factors including more exposed surface area of F₆₄PcZn and greater thickness of the PES membrane which leads to lower flow rate of MO solution. Another important factor that lowers the degradation rate is the incubation time of MO solution in the F₆₄PcZn/PTFE membrane. A higher incubation time resulted in greater degradation rate of MO solution. Here the incubation time defines the period of MO solution is in contact with the membrane filter. The thickness of F₆₄PcZn/PTFE and F₆₄PcZn/PES membranes are 0.2 and 0.5 mm. The respective MO solution flow rates are 0.09 and 0.03 mL/min. F₆₄PcZn loading density for both the membranes is 0.4 μmol/cm². The period of MO solution in contact with the membrane under illumination is 3 times higher for F₆₄PcZn/PES and thus shows a better percentage of MO photodegradation. These results revealed the ability of F₆₄PcZn deposited on PTFE and PES membranes to degrade MO under visible light illumination. We can notice the concentration of MO test solution is very low, 1 μM for these experiments. Unlike F₆₄PcZn deposited on nanoparticle, the filter membranes incorporated with F₆₄PcZn did not show much efficiency in degrading MO under visible light irradiation. This could be related to the higher surface area of nanoparticles.

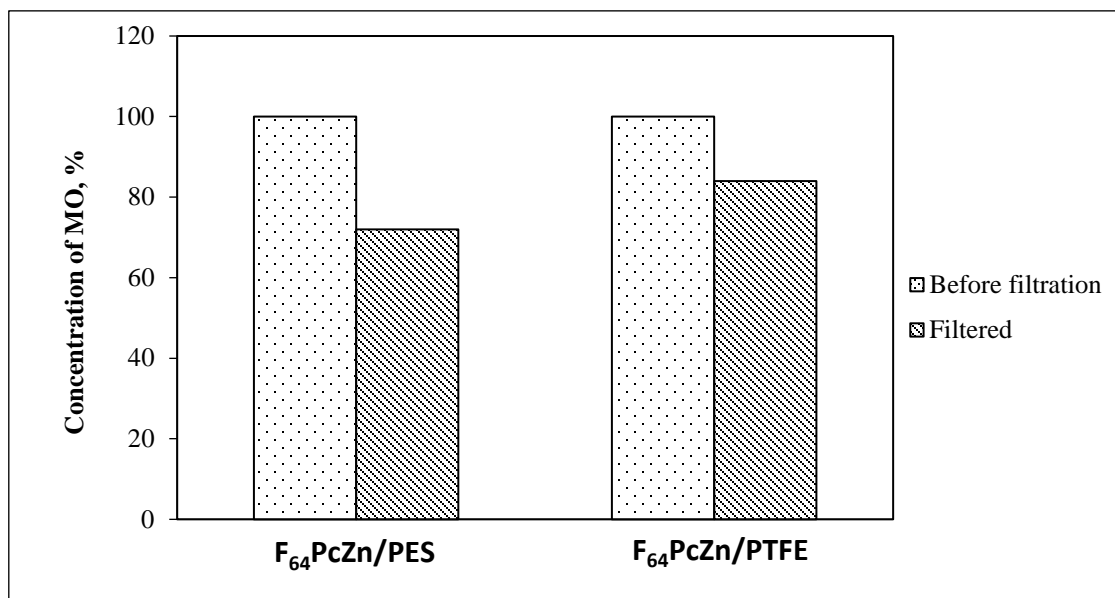


Figure 8. Comparison of visible light MO photodegradation rate for F₆₄PcZn/PES and F₆₄PcZn/PTFE membranes under 130,000 lx intensity of visible light irradiation.

5.3.4. F₆₄PcZn/PP Membrane Photocatalytic Degradation of Methyl Red under Static Condition

For the PP membrane system, MR at the same concentration as MO, *i.e.*, 1 μ M, is used as a model organic pollutant. The photodegradation of MR performed at static conditions suggested F₆₄PcZn/PP can degrade the azo dye. MR photodegradation results for F₆₄PcZn/PP membrane are shown in Figure 9.

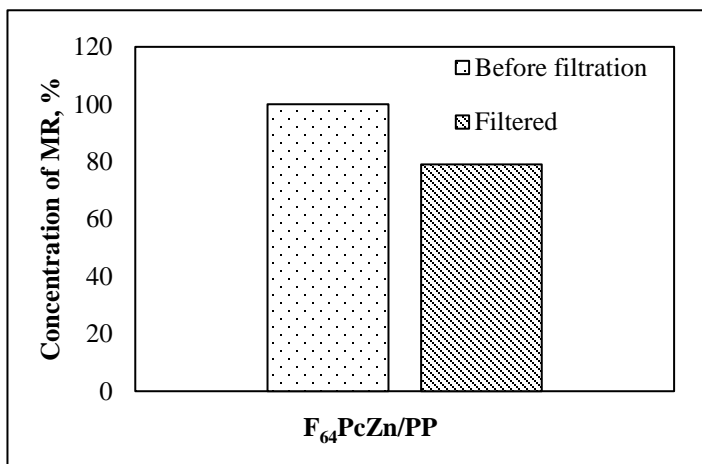


Figure 9. MR visible light photodegradation by F₆₄PcZn coated PP membrane.

Since we noticed a better adsorption of F₆₄PcZn as revealed by SEM micrographs (Figure 6) on PES membrane containing sulfone group -(O=S=O) in the molecular structure, we functionalized the PP membrane with sulfonic acid group (-SO₃H). The photocatalytic efficiency of F₆₄PcZn/FPP membrane is investigated using 10 μM MR solution under irradiation of 3 Suns, 390,000 lx. The results are discussed in the following sections.

5.3.5. Photodegradation of MR using F₆₄PcZn/FPP Membrane for Three Repeated Cycles under Dynamic Condition

A 200 ml of 10 μM MR solution was recirculated using the F₆₄PcZn/FPP membrane mounted on the filtration device and irradiated with 3 Suns of visible light for three cycles up to 4 h, each. It was found from Figure 10 that at the end of first cycle 20% of MR has been degraded.

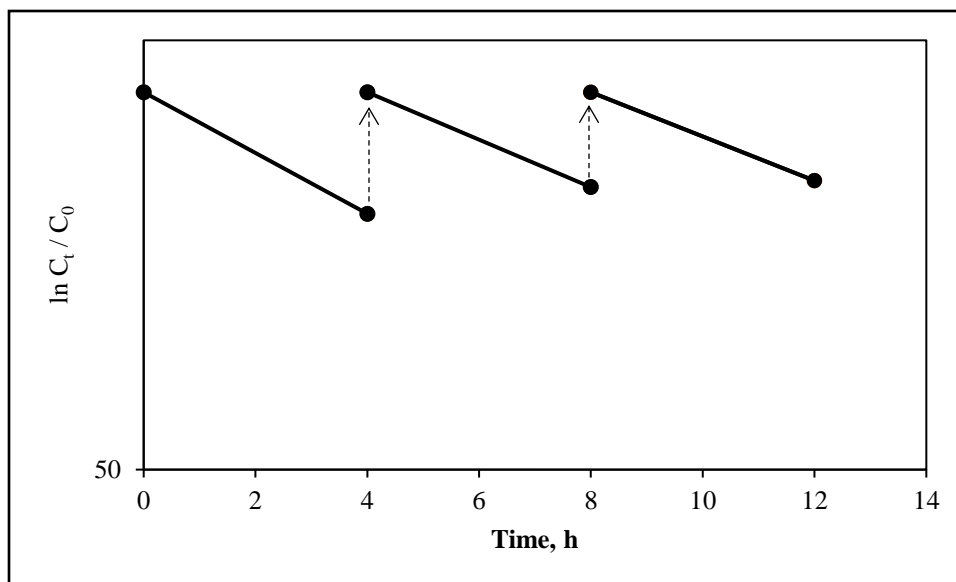


Figure 10. Three cycles of MR photodegradation using $F_{64}PcZn/FPP$ membrane.

Lower degradation rates of 16% and 15% are observed for the second and third cycles. After these three cycles the $F_{64}PcZn/FPP$ membrane was examined using IR spectroscopy to determine its integrity.

5.3.6. Evaluation of the Integrity of FPP Membranes after Photoreaction under Dynamic Conditions

The free radicals produced during photooxidation process may oxidize polypropylene of $F_{64}PcZn/FPP$ membrane which leads to the formation of carbonyl groups that can be recognized using IR analysis. Therefore, IR measurements are carried out to investigate the chemical stability of FPP membrane after photodegradation reaction (Figure 11). We can see from the spectra, $F_{64}PcZn/FPP$ membrane exhibits the peaks for $-CH_3$ groups of polypropylene. Additional peaks

attributed to -C-F and -C-N bonds³² are observed around 1250 and 1260-1320 cm^{-1} because of the deposition of F_{64}PcZn on FPP membrane.³³ The IR spectra weren't corrected for the CO_2 and H_2O from air. These results suggest that there is no adverse degradation of PP polymer of $\text{F}_{64}\text{PcZn}/\text{FPP}$ membrane during these three photodegradation cycles.

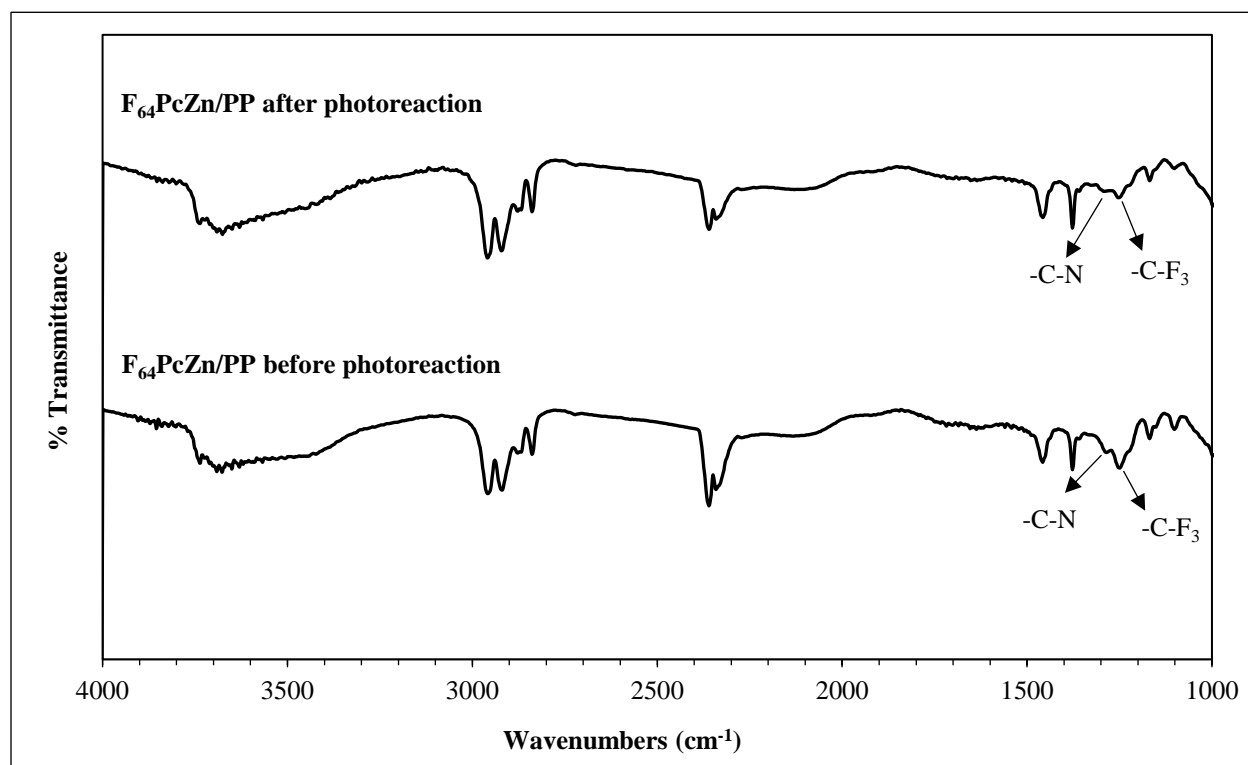


Figure 11. Comparison of IR spectra of $\text{F}_{64}\text{PcZn}/\text{FPP}$ before and after 3 cycles of MR photodegradation reaction.

The microstructure of the membranes was analyzed using an optical microscope to support the IR spectral observations. The results are discussed below.

5.3.7. Comparison of the Microstructure of F₆₄PcZn/FPP Membrane before and after MR Photodegradation Reaction

The membranes microstructure was analyzed before and after MR photodegradation reactions repeated for three cycles of 4 h duration to study the robustness of the membrane. Figure 12 exhibits the optical micrographs of F₆₄PcZn/FPP membrane before and after photodegradation reaction. No differences are being observed suggesting that the FPP membrane is structurally robust after the MR photodegradation reaction.

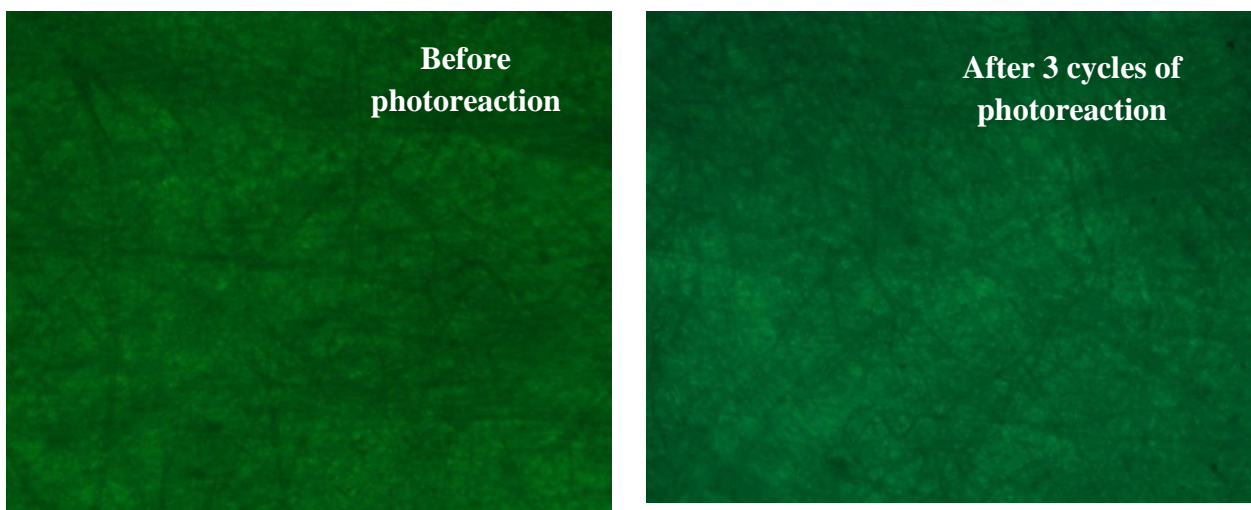


Figure 12. Optical micrographs showing the structural robustness of F₆₄PcZn/PP membrane before and after MR photodegradation. Magnification: 4X.

F₆₄PcZn strongly absorbs light between 590 to 740 nm thus the micrographs look green in color. A slight color change of the membrane observed after MR photodegradation reaction is because of the adsorption of MR on the filter during dynamic recirculation which can be identified by naked eye.

5.3.8. Effect of F₆₄PcZn Loading Density on Catalytic Efficiency of F₆₄PcZn/FPP Membrane

The rate of MR photodegradation as a function of the amount of catalyst loading is shown in Figure 13. MR concentration decreases linearly with photodegradation time, the reaction obeying 1st order kinetics. After a slow initial increase, the reaction rate steadily increases with raising the amount of catalyst suggesting more number of catalyst molecules are active at higher amounts, the catalyst does not deactivate because of the formation of surface aggregates. As a larger number of F₆₄PcZn molecules are available for photocatalytic reaction, the efficiency of the F₆₄PcZn/FPP membrane in degrading the organic dye also increases.

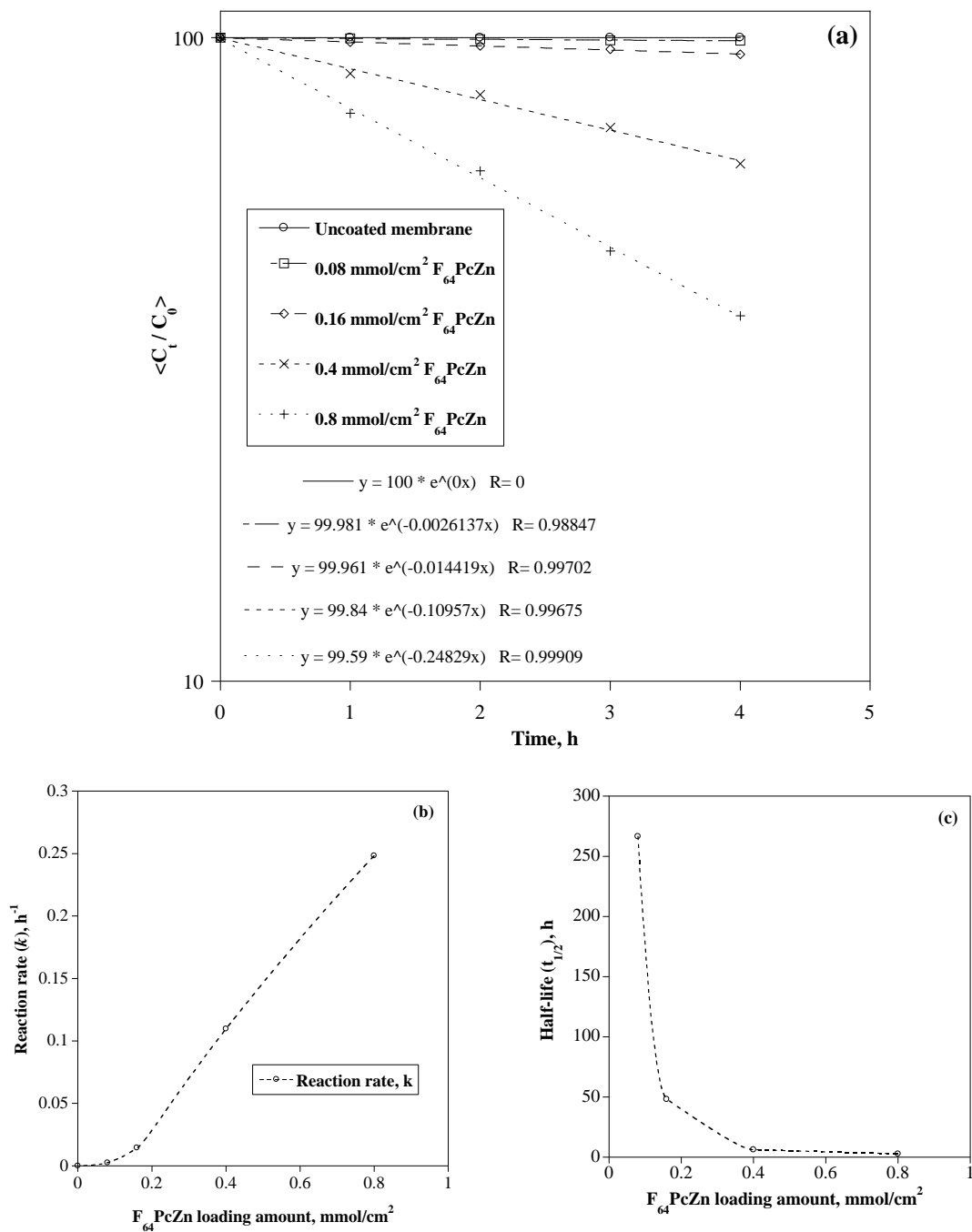


Figure 13. Effect of $F_{64}PcZn$ loading density in $F_{64}PcZn/FPP$ membrane on the photodegradation rate of MR, followed by monitoring the variation of the: a) dye concentration, b) reaction rate. c) reaction half-life, $t_{1/2}$.

A half-life of 2.8 h for MR photodegradation can be reached with F₆₄PcZn loading amount of 0.8 μmol/cm² for F₆₄PcZn/FPP membrane. The bulky peripheral perfluoroalkyl group of F₆₄PcZn hinder the π-π stacking which adversely affects the efficiency of the phthalocyanines, thus an increase in the reaction rate with increasing F₆₄PcZn loading amount is achieved.

5.3.9. Red and White LEDs as Light Sources

A comparison of the three light sources used thus far for the breakdown of MR, namely tungsten halogen light, LED white light and LED red light is shown in Figure 14. The results shown in Figure 14 have been obtained by an exponential fit of the dye concentration decrease versus time. The fit suggests that in all 3 cases, regardless of the wavelength of the light the dye decomposition follows 1st order kinetics. Furthermore, the reaction rate for the red LED, 0.34 h⁻¹, is significantly higher than the one obtained using white LED light, 0.12 h⁻¹.

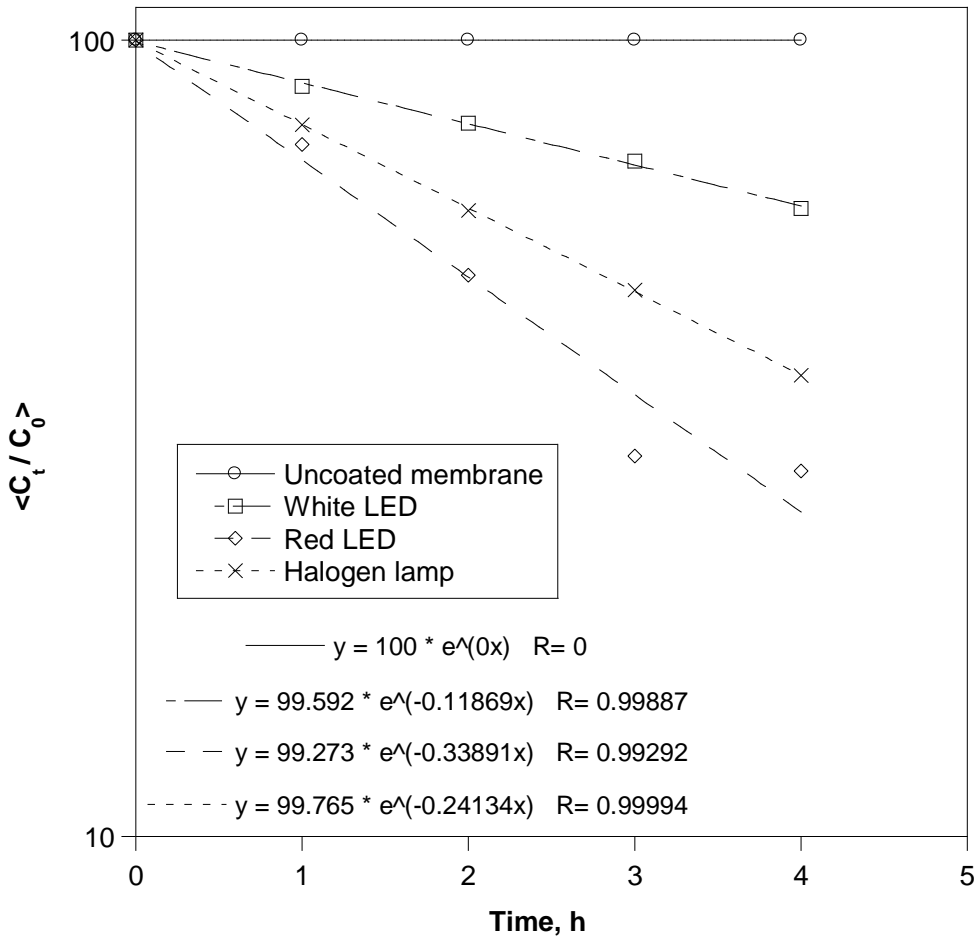


Figure 14. Comparison of different light sources such as tungsten halogen light, LED white light and LED red light for MR photodegradation process using $0.8 \mu\text{mol}/\text{cm}^2$ F_{64}PcZn loaded $\text{F}_{64}\text{PcZn}/\text{FPP}$ membrane.

F_{64}PcZn has an intense absorption in the red region. F_{64}PcZn adsorbs light with major peaks at following wavelengths [λ , nm] ($\log \epsilon$): 322 (4.38), 396 (4.56), 620 (4.42) and 686 (5.24), where ϵ is the molar absorption coefficient, $\text{M}^{-1} \cdot \text{cm}^{-1}$.¹⁶⁻¹⁹ The light intensities of red LEDs, white LEDs and tungsten halogen lamp are 20,000, 80,000 and 390,000 lx at the test solution surface, respectively. Here we used red LEDs that has an emission in the red region of 660 ± 15 nm with 20,000 lx intensity as a red light source. The HOMO-LUMO gap for F_{64}PcZn occurs at 686 nm.

F₆₄PcZn absorbs light around 620 and 686 nm that falls in the red region. MR decomposition occurs more efficiently while using red LEDs providing reaction rate, k as 0.34 h⁻¹. The $n \rightarrow \pi^*$ and $\pi \rightarrow \pi^*$ transitions predominantly occur at F₆₄PcZn while irradiating with red LEDs.

If we consider the white LEDs, regardless of the 4 times higher light intensity, 80,000 lx, the highest peak intensity is in the blue region and it has a very small portion of red light. MR degradation still occurs because F₆₄PcZn absorbs light at wavelengths 322 and 396 nm. But MR degradation reaction rate k is three times lesser while comparing with shining red LEDs. When shining tungsten halogen lamp that consists of a significant portion of red light with 390,000 lx intensity, again a higher MR degradation rate of 0.24 h⁻¹ is obtained. A higher reaction rate is observed since tungsten halogen lamp covers a wide range of wavelengths in addition to comprising of larger intensity red light than white LEDs. Based on the above results, it can be concluded that F₆₄PcZn will be a more efficient photosensitizer while deposited on PP membranes if excited with a red-light source.

5.4. CONCLUSIONS

F₆₄PcZn impregnated on polymer membranes efficiently degrades model organic pollutants in water. IR and microstructural analysis revealed the PP polymer did not degrade by the photooxidation process for the tested durations. F₆₄PcZn/polymer membranes are photochemically stable and able to degrade organic pollutants for three continuous runs each of 4 h duration.

In addition to the results obtained, further characterization of F₆₄PcZn/FPP polymer membrane is required to understand the mode of adsorption of F₆₄PcZn on the FPP membrane. The life-time of F₆₄PcZn/FPP polymer membrane required to be tested for longer duration to recognize the applicability of this F₆₄PcZn/FPP polymer membrane system in water decontamination. Because of these requirements of additional characterization for F₆₄PcZn/FPP polymer membrane, this Chapter is added under the title of supplementary in this thesis.

REFERENCES

- (1) Baldez, E. E.; Robaina, N. F.; Cassella R. J. *J. Hazard. Mater.* **2008**, *159*, 580-586.
- (2) Gupta S. V. K. *J. Environ. Manag.* **2009**, *90*, 2313-2342.
- (3) Li, Q.; Guo, B. D.; Yu, J. G.; Ran, J. R.; Zhang, B. H.; Yan, H. J.; Gong, J. R. *J. Am. Chem. Soc.* **2011**, *133*, 10878-10884.
- (4) Lucarelli, L.; Nadtochenko, V.; Kiwi J. *Langmuir* **2000**, *16*, 1102-1108.
- (5) Howell, J.; Noworyta A. (Eds.) *Towards hybrid membrane and biotechnology solutions for Polish environmental problems*, Wroclaw Technical University Press, Wroclaw, 1995.
- (6) Caetano, M. N. De Pinho, E. Drioli, H. Muntau (Eds.), *Membrane technology: applications to industrial wastewater treatment*, Kluwer Academic Publishers, The Netherlands, 1995.
- (7) Ruiz-Martinez, E.; Sanchez-Hervas, J. M.; Otero-Ruiz J. *Appl. Catal. B: Environ.* **2004**, *50*, 195-206.
- (8) Song, K.; Lee W. Y. *Appl. Catal. A: Gen.* **2003**, *256*, 77-98.
- (9) Goethals, A.; Mugadza, T.; Arslanoglu, Y.; Zugle, R.; Antunes, E.; Hulle, S. W. H. V.; Nyokong, T.; Clerck, K. D. *J. Appl. Polym. Sci.* **2014**, *131*, 40486 pp1-7.
- (10) Han, H.; Bai, R. *Separation and purification Technol.* **2010**, *73*, 142-150.

- (11) Rabek, J.F. *Polymer Photodegradation*, Chapman and Hall, London, 1995, p. 655.
- (12) Andrady, A. L.; Hamid, S. H.; Hu, X.; Torikai, A. *J. Photochem. Photobio. B: Biol.* **1998**, *46*, 96-103.
- (13) Fard, A. K.; McKay, G.; Buekenhoudt, A.; Sulaiti, H. A.; Motmans, F.; Khraisheh, M.; Atieh, M. *Materials (Basel)*, **2018**, *11*, 74, 1-47.
- (14) Bird, A. J.; Trimm, D. L. *Carbon*, **1983**, *21*, 177-180.
- (15) Cheryan, M.; Rajagopalan, N. *J. Mem. Sci.* **1998**, *151*, 13-28.
- (16) Bench, A.; Brennessel, W. W.; Lee, H. J.; Gorun S. M. *Angew. Chem. Int. Ed.* **2002**, *41*, 750-754.
- (17) Liao, M. S.; Watts, J. D.; Gorun, S. M.; Scheiner, S.; Huang M. J. *J. Theor. Comp. Chem.* **7**, **2008**, 541-563.
- (18) (a) Bench, B. A.; Beveridge, A.; Sharman, W. M.; Diebold, G. J.; Lier, J. E.; Gorun, S. M. *Angew. Chem. Int. Ed.* *41*, **2002**, 748-750. (b) D. Drozda, K. Szczubialka, Ł. Łapok, M. Skiba, H. Patel, S. M. Gorun, M. Nowakowska *Applied Catalysis B: Environmental* **125** (2012) 35-40.
- (19) Loas, A.; Gerdes, R.; Zhang, Y.; Gorun, S. M. *Dalton Trans.* *40*, **2011**, 5162-5165.
- (20) Patel, P.; Patel, H.; Borland, E.; Gorun, S. M.; Sabatino D. *Chem. Commun.* *50*, **2014**, 6309-6311.
- (21) Moons, H.; Loas, A.; Gorun, S. M.; Van Doorslaer S. *Dalton Trans* *43*, **2014**, 14942-14948.
- (22) Kuvarega, A. T.; Mamba, B. B. Semiconductor photocatalysis, Photocatalytic membranes for efficient water treatment, Cao, W. (Ed), *IntechOpen*, Aug 24th **2016**, DOI: 10.5772/62584, page1266.

- (23) Bet-moushoul, E.; Mansourpanah, Y.; Farhadi, K. H.; Tabatabaei, M. *Chem. Eng. J.*, **2016**, 283, 29-46.
- (24) Leong, S.; Razmjou, A.; Wang, K.; Hapgood, K.; Zhang, X.; Wang, H. *J. Membr. Sci.*, **2014**, 472, 167-184.
- (25) Adarsh, K. J.; Madhu G. *Int. J. Innov. Res. Sci., Eng. and Tech.*, **2013**, 2, 2943-2951.
- (26) Ledson, D. L.; Twigg, M. V. *Inorganica Chimica Acta*, **1975**, 13, 43-46.
- (27) Kadish, K. M.; Smith, K. M.; Guillard, R. *The Porphyrin Handbook, Vol. 19 / Applications of Phthalocyanines*, Academic Press, 2003.
- (28) Matos, J. P.; Sansiviero, M. T. C.; Lago, R. M.; *J. Appl. Polym. Sci.* **2010**, 115, 3586.
- (29) Cheryan, M. *Ultrafiltration and Microfiltration Handbook*, CRC Press, Jan 26, **1998**, pp 45.
- (30) Sorenson, T. S. *Surface Chemistry and Electrochemistry of Membranes*, CRC Press, Feb 16, **1999**, pp 231.
- (31) Franken, A. C. M.; Nolten, J. A. M.; Mulder, M. H. V.; Bargeman, D.; Smolders, C. A. *J. Membrane Sci.* **1987**, 33, 315-328.
- (32) Chang, F. M.; Hong, S. J.; Sheng, Y. J.; Tsao, H. K. *App. Phy. Lett.* **2009**, 95, 064102-1-064102-3.
- (33) Schmidt, D. L.; Brady, R. F.; Karen, L.; Schmidt, D. C.; Chaudhury, M. K. *Langmuir* **2004**, 20, 2830-2836.
- (34) Silverstein, R. M.; Webster, F. X. *Spectrometric Identification of Organic Compounds*, 6th ed.; John Wiley: New York, **1996**, Chapter 3, p 80.
- (35) G. Kang, H. Ko, C. Choi, *J. Korean Physical Society*, **2003**, 42, 676-681.

- (36) Stuart, B. H. *Analytical techniques in the sciences, Infrared spectroscopy: Fundamentals and Applications*, Wiley, 2004.